Optical and Morphological Aspects of Incommensurate Crystals

M. Kremers

Optical and Morphological Aspects of Incommensurate Crystals

Marcel Kremers

CIP-GEGEVENS KONINKLIJKE BIBLIOTHEEK, DEN HAAG

Kremers, Marcel

Optical and morphological aspects of incommensurate
crystals / Marcel Kremers. - [S.l. : s.n.](Meppel :
Krips Repro). - Ill.
Proefschrift Nijmegen. - Met lit. opg.
ISBN 90-9007948-3
Trefw.: kristallen / morfologie / optica.

Optical and Morphological Aspects of Incommensurate Crystals

een wetenschappelijke proeve op het gebied van
de Natuurwetenschappen

Proefschrift

ter verkrijging van de graad van doctor
aan de Katholieke Universiteit Nijmegen,
volgens besluit van het College van Decanen
in het openbaar te verdedigen op
maandag 3 april 1995,
des namiddags om 1.30 uur precies

door

Marcel Kremers

geboren op 24 mei 1967
te Gassel, gemeente Beers

1995
Druk: Krips Repro Meppel

Promotores:	Prof. Dr. A.G.M. Janner
	Prof. Dr. P. Bennema
	Prof. Dr. T. Janssen, Universiteit Utrecht
Co-promotor:	Dr. H.L.M. Meekes
Manuscriptcommissie:	Prof. Dr. J.P.J.M. van der Eerden
	Prof. Dr. A.M. Glazer

De totstandkoming van dit proefschrift vindt zijn oorsprong bij het practicum Materiaalkunde. Ondanks het volledig mislukken van de practicumopdracht bleek onze begeleider Erwin in staat mij voor de wetenschap van de vaste stof te interesseren. Niet lang daarna werkte ik samen met Marijn aan het operationeel maken van een ellipsometer. De belangstelling voor de wetenschap van de vaste stof bleef groeien en werd door Erwin voortdurend gevoed. Op deze plaats wil ik daarvoor mijn dankbaarheid uitspreken.

Erwin was wel de eerste, maar niet de enige die van groot belang is geweest. Tijdens mijn afstudeerwerk sprak ik met Hugo over een onderwerp voor een bijvak, waarna ik besloot om puntcontactspectroscopie aan calaveriet te gaan doen. Er ging weer een wereld voor mij open, om met Hugo te spreken. Bij deze bedank ik iedereen van Vaste Stof Fysica II en het Laboratorium voor Hoge Magneetvelden voor de tijd die ik op deze afdelingen heb mogen doorbrengen. Met name wil ik Henk en Richard noemen. De laatste was ook belangrijk voor mijn muzikale bezigheden. Het bleek dat ik het met de leden van het Micro Canoniek Ensemble niet alleen muzikaal maar ook wetenschappelijk goed kon vinden. Het MCE was het begin van een reeks muzikale avonturen. Naast wetenschap is ook muziek een passie geworden.

Na mijn afstuderen kon ik, onder directe begeleiding van Hugo, gaan werken op een gemeenschappelijk project van Aloysio en Piet. Op deze plaats wil ik Hugo bedanken voor vijf enerverende jaren waar ik steeds met veel plezier aan terug zal blijven denken. Het valt niet mee mijn waardering voor Hugo onder woorden te brengen, maar iedereen die ons aan het werk gezien heeft zal begrijpen wat ik bedoel. Tijdens het promotieonderzoek openbaarde zich een nieuw boeiend gebied van de fysica: de theorie. Ted heeft altijd voor me klaar gestaan bij het oplossen van theoretische vraagstukken. Daarnaast is vooral Aloysio essentieel geweest voor mijn kennismaking met de fysica. Zijn motivatie, inzicht en ervaring zijn zeldzaam en hebben mij voortdurend geïnspireerd. Ook in de periode dat ik wat minder energiek was heeft hij me onvoorwaardelijk gesteund.

Betreffende het gebied van de bandenstructuurberekeningen wil ik John en Ben bedanken voor het kijkje in de keuken dat ze me gegund hebben.

Het tweede deel van dit proefschrift beschrijft de resultaten van het zogenaamde 'gemoduleerde clubje', dat door Piet geleid werd. Zijn oorspronkelijke idee heeft een ontwikkeling in gang gezet waarin ik me heb kunnen uitleven. Ook denk ik met veel plezier terug aan de (wetenschaps)filosofische discussies en maatschappelijke beschouwingen die Piet met anderen en mij op touw zette. Bij deze wil ik graag iedereen van de afdeling Vaste Stof Chemie bedanken voor de prettige atmosfeer waarin ik heb mogen werken. Vanzelfsprekend geldt dit met name voor de vaste staf en de studenten die ik tot hun afstuderen heb mogen begeleiden.

Een aantal mensen hebben een belangrijke bijdrage geleverd door het oplossen van technische problemen. Alle ondersteunende afdelingen van de faculteit verdienen daarvoor lof. Daarnaast wil ik Ed bedanken voor zijn essentiele bijdrage aan de verbetering van het polijsten van de kristaloppervlakken.

I would like to acknowledge Prof. Glazer, Prof. Schmid and Prof. Lefebvre for their kind hospitality during my visits at their laboratories.

Behalve de wetenschap is er in Nijmegen en omgeving een aantal mensen erg belangrijk voor me. Sommigen van hen is het gelukt om me regelmatig in contact te brengen met de wereld buiten de wetenschap. Ik weet niet wat de toekomst brengt, maar ik hoop dat in ieder geval deze contacten blijven bestaan. In dit verband is er natuurlijk één persoon enorm belangrijk. Ik hoop dat vooral deze passie zal blijven groeien, wat er ook gebeurt.

Contents

Concise Introduction

Naturally occurring crystals have fascinated mineralogists since long. In 1669 Steno discovered that the faces on different crystals, with the same composition, always have fixed angles with respect to each other. Haüy proposed later that this regularity could be understood if crystals were composed of a stacking of identical building blocks (molécules intégrantes) with the same orientation. In other words, he proposed that the building block is a unit cell of a lattice in 3-dimensional space. It was then understood that crystal faces obey the law of rational indices. In 1848 Bravais established that crystal faces are perpendicular to vectors of the so-called reciprocal lattice. The combination of symmetry elements, such as mirrors and n-fold rotation axes ($n = 2,3,4,6$) with lattice translational periodicity led to the classification of the 3-dimensional space groups by Schoenflies and Von Fedorov in 1891. These symmetry groups are relevant for the shape of crystals, i.e. their morphology. This is worked out later on in the introduction to the morphology of crystals. Finally, in 1913, the connection with the microscopic structure was made by von Laue, Friedrich and Knipping using X-ray diffraction. The concept of 3-dimensional lattice translational symmetry is not only important for the understanding of crystal morphology. It has proven to be a basic concept for the understanding of many other physical properties of crystals.

More recently, however, incommensurately modulated phases were discovered in, for example, $NaNO_2$ (Tanisaki, 1961), Thiourea (Futama et al., 1967), Na_2CO_3 (de Wolff, 1972) and K_2SeO_4 (Iizumi et al., 1977). The latter compound is a member of a large family of A_2BX_4 crystals with a $\beta-K_2SO_4$ structure at high temperature and an incommensurately modulated phase at lower temperatures (see for a review Cummins, 1990). In this thesis several members of this family are studied. Modulated crystals arise from a periodic distortion (the modulation) of the lattice periodicity, which still applies to the averaged structure. When the period length of the modulation has a fixed rational ratio with the period length of this lattice, the deformed crystal forms a superstructure. Otherwise, the ratio can be considerd to be irrational and one has an incommensurately modulated crystal. In this case the lattice translational symmetry is broken, therefore, in at least one direction. It is then no longer possible to define a finite unit cell and to apply the normal crystallographic laws.

An example of another type of incommensurate crystals is the low temperature phase of $Hg_{3-\delta}AsF_6$ (Heilmann et al., 1979). This crystal consists of three different subsystems. Two of the subsystems are formed by chains of Hg atoms in mutually orthogonal directions. The third subsystem is the AsF_6 host structure. The crystal is incommensurate, because the distance between the Hg atoms is irrational with respect to the lattice constant of the (tetragonal) host structure. This is an example of the so-called incommensurate composite crystals.

A discovery that drew much more attention was that of an icosahedral phase in Al alloys with 10-14% Mn, Fe or Cr by Shechtman et al. (1984). A 5-fold symmetry axis was observed in the electron diffraction pattern of this interesting alloy. It was known since long, however, that such a rotational symmetry is incompatible with 3-dimensional lattice translational symmetry. Therefore, one adopted the name quasi-crystal for this kind of structures.

The just mentioned classes of incommensurate crystals (i.e. incommensurately modulated, incommensurate composite and quasi-crystals) have in common that they all are quasi-periodic. This means that the Fourier transform of the density function $\rho(\boldsymbol{r})$ can be written as

$$\rho(\boldsymbol{r}) = \sum_{\boldsymbol{k}\in \mathrm{M}^*} \hat{\rho}(\boldsymbol{k}) \exp(i\boldsymbol{k}\cdot\boldsymbol{r}),$$

where M* is the Fourier module of all vectors $\boldsymbol{k}$ that are of the form

$$\boldsymbol{k} = \sum_{i=1}^{n} h_i \boldsymbol{a}_i^*, \qquad h_i \in \mathbb{Z},$$

for a finite set of n rationally independent basis vectors $\boldsymbol{a}_1^*, \ldots \boldsymbol{a}_n^*$. The rank of the Fourier module is then n. Its dimension, on the other hand, is that of the space spanned by the basis vectors and is usually three. Incommensurate crystals are characterised by the fact that the rank of M* is larger than the dimension. The incommensurately modulated crystals discussed above have a rank 4 (one modulation wave) or higher (more modulation waves). The icosahedral quasi-crystal has a rank 6 Fourier module.

Important developments for the structural description of incommensurate crystals started around 1980 (de Wolff (1974), Janner and Janssen (1977), de Wolff et al. (1981), Janner et al. (1983)). The basic idea is that a quasi-periodic structure can be considered to be the restriction to the physical 3-dimensional space of a lattice periodic structure in n dimensions which takes into account the n fundamental periodicities of the Fourier module. One can speak, therefore, of the embedding of an incommensurate crystal in an n-dimensional superspace. The embedded structure then has an n-dimensional space group symmetry, called superspace group. The known quasi-crytals also show scaling symmetries, which in the superspace give rise to non-Euclidean crystallographic symmetries. The simultaneous presence of Euclidean and non-Euclidean symmetries has led to the use of so-called multi-metrical groups by Janner (1991a) (see also Janner, 1991b).

More details on the superspace approach and the properties of incommensurate crystals in terms of phenomenological theory or microscopic origin of the stability of such phases can be found in the review paper by Janssen and Janner (1987) and references therein.

The incommensurateness has definite consequences for the morphology. In part II of this thesis this aspect is studied from a theoretical point of view for both incommensurately modulated crystals and for quasi-crystals (though less extensively). It will be clear, however, that the absence of 3-dimensional lattice translational symmetry can have important consequences for other physical properties as well For example, much smaller wave vectors can be found for the structures of incommensurate crystals than for classical, commensurate crystals. Therefore, it is interesting to investigate the response to fields that have comparable wave vectors. In part I of this thesis the optical properties of incommensurately modulated crystals are studied, in this respect, from an experimental point of view. In the introduction to crystal optics it is explained which optical effects may be influenced by the presence of the incommensurate modulation.

The work presented in this thesis is intended to contribute to the research that may lead, in the end, to a better understanding and description of the physical properties of incommensurate crystals.

References

Cummins, H. Z., *Phys. Rep.* **185**, 211 (1990).

Futama, H. et al., *Physics Letters* **25**A, 8 (1967).

Heilmann, I. U., Axe, J. D., Hastings, J. M., Shirane, G., Heeger, A.J., and MacDiarmid, A. G., *Phys. Rev. B* **20**, 751 (1979).

Iizumi, M., Axe, J.D., Shirane, G., and Shimaoka, K., *Phys. Rev. B* **15**, 4392 (1977).

Janner, A., and Janssen, T., *Phys. Rev. B* **15**, 643 (1977).

Janner, A., Janssen, T., and de Wolff, P. M., *Acta Cryst. A* **39**, 671 (1983).

Janner, A., *Phys. Rev. B: Condensed matter* **43**, 13206 (1991a).

Janner, A., *Phys. Rev. Lett.* **67**, 2159 (1991b).

Janssen, T. and Janner, A., *Adv. Phys.* **36**, 519 (1987).

Shechtman, D., Blech, I., Gratias, D., and Cahn, J.W., *Phys. Rev. Lett.* **53**, 1951 (1984).

Tanisaki, S., *J. Phys. Soc. Japan* **16**, 579 (1961).

de Wolff, P. M., *Acta Cryst. A* **28**, S111 (1972).

de Wolff, P. M., *Acta Cryst. A* **30**, 777 (1974).

de Wolff, P. M., Janssen, T., and Janner, A., *Acta Cryst. A* **37**, 625 (1981).

Part I

Optical Aspects of Incommensurate Crystals

Chapter 1

Introduction to (incommensurate) crystal optics

Introduction to (incommensurate) crystal optics

M. Kremers

1.1 Introduction

Crystal optics is concerned with the propagation of electromagnetic radiation, in the form of light, in crystals. First, we give a restricted survey of the optical effects that can occur in classical crystals, concerning the transmission of light. This is done by means of a macroscopic, phenomenological treatment. The microscopic origins for the optical effects are not discussed. Moreover, the influence of externally applied electric or magnetic fields or elastic deformations is not described. Afterwards, we review the descriptions that have been developed for the optics of incommensurate crystals. It is explained why the optical properties of incommensurately modulated crystals are of interest.

1.2 Classical crystal optics

1.2.1 The constitutive equations

The macroscopic Maxwell equations can be obtained from the fundamental microscopic Maxwell equations by means of an appropriate way of averaging (see for example Mazur and Nijboer, 1953). The macroscopic electromagnetic field in a crystal must then, of course, satisfy these macroscopic Maxwell's equations:

$$\begin{aligned}
\nabla \times \boldsymbol{H} &= \frac{1}{c}\frac{\partial \boldsymbol{D}}{\partial t} + \frac{\boldsymbol{j}}{c} \\
\nabla \times \boldsymbol{E} &= -\frac{1}{c}\frac{\partial \boldsymbol{B}}{\partial t} \\
\nabla \cdot \boldsymbol{D} &= \rho \\
\nabla \cdot \boldsymbol{B} &= 0,
\end{aligned} \tag{1.1}$$

where

$\boldsymbol{E}$ is the electric field
$\boldsymbol{D}$ is the electric induction or displacement field
$\boldsymbol{H}$ is the magnetic field
$\boldsymbol{B}$ is the magnetic induction
$\boldsymbol{j}$ is the current density
ρ is the charge density
c is the velocity of light in vacuum.

The propagation of light in a crystal is further determined by the so-called constitutive equations. In order to find these, we assume that the frequency of the light is much larger than the frequencies of magnetic resonances in the crystal. The magnetisation of the crystal can, in that case, not follow the rapid oscillations of the magnetic component of the light. The magnetic permeability tensor $\boldsymbol{\mu}$ in the constitutive equation $\boldsymbol{B} = \boldsymbol{\mu}\boldsymbol{H}$ can be taken equal to the second rank unit tensor $\mathbf{1}$.

The electric field $\boldsymbol{E}$ of the light can induce a current density $\boldsymbol{j}$ according to the constitutive equation:

$$\boldsymbol{j} = \boldsymbol{\sigma}\boldsymbol{E}, \tag{1.2}$$

where $\boldsymbol{\sigma}$ is the specific conductivity tensor. It is well known (Born, 1985), however, that the conductivity of a medium can be taken into account by defining a complex dielectric permeability tensor and renormalising the displacement field $\boldsymbol{D}' = \boldsymbol{D} + \frac{1}{c}\boldsymbol{j}$ (Ramachandran and Ramaseshan, 1961). The macroscopic Maxwell equations can then be used with $\boldsymbol{j} = 0$, $\rho = 0$ and substituting $\boldsymbol{D}'$ for $\boldsymbol{D}$.

In addition, the crystal is taken to be a linear, time independent and unbounded medium. It can, however, be spatially inhomogeneous. Thus, the constitutive equations can be written:

$$\begin{aligned} B_i(\boldsymbol{r}) &= H_i(\boldsymbol{r}) && (1.3)\\ D_i(\boldsymbol{r}) &= \int \varepsilon_{ij}(\boldsymbol{r},\boldsymbol{r}')E_j(\boldsymbol{r}')d\boldsymbol{r}'. && (1.4)\end{aligned}$$

In this introduction we use the Einstein summation convention. The Fourier transform of equation (1.4), for a crystal with a reciprocal lattice Λ^* can be written (see Agranovich and Ginzburg, 1984):

$$D_i(\boldsymbol{k}) = \hat{\varepsilon}_{ij}(\boldsymbol{k},0)E_j(\boldsymbol{k}) + \sum_{\boldsymbol{h}\neq 0,\boldsymbol{h}\in\Lambda^*} \hat{\varepsilon}_{ij}(\boldsymbol{k},\boldsymbol{h})E_j(\boldsymbol{k}-\boldsymbol{h}). \tag{1.5}$$

The wavevectors $\boldsymbol{k}$ of visible light are, however, very small compared to any $\boldsymbol{h} \neq 0$. This means that only the first term on the right hand side of equation (1.5) has to be retained, because the coupling between the long wavelength field $\boldsymbol{D}(\boldsymbol{k})$ and the short wavelength fields $\boldsymbol{E}(\boldsymbol{k}-\boldsymbol{h}) \approx \boldsymbol{E}(-\boldsymbol{h})$ can be neglected (see also, Agranovich and Ginzburg, 1984). In classical crystal optics, one therefore assumes that

$$D_i(\boldsymbol{k}) \approx \hat{\varepsilon}_{ij}(\boldsymbol{k})E_j(\boldsymbol{k}). \tag{1.6}$$

The fact that $\hat{\boldsymbol{\varepsilon}}$ is a function of $\boldsymbol{k}$ is called spatial dispersion. In the optical region, however, the spatial dispersion will be weak. The reason for this is, again, that $\boldsymbol{k}$ is always small with respect to any non-zero reciprocal lattice vector $\boldsymbol{h} \in \Lambda^*$:

$$\frac{|\boldsymbol{k}|}{|\boldsymbol{h}|} \approx \frac{a}{\lambda},$$

where a is the typical dimension of the unit cell of the lattice Λ and λ is the wavelength of the light. The finiteness of the wavelength of the light can, therefore, be taken into account by expanding $\hat{\boldsymbol{\varepsilon}}$ up to first order terms in $\boldsymbol{k}$:

$$\hat{\varepsilon}(\boldsymbol{k}) \approx \hat{\varepsilon}(0) + i\hat{\gamma}(0)\boldsymbol{k}. \tag{1.7}$$

Thus, one finds

$$D_i(\boldsymbol{k}) \approx \left(\hat{\varepsilon}_{ij}(0) + i\hat{\gamma}_{ijk}(0)k_k\right) E_j(\boldsymbol{k}). \tag{1.8}$$

Finally, the Fourier transform of this equation gives the following constitutive equation, that is to be used in classical crystal optics:

$$\boldsymbol{D}(\boldsymbol{r}) = (\boldsymbol{\varepsilon} + \boldsymbol{\gamma}\boldsymbol{\nabla}_{\boldsymbol{r}})\, \boldsymbol{E}(\boldsymbol{r}), \tag{1.9}$$

where $\boldsymbol{\varepsilon}$ and $\boldsymbol{\gamma}$ are space-averaged, macroscopic tensors. It is now clear that weak spatial dispersion can be taken into account by including such a non-local response of the displacement field $\boldsymbol{D}$ on the electric field $\boldsymbol{E}$. The optical effects caused by this additional term can be expected to have a typical magnitude a/λ.

The constitutive equations for classical crystal optics can thus be written:

$$\begin{aligned} D_i(\boldsymbol{r}) &= \varepsilon_{ij}E_j(\boldsymbol{r}) + \gamma_{ijk}\frac{\delta E_j(\boldsymbol{r})}{\delta r_k} \equiv \tilde{\varepsilon}_{ij}E_j(\boldsymbol{r}) \\ B_i(\boldsymbol{r}) &= H_i(\boldsymbol{r}). \end{aligned} \tag{1.10}$$

1.2.2 Restrictions on the material tensors

The so-called material tensors $\boldsymbol{\varepsilon}$ and $\boldsymbol{\gamma}$ in equation (1.10) determine the optical properties of the crystal. In general, all components of these tensors can be different and complex. In many cases, however, restrictions can be imposed on these tensors, for example by a requirement of losslessness or by the 'Onsager principle'.

The *electric loss* of the electromagnetic field of light in a crystal is given by an integral over the volume $\int \boldsymbol{E} \cdot \frac{\partial \boldsymbol{D}}{\partial t} dV$ (Landau and Lifshitz, 1984). In a non-absorbing crystal there is no electric loss. This requirement gives the following restrictions for the material tensors:

$$\begin{aligned} \varepsilon_{ij} &= \varepsilon^*_{ji} \\ \gamma_{jik} &= -\gamma^*_{ijk}. \end{aligned} \tag{1.11}$$

This means that in a non-absorbing crystal, the tensor $\boldsymbol{\varepsilon}$ can only have a real symmetric part and an imaginary antisymmetric part:

$$\boldsymbol{\varepsilon} = \boldsymbol{\varepsilon}'^s + i\boldsymbol{\varepsilon}''^a. \tag{1.12}$$

Furthermore, the tensor γ can only have a real antisymmetric (in the first two indices) part and an imaginary symmetric part:

$$\gamma = \gamma'^{a} + i\gamma''^{s}. \tag{1.13}$$

Moreover, from the study of energy change of the electromagnetic field in the crystal it can be derived that the absorption of light is determined by the imaginary part of the tensor $\tilde{\varepsilon}$. By means of thermodynamic arguments (increase of entropy) one derives that the imaginary part of $\tilde{\varepsilon}$ is positive. There is no physical restriction for the sign of the real part of this tensor (Landau and Lifshitz, 1984). For a detailed thermodynamic treatment of the electomagnetic field in crystals with spatial dispersion, we refer to Agranovich and Ginzburg (1984).

The tensors ε''^{a} and γ'^{a} are odd functions of the frequency ω of the light (Post, 1962). They can, therefore, not contain a constant part. This implies that the optical effects that are associated with these tensors are essentially frequency dispersive. The tensors ε'^{s} and γ''^{s}, on the other hand, are even functions of the frequency. The optical effects related to these tensors are, therefore, not necessarily frequency dispersive. They can be constant, independent of the frequency ω.

In case that the crystal is symmetric under time reversal, one can apply the *'Onsager principle'*. This is also known as *'the generalised principle of the kinetic coefficients'*. Time reversal symmetry can be broken in magnetic crystals (see, O'Dell, 1970). For (absorbing) non-magnetic crystals, however, the 'Onsager principle' gives (see again Landau and Lifshitz, 1984):

$$\begin{aligned} \varepsilon_{ij} &= \varepsilon_{ji} \\ \gamma_{ijk} &= -\gamma_{jik}. \end{aligned} \tag{1.14}$$

This means that in a crystal that is non-magnetic, the tensor ε can only have a real symmetric part and an imaginary symmetric part:

$$\varepsilon = \varepsilon'^{s} + i\varepsilon''^{s}. \tag{1.15}$$

In addition, the tensor γ can only have a real antisymmetric part and an imaginary antisymmetric part:

$$\gamma = \gamma'^{a} + i\gamma''^{a}. \tag{1.16}$$

If a crystal is neither lossless nor non-magnetic, the tensor ε can also have a real antisymmetric part, ε'^{a}, and the tensor γ can have a real symmetric part, γ'^{s}. In this way, one can distinguish eight different tensors. It is explained below that each of these tensors corresponds to a certain optical effect:

1.2.3 Proper Waves

In general, the optical properties of a medium are characterised by the proper waves, i.e. the electromagnetic waves that can propagate without change of their polarisation. Usually, one searches for plane wave solutions that satisfy both the Maxwell equations and the constitutive equations. Plane waves are of the form:

$$\boldsymbol{E},\boldsymbol{H},\boldsymbol{D},\boldsymbol{B} = \boldsymbol{E}_0,\boldsymbol{H}_0,\boldsymbol{D}_0,\boldsymbol{B}_0 \ \exp\left(-i\omega\left[t-\boldsymbol{r}\cdot\boldsymbol{s}\frac{n}{c}\right]\right), \tag{1.17}$$

where ω is the circular frequency of the light, n is the (complex) refractive index and $\boldsymbol{s}$ is a unit vector in the direction of the wave normal.
The wave vector $\boldsymbol{k}$ is then:

$$\boldsymbol{k} = \frac{\omega n}{c}\boldsymbol{s}. \tag{1.18}$$

At this point we want to point out that specific cases exist, in absorbing crystals, where the use of plane waves does not give satisfactory results (see, for example Khapalyuk, 1963). Nevertheless, in most cases plane waves solutions can be obtained.

For the plane waves of equation (1.17), the first two of the macroscopic Maxwell equations (1.1) become:

$$\begin{aligned} n\boldsymbol{H}\times\boldsymbol{s} &= \boldsymbol{D} \\ -n\boldsymbol{E}\times\boldsymbol{s} &= \boldsymbol{B}. \end{aligned} \tag{1.19}$$

Using the second of the constitutive equations (1.10), the vector $\boldsymbol{H}$ can be eliminated. Thus, one finds:

$$\boldsymbol{D} = n^2\{\boldsymbol{E}-(\boldsymbol{E}\cdot\boldsymbol{s})\boldsymbol{s}\}. \tag{1.20}$$

It is found that the proper waves must satisfy simultaneously equation (1.20) and the first of the constitutive equations (1.10). The combination of (1.20) and (1.10) leads to the so-called Fresnel equations. Solving these, one finds the polarisations $\boldsymbol{E}_0$ and the refractive indices n of four waves with wave vector $\boldsymbol{k}$. Two proper waves correspond to propagation in the direction $+\boldsymbol{s}$ and the other two correspond to propagation in the direction $-\boldsymbol{s}$. The light propagation is said to be non-reciprocal if the solutions for $+\boldsymbol{s}$ and $-\boldsymbol{s}$ are different. Otherwise, it is reciprocal.

In the following subsections, we consider the proper waves defined by each of the eight different material tensors. Moreover, the influence of the symmetry of the crystal is discussed.

1.2.3.1 The tensor $\boldsymbol{\varepsilon}'^{s}$: linear birefringence

The two proper waves defined by $\boldsymbol{\varepsilon}'^{s}$ for a propagation direction $\boldsymbol{s}$ are linearly polarised and mutually orthogonal. The corresponding refractive indices are real and invariant under reversal of the direction of the light propagation. The tensor $\boldsymbol{\varepsilon}'^{s}$ is non-zero for all crystals. However, the (non-magnetic) point group, K, of the crystal imposes symmetry restrictions on $\boldsymbol{\varepsilon}'^s$ (see for example Born, 1985). Under an orthogonal transformation $\boldsymbol{R} \in K$ the tensor transforms according to:

$$\left(\varepsilon'^s_{ij}\right)' = R_{ik}R_{jl}\,\varepsilon'^s_{kl}. \tag{1.21}$$

Since the tensor $\boldsymbol{\varepsilon}'^s$ is real and symmetric, it can be diagonalised. If, then, the diagonal elements are ε_1, ε_2 and ε_3, one can define the so-called indicatrix (see for example Nye, 1985) in the following way:

$$\frac{x_1^2}{n_1^2} + \frac{x_2^2}{n_2^2} + \frac{x_3^2}{n_3^2} = 1, \tag{1.22}$$

where $n_1 = \sqrt{\varepsilon_1}$, $n_2 = \sqrt{\varepsilon_2}$ and $n_3 = \sqrt{\varepsilon_3}$ are the principal refractive indices. By means of a geometrical construction one can use the indicatrix to find the refractive indices for the proper waves propagating in any direction. Essentially three different cases can be distinguished; isotropic, uniaxial and biaxial crystals. In isotropic crystals, the value of the refractive index is independent of both the propagation direction $\boldsymbol{s}$ and of the polarisation of the light. The indicatrix of an isotropic crystal is a sphere. In uniaxial crystals, there is only one direction, the optic axis, for which the refractive indices of the two proper waves are equal. In all other directions the phenomenon of double refraction can be observed. This optical effect was discovered in 1669 by Erasmus Bartholinus in crystals of calcite (Lowry, 1935). The indicatrix of a uniaxial crystal is necessarily an ellipsoid of revolution about the optic axis. The fact that, in general, the two linearly polarised proper waves for a certain propagation direction have different refractive indices (and, therefore, different wave normal velocities) is usually referred to as linear birefringence. In biaxial crystals there are two optic axes and the indicatrix is a triaxial ellipsoid. The linear birefringence is again zero for light propagation along the two optic axes in this case.

1.2.3.2 The tensor $\boldsymbol{\varepsilon}''^s$: linear dichroism

The optical effect associated with the tensor $\boldsymbol{\varepsilon}''^s$ is called linear dichroism. It was first observed by Biot (1815) in crystals of tourmaline. Linear dichroism can not exist in lossless crystals. The proper waves derived from the Fresnel equations with $\boldsymbol{\varepsilon}''^s$ are again mutually orthogonal and linearly polarised. The corresponding refractive indices are imaginary, corresponding to the fact that these waves are absorbed in the crystal. Linear dichroism is a reciprocal effect. Again, the (non-magnetic) point group imposes symmetry restrictions, in the same way as for linear birefringence. It must be noted, however, that the principal axes of the tensors $\boldsymbol{\varepsilon}'^s$ and $\boldsymbol{\varepsilon}''^s$ can lie along different directions in the case of biaxial crystals. Moreover, analogous to optic axes in linear birefringent crystals, there exist axes in linear dichroic crystals where the linear dichroism is zero. In case of biaxial crystals that are both linearly birefringent and dichroic, the directions of these axes do not necessarily coincide with the directions of the optic axes.

1.2.3.3 The tensor ε''^a: the Faraday effect

The imaginary antisymmetric part of ε gives rise to a non-reciprocal optical effect, which is known as the Faraday effect. It was discovered by Faraday (1846) in lead-glass by applying a static magnetic field in the direction of the wave vector of the light. The time reversal symmetry is broken in this way, so that the tensor ε''^a is non-zero. The Faraday effect, however, can also occur in magnetic crystals without an external static magnetic field (see Pisarev, 1970). The proper waves that follow from the Fresnel equations are a left- and right-circularly polarised wave, having different propagation velocities (different real refractive indices). Therefore, linearly polarised light that is incident on a crystal can be thought to be resolved in these two proper waves. After passage through the crystal, the light is again linearly polarised, but rotated with respect to the incident polarisation. If the direction of the applied magnetic field or, alternatively, the magnetisation of the crystal is reversed, also the sense of rotation of the polarisation of the light is reversed.

1.2.3.4 The tensor ε'^a: magnetic circular dichroism

Magnetic or non-reciprocal circular dichroism can only exist in absorbing media. In 1932 it was observed in solutions of cobalt salts and of thiobenzophenone by Cotton and Schérer (source: Lowry, 1935) using a powerful electromagnet. The proper waves are circularly polarised in the same way as they are in case of the Faraday effect. The refractive indices, however, are imaginary. The proper waves are, therefore, absorbed in the crystal. For the existence of magnetic circular dichroism it is necessary that time reversal symmetry is broken. Recently, there has been a lot of interest to detect this effect in high-T_c superconductors (Krichevtsov et al., 1991), because this would give evidence of broken time reversal symmetry in these systems. The breaking of both time reversal and spatial inversion symmetry is predicted by the so-called anyon model of superconductivity (Laughlin, 1988).

1.2.3.5 The tensor γ'^a: circular birefringence

Circular birefringence is related to the antisymmetric real part of the tensor γ. The existence of this effect was first observed by Arago (1811) in quartz crystals. It is also well-known under the name natural optical activity. The proper waves are left- and right-circularly polarised and the refractive indices are real, so that an incident linear polarisation can be rotated after passage through the crystal (Fresnel, 1866). The sense of rotation, however, remains invariant under reversal of the propagation direction of the light. One can express this by saying that there is a fixed screw sense in the crystal. For reasons that become apparent later on, the investigation of circular birefringence in incommensurately modulated crystals is one of the main subjects of this thesis. Therefore, we want to elaborate at this point the equations that are commonly used for the description of circular birefringence (Sommerfeld, 1959).

For plane waves (1.17) the first of the constitutive equations (1.10) can be written:

$$D_i = (\varepsilon_{ij} + \frac{i\omega n}{c}\gamma_{ijk}s_k)E_j. \tag{1.23}$$

In case that γ is a real third rank tensor, antisymmetric in the first two indices, one can introduce a second rank antisymmetric tensor γ:

$$\gamma_{ij} = \frac{\omega n}{c}\gamma_{ijk}s_k. \tag{1.24}$$

Instead of equation (1.23) one then has

$$D_i = (\varepsilon_{ij} + i\gamma_{ij})E_j. \tag{1.25}$$

Subsequently, the gyration vector γ is usually introduced:

$$\gamma_i = \frac{1}{2}e_{ijk}\gamma_{jk}, \tag{1.26}$$

where $e_{ijk} = \frac{1}{2}(i-j)(j-k)(k-i)$ is the antisymmetrical unit tensor. It follows that

$$\boldsymbol{D} = \boldsymbol{\varepsilon E} - i\boldsymbol{\gamma} \times \boldsymbol{E}. \tag{1.27}$$

On the other hand, it is also possible to define a real, second rank, pseudo gyration tensor $\boldsymbol{g}$ due to the antisymmetry of the third rank tensor γ:

$$g_{il} = -\frac{1}{2}\frac{\omega n}{c}e_{ijk}\gamma_{jkl}. \tag{1.28}$$

In terms of this pseudo tensor $\boldsymbol{g}$ the constitutive equation becomes:

$$\boldsymbol{D} = \boldsymbol{\varepsilon E} + i\boldsymbol{g}(\boldsymbol{s} \times \boldsymbol{E}). \tag{1.29}$$

Using the second Maxwell equation (1.19) for plane waves and $\boldsymbol{B} = \boldsymbol{H}$, one obtains

$$\begin{aligned} \boldsymbol{D} &= \boldsymbol{\varepsilon E} - i\frac{1}{n}\boldsymbol{gH} \\ &= \boldsymbol{\varepsilon E} + \frac{1}{n\omega}\boldsymbol{g}\frac{\partial \boldsymbol{H}}{\partial t}. \end{aligned}$$

It is now clear, that a crystal is circularly birefringent if it generates an electric dipole moment when subjected to a change of the magnetic field. This can be understood to be one of the effects caused by a non-local dependence of the displacement vector $\boldsymbol{D}$ on the electric field $\boldsymbol{E}$.

To a good approximation, the amount of gyration, G, for light propagating in a direction $\boldsymbol{s}$ not too close to an optic axis of the linear birefringence, is given by (see for example Born, 1985):

$$G = g_{ij}s_is_j = -\boldsymbol{\gamma} \cdot \boldsymbol{s}. \tag{1.30}$$

From G, the so-called rotatory power ρ can be calculated (Nye, 1985):

$$\rho = \frac{\pi G}{\lambda_0 \tilde{n}}, \tag{1.31}$$

where λ_0 is the wavelength of the light in vacuum and $\tilde{n}$ can be taken as the average of the three principal refractive indices related to the linear birefringence (see Born, 1985). Although the pseudo tensor $\boldsymbol{g}$ is not necessarily symmetric, equation (1.30) shows that the antisymmetric part of $\boldsymbol{g}$ does not contribute to the amount of gyration. Therefore, $\boldsymbol{g}$ is usually taken symmetric to describe the natural optical activity.

Also for this circular birefringence, the (non-magnetic) point group of the crystal imposes symmetry restrictions on the tensor $\boldsymbol{g}$. However, since $\boldsymbol{g}$ is a pseudo tensor, it transforms as:

$$g'_{ij} = \det(R) R_{ik} R_{jl}\, g_{kl} \tag{1.32}$$

under an orthogonal element $\boldsymbol{R}$ of the point group. In case of the presence of an inversion center, $\bar{1}$, one has

$$\boldsymbol{R}(\bar{1}) = \begin{pmatrix} \bar{1} & 0 & 0 \\ 0 & \bar{1} & 0 \\ 0 & 0 & \bar{1} \end{pmatrix}$$

and

$$g'_{ij} = -g_{ij}.$$

The gyration tensor is, therefore, necessarily zero if the crystal is invariant under spatial inversion.

1.2.3.6 The tensor γ''^{a}: circular dichroism

Circular dichroism is related to circular birefringence as linear dichroism is to linear birefringence. The proper waves in a purely circularly dichroic crystal are right- and left-circularly polarised. The corresponding (different) refractive indices are imaginary, so that the waves are absorbed in the crystal. The existence of circular dichroism was first observed by Haidinger (1847) in amethyst quartz. Lossless crystals, or crystals that are centrosymmetric can not exhibit circular dichroism.

1.2.3.7 The tensor γ''^{s}: gyrotropic birefringence

The name gyrotropic birefringence indicates, on the one hand, that it is an effect related to the third rank tensor γ and, on the other hand, that the optical effect is a special kind of linear birefringence. An alternative name for this effect is non-reciprocal linear birefringence, indicating that it is a non-reciprocal effect. The possible existence of gyrotropic birefringence was first suggested by Brown et al. (1963). Both spatial inversion and time reversal symmetry have to be broken for the occurrence of this effect. However, if the product of the two, $\bar{1}'$, is a symmetry, gyrotropic birefringence is allowed (Fuchs

(1965), Birss and Shrubsall (1967)). It can, therefore, occur in magneto-electric crystals, in which an applied static magnetic field induces a static electric polarisation and vice versa (O'Dell, 1970). In fact, gyrotropic birefringence can be seen as the induction of an electric polarisation by the magnetic field of the light itself and vice versa. The proper waves, typical for the tensor $\gamma^{\prime\prime s}$ are linearly polarised. However, due to the magnetic point group, the directions of polarisation can differ from those determined by the indicatrix that is defined by the tensor $\varepsilon^{\prime s}$. This is even the case if the principal axes of this indicatrix have a fixed direction that is determined by the non-magnetic point group. An estimation made by Hornreich and Shtrikman (1968) shows that the change in the direction of polarisation caused by the gyrotropic birefringence is in the order of 10^{-6} rad. Pisarev et al. (1991) have performed experiments that show that the effect may be larger in the case of Cr_2O_3.

1.2.3.8 The tensor $\gamma^{\prime s}$: gyrotropic dichroism

In absorbing crystals another non-reciprocal effect can exist, related to gyrotropic birefringence, that could be called gyrotropic dichroism (Graham and Raab, 1983). The symmetry properties under space inversion and time reversal are the same as for gyrotropic birefringence. The corresponding two proper waves are linearly polarised and their refractive indices are imaginary. Therefore, the proper waves are absorbed. As far as we know, no experimental observations of gyrotropic dichroism have been made up to now.

1.2.3.9 Summary of optical effects in classical crystals without external fields

The optical properties of classical crystals that have been discussed above are summarised in table 1.1.

tensor	optical effect	lossless	$1'$	$\bar{1}$	$1'$ and $\bar{1}$	$\bar{1}' = \bar{1}1'$
ε'^{s}	Linear Birefringence	+	+	+	+	+
ε''^{s}	Linear Dichroism	−	+	+	+	+
ε''^{a}	Faraday effect	+	−	+	−	−
ε'^{a}	Magnetic Circular Dichroism	−	−	+	−	−
γ'^{a}	Circular Birefringence	+	+	−	−	−
γ''^{a}	Circular Dichroism	−	+	−	−	−
γ''^{s}	Gyrotropic Birefringence	+	−	−	−	+
γ'^{s}	Gyrotropic Dichroism	−	−	−	−	+

Table 1.1 Properties of the real or imaginary and symmetric or antisymmetric parts of the material tensors $\boldsymbol{\varepsilon}$ and $\boldsymbol{\gamma}$ in equation (1.10). The properties under space inversion $\bar{1}$, time reversal $1'$ or their product $\bar{1}'$ are indicated. The symbols + indicates that the tensor is invariant under the operation whereas the symbol − indicates that the tensor changes sign under the operation. Note the difference between the last two columns of this table. Although losslessness is not a symmetry operator, the symbol − in the corresponding column means that the tensor is necessarily zero. On the other hand, the symbol + means that the corresponding optical effect can exist.

1.2.3.10 Combined optical effects

Although, in the previous subsections, the proper waves have been treated that correspond to specific parts of the material tensors $\boldsymbol{\varepsilon}$ and $\boldsymbol{\gamma}$, in general, a combination of these tensors determines the optical properties of the crystal. The proper waves are then more involved and the Fresnel equations are most difficult to solve. However, neglecting for the moment the gyrotropic birefringence and gyrotropic dichroism, the following classification of proper waves can be given (Ramachandran and Ramaseshan (1961), Grechushnikov and Konstantinova (1988)).

In transparent (i.e. non-absorbing), non-gyrotropic crystals two linearly polarised waves can propagate that are orthogonal to each other.

Two elliptical proper waves exist in crystals that are non-absorbing and optically active. The ellipses are similar and orthogonal. Their major axes coincide with the directions of oscillations in the same, but non-gyrotropic, crystal. The procession, in time, of the electric field vectors over the two ellipses is opposite.

In absorbing, non-gyrotropic crystals also two elliptical proper waves exist. Again, the ellipses are similar and orthogonal, but the procession of the electric field vector over the ellipses is for both waves in the same direction. The major axes of the ellipses, however, again coincide with the directions of oscillations in the same, but non-absorbing, crystal.

If the crystal is both absorbing and gyrotropic, the proper waves are no longer orthogonal. Moreover, the ellipticities of the proper waves are different. Nevertheless, in a direction where there is considerable birefringence, not too close to an optic axis, the ellipticities χ_1 and χ_2 of the proper waves can be well approximated by (Grechushnikov and Konstantinova, 1988):

$$\begin{aligned} \chi_1 &= k_s - k_a \\ \chi_2 &= k_s + k_a, \end{aligned}$$

where k_s would be the ellipticity if the crystal were non-gyrotropic and k_a would be the ellipticity if there were no absorption. These approximations are a demonstration of the fact that in many cases the so-called method of superposition can be used in crystal optics.

In this introduction to crystal optics the method of superposition is not worked out, but we give references to the relevant literature. The principle ideas of this method have been explained very nicely by Pancharatnam (1958). The method finds its application in the Poincaré sphere representation of the polarisation of light (see for example Ramachandran and Ramaseshan, 1961) and in the well-known Jones matrix calculus for light propagation through optical systems (Jones (1948), Azzam and Bashara (1989)).

1.2.4 Alternative set of constitutive equations

In the case of magnetic crystals, it may seem more appropriate to use, instead of the equations (1.10), the following constitutive equations:

$$\begin{aligned} D_i &= \epsilon_{ij} E_j + \alpha_{ij} H_j \\ B_i &= \beta_{ij} E_j + \mu_{ij} H_j, \end{aligned} \qquad (1.33)$$

so that the impermeability tensor μ is explicitly taken into account. It has been shown by Hornreich and Shtrikman (1968) that, in this case, the demand of losslessness gives the following restrictions:

$$\begin{aligned} \epsilon_{ij} &= \epsilon^*_{ji} \\ \left(\mu^{-1}\right)_{ij} &= \left(\mu^{-1}\right)^*_{ji} \\ \alpha_{ij} &= \beta^*_{ji}. \end{aligned}$$

The same authors showed that it is possible to renormalise these equations, so that tensors are obtained that are analogous to those that describe the optical effects treated in the previous section for lossless crystals. Unfortunately, however, these tensors are involved combinations of the tensors $\boldsymbol{\epsilon}$, $\boldsymbol{\mu}$ and $\boldsymbol{\alpha}$. Therefore, unless there are indications that the tensor $\boldsymbol{\mu}$ can really differ from the unit tensor, it is more convenient to use the constitutive equations (1.10).

1.3 Incommensurate crystal optics

One of the basic ingredients in the description of the optical properties of classical crystals is the fact that the wavelength of the light is much larger than the periodicities present in the crystal, $\lambda >> a$. In incommensurate crystals, however, the situation can be different.

Consider an incommensurately modulated crystal with a one-dimensional modulation. The wave vectors of the Fourier transform of the charge density are of the form:

$$\boldsymbol{h} = \sum_{i=1}^{4} h_i \boldsymbol{a}_i^*, \quad h_i \text{ integers.} \tag{1.34}$$

The first three vectors, $\boldsymbol{a}_1^*$, $\boldsymbol{a}_2^*$ and $\boldsymbol{a}_3^*$ can be considered to span the reciprocal lattice of the structure that would be obtained by averaging the effect of the modulation. The vector $\boldsymbol{a}_4^*$ is the modulation wave vector, that is also often denoted with $\boldsymbol{q}$. The wave vectors $\boldsymbol{h}$ span a $\mathbb{Z}$-module, M^*, of rank 4 and dimension 3, which implies that there can be no 3-dimensional lattice translational symmetry. There is no integral linear combination of the four vectors $\boldsymbol{a}_i^*$ that equals zero, because the modulation wave vector has the form:

$$\boldsymbol{q} = \boldsymbol{a}_4^* = \sum_{i=1}^{3} q_i \boldsymbol{a}_i^* \tag{1.35}$$

and at least one of the three numbers q_i is irrational. Consequently, periodicities are present in the crystal that are much longer than the lattice constants of the non-modulated crystal. For example, if $q_1 = q_2 = 0$ and $q_3 = (\frac{h}{m} - \delta)$, where h and m are integers and δ is a small irrational number, there is a vector

$$\boldsymbol{h} = h\boldsymbol{a}_3^* - m\boldsymbol{a}_4^* = m\delta \boldsymbol{a}_3^*.$$

For each irrational number q_3, integer values for h and m can be chosen such that δ becomes arbitrarily small. Thus, in principle, arbitrarily small wave vectors $\boldsymbol{h}$ can be found, implying that long wavelength periodicities are present in the crystal. It is well known, however, that the structural information, carried by a wave vector, becomes less as the indices h_i of equation (1.34) become larger. Nevertheless, it is clear that in an incommensurately modulated crystal it is no longer valid to take a as the typical periodicity of the crystal. As a consequence, the spatial dispersion of the material tensors is no longer weak and the approximations made for the optical properties of classical crystals must be reconsidered.

1.3.1 Constitutive equations

The starting point for the optical properties of incommensurately modulated crystals that has been chosen by Meekes and Janner (1988) and Dijkstra et al. (1992) is the constitutive equation:

$$D_i(\boldsymbol{k}) = \sum_{\boldsymbol{h}\in M^*} \hat{\varepsilon}_{ij}(\boldsymbol{k},\boldsymbol{h})E_j(\boldsymbol{k}-\boldsymbol{h}) \tag{1.36}$$

This very much resembles equation (1.5), but the vectors $\boldsymbol{h}$ are here taken to run through the $\mathbb{Z}$-module M^*. This is fully justified, because these vectors precisely represent the periodicities that are present in the crystal. It has been explained above, that not only the $\boldsymbol{h}=0$ component is expected to be important now. Therefore, one expands all tensors $\hat{\boldsymbol{\varepsilon}}(\boldsymbol{k},\boldsymbol{h})$ up to first order in $\boldsymbol{k}$:

$$\hat{\boldsymbol{\varepsilon}}(\boldsymbol{k},\boldsymbol{h}) = \hat{\boldsymbol{\varepsilon}}(\boldsymbol{h}) + \hat{\boldsymbol{\gamma}}(\boldsymbol{h})\boldsymbol{k}. \tag{1.37}$$

Note, that for $\boldsymbol{h}=0$ this reduces to equation (1.7) used in classical crystal optics.

Thus, the following equation is obtained:

$$D_i(\boldsymbol{k}) = \sum_{\boldsymbol{h}\in M^*} \hat{\varepsilon}_{ij}(\boldsymbol{h})E_j(\boldsymbol{k}-\boldsymbol{h}) + \sum_{\boldsymbol{h}\in M^*} \hat{\gamma}_{ijk}(\boldsymbol{h})k_kE_j(\boldsymbol{k}-\boldsymbol{h}). \tag{1.38}$$

Subsequently, the symmetry restrictions on the tensors $\hat{\boldsymbol{\varepsilon}}(\boldsymbol{h})$ and $\hat{\boldsymbol{\gamma}}(\boldsymbol{h})$ are worked out and the Fresnel equations are solved by taking a limited number of important wave vectors $\boldsymbol{h}$ into account. These procedures are shortly summarised in the following subsections, but for the details we refer to the original papers of Meekes and Janner (1988) and Dijkstra et al. (1992).

In order to understand equation (1.38) better, we give the corresponding equation in real space:

$$\boldsymbol{D}(\boldsymbol{r}) = \left(\boldsymbol{\varepsilon}(\boldsymbol{r}) + \boldsymbol{\gamma}(\boldsymbol{r})\nabla_{\boldsymbol{r}}\right)\boldsymbol{E}(\boldsymbol{r}). \tag{1.39}$$

The tensors $\boldsymbol{\varepsilon}$ and $\boldsymbol{\gamma}$, that are constant in classical crystal optics, now have a spatial dependence. The nonlocal response, however, is taken into account in the same way as for the classical case, by including the dependence of the displacement field on the gradient of the electric field.

At this point we would like to refer to the works of Golovko and Levanyuk (1979) and Fousek and Kroupa (1986). These authors have studied the light propagation in incommensurately modulated crystals for specific examples. They considered a space dependent dielectric tensor that depends on the order parameter as obtained from a Landau-like approach. For a comparison of their results with the approach described above, we refer to Meekes and Janner (1988).

1.3.2 Space dependent dielectric tensor

An incommensurately modulated crystal has no 3-dimensional lattice translational periodicity. Moreover, a normal space group description is not possible. The crystal can, however, be embedded in a so-called superspace (Janner and Janssen, 1977), in which the lattice translational periodicity is restored. Consequently, the symmetry of the crystal can be described by means of a superspace group G_s. In case of a crystal with a 1-dimensional modulation, the superspace is $3+1$-dimensional. It has a 3-dimensional subspace, called external space, which is in fact the physical space. Perpendicular to this external space is the 1-dimensional, so-called, internal space. A general element g_s of the superspace group G_s can be written as $g_s = \{\boldsymbol{R}_s |\, \boldsymbol{t}_s\} = \{\boldsymbol{R}, R_I |\, \boldsymbol{t}_s\}$, where $\boldsymbol{R}$ is an orthogonal transformation in external space and R_I is the part in internal space. The vector $\boldsymbol{t}_s = (\boldsymbol{t}, t_I)$ is a translation in superspace.

It has been shown by Janner and van Beest (1983) that the superspace group G_s of an incommensurately modulated crystal can be used to describe the invariance of the Fourier components of the material tensors. In case of the dielectric tensor, this invariance is given by:

$$\varepsilon_{ij}(\boldsymbol{h}) = \varepsilon'_{ij}(\boldsymbol{h}) = R_{ij}R_{jl}\varepsilon_{kl}(\boldsymbol{Rh})\exp\left(i\,(\boldsymbol{R}_s\boldsymbol{h}_s)\cdot\boldsymbol{t}_s\right), \tag{1.40}$$

where the vectors $\boldsymbol{h}$ have been embedded as vectors $\boldsymbol{h}_s$ in reciprocal superspace. Note, that the case of classical optics can be obtained by substituting $\boldsymbol{h} = 0$ and, therefore, $\boldsymbol{h}_s = 0$.

Meekes and Janner (1988) give the form of the Fourier components of $\boldsymbol{\varepsilon}$ for the superspace group $G_s = \mathrm{Pcmn}(00\gamma)(\mathrm{ss}\bar{1})$ and Dijkstra et al. (1992) for the superspace group $G_s = \mathrm{Pcmn}(00\gamma)(1\mathrm{s}\bar{1})$. These forms are shown to depend on the parity (even/odd) of h_3 and h_4. However, for each tensor-element ε_{ij} a combination of parities can be found that allows the element to be non-zero, even though the averaged structure is orthorhombic. Thus, it is found that the superspace group allows for a local symmetry breaking with respect to the average orthorhombic structure. The dielectric tensor can be considered to wiggle on a mesoscopic scale (see Dijkstra, 1991). In case that the Fresnel equations are solved using a limited number of Fourier components $\boldsymbol{\varepsilon}(\boldsymbol{h})$, it is found that the solutions are no longer proper waves, because the polarisations of the waves that can propagate are space dependent. Moreover, due to the presence of the modulation, the propagation velocities are changed. For the details we refer to the literature mentioned above. Here, however, we want to point out that there may be consequences of a wiggling dielectric tensor that can be observed experimentally.

For example, in a classical orthorhombic crystal the orientation of the indicatrix is fixed. The question is now raised, whether in the incommensurate crystal the wiggling of the dielectric tensor can give rise to the observation of a change in the orientation of the indicatrix. The concept of a wiggling dielectric tensor has been worked out by Dijkstra (1991) and Dijkstra et al. (1992) for the centrosymmetric superspace group

G_s =Pcmn(00γ)(1s$\bar{1}$) and later by Kushnir and Vlokh (1993). Also it was shown that the wiggling of the dielectric tensor can cause a sample of the incommensurate crystal to be optically active, although this effect depends on the position of the boundaries. Nevertheless, it shows that in an incommensurately modulated crystal that has a centrosymmetric average structure optical activity may be caused by a space dependent dielectric tensor $\boldsymbol{\varepsilon}(\boldsymbol{r})$. In classical crystal optics, optical activity can not occur in centrosymmetric crystals and in non-centrosymmetric crystals it is described with the gyration tensor $\boldsymbol{\gamma}$ instead of the dielectric tensor $\boldsymbol{\varepsilon}$.

Both a rotation of the indicatrix and the presence of optical activity may thus be caused by an incommensurate modulation of an orthorhombic and centrosymmetric basic crystal structure. The magnitude of such effects can not be derived, of course, from a phenomenological theory.

1.3.3 Long wavelength Fourier components of the gyration tensor

Thus far, the Fourier components of the tensor $\boldsymbol{\gamma}$ have not been discussed. The invariance of this tensor can also be described by means of the superspace group G_s:

$$\gamma_{ijk}(\boldsymbol{h}) = \gamma'_{ijk}(\boldsymbol{h}) = R_{im}R_{jn}R_{kp}\gamma_{mnp}(\boldsymbol{Rh})\exp\left(i\left(\boldsymbol{R}_s\boldsymbol{h}_s\right)\cdot\boldsymbol{t}_s\right). \qquad (1.41)$$

Also here, the case of classical crystal optics is represented by substituting $\boldsymbol{h} = 0$ and $\boldsymbol{h}_s = 0$.

In the introduction to classical crystal optics, it has been explained how the third rank tensor $\boldsymbol{\gamma}$ can be contracted to a vector $\boldsymbol{\gamma}$. The forms of vectors $\boldsymbol{\gamma}(\boldsymbol{h})$ that are obtained in this way have been determined by Meekes and Janner (1988) for the superspace group G_s = Pcmn(00γ)(ss$\bar{1}$). Again, the forms depend on the parities of h_3 and h_4. No solutions were derived for the Fresnel equations in which these tensors $\boldsymbol{\gamma}(\boldsymbol{h})$ were included. Nevertheless, a rotation of the polarisation around the wave normal $\boldsymbol{k}$ can be expected, whenever $\boldsymbol{k}\cdot\boldsymbol{\gamma}(\boldsymbol{r}) \neq 0$ (see equation 1.27).

Therefore, it can be expected that also the spatial dependence of the tensor $\boldsymbol{\gamma}$, caused by the presence of the incommensurate modulation, gives rise to possible optical activity in a modulated crystal that is centrosymmetric on the average. Also in this case, the phenomenological analysis does not predict the magnitude of such effects. Nevertheless, the conclusions of the presented treatment are enough reason in itself to try to observe experimentally the influence of the incommensurate modulation on the optical effects.

1.4 Earlier experiments; starting point of the present investigations

The first report on the observation of optical activity in an incommensurately modulated crystal was made by Kobayashi et al. (1981). These authors measured a non-zero element g_{13} (in case of the crystallographic settings of this thesis) in the incommensurate phase of $(NH_4)_2BeF_4$. They used a new polarimetric technique, that was later introduced by Kobayashi and Uesu (1983) as the High Accuracy Universal Polarimeter (HAUP). The HAUP technique allows for the simultaneous measurement of small optical activity as well as (considerably larger) linear birefringence. This is, of course, one of the problems that have to be overcome when different gyration tensor elements g_{ij} are to measured in non-isotropic crystals.

The crystal $(NH_4)_2BeF_4$ is a member of a whole family of A_2BX_4 compounds that exhibit a phase transition from a centrosymmetric paraelectric phase, with a $\beta-K_2SO_4$ structure, into an incommensurately modulated phase (Cummins, 1990). For some of these crystals, but not all, the superspace group symmetry has been determined and has been shown to be centrosymmetric (Hogervorst, 1986). Kobayashi and co-workers applied the HAUP method to many members of this family. Several different gyration tensor elements g_{ij} were measured, but in all cases g_{13} was found to be non-zero, whereas the other elements g_{ij} were generally zero. Surprisingly, however, for the crystal of $(C_3H_7NH_3)_2MnCl_4$ a non-zero g_{33} was found (Saito and Kobayashi, 1991). Unfortunately, no other gyration tensor elements were measured for this compound. The reason for this is, probably, that it is very difficult to prepare samples for other directions of measurement. Besides this result, we want to mention two other interesting effects that have been reported by workers of the group of Prof. Kobayashi.

In the incommensurate phase of $((CH_3)_4N)_2CuCl_4$ the indicatrix was seen to rotate (Uesu and Kobayashi, 1985). Note that the paraelectric phase is orthorhombic, so that the orientation of the indicatrix is fixed in that phase. In addition, however, a large global hysteresis was observed in the incommensurate phase for both the linear birefringence and the optical activity. We want to point out that one should be careful then, because such hysteresis may indicate that the modulation wave vector is locked at commensurate values in the incommensurate phase. This locking can, for example, be attributed to the presence of defects (compare the results of Bziouet et al. (1987) and Kapustianik et al. (1992)).

The second interesting observation was reported by Saito et al. (1985). About 1.5 °C below the phase transition from the paraelectric to the incommensurate phase a huge electro-optic effect was measured with HAUP in crystals of $((CH_3)_4N)_2ZnCl_4$. The derived electro-optical constants were found to be 10^5 times as large as those for normally available electro-optic materials. In Nijmegen, it was tried to reproduce these experiments (Gelinck, 1992). No influence of an externally applied electric field could be observed, however.

After Kobayashi, the group of Prof. Günter in Zürich also built a HAUP. Sanctuary (1985) measured the gyration tensor element g_{13} in crystals of Rb_2ZnCl_4 with this set-up. It was found to be non-zero, but a large temperature hysteresis was observed. With respect to this observation, we would like to refer to the work of Hedoux et al. (1989). These authors showed that the behaviour of the modulation wave vector in the incommensurate phase of Rb_2ZnCl_4 depends very sensitively on the method of crystal growth. A coexistence of phases with different modulation wave vector is even possible. In order to obtain decisive results concerning the behaviour of optical activity in (centrosymmetric) incommensurately modulated crystals it is, therefore, very important to use high quality crystals with low defect concentrations.

Using the same HAUP apparatus in Zürich, Meekes and Janner (1988) investigated the tensor elements g_{11}, g_{12} and g_{13} in crystals of Rb_2ZnBr_4. In one sample it was found that g_{13} was non-zero. Unfortunately, a closer look at this sample with a polarisation microscope has recently revealed that it consists of several parts that are slightly misoriented with respect to each other. In a second sample no gyration g_{13} could be observed in the paraelectric and incommensurate phase. Also g_{11} and g_{12} were found to be zero. It must be mentioned that also in the incommensurate phase of Rb_2ZnBr_4 the modulation wave vector is often locked at a commensurate value (see Hogervorst, 1986). It is important to realise, that the space group of this commensurate phase is believed to be $Pc2_1n$, which is a non-centrosymmetric space group that allows for a non-zero element g_{13}.

The following important developments were reported by Ortega et al. (1992). With a HAUP system built in their laboratory, these authors measured the element g_{13} in crystals of Rb_2ZnBr_4 and the g_{33} element in crystals of $((CH_3)_4N)_2CuCl_4$. In both cases, however, they could *not* observe detectable values of the gyration. The same group (Folcia et al., 1993) performed measurements of the g_{33} element in $((CH_3)_4N)_2ZnCl_4$. Also in this case, the results indicated that there was no optical activity.

The results of the Spanish group of workers disagreed, in turn, with the observations made by Dijkstra, Kremers and Meekes (1992). With the HAUP instrument built in Nijmegen (Dijkstra, 1991) it had been observed that even five elements of the gyration tensor were non-zero in the case of $((CH_3)_4N)_2ZnCl_4$. Moreover, already in the paraelectric phase non-zero values of the gyration were detected. The latter effect was also reported by Kushnir et al. (1993) in the case of the element g_{33} for $((CH_3)_4N)_2ZnCl_4$ crystals. These authors, however, did not use the HAUP technique.

For the case of $((CH_3)_4N)_2ZnCl_4$, new measurements have been published by Kobayashi et al. (1993). All tensor elements g_{ij} were measured with HAUP. Contrary to the just described results of other authors, it was found that there was gyration g_{13}, but only in the incommensurate phase. In the paraelectric phase it was found to be clearly zero. Furthermore, all other tensor elements were zero in both the paraelectric and incommensurate phase.

The just summarised developments were the starting point for the work reported in the first part of this thesis. In view of all the controversial results, it is obvious that several problems were still present, at the time, concerning the measurement of optical activity in incommensurately modulated crystal phases. The HAUP method for the measurement of optical activity in the presence of linear birefringence is, therefore, critically reviewed in chapter 2 of the present thesis. It is shown, that several improvements to both the HAUP set-up and the interpretation of the data were indeed necessary. In chapter 3 it is subsequently explained, how the HAUP method can be extended for the measurement of the different optical effects that can be present in absorbing, gyratory and even magnetic crystals. Then, new measurements are reported in chapter 4 for the crystal of $((CH_3)_4N)_2ZnCl_4$ that have been obtained by means of the improved HAUP method. The results of measurements on incommensurate $((CH_3)_4N)_2CuCl_4$ are presented in chapter 5. Crystals of $((CH_3)_4N)_2CuCl_4$ are dichroic, which makes the use of the extended HAUP method necessary. Finally, in chapter 6, the results are presented of HAUP measurements on crystals of $((CH_3)_4N)_2ZnCl_{4-x}Br_x$. The symmetry is intrinsically broken by the replacement of Cl for Br. These crystals are, therefore, optically active already in the paraelectric phase. We study the influence of the incommensurate modulation on the optical activity in the incommensurate phase.

References

Agranovich, V. M., and Ginzburg, V. L., *Crystal Optics with Spatial Dispersion, and Excitons* (Berlin: Springer-Verlag, 1974).

Arago, *Mém. Inst.* Part 1, 93 (1811).

Azzam, R. M. A., and Bashara, N. M., *Ellipsometry and polarized light* (Amsterdam: North-Holland, 1989).

Biot, *Bull. Soc. Philom.* 26 (1815).

Birss, R. R., and Shrubsall, R. G., *Phil. Mag.* **15**, 687 (1967).

Born, M., *Optik* (Berlin: Springer-Verlag, 1985).

Brown, W. F., Shtrikman, S., and Treves, D., *J. Appl. Phys.* **34**, 1233 (1963).

Bziouet, M., Almairac, R. and Saint-Grégoire, P., *J. Phys. C: Solid State Phys.* **20**, 2635 (1987).

Cummins, H. Z., *Phys. Rep.* **185**, 211 (1990).

Dijkstra, E., *J. Phys.: Condens. Matter* **3**, 141 (1991).

Dijkstra, E., Meekes, H., and Kremers, M., *J. Phys. D: Appl. Phys.* **24**, 1861 (1991).

Dijkstra, E., Janner, A., and Meekes, H., *J. Phys.: Condens. Matter* **4**, 693 (1992).

Dijkstra, E., Kremers, M., and Meekes, H., *J. Phys.: Condens. Matter* **4**, 715 (1992).

Faraday, M., *Philos. Trans. Roy. Soc., Lond.*, 1 (1846).

Folcia, C. L., Ortega, J. and Etxebarria, J., *Phys. Rev. B* **48**, 695 (1993).

Fousek, V. A., and Kroupa, J., *Czech. J. Phys.* B**36**, 1192 (1986).

Fresnel, A., *Oeuvr. Compl.* **1**, 731 (Paris 1866).

Fuchs, R., *Phil. Mag.* **11**, 647 (1965).

Gelinck, G., *An optical study of phase transitions in incommensurate crystals*, master thesis, Nijmegen (1992).

Golovko, V. A., and Levanyuk, A. P., *Sov. Phys. JETP* **50**, 780 (1979).

Graham, E. B., and Raab, R. E., *Proc. R. Soc. Lond.* A**390**, 73 (1983).

Grechushnikov, B. N., and Konstantinova, A. F., *Comput. Math. Applic.* **16**, 637 (1988).

Haidinger, *Pogg. Ann.* **70**, 531 (1847).

Hedoux, A., Grebille, D., Lefebvre, J., and Perret, R., *Phase Transitions* **14**, 177 (1989).

Hogervorst, A. C. R., *Comparative study of the modulated structures in* Rb_2ZnCl_4 *and in related compounds*, thesis Delft (1986).

Hornreich, R. M. and Shtrikman, S., *Phys. Rev.* **171**, 1065 (1968).

Janner, A., and Janssen, T., *Phys. Rev. B* **15**, 643 (1977).

Janner, A., and van Beest, B. W. *Proc. 11th Int. Colloquium on Group Theoretical Methods in Physics (Istanbul, 1982) Springer Lectures Notes in Physics* **180**, 269, ed. Serdaroglu, M., and Inonu, E., (Berlin: Springer, 1983).

Jones, R. C., *J. Opt. Soc. Am.* **38**, 671 (1948).

Kapustianik, V. B., Polovinko, I. I., Sveleba, S. A., Vlokh, O. G. and Zhmurko, V. S., *Europhys. Lett.* **19**, 429 (1992).

Khapalyuk, A. P., *Soviet Physics-Crystallography* **7**, 588 (1963).

Kobayashi J., Uesu, Y., Yamada, Y., and Takehara, H., *Ferroelectrics* **36**, 371 (1981).

Kobayashi, J. and Uesu, Y., *J. Appl. Cryst.* **16**, 204 (1983).

Kobayashi, J., Saito, K., Takahashi, N. and Kamiya, I., *Phys. Rev. B* **48**, 10038 (1993).

Krichevtsov, B. B., Pavlov, V. V., Pisarev, R. V. and Sherman, A. B., *JETP Lett.* **54**, 83 (1991).

Kushnir, O. S., Shopa, Y. I. and Vlokh, O. G., *Europhys. Lett.* **22**, 389 (1993).

Kushnir, O. S., and Vlokh, O. G. *J. Phys.: Condens. Matter* **5**, 7017 (1993).

Landau, L. D., and Lifshitz, E. M., *Electrodynamics of continuous media* (Oxford: Pergamon Press, 1984).

Laughlin, R. B., *Science* **242**, 525 (1988).

Lowry, T. M., *Optical Rotary Power* (Longmans, Green, 1935).

Mazur, P., and Nijboer, B. R. A., *Physica XIX*, 971 (1953).

Meekes, H., and Janner, A., *Phys. Rev. B* **38**, 8075 (1988).

Nye, J. F., *Physical properties of crystals* (Oxford: Oxford University Press, 1985).

O'Dell, T. H., *The electrodynamics of magneto-electric media* (Amsterdam: North-Holland, 1970).

Ortega, J., Etxebarria, J., Zubillaga, J., Breczewski, T., and Tello, M.J., *Phys. Rev. B* **45**, 5155 (1992).

Pancharatnam, S., *Proc. Ind. Acad. Sci.* **48**, 277 (1958).

Pisarev, R. V., *Soviet Physics JETP* **31**, 761 (1970).

Pisarev, R. V., Krichevtsov, B. B., and Pavlov, V. V., *Phase Transitions* **37**, 63 (1991).

Post, E. J., *Formal structure of electromagnetics* (Amsterdam: North-Holland, 1962).

Ramachandran, G. N., and Ramaseshan, S., *Crystal Optics*, (Handbuch der Phusik XXV/1, editor S. Flügge, 1961).

Saito, K., Kunishima, I., Kobayashi, J., and Uesu, Y., *Ferroelectrics* **64**, 137 (1985).

Saito, K., and Kobayashi, J., *Japanese Journal of Applied Physics* **30**, 2416 (1991).

Sanctuary, R. A., *Optische, elektrooptische und nichtlinear optische eigenschaften von* Rb_2ZnCl_4 , thesis, Zürich (1985).

Sommerfeld, A., *Vorlesungen über Physik IV, Optik* (Leipzig: Geest and Portig, 1959).

Uesu, Y., and Kobayashi, J., *Ferroelectrics* **64**, 115 (1985).

Chapter 2

The interpretation of HAUP measurements: a study of the systematic errors

The interpretation of HAUP measurements: a study of the systematic errors

M. Kremers and H. Meekes

Abstract

The HAUP method for determining the linear optical properties of crystals is critically reconsidered. The expressions that describe the method are rederived rigorously and the fitting procedures that are used by several authors are reviewed. The systematic errors, being crucial in HAUP measurements, are investigated by means of experiments on test samples. The understanding of both the origin and the behaviour of these errors leads to an improvement of the fitting procedures and of the interpretation of the data. In this way, the reliability and the sensitivity of the HAUP method have been increased, which should provide a mean to reconsider contradictory results of previous experiments, excluding systematic errors as a source of the dispute.

2.1 Introduction

The merits of the High Accuracy Universal Polarimeter (HAUP), introduced by Kobayashi and Uesu (1983), lie in the possibility of measuring simultaneously optical activity and birefringence of crystals very accurately. In addition, the rotation of the optical indicatrix is detected with a high sensitivity. The measurements require optically transparent, birefringent platelets of single crystals, with flat (polished) plane-parallel faces. It is very important to perform the measurements as a function of some external parameter in order to separate systematic errors from the optical properties. In the experiments described in this paper, the wavelength λ of the light is the external parameter. Additional parameters can be temperature, electric fields (electro-optics) or magnetic fields (magneto-optics).

The presence and nature of structural phase transitions can often be revealed by the birefringence (Ivanov (1991), Gehring (1977)). The point symmetry of a specific phase can be studied by measuring the optical activity in several directions in a crystal, since optical activity is a tensorial property, sensitive to the symmetry (Nye, 1985). HAUP is, therefore, a powerful instrument in crystal optics.

A very interesting problem in this field is encountered for incommensurately modulated crystals, with a centrosymmetric paraelectric phase (Cummins, 1990). Often, the incommensurate phase is a (small) periodic deformation of the centrosymmetric paraelectric phase. The wavelength of the periodic deformation is incommensurate with the lattice of the average structure. Therefore, the lattice translational symmetry is broken in at least one direction. Of course, the question arises whether this phase can be optically active, because optical activity is forbidden in a centrosymmetric crystal (Nye, 1985). However, optical activity can be allowed if in such a phase the spatial inversion symmetry is broken by the modulation. Nevertheless, such an effect might be quite small. The HAUP method has been applied extensively to several incommensurately modulated structures. Unfortunately, the results obtained so far by different groups contradict each other, in the sense that in some cases a small, but clearly non-zero optical activity has been found (Meekes and Janner (1988), Kobayashi et al. (1988a), Dijkstra et al. (1992)), while, for the same structures, measurements by others indicate no detectable optical activity (Folcia et al. (1993), Ortega et al. (1994)).

In order to exclude the possibility that these differences are caused by the way of measuring or the way of interpreting the measurements, we feel it necessary to reconsider very precisely the working principles of the HAUP method. In this paper, we rederive rigorously the HAUP intensity formula (section 2.2). Experiments have been performed both on a centrosymmetric crystal with zero optical activity and on the non-centrosymmetric room-temperature phase of quartz, having a large optical activity (section 2.3). In section 2.4 the obtained results are used to reconsider critically the fitting procedures with which the optical properties are extracted from the measurements. Moreover, in section 2.5, the behaviour and origin of the systematic errors will be studied thoroughly. The quality and sensitivity of HAUP measurements is addressed in section 2.6. For all aspects of the HAUP method, we discuss and take into account the experience gained by other authors that work with HAUP (for example, the papers of Moxon and Renshaw, 1990) (and Dijkstra et al., 1991). Only the case of non-absorbing crystals is treated. Absorption will be dealt with in a forthcoming paper.

Although we will not be able to explain the contradictory results of the experiments performed by different researchers up to now, we present an interpretation of HAUP data that should provide a mean to reconsider these data, excluding systematic errors as a cause of the dispute.

2.2 The working principle of HAUP and the derivation of the (general) HAUP intensity formula

The measurement of optical activity in presence of birefringence is accomplished in HAUP by virtue of the fact that one can derive an expression for the intensity-change of light traversing the optical system of the polarimeter. This expression is called the HAUP intensity formula. It can be derived by using Jones calculus (Jones, 1948). We use the exact notation as given by Jones (1948), because the work of this author is well-known among researchers working in optics. (A list of symbols with explanations has been added at the end of this paper.) The optical system, which is kept very simple, is represented in figure 2.1. It consists only of a polariser (Jones vector $\boldsymbol{P}$), the sample (Jones matrix $\boldsymbol{S}$) and an analyser (Jones vector $\boldsymbol{A}$), which is a second polariser. The intensity change Γ/Γ_0 of the light traversing this system is then given by (Dijkstra et al., 1991):

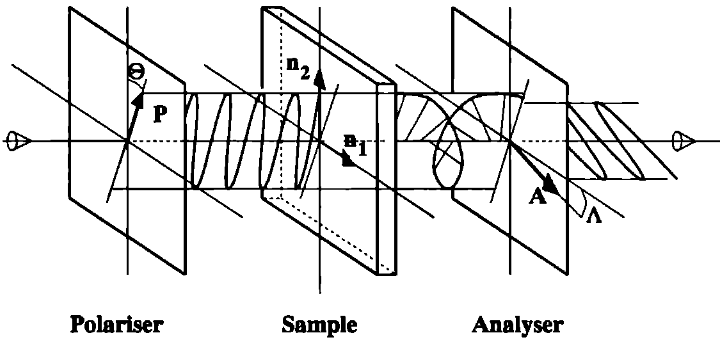

Figure 2.1 The optical system of HAUP, consisting only of a polariser, the sample and an analyser. The vectors ($\boldsymbol{n}_2$, $\boldsymbol{n}_1$) and the angles (Θ, Λ) are referred to in the text.

$$\Gamma/\Gamma_0 = \left|\boldsymbol{A}^\dagger \boldsymbol{S}\boldsymbol{P}\right|^2 = (\boldsymbol{A}^\dagger \boldsymbol{S}\boldsymbol{P})(\boldsymbol{A}^\dagger \boldsymbol{S}\boldsymbol{P})^*, \tag{2.1}$$

where Γ_0 is the intensity of the monochromatic, circularly polarised or unpolarised light beam incident on the polariser and Γ is the intensity of the light emerging from the analyser.

Only two (mutually orthogonal) eigenpolarisations, represented in figure 2.1 with the vectors $\boldsymbol{n}_2$ and $\boldsymbol{n}_1$, can propagate in the sample, each with a different velocity, determined by the corresponding refractive index n_2, respectively n_1 (Born (1985), Ramachandran and Ramaseshan (1961)). The angle Θ defines the orientation of the polariser with respect to the major axis $\boldsymbol{n}_2$ of one of the eigenpolarisations and the angle Λ defines the orientation of the analyser with respect to the major axis $\boldsymbol{n}_1$ of the other one.

If the polarisers were ideal, their representing Jones vectors would be:

$$P = \begin{pmatrix} \cos\Theta \\ \sin\Theta \end{pmatrix} \text{and } A = \begin{pmatrix} \cos(\frac{\pi}{2}+\Lambda) \\ \sin(\frac{\pi}{2}+\Lambda) \end{pmatrix} = \begin{pmatrix} -\sin\Lambda \\ \cos\Lambda \end{pmatrix}. \tag{2.2}$$

However, even if very high quality polarisers are used, the light transmitted by the polarisers is not ideally linearly polarised. It has a very small ellipticity. The ratio between the lengths of the major and minor axes of the elliptic polarisation is in the order of 10^{-4} (Dijkstra et al., 1991). The ellipticities, denoted p and a for the polariser and analyser respectively, are systematic errors characteristic for HAUP. They must be included in the derivation of the HAUP intensity formula, because one aims to measure optical effects that are of even smaller magnitude. In order to avoid too many of such systematic errors, the number of optical components, present in HAUP, is limited. The Jones vectors of the non-ideal polarisers become (Dijkstra et al., 1991):

$$\begin{aligned} P &= \begin{pmatrix} P_1 \\ P_2 \end{pmatrix} = \begin{pmatrix} \cos\Theta\cos p - i\sin\Theta\sin p \\ \sin\Theta\cos p + i\cos\Theta\sin p \end{pmatrix} \\ A &= \begin{pmatrix} A_1 \\ A_2 \end{pmatrix} = \begin{pmatrix} -\sin\Lambda\cos a - i\cos\Lambda\sin a \\ \cos\Lambda\cos a - i\sin\Lambda\sin a \end{pmatrix}. \end{aligned} \tag{2.3}$$

One of the basic principles of HAUP is that the rotation angles Θ and Λ are restricted to very small values (maximally being about 10^{-2} rad). However, it must still be possible to set the polarisers with high accuracy at different positions within these ranges. This, then, allows for an expansion of P and A for small Θ, Λ, p and a. Our aim is, however, to calculate the HAUP intensity formula. Therefore, we first write

$$A^{\dagger}SP = P_1A_1^*s_{11} + P_2A_1^*s_{12} + P_1A_2^*s_{21} + P_2A_2^*s_{22} \tag{2.4}$$

and expand the terms $P_iA_j^*$ (the s_{ij} are the matrix elements of S). In the literate it is usually assumed that it is sufficient to expand up to second or third order, but in appendix A the result of an expansion up to fourth order is given. In this way we can estimate, for the rotation angles used, the contribution of the normally neglected higher order terms to the intensity Γ.

Once the sample matrix S is specified, one can calculate the HAUP intensity formula from equation (2.1). The advantage of this procedure is, that for a different sample matrix (for example for absorbing crystals, not treated here) one can again start directly from the results in appendix A.

In the notation of Jones (1948), the linear birefringence $(n_1 - n_2) \equiv \Delta n$ is represented by $g_o = \frac{\pi}{\lambda}\Delta n$. Here, n_2 is the refractive index belonging to the eigenpolarisation that has its major axis along the polarisation of the light emerging from the polariser when $\Theta = 0$. This means that Δn and g_o are positive when this polarisation is the fast (smaller index) axis.

Optical activity is included in the description via the circular birefringence $n_r - n_l$, in which n_r and n_l are the refractive indices for respectively right and left circularly polarised light. If one defines $\omega \equiv \frac{\pi}{\lambda}(n_r - n_l)$, laevorotatory crystals have a positive ω and dextrorotatory crystals have a negative ω. This definition is consistent with the one used by Glazer and Stadnicka (1986). It should be noted that optical activity is not the only effect that can give rise to circular birefringence (see, for example, Dijk91b, Dijkstra et al. (1992b)).

For a totally transparent, birefringent and optically active crystal, the sample matrix $\boldsymbol{S}$ becomes (Jones, 1948):

$$\boldsymbol{S} = \begin{pmatrix} \cosh(\mathrm{Q_N}z) + \frac{ig_o}{Q_N}\sinh(Q_N z) & -\frac{\omega}{Q_N}\sinh(\mathrm{Q_N}z) \\ \frac{\omega}{Q_N}\sinh(\mathrm{Q_N}z) & \cosh(\mathrm{Q_N}z) - \frac{ig_o}{Q_N}\sinh(\mathrm{Q_N}z) \end{pmatrix} \tag{2.5}$$

where z is the thickness of the crystal platelet and
$Q_N^2 = (ig_o)^2 - \omega^2 = -(g_o^2 + \omega^2)$.

The circular birefringence is, apart from the case of light propagating close to an optic axis of the crystal, generally much smaller than the linear birefringence ($\frac{\omega}{g_o}$ is in the order of 10^{-3} or smaller). The matrix elements s_{ij} can, therefore, be expanded for small ω. An expansion up to third order in ω is sufficient for the derivation of the HAUP intensity formula up to fourth order terms in ω, p, a, Θ and Λ. The corresponding Taylor expansions are:

$$\begin{aligned}
\cosh\left[\left(-g_o^2 - \omega^2\right)^{\frac{1}{2}} z\right] &= \cos(g_o z) - \frac{1}{2}\omega^2 \left\{\frac{z\sin(|g_o|\,z)}{|g_o|}\right\} + \mathcal{O}(4) \\
\frac{ig_o \sinh\left[(-g_o^2 - \omega^2)^{\frac{1}{2}} z\right]}{(-g_o^2 - \omega^2)^{\frac{1}{2}}} &= i\,g_o \frac{\sin(|g_o|\,z)}{|g_o|} + \frac{1}{2}i\,g_o\omega^2 \left\{-\frac{\sin(|g_o|\,z)}{|g_o|^3} + \frac{z\cos(g_o z)}{g_o^2}\right\} + \mathcal{O}(4) \\
\frac{\omega \sinh\left[(-g_o^2 - \omega^2)^{\frac{1}{2}} z\right]}{(-g_o^2 - \omega^2)^{\frac{1}{2}}} &= \omega\,\frac{\sin(|g_o|\,z)}{|g_o|} + \frac{1}{2}\omega^3 \left\{-\frac{\sin(|g_o|\,z)}{|g_o|^3} + \frac{z\cos(g_o z)}{g_o^2}\right\} + \mathcal{O}(4).
\end{aligned}$$

and with these approximations the sample matrix elements s_{ij} are found to be:

$$\begin{aligned}
s_{11} &= \left[1 + \frac{1}{2}i\,(g_o z)\left(\frac{\omega}{g_o}\right)^2\right]\left[\cos(g_o z) + i\sin(g_o z)\right] - \frac{1}{2}i\left(\frac{\omega}{g_o}\right)^2 \sin(g_o z) \\
s_{12} &= -s_{21} = -\frac{1}{2}(g_o z)\left(\frac{\omega}{g_o}\right)^3 \cos(g_o z) - \left[\frac{\omega}{g_o} - \frac{1}{2}\left(\frac{\omega}{g_o}\right)^3\right]\sin(g_o z) \\
s_{22} &= \left[1 - \frac{1}{2}i\,(g_o z)\left(\frac{\omega}{g_o}\right)^2\right]\left[\cos(g_o z) - i\sin(g_o z)\right] + \frac{1}{2}i\left(\frac{\omega}{g_o}\right)^2 \sin(g_o z).
\end{aligned}$$

Within the approximations made, the circular birefringence never appears in the arguments of the sine and cosine functions. It is for this reason, that the HAUP method allows for a true separation of linear and circular birefringence. In previous descriptions (Kobayashi and Uesu (1983), Dijkstra et al. (1991)) half of the total retardation, $\frac{\Delta}{2} = z\sqrt{g_o^2 + \omega^2}$, was put in the arguments instead of $g_o z$. This, however, is incorrect considering the expansions given above.

The HAUP intensity formula can now be calculated, but usually one first changes to another reading system for the analyser (Kobayashi and Uesu, 1983). Instead of Λ, one uses Y, which is read with respect to the polariser position Θ in such a way, that for $Y = 0$ the polarisers are crossed. This can be achieved by substituting $\Theta + Y$ for Λ.

Furthermore, Kobayashi et al. (1986) have shown that it is essential to include another systematic error, denoted δY, in the description of the HAUP method. It describes a (small) deviation of the analyser position from its supposed position. The origin of this systematic error is one of the subjects of this paper and is dealt with in detail further on. One takes this so-called δY-error into account by substituting $Y + \delta Y$ for Y.

The HAUP intensity formula has been derived in this way, by expanding up to fourth order in p, a, Θ, Y, δY and can be written in the following manner (Moxon and Renshaw, 1990):

$$\Gamma/\Gamma_0 = \begin{pmatrix} 1 & Y & Y^2 & Y^3 & Y^4 \end{pmatrix} C^{\text{e.p.}}_{(5\times5)} \begin{pmatrix} 1 \\ \Theta \\ \Theta^2 \\ \Theta^3 \\ \Theta^4 \end{pmatrix} . \tag{2.6}$$

The matrix elements of $C^{\text{e.p.}}_{(5\times5)}$ are given in appendix B. The superscript e.p. means eigenpolarisation, referring to the fact that this expression has been derived with one of the eigenpolarisations of the sample as the origin for the reading of Θ. However, in an actual experiment it is impossible to find that position with any accuracy. Fortunately, another origin for Θ can be chosen, using the following procedure. Both polarisers are rotated simultaneously (or the sample instead), while keeping them exactly crossed ($Y = 0$). In this way one searches for a so-called extinction direction, which is a position of minimal intensity for crossed polarisers. The corresponding polariser position is denoted Θ_0. It is this position that is subsequently used as origin for the reading of Θ. When the polarisers are rotated over 2π, four extinction directions are encountered. It follows, that in a HAUP intensity formula, Θ_0 is the value of Θ for which:

$$\left.\frac{\delta\Gamma}{\delta\Theta}\right|_{Y=0} = 0. \tag{2.7}$$

Therefore, in order to interpret the measurements one must substitute $\Theta + \Theta_0$ for Θ, using the correct expression for Θ_0 that is obtained by equation (2.7). Unfortunately, it is impossible to solve equation (2.7) analytically, using the HAUP intensity formula (2.6) that has been expanded up to fourth order in Θ and Y. However, after omitting all fourth order terms in appendix B, equation (B.1), we find:

$$\Theta_0 = \frac{1}{2}(p+a)\cot(g_o z) - \frac{1}{2}\delta Y + \delta\Theta_{\text{indicatrix}}. \tag{2.8}$$

The $\delta\Theta_{\text{indicatrix}}$ term has been added in order to take a possible rotation of the optical indicatrix into account.

According to several authors (Moxon and Renshaw (1990), Kushnir and Vlokh (1993)), even totally transparent crystals can show a small linear dichroism $\kappa_1 - \kappa_2 \equiv \Delta\kappa$. For example, the polishing of the samples might cause a small anisotropic surface scattering due to a preferential abrasion direction in the crystal structure. Linear dichroism is represented by $p_o = \frac{\pi}{\lambda}\Delta\kappa$ in the Jones formalism. If we include small linear dichroism in the way described by Dijkstra et al. (1991), the following HAUP intensity formula is found:

$$\Gamma/\Gamma_0 = \begin{pmatrix} 1 & Y & Y^2 & Y^3 \end{pmatrix} C^{\Theta_0}_{(4\times4)} \begin{pmatrix} 1 \\ \Theta \\ \Theta^2 \\ \Theta^3 \end{pmatrix}, \tag{2.9}$$

where

$$\begin{aligned}
C^{\Theta_0}_{11} &= \left(\delta Y\cos(g_o z) - \left((p-a) + \frac{\omega}{g_o}\right)\sin(g_o z)\right)^2 \\
&\quad -2p_o z(p+a)\left((p-a) + \frac{\omega}{g_o}\right) + 2p_o z\delta Y(p+a)\cot(g_o z) \\
C^{\Theta_0}_{12} &= 0 \\
C^{\Theta_0}_{13} &= 4\sin^2(g_o z) \\
C^{\Theta_0}_{21} &= 2\delta Y\cos^2(g_o z) - \left((p-a) + \frac{\omega}{g_o}\right)\sin(2g_o z) + 2p_o z(p+a)\cot(g_o z) \\
C^{\Theta_0}_{22} &= 4\sin^2(g_o z) + 4p_o z \\
C^{\Theta_0}_{23} &= 0 \\
C^{\Theta_0}_{31} &= 1 + 2p_o z \\
C^{\Theta_0}_{32} &= 0 \\
C^{\Theta_0}_{33} &= 0 \\
C^{\Theta_0}_{i4} &= 0; \qquad i = 1,2,3,4 \\
C^{\Theta_0}_{4j} &= 0; \qquad j = 1,2,3,4.
\end{aligned} \tag{2.10}$$

The superscript Θ_0 indicates, that an extinction direction has been used as the origin of the Θ reading. Putting $p_o = 0$ in equation (2.10), gives exactly the result for the case where linear dichroism is not taken into account.

In a HAUP experiment, intensities are measured at a series of (Θ, Y) combinations. These intensities are fitted to a polynomial equation in the angles Θ and Y. The sample properties ω, g_o and p_o, as well as the systematic errors p, a and δY, are then contained in the fitting-parameters. They can be extracted by a comparison of the fitting-parameters with the matrix elements $C_{ij}^{\Theta_0}$ of the HAUP intensity formula. Furthermore, the wavelength dependence of the fitting-parameters must be studied. Namely, the systematic errors are supposed to be independent of the wavelength of the light, contrary to the sample properties.

2.3 Experiments

2.3.1 Improvements to the HAUP set-up and the sample treatment

The basic set-up of the HAUP apparatus built in our laboratory has been described elsewhere (Dijkstra et al., 1991). Here, we report on changes and improvements that have been made in this apparatus.

At present, it is possible to perform measurements as a function of the wavelength λ of the light, for λ between 650 nm and 350 nm. A small monochromator with a resolution of 2.22 nm is placed behind a 150 W Xenon light source. In order to correct for intensity variations, a beam splitter is put between the monochromator and the polariser. With a second photomultiplier tube the intensity of the reference beam, that is created in this way, is measured and subsequently used to correct for intensity changes. The photomultiplier signals are fed to a two-channel photon counting system. Previously, a photon counter was used that displayed the intensities with only three digits and an exponent. Especially in cases where the linear birefringence becomes small this proved to be inadequate. Presently, the intensities are measured with eight digits by a new photon counter for both photomultiplier tubes.

Besides changing the wavelength of the light, also the temperature of the sample can be changed using a cold finger technique (Dijkstra et al., 1991). Some improvements have been made to the temperature regulation system. Therefore, the temperature can now be stabilised within ± 0.01 K if it can be kept at a constant value. If the temperature must be changed continuously during a HAUP measurement, the stability will become less, ± 0.025 K.

Next to improvements to the apparatus, also the polishing of the samples has been improved. The technique of polishing has been adjusted, such that the two polished faces of the sample are better plane-parallel than before and the edges of the faces are less rounded. Except for these rounded edges, the change in sample thickness over the total sample surface is less than 5μm. This means that within the spot of the light beam on the sample, we can estimate the change in thickness to be less than 3μm. The relevant quantity in HAUP measurements is the variation of $g_o z/\pi$ over the spot, which thus depends on the magnitude of the birefringence. A larger birefringence requires more careful polishing.

2.3.2 The measurement procedure

Before any measurement is started, the polarisers are put in crossed position. Then, the sample is prepared and it is placed in the HAUP between the polarisers. The incident light beam is directed through a diafragm onto the sample. The orientation of the sample is adjusted until the reflected light from its surface passes through the same diafragm, in order to get the front face perpendicular to the light beam.

The measurement procedure is started by a search for an extinction direction, thus determining Θ_0. Then, intensities are measured at 15 × 15 combinations of polariser and analyser positions located around the extinction direction. These combinations can be represented as $\Theta = (i+j)\Delta\phi$ and $Y = -j\Delta\phi \Rightarrow \Lambda = Y + \Theta = i\Delta\phi$ where i and j take all integer values $+7, 6, \ldots, -6, -7$. Instead of performing measurements situated around an extinction direction other authors (Moxon and Renshaw (1990), Ortega et al. (1992)) perform their measurements around those positions for the polariser and analyser at which the intensity is absolutely minimal. In general, this will not be the crossed polarisers position and the disadvantage is that one has to set up a scheme for finding the absolute intensity minimum. It can be expected, however, that the fitting procedures described in section 2.4 can give somewhat more accurate results for such a measurement. Nevertheless, it is shown later that the results obtained with our way of data-taking are already highly accurate.

Both polarisers are mounted on rotation stages that are driven by stepping motors. The smallest rotation in our apparatus is $2 \cdot 10^{-3\,\circ} \approx 3.49 \cdot 10^{-5}$ rad corresponding to one step. The reproducibility is $\pm 1'' \approx \pm 4.8 \cdot 10^{-6}$ rad. This is of the same order of magnitude as the reproducibility (or accuracy) given by other authors for their HAUP (table 2.1) except for the one given by Kobayashi and Uesu (1983). The latter authors claim an extremely high accuracy. Unfortunately, however, they give no information about the way in which this can be accomplished.

Kobayashi and Uesu (1983)	$4.8 \cdot 10^{-7}$
Moxon et al. (1991)	$3.5 \cdot 10^{-6}$
Dijkstra et al. (1991)	$4.8 \cdot 10^{-6}$
Ortega et al. (1992)	$8.1 \cdot 10^{-6}$

Table 2.1 The reproducibility/accuracy of polariser positions used by different authors

In all measurements performed so far $\Delta\phi$ was 40 steps $\approx 1.39 \cdot 10^{-3}$ rad. This implies that the polariser rotates maximally $1.95 \cdot 10^{-2}$ rad away from the extinction position and the analyser maximally $9.77 \cdot 10^{-3}$ rad. The 225 measured intensities of this (first) extinction direction and the value of Θ_0 are stored in a computer that controls the HAUP. At this point, the first extinction direction has been measured.

Next, both polarisers are rotated over $\frac{1}{2}\pi$ and the just described process is repeated, including the determination of Θ_0. This is the measurement of the second extinction direction. Also the third and fourth extinction direction are usually measured, although the measurement of one extinction direction can be enough to determine the linear optical properties of the sample. Measuring four extinction directions, however, is a nice way of studying the behaviour of the systematic errors as a function of polariser positions (section 2.5). Moreover, since the sample properties are independent of the specific extinction direction being measured, one can get an idea of the accuracy with which these properties have been found by comparing their values for the four extinction directions.

In the Jones description of the HAUP system, presented in the previous section, two succeeding eigenpolarisations only differ in the sign of their linear birefringence. Therefore, the same HAUP intensity formula can be used for all extinction directions. Labeling the extinction directions one expects that:

$$\begin{array}{rcrcrcr} p_1 & = & p_2 & = & p_3 & = & p_4 \\ a_1 & = & a_2 & = & a_3 & = & a_4 \\ \omega_1 & = & \omega_2 & = & \omega_3 & = & \omega_4 \\ -g_{01} & = & +g_{02} & = & -g_{03} & = & +g_{04} \\ -\omega_1/g_{01} & = & +\omega_2/g_{02} & = & -\omega_3/g_{03} & = & +\omega_4/g_{04}. \end{array} \qquad (2.11)$$

This would be correct in case of an ideal HAUP, but the experiments in this paper and the findings of other authors have shown that in practice the situation is more complicated than suggested by equation (2.11).

After the measurement of all four extinction directions, another wavelength is set and again all extinction directions are measured. Repeating this for at least, say, twenty wavelengths one obtains a set of measurements from which the sample properties and the systematic errors can be extracted, for each extinction direction.

2.3.3 Samples

We have selected two samples for the investigations. The first is tetramethylammonium tetrachloro-zincate
$((CH_3)_4N)_2ZnCl_4$ which has a high-temperature paraelectric phase in which optical activity is forbidden by symmetry. The second is quartz which shows a relatively large natural optical activity.

2.3.3.1 The paraelectric phase of $((CH_3)_4N)_2ZnCl_4$

At temperatures above 297.6 K the structure of $((CH_3)_4N)_2ZnCl_4$ is orthorhombic and centrosymmetric (Wiesner et al., 1967). The space group is Pcmn. Totally transparent crystals of about 1 cm^3 with large natural faces were grown by a thermal convection method (Arend et al., 1986). They contained no observable inclusions. One of the crystals was oriented with an optical goniometer and a platelet with face-normal along the a-axis of the crystal was cut with a wire saw. Both sides of the platelet were polished on felt, with diamond paste down to 1 μm size. The final thickness was 1.50 mm. As described before, the total thickness variation within the spot of the light beam is estimated to be less than 3μm. In the case of this crystal this means that the variation in g_o/π was less than $5 \cdot 10^{-4}$.

The HAUP measurement has been performed in the paraelectric phase as a function of the wavelength of the light at constant temperature T = 320 K. There is a larger change of the linear birefringence with wavelength than with temperature in this phase. It even becomes zero for approximately $\lambda = 400$ nm at the chosen temperature. This is an interesting wavelength, because the expansions made in deriving the HAUP intensity formula expect the circular birefringence to be small with respect to $\sin(g_o z)$, which becomes zero if the linear birefringence is zero. Therefore, the expansions considered above are not valid anymore at such wavelength.

The circular birefringence, $(n_r - n_l)$, is related to the gyration G in the following way:

$$G = \tilde{n}(n_r - n_l) \tag{2.12}$$

where $\tilde{n}$ is the average of all main refractive indices. The gyration G being probed, is:

$$G = g_{ij} s_i s_j \tag{2.13}$$

where the g_{ij} are elements of the gyration tensor $\boldsymbol{g}$ (see, Nye, 1985) and the s_i are the components of the unit wave vector $\boldsymbol{s}$ of the light. In this experiment $\boldsymbol{s} = (1, 0, 0)$, so that the gyration tensor element g_{11} is measured. The detected birefringence is correspondingly denoted Δn_{11}. As the crystal is centrosymmetric all gyration tensor elements g_{ij} must be zero. From the measured noise around zero we get an idea of how small values of circular birefringence can be distinguished from zero with HAUP.

The fitting procedures are simplified due to the fact that there is no circular birefringence. Therefore, this sample is ideal for the study of the systematic errors as a function of polariser position. Consequently, all four extinction directions have been measured.

2.3.3.2 Optically Active Quartz

Quartz is known to have a large natural optical activity and a wavelength dispersion of the linear birefringence. The sample that we have used was obtained by etching the gold layers of a commercially available transducer. The flat and plane-parallel faces were unaffected by the etching. In this way, an x-platelet of thickness $z = 0.28$ mm was obtained that allows for the measurement of g_{11} and Δn_{11} with HAUP. The measurements were performed at constant temperature T = 303.75 K as a function of the wavelength of the light. The value of $g_o z$ becomes equal to an integer multiple of π several times in this wavelength interval for this sample, due to the wavelength dispersion. This is interesting, since at all of these points $\sin(g_o z)$ is zero and again the expansions made in deriving the HAUP intensity formula are no longer valid. The HAUP measurements of this sample will show how well one can indeed separate linear birefringence from circular birefringence. As there is circular birefringence, this sample is less suited for the study of the systematic errors, because the fitting procedures become more involved. Therefore only one extinction direction has been measured. The results are compared to earlier HAUP measurements of quartz (Kobayashi et al. (1988b), Moxon et al. (1991)).

2.4 Fitting procedures

In order to obtain the optical properties of the sample one must interpret the measured intensities by making use of the HAUP intensity formula. This is done in two steps*.

2.4.1 The first step in the fitting procedure

First, the total set of intensities (225 in our case) belonging to one particular extinction direction and fixed wavelength is fitted with a linear least squares method (Deming and Morgan, 1979) to a polynomial equation of the form (Moxon and Renshaw, 1990):

$$\Gamma/\Gamma_0 = \begin{pmatrix} Y^0 & Y^1 & \ldots & Y^n \end{pmatrix} C_{(n \times n)} \begin{pmatrix} \Theta^0 \\ \Theta^1 \\ \ldots \\ \Theta^n \end{pmatrix}. \tag{2.14}$$

In the fit, one can choose the value of n and one can constrain matrix elements C_{ij} to zero. The obtained fitting-parameters C_{ij} can then directly be assigned to the expressions as they occur in the corresponding HAUP intensity formula that one has chosen to use (in our case, equation (2.9)). This is subsequently repeated for all wavelengths and all extinction directions.

A nice way of inspecting the results, has been suggested by Moxon and Renshaw (1990). It consists of drawing intensity contour diagrams in the Θ, Y plane, using the measured intensities or the obtained fitting-parameters. From the contour diagrams one gets a rough idea of the magnitude of some of the relevant parameters (see, for a more detailed explanation, Moxon and Renshaw, 1990).

In this section, we show the fitting-parameter C_{21} obtained from fits, using equation (2.14), for one of the extinction directions of the $((CH_3)_4N)_2ZnCl_4$ sample, because this is the element from which the value of the circular birefringence is extracted in the second

---

*The C-sources of the used computer programs can be obtained from M. Kremers, e-mail address: mkremers@sci.kun.nl or hugom@sci.kun.nl step of the fitting procedure. The extraction of the other sample properties is relatively easy (see section 2.4.2.1 and 2.4.2.2).

In order to be able to compare the results with the HAUP intensity formula, eqn. (2.9), a fit has been performed using expression (2.14) with $n = 3$ and six fitting-parameters (C_{11}, C_{12}, C_{13}, C_{21}, C_{22}, and C_{31}). The parameter C_{12} is included in order to be able to take account of an additional error in Θ_0 as described in section 2.4.1.1. The result for C_{21} as a function of wavelength is given in figure 2.2.

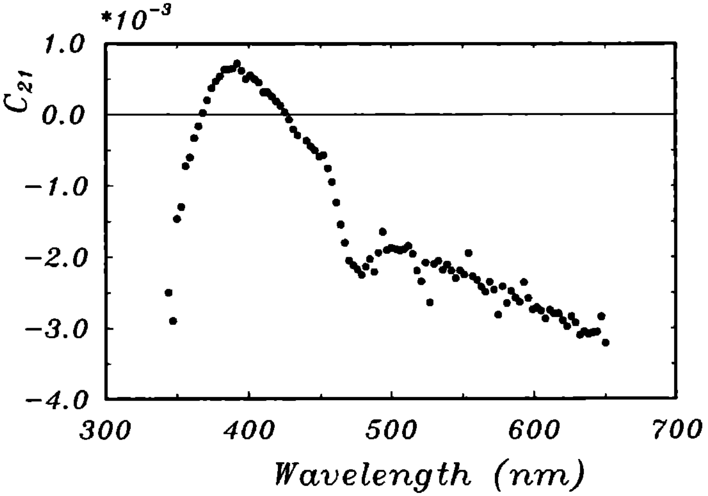

Figure 2.2 Fitting-parameter C_{21} (see equation 2.14) for the $((CH_3)_4N)_2ZnCl_4$ sample as a function of the wavelength No corrections have been made during the fitting

Although it is possible to use these data in the second step of the fitting procedure, it is possible and sensible to perform first several corrections, that are expected to increase the reliability of the obtained fitting-parameters.

In the following subsections, each time an extra correction is added and the obtained C_{21} values are shown.

2.4.1.1 The $\Delta\Theta$-correction

Before the measurement of the 225 intensities the extinction direction, Θ_0, is determined. It is also possible, however, to derive the value of Θ_0 from the obtained fitting-parameters C_{ij} that follow from the total set of intensities measured (Moxon and Renshaw, 1990). Since, then, more intensities are used this value is more accurate. In general, it differs by some amount $\Delta\Theta$ from the value obtained by searching the extinction direction.

One can determine $\Delta\Theta$ in the following way from the C_{ij}. The HAUP intensity formula (eqn. (2.9)) can be written as:

$$\frac{\Gamma(Y,\Theta)}{\Gamma_0} = C_{11}^{\Theta_0} + C_{13}^{\Theta_0}\,\Theta^2 + C_{21}^{\Theta_0}\,Y + C_{22}^{\Theta_0}\,Y\Theta + C_{31}^{\Theta_0}\,Y^2. \tag{2.15}$$

Now, suppose that the polariser angles Θ have been read with respect to $\Theta_0 + \Delta\Theta$ instead of with respect to Θ_0. In fact, they are then $\Theta + \Delta\Theta \equiv \Theta'$. It follows, that $\Theta = \Theta' - \Delta\Theta$. If we substitute $\Theta' - \Delta\Theta$ for Θ in equation (2.15), the HAUP intensity formula is obtained in terms of Θ' and Y.

$$\begin{aligned}
\frac{\Gamma\left(Y,\Theta'\right)}{\Gamma_0} &= C_{11}^{\Theta_0+\Delta\Theta} + C_{13}^{\Theta_0+\Delta\Theta}\,\Theta'^2 + C_{21}^{\Theta_0+\Delta\Theta}\,Y + C_{22}^{\Theta_0+\Delta\Theta}\,Y\Theta' && (2.16)\\
&\quad + C_{31}^{\Theta_0+\Delta\Theta}\,Y^2 + C_{12}^{\Theta_0+\Delta\Theta}\,\Theta' \\
&= C_{11}^{\Theta_0} + C_{13}^{\Theta_0}(\Delta\Theta)^2 + C_{13}^{\Theta_0}\,\Theta'^2 + \left(C_{21}^{\Theta_0} + C_{22}^{\Theta_0}\Delta\Theta\right)\,Y + C_{22}^{\Theta_0}\,Y\Theta' \\
&\quad + C_{31}^{\Theta_0}\,Y^2 + 2C_{13}^{\Theta_0}(\Delta\Theta)\,\Theta'. && (2.17)
\end{aligned}$$

The fitting-parameters, in this case denoted C'_{ij}, obtained from a fit as presented above (eqn. (2.14)), must now be compared with the $C_{ij}^{\Theta_0+\Delta\Theta}$ instead of with the $C_{ij}^{\Theta_0}$. These fitting-parameters C'_{ij} can be used to calculate the value of $\Delta\Theta$ and the values of the fitting-parameters C_{ij} that would have been obtained if Θ_0 would have been the origin of the polariser angle reading:

$$\begin{aligned}
C_{11} &= C'_{11} - C'_{13}(\Delta\Theta)^2 \\
C_{21} &= C'_{21} - C'_{22}\Delta\Theta \\
C_{13} &= C'_{13} \\
C_{22} &= C'_{22} \\
C_{31} &= C'_{31} \\
\Delta\Theta &= \frac{C'_{12}}{2C_{13}} = \frac{C'_{12}}{2C'_{13}}.
\end{aligned} \tag{2.18}$$

The $\Delta\Theta$-correction, obtained in this way for the $((CH_3)_4N)_2ZnCl_4$ sample was on the average 25 steps $\approx 8.7 \cdot 10^{-4}$ rad. This is quite large, but in these measurements the extinction direction has been determined only roughly, using relatively large rotation angles for the polarisers. When more attention is paid to the determination of the extinction direction it is easily possible to obtain corrections $\Delta\Theta$ in the order of 1 step $\approx 3.49 \cdot 10^{-5}$ rad, except, when the value of $g_o z$ becomes close to an integer times π. Then, the corrections become much larger.

As can be seen from equation (2.18) the value of C_{21} is also affected by the $\Delta\Theta$-correction. In figure 2.3, the thus obtained corrected values of C_{21} are shown for the same measurement as in figure 2.2. A clear change in the results can be observed.

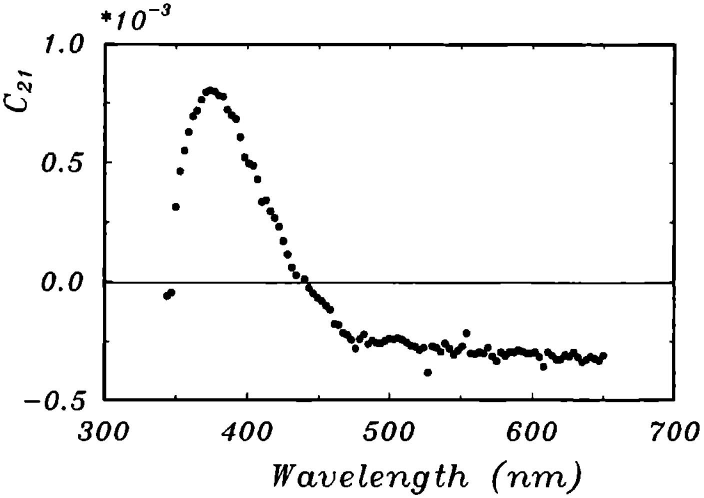

Figure 2.3 Fitting-parameter C_{21} for the $((CH_3)_4N)_2ZnCl_4$ sample as a function of the wavelength. With respect to figure 2.2 the $\Delta\Theta$-correction has now been performed.

In figures 2.4 and 2.5, the Θ_0 values for this measurement are given before and after the $\Delta\Theta$-correction. There is a clear cotangent behaviour in both cases, but there appears to be some extra structure at about $\lambda = 475$ nm in the uncorrected data. This structure has disappeared after the correction,. The expression for Θ_0 is given by equation (2.8). The systematic errors (p, a and δY) are expected to be constants for a particular extinction direction. Since the paraelectric phase of $((CH_3)_4N)_2ZnCl_4$ is orthorhombic, indicatrix rotation is forbidden by symmetry (Nye, 1985). Furthermore, g_o decreases monotonically with wavelength as we present later (figure 2.10). Therefore, one expects Θ_0 to behave nicely as a cotangent function. Hence, the corrected results for Θ_0 have definitely improved.

Remarkably, a clear difference between figures 2.2 and 2.3 is again the disappearance of the structure at 475 nm after the $\Delta\Theta$-correction.

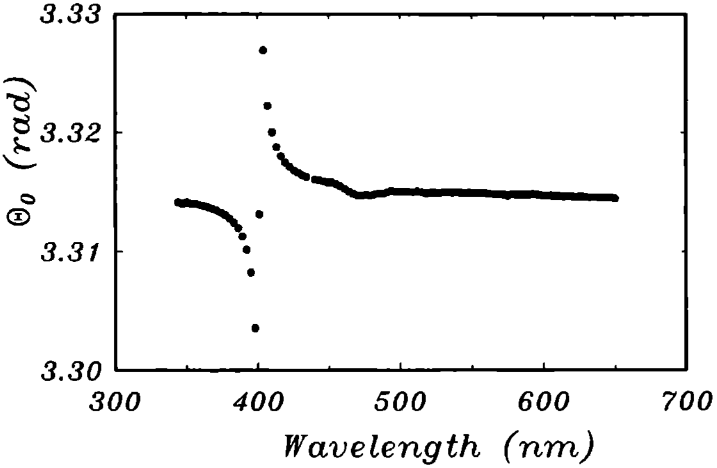

Figure 2.4 The extinction direction $\Theta_0\left(-\frac{1}{2}\pi\right)$ (see equation (2.8)) corresponding to figure 2.2, as a function of the wavelength. No corrections have been made. Sample: $((CH_3)_4N)_2ZnCl_4$.

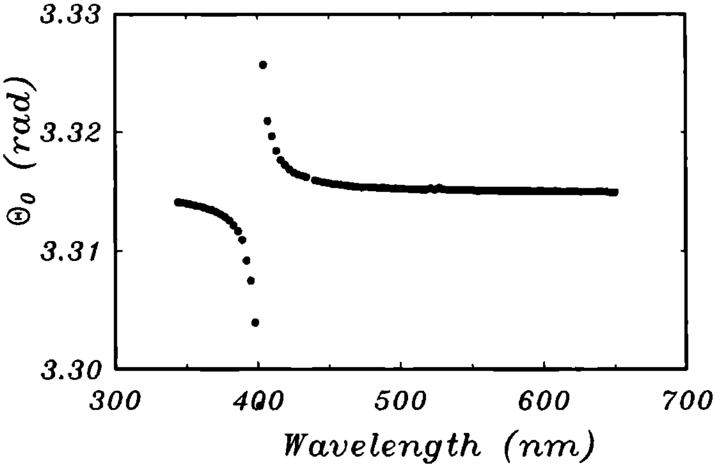

Figure 2.5 The extinction direction $\Theta_0\left(-\frac{1}{2}\pi\right)$ as a function of the wavelength. The $\Delta\Theta$-correction has been performed. Sample: $((CH_3)_4N)_2ZnCl_4$.

2.4.1.2 The ΔY-correction

Before searching an extinction direction for a certain sample, one must make sure, that the polariser and analyser are crossed. This can be done by rotating the analyser at a fixed polariser position and searching the position of minimal intensity with no sample in between. In our apparatus, it appeared that the analyser was not always at a minimal intensity position if the polariser and analyser next both were rotated over the same angle. This is shown in figure 2.6, where the full circles give the correction ΔY to the analyser position, at each polariser position, necessary to have the polarisers crossed. Also shown is a fit to this behaviour with a sixth order polynomial. With this (arbitrary) polynomial it has been tried to find a reasonable description of the behaviour with a limited number of parameters. For some reason, apparently, the positions as determined by the stepping motor controller can deviate in the order of 10^{-3} rad from their actual positions. This may be due to eccentricities of the rotation stages on which the polarisers are mounted (Dijkstra et al. (1991), Moxon and Renshaw (1990)), or other mechanical inaccuracies. As we show later, these ΔY values are the main cause for the necessity of including the systematic error δY in the HAUP intensity formula.

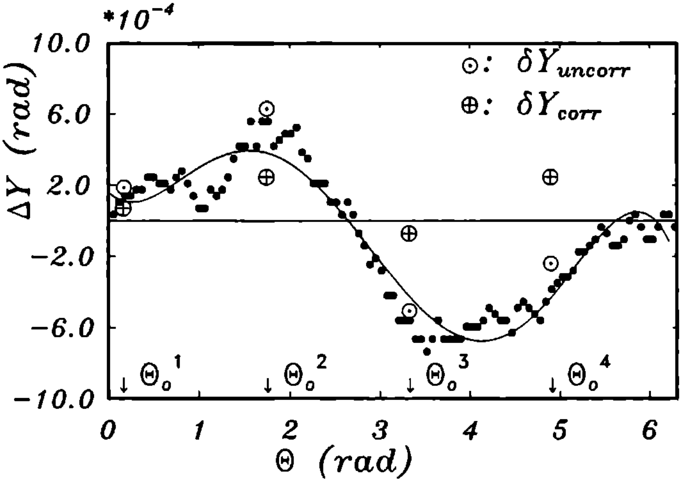

Figure 2.6 Correction ΔY (full circles •) to the analyser position, necessary to have the analyser exactly crossed with respect to the polariser, as a function of polariser position. No sample is present. The solid line is the result of a sixth order polynomial fit to these data. Also indicated are the positions $\Theta_0^{1,2,3,4}$ of the four extinction directions measured for the $((CH_3)_4N)_2ZnCl_4$ sample. In addition, the values of $-\delta Y_{\mathrm{uncorr}}$ (⊙) and $-\delta Y_{\mathrm{corr}}$ (⊕) at each extinction direction have been depicted. These parameters are explained in section 2.5.2

The sixth order polynomial fitted to the data in figure 2.6, was used to correct the values of Y in the linear least squares fit of the HAUP measurement with equation (2.14), in the following manner. For each of the 225 (Θ, Y) pairs, the Y value was changed with the value of the polynomial at the value of Θ. This, of course, changes all fitting-parameters. The changed values of C_{21} with respect to those of figure 2.3 are given in figure 2.7.

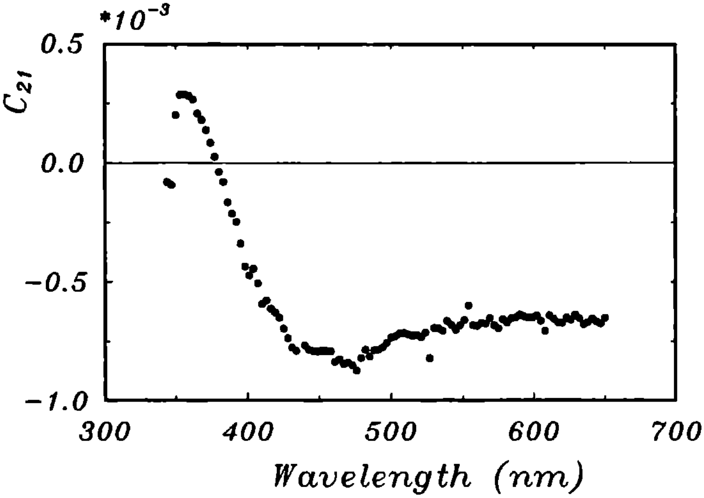

Figure 2.7 Fitting-parameter C_{21} (see equation 2.14) for the $((CH_3)_4N)_2ZnCl_4$ sample as a function of the wavelength. With respect to figure 2.2, in this case the $\Delta\Theta$-correction (see section 2.4.1.1) and ΔY-correction have been performed.

2.4.1.3 Fitting to fourth order in Θ and Y

The maximum rotation of the polariser was $1.95 \cdot 10^{-2}$ rad and the maximum rotation of the analyser was $9.77 \cdot 10^{-3}$ rad in our measurements. These angles may be too large for a correct description of the intensities with the HAUP intensity formula (2.9). However, one should still be able to obtain a value of C_{21} that can be compared with $C_{21}^{\Theta_0}$ of the HAUP intensity formula, in case the measurements are fitted to expression (2.14) with more parameters, for example, up to fourth order in the angles Θ and Y $(n = 5)$. This has been done and the result is given in figure 2.8. In order to compare the result with figure 2.7, also the $\Delta\Theta$-correction and the ΔY-correction were performed in this case. A change in the behaviour with respect to the values of figure 2.7 can be observed, but, most importantly, the noise has increased.

In figure 2.9, the fitting-parameter C_{41} (for the Y^3 term) has been plotted as obtained from a similar fit $(n = 5)$ for the $((CH_3)_4N)_2ZnCl_4$ sample. No further corrections have been performed, because the $\Delta\Theta$-correction has only been worked out for second order terms in the angles Θ and Y. By performing this fit we wanted to check whether there still is some information in this term, despite the small rotation angles used.

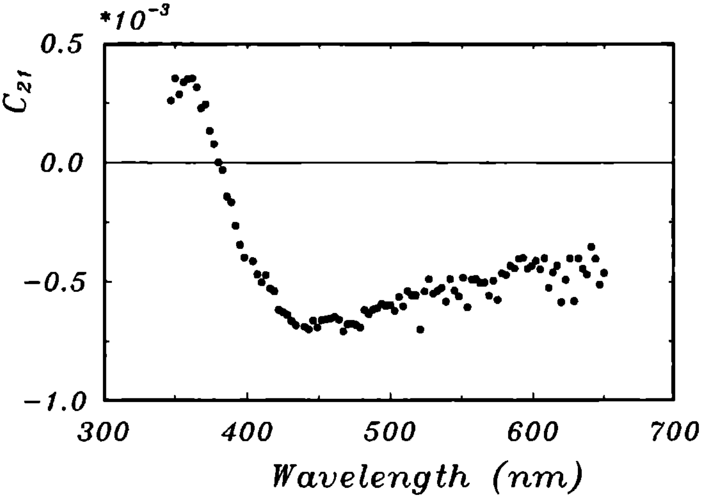

Figure 2.8 Fitting-parameter C_{21} (see equation 2.14) for the $((CH_3)_4N)_2ZnCl_4$ sample as a function of the wavelength. The $\Delta\Theta$-correction and the ΔY-correction have been performed. Furthermore, the data have been fitted up to fourth order in Θ and Y, using $n = 5$ in equation (2.14).

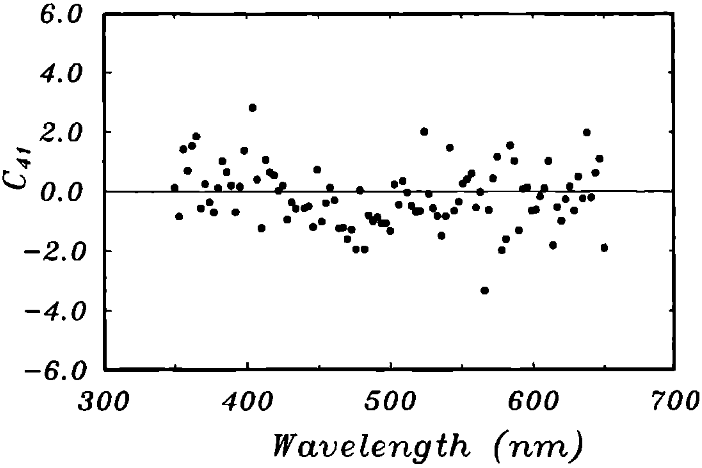

Figure 2.9 Fitting-parameter C_{41} for the Y^3 term as a result of a fit up to fourth order in Θ and Y, using $n = 5$ in equation (2.14), for the $((CH_3)_4N)_2ZnCl_4$ sample. No corrections have been performed.

Although we have no explicit expression for $C_{41}^{\Theta_0}$, something can still be learned by comparing the obtained results with $C_{41}^{e.p.}$, given in appendix B. This $C_{41}^{e.p.}$ behaves like $-\frac{4}{3}\delta Y + \sin(2g_o z)\left[\frac{2}{3}(\frac{\omega}{g_o}) + \frac{4}{3}p\right]$. The data in figure 2.9, however, just scatter around zero. Therefore, they contain only noise and no information. This means that the used rotation angles for the polarisers are so small, that one can only find reliable information in the fitting-parameters belonging to terms of second order in the angles Θ and Y. In case of a similar fit for the quartz sample, we found values for the fitting-parameter C_{41} of the same order of magnitude, also scattering around zero.

If we assume that the systematic errors p, a and δY are of the order of 10^{-3} rad and the values of Θ and Y are maximally 10^{-2} rad we find, making use of the HAUP intensity formula of appendix B, that the zeroth order terms in Θ and Y contribute maximally 10^{-6}, the first order terms 10^{-5}, the second order terms 10^{-4}, the third order terms 10^{-9} and the fourth order terms 10^{-8} to Γ/Γ_0. This suggests that neglecting the third order and fourth order terms in Θ and Y, erroneous contributions of maximally 10^{-8} can be put in the fitting-parameters. Therefore, one can roughly expect errors in C_{21} (first order in Y) of 0.1 percent.

We conclude, that using expression (2.14) with $n = 3$, is adequate enough for the rotation angles used.

2.4.2 The second step in the fitting procedure

The second step in the interpretation consists of separating the sample properties (g_o, p_o and ω) from the systematic errors (p, a and δY), for each extinction direction. This is done by studying the variation of the fitting-parameters C_{ij} with wavelength and assuming that the systematic errors are independent of the wavelength. The sample properties, on the contrary, are expected to show a wavelength dependence. In all cases presented in this section the values of the fitting-parameters C_{ij} have been obtained from the first step of the fitting procedure, using both the $\Delta\Theta$- and ΔY-corrections. Although not necessary, also fitting up to fourth order, using equation (2.14) with $n = 5$, has been used, except in some cases where it is explicitly mentioned.

2.4.2.1 The linear birefringence

Comparing the fitting-parameters C_{ij} of equation (2.14) with the $C_{ij}^{\Theta_0}$ of equation (2.10), one can determine the value

$$4\sin^2(g_o z) = \tfrac{1}{2}\left(C_{13} + C_{22} - 2(C_{31} - 1.0)\right).$$

This, in fact, is an average over two values of $4\sin^2(g_o z)$, correctly taking into account the possible presence of small linear dichroism. By taking this average it is hoped that the result becomes more accurate.

In addition, the value of the total retardation $\Delta = 2z\sqrt{g_o^2 + \omega^2}$ is usually determined separately for one wavelength of the light. This can be done, for example, with a compensation method and a polarising microscope. This value will not differ substantially from the value of $2g_o z$, since the circular birefringence is usually much smaller than the linear birefringence. Therefore, with the help of this value Δ, the wavelength dependence of $2g_o z$ can be resolved from the $4\sin^2(g_o z)$ values, if there is a continuous change with wavelength and the sign of the slope of the change is known. In order to elucidate the behaviour of g_o with wavelength it can sometimes be very useful to perform a second HAUP measurement on a similar sample that has, however, another thickness.

The linear birefringence Δn can be calculated from $2g_o z$, the sample thickness z and the wavelength of the light λ:

$$\Delta n = \frac{\lambda}{2\pi z} 2g_o z. \tag{2.19}$$

In figure 2.10 the linear birefringence Δn_{11} is plotted for $((CH_3)_4N)_2ZnCl_4$ and in figure 2.11 for quartz. The discontinuities in both figures correspond to wavelengths where $2g_o z$ is an integer multiple of 2π. The positions of these discontinuities depend on the thickness of the sample. This is a demonstration of the fact that the HAUP intensity formula, as it is used, is not valid for these cases.

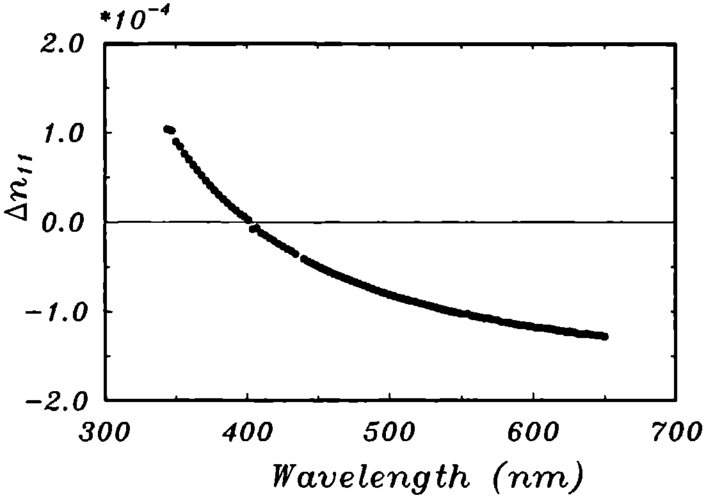

Figure 2.10 The linear birefringence Δn_{11} of $((CH_3)_4N)_2ZnCl_4$ as a function of the wavelength. The discontinuity at $\lambda = 400$ nm is a result of the fact that the HAUP intensity formula expansion is not valid for $\Delta n = 0$.

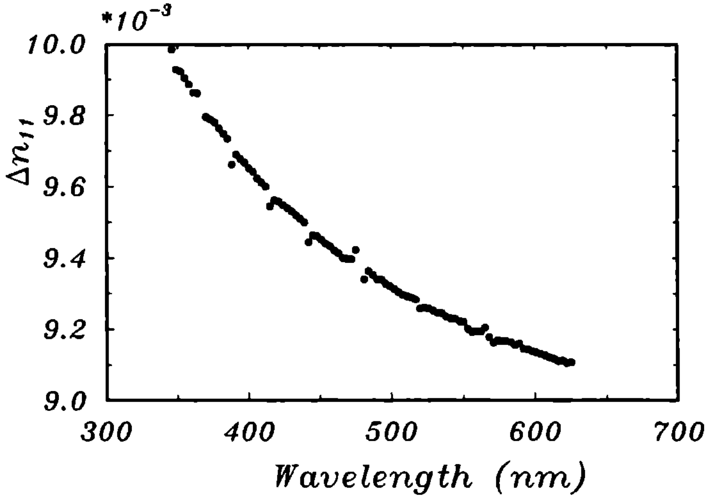

Figure 2.11 The linear birefringence Δn_{11} of quartz as a function of the wavelength. The discontinuities occur at wavelengths where the value of $2g_oz$ equals an integer times 2π. In such cases, the HAUP intensity formula expansion is not valid.

2.4.2.2 The linear dichroism

In order to check whether some anisotropic surface scattering was present, the linear dichroism $\Delta\kappa$ has been taken into account. It can be extracted from the fitting-parameters in the following way.
First one calculates

$$2p_o z = \tfrac{1}{2}\left[C_{31} - 1.0 + \tfrac{1}{2}(C_{22} - C_{13})\right]$$

and from this the linear dichroism $\Delta\kappa = \frac{\lambda}{\pi} p_o$ can be found. Figure 2.12 shows the results

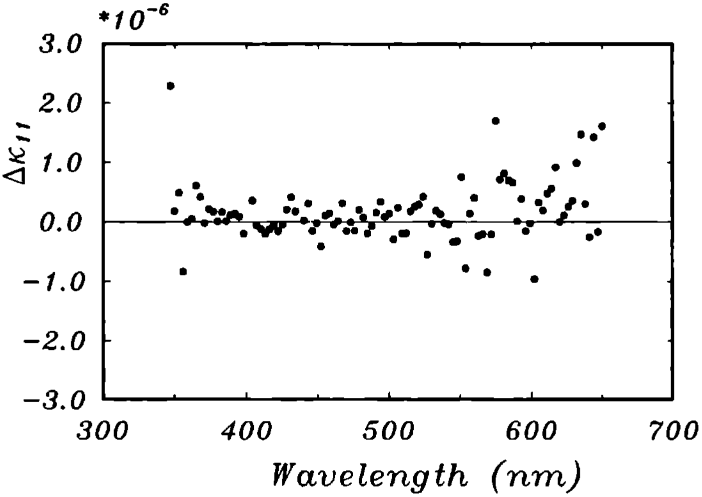

Figure 2.12 The linear dichroism $\Delta\kappa_{11}$ of $((CH_3)_4N)_2ZnCl_4$ as a function of the wavelength.

$\Delta\kappa_{11}$ for the $((CH_3)_4N)_2ZnCl_4$ sample (the notation is the same as used for the linear birefringence). No clear linear dichroism can be observed. In case of the quartz sample, the absolute value of the linear dichroism $|\kappa_{11}|$ was smaller than $6 \cdot 10^{-6}$ for all wavelengths. Therefore, it was also negligible.

2.4.2.3 The circular birefringence and the systematic errors

Unfortunately it is not possible to calculate simply at each wavelength the value of ω, representing the circular birefringence, since the matrix elements $C_{11}^{\Theta_0}$ and $C_{21}^{\Theta_0}$ (eqn. (2.9)) containing ω also contain the systematic errors p, a and δY. This means, that first the values of these systematic errors have to be found. This can be done by considering the wavelength dependence of the fitting-parameters. Here, we outline the methods used by most authors and we also propose a new method.

$C_{21}/\sin\Delta$ versus $\cot\left(\frac{\Delta}{2}\right)$

If there is no circular birefringence $2g_o z$ equals Δ. Then, both the values of δY and $\gamma \equiv (p-a)$ can be found by plotting $C_{21}/\sin\Delta$ against $\cot(\frac{\Delta}{2})$ (Kobayashi et al., 1988b). The slope of the obtained straight line is δY and the intercept of the ordinate-axis is $-\gamma$. Namely, without circular birefringence and neglecting the linear dichroism:

$$C_{21}^{\Theta_0}/\sin\Delta = -\gamma + \delta Y \cot(\tfrac{\Delta}{2}).$$

The result of this procedure for the fourth extinction direction of the $((CH_3)_4N)_2ZnCl_4$ sample has been plotted in figure 2.13. The values C_{21} of figure 2.8 have been used.

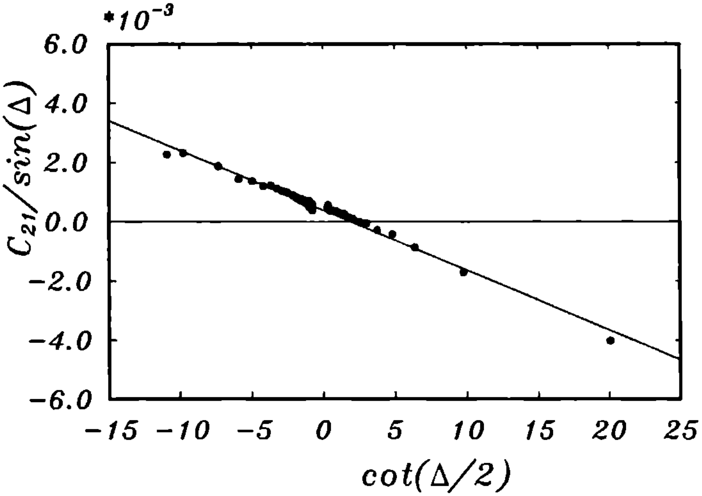

Figure 2.13 A plot of $C_{21}/\sin\Delta$ versus $\cot\left(\frac{\Delta}{2}\right)$ for the $((CH_3)_4N)_2ZnCl_4$ sample. The straight line is a least squares fit.

The straight line is the result of a least squares fit. In this way, we obtain the values $\delta Y = -2.02 \cdot 10^{-4}$ and $\gamma = -3.89 \cdot 10^{-4}$. Using for this procedure the values of C_{21} from figure 2.2, obtained without any corrections in the first step of the fitting procedure, yields a figure in which no straight line can be recognised. This again shows the usefulness of performing the $\Delta\Theta$-correction.

Evaluation of C_{21} in the case that $\sin(2g_o z) = 0$

In case that the circular birefringence is non-zero, the procedure just described can not be applied. The value of δY can, nevertheless, still be obtained if there are some wavelengths (one is in principle enough) for which $\sin 2g_o z = 0$. For such wavelengths $C_{21}^{\Theta_0}$ equals

$2\delta Y$. The linear birefringence Δn_{11} for the $((CH_3)_4N)_2ZnCl_4$ sample becomes zero at approximately $\lambda = 400$ nm as can be observed in figure 2.10. The value of C_{21} in figure 2.8 at that wavelength is $-4.15 \cdot 10^{-4}$. From this we calculate $\delta Y = -2.08 \cdot 10^{-4}$ which indeed is very close to the value $-2.02 \cdot 10^{-4}$ obtained from the $C_{21}/\sin\Delta$ against $\cot(\frac{\Delta}{2})$ plot.

Θ_0 versus cot($g_o z$)

If there is no rotation of the optical indicatrix ($\delta\Theta_{\text{indicatrix}} = 0$), the value of $p + a$ can be found by plotting Θ_0 against $\cot(g_o z)$ (Kobayashi et al., 1988b) as has been done in figure 2.14 for $((CH_3)_4N)_2ZnCl_4$. The slope of the obtained straight line is $\frac{1}{2}(p + a)$, because then $\Theta_0 = \frac{1}{2}(p+a)\cot(g_o z) - \frac{1}{2}\delta Y$. In this case, the intercept with the ordinate-axis gives no information, since the values of Θ_0 are measured with respect to an arbitrary origin (Θ_0 itself is used as origin for the measurement of Θ values). The value for $p + a$ that is obtained from a least squares fit to the data in figure 2.14 is $-1.43 \cdot 10^{-3}$. This procedure can of course also be performed if circular birefringence is present, because the expression for Θ_0 is independent of ω.

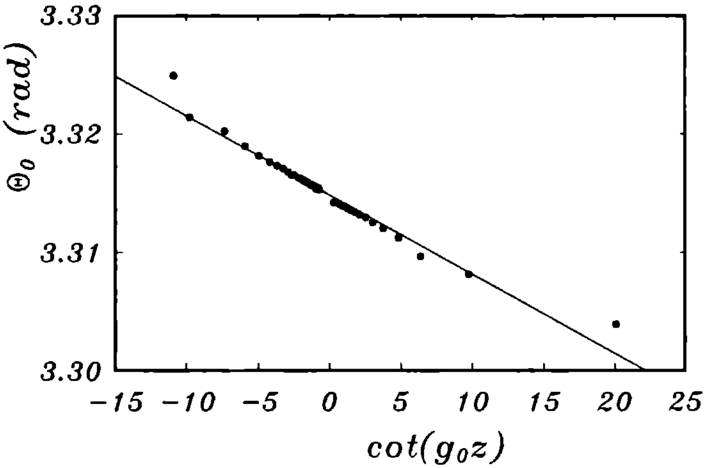

Figure 2.14 A plot of Θ_0 versus $\cot(g_o z)$ for the $((CH_3)_4N)_2ZnCl_4$ sample. From Θ_0, $\frac{1}{2}\pi$ has been subtracted. The straight line is a least squares fit to the data.

From the values of $(p+a)$ and $\gamma = (p-a)$ obtained from the $C_{21}/\sin\Delta$ versus $\cot(\frac{\Delta}{2})$ fit one can calculate the ellipticities p and a.

In case that there is no region where the circular birefringence is zero $\gamma = (p - a)$ can not be obtained. However, if one assumes p to be an apparatus constant, denoted $\overline{p}$, it could be measured using an optically inactive ($\omega = 0$) reference crystal, as has been done by Kobayashi et al. (1988b). Then, from $\bar{p}$ and $\bar{p}+a$, one can get a and thus $\gamma = (\bar{p}-a)$. It is stated by Kobayashi et al. (1988b) that a is not an apparatus constant, because it depends on the exact way the light beam traverses the analyser. We show later that also p can not be considered to be an apparatus constant and that the use of a reference crystal method is dangerous, therefore.

A new method: A total fit to C_{21}

Here, we propose a new method for obtaining γ, δY and $(p+a)$. Consider the expression for $C_{21}^{\Theta_0}$ when there is no circular birefringence:

$$C_{21}^{\Theta_0}(\omega = 0) = 2\delta Y \cos^2(g_o z) - (p-a)\sin(2g_o z) + (p+a)2p_o z\cot(g_o z).$$

Since, at this stage of the interpretation, both g_o and p_o are known we can perform a linear least squares fit (Deming and Morgan, 1979) to the data. The fitting-parameters are $2\delta Y$, $-(p-a)$ and $(p+a)$. The value of $(p+a)$ is of course only reliable if the linear dichroism is non-zero.

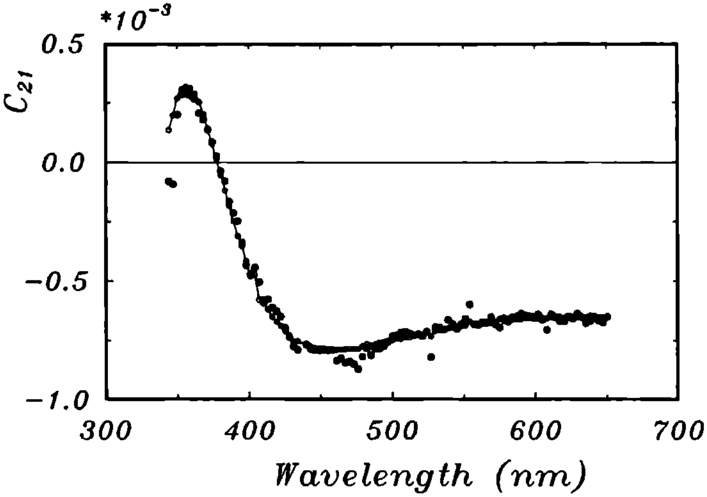

Figure 2.15 Total fit to the $C_{21}(\omega = 0)$ values of figure 2.7 for the $((CH_3)_4N)_2ZnCl_4$ sample. The full circles (•) are the data of figure 2.7 and the open circles (∘) the fitted values. A line has been drawn through the latter to guide the eye.

In figure 2.15 we show the result of such a fit to the C_{21} data of figure 2.7. As explained in section 2.4.1.3, a fit with $n = 3$ using expression (2.14) in the first step of the fitting procedures is adequate for the followed measurement procedure. Therefore we took the data of figure 2.7 (fit up to second order in Θ and Y) rather than those of figure 2.8 (fit up to fourth order in Θ and Y), because the noise is less in figure 2.7 and we want to demonstrate the optimal performance of our HAUP. As one can see in figure 2.15, an almost perfect fit is possible. The largest deviation between the fit and the data is about $6{\cdot}10^{-5}$. We obtain $\delta Y = -2.31{\cdot}10^{-4}$, $\gamma = (p-a) = -5.09{\cdot}10^{-4}$ and $(p+a) = -1.07{\cdot}10^{-3}$.

From a similar fit to the data of figure 2.8 (obtained by fitting up to fourth order in Θ and Y in the first step of the fitting procedure), we obtain the values: $\delta Y = -1.77 \cdot 10^{-4}$, $\gamma = (p-a) = -4.08 \cdot 10^{-4}$ and $(p+a) = -7.13 \cdot 10^{-4}$. In case of δY and γ these results agree reasonably with those obtained from the $C_{21}/\sin\Delta$ versus $\cot(\frac{\Delta}{2})$ plot ($\delta Y = -2.02 \cdot 10^{-4}$ and $\gamma = -3.89 \cdot 10^{-4}$). The value of (p+a) is indeed clearly wrong as expected, since there is no linear dichroism. If there is circular birefringence, like in quartz, a fit as proposed here will give the wrong values for the parameters δY, $p-a$ and $p+a$, because the influence of ω/g_o is not included. However, when the fit is performed anyway one will observe considerable differences between the fit and the data. This is, therefore, an elegant method to inspect whether there is circular birefringence or not, in samples where it is unclear. Quartz is optically active and this can immediately be seen in figure 2.16 where the obtained data for C_{21} and the fit to these data are shown. The fit matches the data at about $\lambda = 475$ nm, but at smaller and larger wavelengths a clear deviation occurs. Differences as large as $1.6 \cdot 10^{-3}$ can be observed. Also shown is

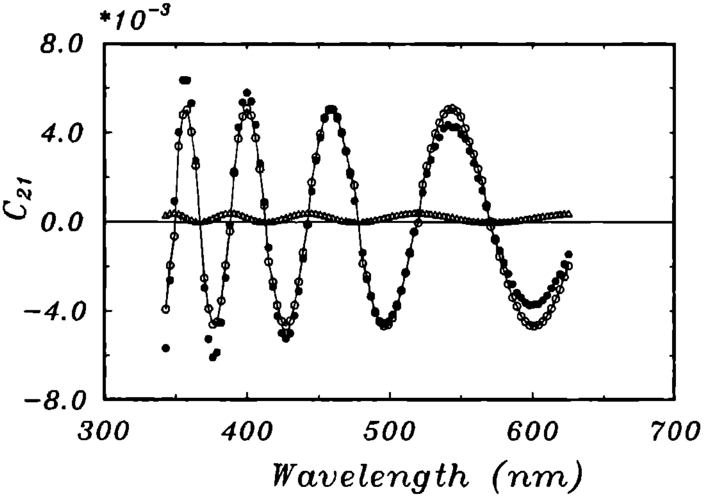

Figure 2.16 Total fit to the C_{21} data of the quartz sample. The full circles (•) are the C_{21} data from the measurement and the open circles (○) are the result of the total fit to these data. A line to guide the eye has been drawn connecting the open circles. The open triangles (△) are the values of the term $2\delta Y \cos^2(g_o z)$ obtained from the total fit.

the term $2\delta Y\cos^2(g_o z)$ as it is found from the fit. The maxima of this term correspond to wavelengths where $g_o z$ is an integer multiple of π. As explained before, in the case that there is circular birefringence one can still find the value of δY by evaluating the C_{21} curve at precisely those points. Remarkably, in figure 2.16, the C_{21} curve intersects the $2\delta Y\cos^2(g_o z)$ curve exactly at its maxima and minima, meaning that the obtained value $\delta Y = 1.73 \cdot 10^{-4}$ from the total fit to C_{21} is correct. Nevertheless, the value for γ is wrong, because if δY is correct the γ obtained from the fit is in fact the average of $((p-a)+\omega/g_o)$ over all wavelengths.

A total fit to C_{11}

In the same way as just described for C_{21}, also a total fit to C_{11} can be performed in case that there is no circular birefringence. The fitting-parameters should give the values of $(\delta Y)^2$, $(p-a)^2$, $-\delta Y(p-a)$, $-(p-a)(p+a)$ and $\delta Y(p+a)$ (see eqn. (2.9)). We have performed such fits, but a good fit to the data was not possible. This is probably due to the fact that one should include in $C_{11}^{\Theta_0}$ an extra term A_0. According to Kobayashi and Uesu (1983) A_0 represents the overall effect of incoherent scattering and of multiple reflections of the light beam at the sample surfaces. It is very likely that this term A_0 is not constant, but varies in an unpredictable way with wavelength. Then, a total fit to C_{11} is not useful.

The calculation of the circular birefringence

After the determination of all systematic errors, in one of the ways described above, one can calculate

$$\omega/2g_o \equiv k$$

from the C_{21} values. k is a measure for the ellipticity of an eigenpolarisation of the light in the sample. Figure 2.17 depicts the values thus obtained from figure 2.7. At wavelengths larger than $\lambda = 525$ nm the results for $|\,k\,|$ are smaller than $2 \cdot 10^{-5}$. At $\lambda = 400$ nm a divergence can be observed. This is expected, since g_o goes through zero at that wavelength.

Subsequently the circular birefringence is calculated as follows:

$$n_r - n_l = \Delta n\,\omega/g_o = 2\Delta n k. \tag{2.20}$$

In this way, one achieves the results given in figure 2.18. As one can see, the absolute value of the circular birefringence is smaller than $6 \cdot 10^{-9}$ for almost all points.

The circular birefringence of the quartz sample was calculated using the δY value $1.73 \cdot 10^{-4}$ as obtained from the total fit to the C_{21} data, described above. There was no need to know the value of $p+a$, as there turned out to be no linear dichroism. In comparison with the results of Moxon et al. (1991) for the values of k, a best match was obtained by taking γ very small (i.e. $\gamma = 0$). The resulting circular birefringence is plotted in figure 2.19. It also agrees very well with the value found by Kobayashi et al. (1988b) for $\lambda = 632.8$ nm. Note that, strictly speaking, the value of γ has not been determined in our HAUP measurement. It has been obtained by comparing the data with measurements of others (Kobayashi et al. (1988b), Moxon et al. (1991)). Unfortunately, we will question their methods of determining γ later on. However, as already stated by Moxon et al. (1991), one at least knows, that for quartz the value of γ is small compared with the value of k, so that only small errors can be made by taking a value $\gamma = 0$.

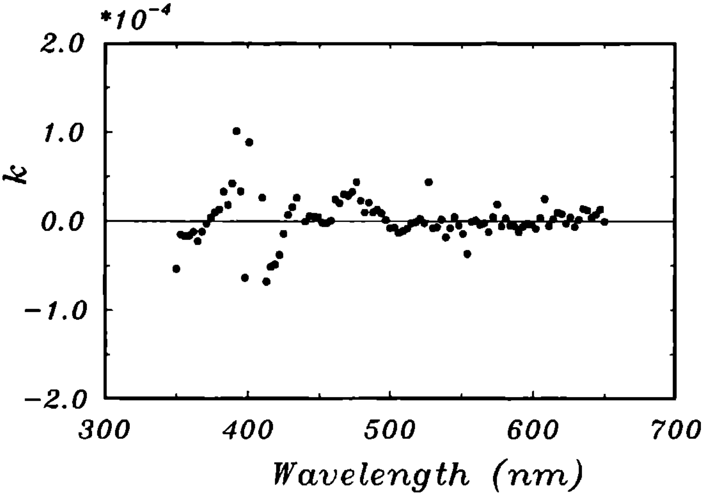

Figure 2.17 The ellipticity $k = (\omega/2g_o)$ as a function of the wavelength for the $((CH_3)_4N)_2ZnCl_4$ sample.

The wavelengths at which $2g_oz$ equals an integer times 2π can clearly be observed as discontinuities in figure 2.19. The most singular points have been omitted from the figure. This measurement shows that the HAUP method is indeed capable of separating linear from circular birefringence, but that very good care must be taken for the cases that $\sin(g_oz)$ becomes small. Moreover, the determination of γ is problematic in the case that there is circular birefringence. This problem is addressed in the next section.

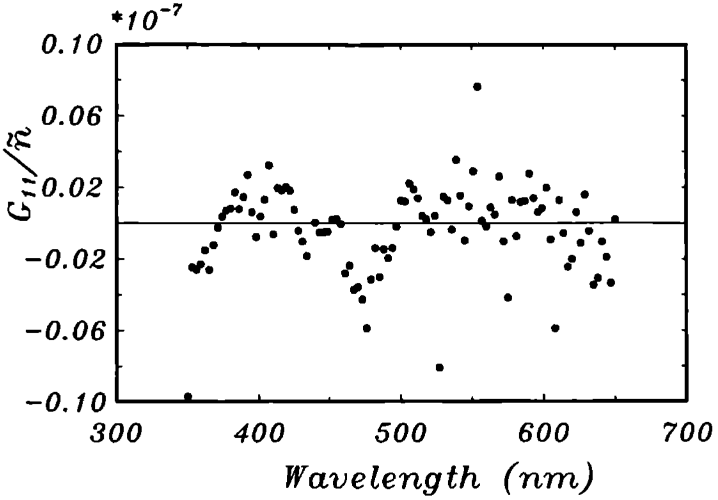

Figure 2.18 The circular birefringence $(G_{11}/\bar{n}) = (n_r - n_l)_{11}$ of $((CH_3)_4N)_2ZnCl_4$ as a function of the wavelength.

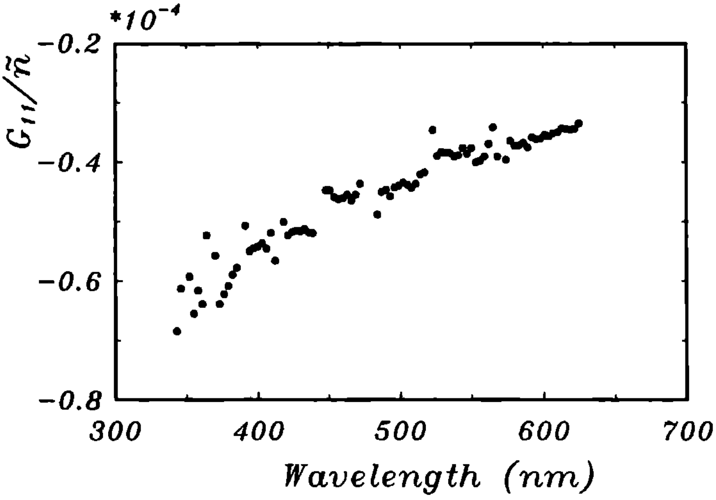

Figure 2.19 The circular birefringence $(G_{11}/\bar{n}) = (n_r - n_l)_{11}$ of quartz as a function of the wavelength. The points corresponding to the discontinuities in figure 2.11 have been omitted, since the HAUP intensity formula is not valid there.

2.5 Behaviour of the systematic errors

All four extinction directions have been measured for the $((CH_3)_4N)_2ZnCl_4$ sample. Because the paraelectric phase is centrosymmetric, it has no circular birefringence. Therefore, it is ideally suited for examining the behaviour of the systematic errors. There are, namely, no problems, of the kind discussed in section 2.4, in determining their values.

Systematic Error and Fit Method	First ext. direction	Second ext. direction	Third ext. direction	Fourth ext. direction
δY from $\frac{C_{21}}{\sin(\Delta)}$ versus $\cot(\frac{\Delta}{2})$	$-8.70 \cdot 10^{-5}$	$-2.23 \cdot 10^{-4}$	$6.88 \cdot 10^{-5}$	$-2.02 \cdot 10^{-4}$
δY from total fit to C_{21}	$-1.03 \cdot 10^{-4}$	$-1.96 \cdot 10^{-4}$	$3.32 \cdot 10^{-5}$	$-1.77 \cdot 10^{-4}$
γ from $\frac{C_{21}}{\sin(\Delta)}$ versus $\cot(\frac{\Delta}{2})$	$-4.77 \cdot 10^{-4}$	$-4.18 \cdot 10^{-4}$	$-4.16 \cdot 10^{-4}$	$-3.89 \cdot 10^{-4}$
γ from total fit to C_{21}	$-4.36 \cdot 10^{-4}$	$-4.30 \cdot 10^{-4}$	$-4.23 \cdot 10^{-4}$	$-4.08 \cdot 10^{-4}$
$p + a$ from Θ_0 versus $\cot(g_o z)$	$1.03 \cdot 10^{-3}$	$-1.53 \cdot 10^{-3}$	$1.08 \cdot 10^{-3}$	$-1.43 \cdot 10^{-3}$

Table 2.2 The values of the systematic errors δY, $\gamma = p - a$ and $p + a$ as obtained from the different ways of fitting, described in the text, for all extinction directions of the $((CH_3)_4N)_2ZnCl_4$ sample.

In table 2.2, the results for the systematic errors are given for all four extinction directions. In the first step of the fitting procedure all corrections as described in section 2.4.1.1, 2.4.1.2 and 2.4.1.3 have been performed.

From the comparison of the first row with the second and the third row with the fourth, we may conclude that the total fit to C_{21} has given approximately the same results as the $C_{21}/\sin(\Delta)$ versus $\cot(\frac{\Delta}{2})$ fit and therefore works very well, as expected.

2.5.1 The ellipticities p and a

In table 2.3 the ellipticities p and a are given as they were calculated from γ (third row of table 2.2) and $p + a$ (fifth row of table 2.2).

From this table we must conclude that neither p nor a can be considered to be an apparatus constant. Remarkably, however, the values for the first and third extinction direction almost coincide and the same holds for the values of the second and fourth extinction direction. We always observe this behaviour in our measurements. It shows that the ellipticity of the light emerging from a polariser depends strongly on the orientation of the polariser. The ellipticity even changes sign upon a rotation of $\pi/2$ in this measurement. Rotating the polarisers over π however, results in an equal ellipticity.

At present, we are not able to explain this behaviour. Ortega et al. (1992) remark, that there is an effect of spurious birefringence of the cryostat windows giving parasitic ellipticities. However, in their case this results from windows between the polarisers and the sample. Therefore, it can not explain the behaviour that we have found, because in our set-up the total polariser-sample-analyser system is in the vacuum cryostat between the windows.

It is important to realise that our experiments have, nevertheless, shown that the ellipticities can be taken constant for a certain extinction direction, if the value of Θ_0 does not vary too much. Problems can be expected if there is a large indicatrix rotation. If the polarisers have to be rotated over an appreciable angle for a new HAUP measurement both ellipticities p and a will change.

Extinction direction	p	a
1	$2.74 \cdot 10^{-4}$	$7.51 \cdot 10^{-4}$
2	$-9.72 \cdot 10^{-4}$	$-5.54 \cdot 10^{-4}$
3	$3.33 \cdot 10^{-4}$	$7.49 \cdot 10^{-4}$
4	$-9.11 \cdot 10^{-4}$	$-5.23 \cdot 10^{-4}$

Table 2.3 The ellipticities p and a as calculated from the third and fifth row of table 2.2.

This means that the method of assuming p to be an apparatus constant $\overline{p}$ and determining it with a reference crystal, as done by Kobayashi et al. (1988b), is only possible if the reference crystal and the sample have exactly the same positions of their extinction directions.

Furthermore, an alternative method that has been proposed by Moxon and Renshaw (1990) and has been used by Dijkstra et al. (1992) will be wrong in general, too. In this method, γ is determined by comparing the C_{21} values of two succeeding extinction directions. They have assumed that upon changing the extinction direction, p and a remain the same and that ω/g_o changes sign. The latter is true, but the values of p and a change (unpredictably) when the polarisers are rotated over $\frac{1}{2}\pi$. In case of the measurements on the $((CH_3)_4N)_2ZnCl_4$ sample we have tried this method, but the values of γ, thus obtained, were always clearly wrong. However, in the set-up used by Moxon and Renshaw (1990) the polarisers remain at their position and the sample is rotated over $\frac{1}{2}\pi$ when the extinction direction is changed. In that way, their method may indeed work, although one still expects that the value of a changes upon rotating the crystal, because the exact way in which the beam traverses the analyser, changes, as the findings of Kobayashi et al. (1988b) have shown.

2.5.2 The behaviour of δY

In this section the behaviour of the systematic error δY and its cause are investigated.

In table 2.4, the δY values obtained from a $C_{21}/\sin\Delta$ against $\cot\left(\frac{\Delta}{2}\right)$ fit are given for all extinction directions of the $((CH_3)_4N)_2ZnCl_4$ sample. For the first column, $\delta Y_{\mathrm{uncorr}}$, the data of figure 2.3 were used and for the second column, δY_{corr}, the data of figure 2.7. The difference between them is thus the correction of the analyser position using a sixth order polynomial, as described in section 2.4.1.2. Also given in table 2.4 are the values ΔY_{fit} of the sixth order polynomial at the four extinction directions, see figure 2.6.

Extinction direction	$\delta Y_{\mathrm{uncorr}}$	δY_{corr}	ΔY_{fit}	$\delta Y_{\mathrm{uncorr}} - (-\Delta Y_{\mathrm{fit}})$	$\delta Y_{\mathrm{corr(II)}}$
1	$-1.85 \cdot 10^{-4}$	$-6.96 \cdot 10^{-5}$	$1.1 \cdot 10^{-4}$	$-7.5 \cdot 10^{-5}$	$3.92 \cdot 10^{-7}$
2	$-6.27 \cdot 10^{-4}$	$-2.45 \cdot 10^{-4}$	$3.8 \cdot 10^{-4}$	$-2.47 \cdot 10^{-4}$	$2.47 \cdot 10^{-6}$
3	$5.07 \cdot 10^{-4}$	$7.09 \cdot 10^{-5}$	$-4.2 \cdot 10^{-4}$	$8.7 \cdot 10^{-5}$	$6.83 \cdot 10^{-7}$
4	$2.41 \cdot 10^{-4}$	$-2.45 \cdot 10^{-4}$	$-4.3 \cdot 10^{-4}$	$-1.89 \cdot 10^{-4}$	$5.80 \cdot 10^{-7}$

Table 2.4 The behaviour of the systematic error δY after fitting with or without corrections, as described in the text.

The values of $-\delta Y_{\mathrm{uncorr}}$ and $-\delta Y_{\mathrm{corr}}$ are also depicted in figure 2.6 at the four Θ_0 values of the extinction directions. Clearly, all four values $-\delta Y_{\mathrm{uncorr}}$ are very close to the measured ΔY curve. Furthermore, the δY_{corr} values are almost precisely equal to $\delta Y_{\mathrm{uncorr}} - (-\Delta Y_{\mathrm{fit}})$. This means that indeed the deviation ΔY of the analyser from its supposed position Y is the main source for the appearance of the systematic error δY instead of a misorientation of the sample as suggested by Kobayashi et al. (1988b).

A very precise knowledge of the analyser position is, therefore, essential for the reduction of δY-errors in HAUP measurements. Such knowledge might be provided by the use of angle encoders as is done by Moxon et al. (1991) and Ortega et al. (1992).

Here, we propose another way in which one can reduce the δY-error, without the use of encoders. Consider the variation in the values of ΔY for all analyser positions belonging to the measurement of a single extinction direction. Since the total rotation of the analyser is only $9.77 \cdot 10^{-3}$ rad in such a measurement the variation in the ΔY values will be extremely small and we think that it is justified to correct all analyser positions with the same value ΔY in the first step of the fitting procedure. Doing so, using $\Delta Y = -\delta Y_{\text{uncorr}}$ from table 2.4, the values $\delta Y_{\text{corr(II)}}$ given in table 2.4 were obtained from a $C_{21}/\sin\Delta$ against $\cot\left(\frac{\Delta}{2}\right)$ fit in the second step of the fitting procedure. The values $\delta Y_{\text{corr(II)}}$ are so small, that their influence is negligible. In this way, without the use of encoders, we have obtained a method of (almost) completely eliminating the systematic error δY. Using encoders (Moxon et al., 1991) the magnitude of the remaining contribution is comparable.

We have also tested the contribution to δY of a misorientation of the sample (Kobayashi et al. (1988b), Moxon and Renshaw (1990)) by deliberately placing the front sample surface clearly non-perpendicular to the light beam. This indeed increases the δY-error. However, we think that in practice the sample can be positioned so well that the contribution to δY from its misorientation is much smaller than the ΔY part described above.

A third contribution to δY can be caused by drift in the motor drivers or rotation stages as observed by Ortega et al. (1992). These authors found a drift of the order of $2 \cdot 10^{-4}$ rad from the initial crossed-polariser position after the time of a typical experiment. In our apparatus, comparable drifts of about $1 \cdot 10^{-4}$ rad can sometimes be observed.

Still other causes for δY have been discussed by Moxon and Renshaw (1990) and Moxon et al. (1991).

2.5.3 The HAUP intensity formula for different extinction directions

The study of the behaviour of the systematic errors has shown that for all extinction directions the same HAUP intensity formula can be used if the following relations are taken into account.

$$\begin{array}{rcrcrcr} p_1 & = & p_3 & \neq & p_2 & = & p_4 \\ a_1 & = & a_3 & \neq & a_2 & = & a_4 \\ \delta Y_1 & \neq & \delta Y_2 & \neq & \delta Y_3 & \neq & \delta Y_4 \\ \omega_1 & = & \omega_2 & = & \omega_3 & = & \omega_4 \\ -g_{o1} & = & +g_{o2} & = & -g_{o3} & = & +g_{o4} \\ -\omega_1/g_{o1} & = & +\omega_2/g_{o2} & = & -\omega_3/g_{o3} & = & +\omega_4/g_{o4} \end{array} \qquad (2.21)$$

The relations (2.11) are thus inadequate and should be replaced by the relations (2.21).

As a result of a HAUP measurement, the magnitude and sign of ω/g_o are found. Unfortunately, the sign of g_o is not obtained, because it must be calculated from $4\sin^2(g_o z)$. Usually, however, it is possible to determine the orientation of the fast and slow axes in a separate experiment (e.g. polarising microscope). If, in the HAUP measurement the fast axis was along the polarisation of the light emerging from the polariser for a certain extinction direction, g_o should be taken positive. In case that it is the slow axis, g_o is negative. With that knowledge then, the sign of ω is found. A negative ω corresponds to a dextrorotatory crystal.

2.6 The quality and sensitivity of HAUP measurements

At this point we would like to point out that there are several possibilities for determining the quality of a HAUP measurement during the fitting procedures.

For example, if in the first step of the fitting procedures the correction $\Delta\Theta$ as described in section 2.4.1.1 is small, the HAUP measurement has indeed been performed in the close neighbourhood of an extinction direction, as is desired. Then one can expect that the goodness-of-fit value that can be calculated for the linear least squares fit to the intensities (Ortega et al., 1992) is optimal.

Furthermore, during the second step of the fitting procedures, the systematic errors obtained from a total fit to C_{21} and those obtained from the $C_{21}/\sin\Delta$ against $\cot\left(\frac{\Delta}{2}\right)$ and Θ_0 against $\cot\,(g_o z)$ plots will be comparable for a good measurement.

A possible test for the quality of the sample preparation is the following. In case that the sample is non-absorbing for the wavelength of the light used, the linear dichroism is expected to be negligible. If, nevertheless, a large linear dichroism is found, one should look carefully at the quality of the sample. It is advisable to examine always the sample under the polarising microscope before performing a HAUP measurement. A clear extinction between crossed polarisers must be observed. Also, it must be very well possible, of course, to compensate the total retardation Δ caused by the sample, with a compensator. Furthermore, if the birefringence is not too small, the polarising microscope can be used to check the plane-parallelism of the sample.

A final test for the quality of a HAUP measurement is that the results for the sample properties should agree nicely between the measurement of different extinction directions. Regarding all these checks, the measurements described in this paper turned out to be very good.

Of course, after having established the possibility of performing high quality measurements, one would like to know how sensitive these measurements are for the various optical properties. In order to get an idea, it is instructive to consider the resolution with which polariser positions can be set.

For example, during the determination of Θ_0, which is used to find a rotation of the optical indicatrix, intensities are measured for a set of polariser positions keeping the analyser crossed. The minimum rotation angle for the polarisers is $3.49 \cdot 10^{-5}$ rad in our instrument. The position of minimal intensity is then determined by fitting a parabola through the measured points. Ideally, one should be able to find this angle with a higher precision than the minimal rotation angle. In practice, the spread in the found minimum is in the order of $1 \cdot 10^{-5}$ rad. This means that the sensitivity for detecting rotations of the optical indicatrix is in the order of $1 \cdot 10^{-5}$ rad. If a $\Delta\Theta$-correction is performed, as described in section 2.4.1.1, the sensitivity may be increased.

The circular birefringence is, in a way, found by determining the position of the absolute intensity minimum in the close neighbourhood of an extinction direction, with respect to the position $\Theta = Y = 0$. This interpretation is explained by Moxon and Renshaw (1990). Therefore, also for the parameter $\omega/g_o = 2k$ one can expect a sensitivity roughly in the order of $1 \cdot 10^{-5}$. Indeed, in figure 2.17 a value for $|k| < 2 \cdot 10^{-5}$ is observed, for not too small values of g_o. This has resulted in values for the circular birefringence $|n_r - n_l| < 6 \cdot 10^{-9}$, but of course the sensitivity for the circular birefringence depends on the magnitude of the linear birefringence.

It is more difficult to get an idea of the sensitivity with which the linear birefringence can be determined. Nevertheless, the HAUP method provides a separation between linear and circular birefringence. In many other methods the linear birefringence is measured as if it were the only optical effect present. The HAUP method takes the presence of circular birefringence correctly into account. In practice, a rough estimate can be made for the sensitivity if several extinction directions are measured. One compares the results for $4\sin^2(g_o z)$ of one extinction direction with those of another, for all wavelengths. In case of the $((CH_3)_4N)_2ZnCl_4$ sample, the differences between these values were on the average 0.02. The corresponding differences in the linear birefringence Δn were smaller than $1 \cdot 10^{-6}$. Probably the accuracy can be increased by averaging first the $4\sin^2(g_o z)$ values of all extinction directions and calculating then the linear birefringence from this average. In case that only one extinction direction has been measured, one can compare the obtained values of C_{13} and C_{22} (see equation (2.9)).

2.7 Conclusions

In this paper, we have conscientiously reexamined the working principle of HAUP. We have described some improvements to the experimental set-up and treatment of the samples, that have been carried out. In addition, the HAUP intensity formula has been derived in a general and rigorous way and the approximations made in this derivation have been discussed. Furthermore, the behaviour of systematic errors and their causes have been studied and discussed. Using this knowledge, the fitting procedures used in the interpretation of HAUP measurements were carefully reviewed and mistakes in the interpretation and experimental set-up used for earlier measurements have been revealed. Moreover, estimates of the sensitivities with which the various optical properties can be determined have been made.

We think that this analysis has led to a better understanding of the way HAUP measurements must be performed. It should provide a mean to investigate the controversies in experimental results. In the very near future we plan to publish measurements of optical activity in incommensurately modulated crystal phases, that have a centrosymmetric average structure, using this improved technique.

2.8 Acknowledgments

We would like to thank Prof. Dr. P. Bennema for all his support. We are very grateful to Prof. Dr. M. Glazer and his group for their hospitality and fruitful discussions during our visit at their laboratory. The authors would like to thank Prof. A. Janner and Prof. T. Janssen for their critical reading of the manuscript. This work is part of the research program of the Stichting voor Fundamenteel Onderzoek der Materie (Foundation for Fundamental Research on Matter).

References

Arend, H., Perret, F., Wüest, H. and Kerkoc, P., *Journ. of Cryst. Growth* **74**, 321 (1986).

Born, M. and Wolf, E., *Principles of Optics* (Oxford: Pergamon, 1969).

Born, M., *Optik* (Berlin: Springer-Verlag, 1985).

Cummins, H. Z., *Phys. Rep.* **185**, 211 (1990).

Deming, S. N. and Morgan, S. L., *Clin. Chem.* **25**, 840 (1979).

Dijkstra, E. and Janner, A., *Ferroelectrics* **105**, [113] /547 (1990).

Dijkstra, E., Meekes, H. and Kremers, M., *J. Phys. D: Appl. Phys* **24**, 1861 (1991).

Dijkstra, E., *J. Phys.: Condens. Matter* **3**, 141 (1991b).

Dijkstra, E., Kremers, M. and Meekes, H., *J. Phys.: Condens. Matter* **4**, 715 (1992).

Dijkstra, E., Janner, A. and Meekes, H., *J. Phys.: Condens. Matter* **4**, 693 (1992b).

Folcia, C. L., Ortega, J., Etxebarria, J. and Breczewski, T., *Phys. Rev. B* **48**, 695 (1993).

Gehring, G. A., *J. Phys. C: Solid State Phys.* **10**, 531 (1977).

Glazer, A. M. and Stadnicka, K., *J. Appl. Cryst.* **19**, 108 (1986).

Ivanov, N. R., *Phase Transitions* **36**, 223 (1991).

Jones, R. C., *J. Opt. Soc. Am.* **38**, 671 (1948).

Kobayashi, J. and Uesu, Y., *J. Appl. Cryst.* **16**, 204 (1983).

Kobayashi, J., Kumomi, H. and Saito, K., *J. Appl. Cryst.* **19**, 377 (1986).

Kobayashi, J., Saito, K., Fukase, H. and Matsuda, K., *Phase Transitions* **12**, 225 (1988a).

Kobayashi, J., Asahi, T., Takahashi, S. and Glazer, A. M., *J. Appl. Cryst.* **21**, 479 (1988b).

Kushnir, O. S. and Vlokh, O. G., *J. Phys.: Condens. Matter* **5**, 7017 (1993).

Meekes, H. and Janner, A., *Phys. Rev. B* **38**, 8075 (1988).

Moxon, J. R. L. and Renshaw, A. R., *J. Phys: Condens. Matter* **2**, 6807 (1990).

Moxon, J. R. L., Renshaw, A. R. and Tebbutt, I. J., *J. Phys. D: Appl. Phys.* **24**, 1187 (1991).

Nye, J. F., *Physical properties of crystals* (Oxford: Oxford University Press, 1985).

Ortega, J., Etxebarria, J., Zubillaga, J., Breczewski, T. and Tello, M. J., *Phys. Rev. B* **45**, 5155 (1992).

Ortega, J., Etxebarria, J. and Folcia, C. L., *submitted to Phys. Rev. B*, (1994).

Ramachandran, G. N. and Ramaseshan, S., *Crystal Optics, Handbuch der Physik, Band XXV/1* (Berlin: Springer, 1961).

Wiesner, J. R., Srivastava, R. C., Kennard, C. H. L., DiVaira, M. and Lingafelter, E. C., *Acta Cryst.* **23**, 565 (1967).

Appendix A

The expansions of the terms $P_iA_j^*$ up to fourth order in Θ, Y, p and a

$$
\begin{aligned}
P_1A_1^* = \;& \left\{ia - \frac{1}{6}ia^3 - \frac{1}{2}iap^2\right\} \\
+ \;& \Lambda\left\{-1 + \frac{1}{2}(a^2+p^2)\right\} + \Theta\{pa\} \\
+ \;& \Lambda\Theta\{ip\} + \Lambda^2\left\{-\frac{1}{2}ia\right\} + \Theta^2\left\{-\frac{1}{2}ia\right\} \\
+ \;& \Lambda\Theta^2\left\{\frac{1}{2}\right\} + \Lambda^3\left\{\frac{1}{6}\right\} + \mathcal{O}(5)
\end{aligned}
\tag{A.1}
$$

$$
\begin{aligned}
P_2A_1^* = \;& \left\{-pa + \frac{1}{6}pa^3 + \frac{1}{6}ap^3\right\} \\
+ \;& \Lambda\left\{-ip + \frac{1}{2}ipa^2 + \frac{1}{6}ip^3\right\} + \Theta\left\{ia - \frac{1}{2}iap^2 - \frac{1}{6}ia^3\right\} \\
+ \;& \Lambda\Theta\left\{-1 + \frac{1}{2}(a^2+p^2)\right\} + \Lambda^2\left\{\frac{1}{2}pa\right\} + \Theta^2\left\{\frac{1}{2}pa\right\} \\
+ \;& \Lambda\Theta^2\left\{\frac{1}{2}ip\right\} + \Theta\Lambda^2\left\{-\frac{1}{2}ia\right\} + \Lambda^3\left\{\frac{1}{6}ip\right\} + \Theta^3\left\{-\frac{1}{6}ia\right\} \\
+ \;& \Lambda\Theta^3\left\{\frac{1}{6}\right\} + \Theta\Lambda^3\left\{\frac{1}{6}\right\} + \mathcal{O}(5)
\end{aligned}
\tag{A.2}
$$

$$
\begin{aligned}
P_1A_2^* = \;& \left\{1 - \frac{1}{2}a^2 - \frac{1}{2}p^2 + \frac{1}{24}a^4 + \frac{1}{24}p^4 + \frac{1}{4}a^2p^2\right\} \\
+ \;& \Lambda\left\{ia - \frac{1}{6}ia^3 - \frac{1}{2}iap^2\right\} + \Theta\left\{-ip + \frac{1}{2}ipa^2 + \frac{1}{6}ip^3\right\} \\
+ \;& \Lambda\Theta\{pa\} + \Lambda^2\left\{-\frac{1}{2} + \frac{1}{4}a^2 + \frac{1}{4}p^2\right\} + \Theta^2\left\{-\frac{1}{2} + \frac{1}{4}a^2 + \frac{1}{4}p^2\right\} \\
+ \;& \Lambda\Theta^2\left\{-\frac{1}{2}ia\right\} + \Theta\Lambda^2\left\{\frac{1}{2}ip\right\} + \Lambda^3\left\{-\frac{1}{6}ia\right\} + \Theta^3\left\{\frac{1}{6}ip\right\} \\
+ \;& \Lambda^2\Theta^2\left\{\frac{1}{4}\right\} + \Lambda^4\left\{\frac{1}{24}\right\} + \Theta^4\left\{\frac{1}{24}\right\} + \mathcal{O}(5)
\end{aligned}
\tag{A.3}
$$

$$
\begin{aligned}
P_2A_2^* = \;& \left\{ip - \frac{1}{2}ia^2p - \frac{1}{6}ip^3\right\} \\
+ \;& \Lambda\{-pa\} + \Theta\left\{1 - \frac{1}{2}(a^2+p^2)\right\} \\
+ \;& \Lambda\Theta\{ia\} + \Lambda^2\left\{-\frac{1}{2}ip\right\} + \Theta^2\left\{-\frac{1}{2}ip\right\} \\
+ \;& \Theta\Lambda^2\left\{-\frac{1}{2}\right\} + \Theta^3\left\{-\frac{1}{6}\right\} + \mathcal{O}(5)
\end{aligned}
\tag{A.4}
$$

Appendix B

The HAUP intensity formula up to fourth order in Θ and Y

$$\Gamma/\Gamma_0 \approx \begin{pmatrix} 1 & Y & Y^2 & Y^3 & Y^4 \end{pmatrix} C^{\text{e.p.}}_{(5\times5)} \begin{pmatrix} 1 \\ \Theta \\ \Theta^2 \\ \Theta^3 \\ \Theta^4 \end{pmatrix} \tag{B.1}$$

where

$$\begin{aligned}
C^{\text{e.p.}}_{11} = {} & (\delta Y)^2 - 2(\delta Y)^2(p^2+a^2) - \frac{1}{3}(\delta Y)^4 \\
& + (\, (p+a)^2 - 2p\delta Y(g_\mathrm{o}z)(\omega/g_\mathrm{o})^2 - \delta Y(g_\mathrm{o}z)(\omega/g_\mathrm{o})^3 \,)\cos^2(g_\mathrm{o}z) \\
& + (\, (\, (p-a) + (\omega/g_\mathrm{o}) \,)^2 - \frac{1}{3}(p-a)^4 - (\omega/g_\mathrm{o})^4 - \frac{4}{3}(p-a)^3(\omega/g_\mathrm{o}) \\
& -2(p-a)(\omega/g_\mathrm{o})^3 - 2(p-a)^2(\omega/g_\mathrm{o})^2 + 2p\delta Y(g_\mathrm{o}z)(\omega/g_\mathrm{o})^2 + \delta Y(g_\mathrm{o}z)(\omega/g_\mathrm{o})^3 \\
& -4p(\delta Y)^2(\omega/g_\mathrm{o}) - 2(\delta Y)^2(\omega/g_\mathrm{o})^2 \,)\sin^2(g_\mathrm{o}z) \\
& + (\, -\delta Y\,(\, 2p + (\omega/g_\mathrm{o}) \,) + (p-a)(g_\mathrm{o}z)(\omega/g_\mathrm{o})^3 - 2pa(g_\mathrm{o}z)(\omega/g_\mathrm{o})^2 \\
& + \frac{1}{2}(g_\mathrm{o}z)(\omega/g_\mathrm{o})^4 + \frac{1}{2}\delta Y(\omega/g_\mathrm{o})^3 + \frac{2}{3}\delta Y(p-a)^3 + \frac{2}{3}\delta Y(p+a)^3 + p\delta Y(\omega/g_\mathrm{o})^2 \\
& + \delta Y(p-a)^2(\omega/g_\mathrm{o}) + \delta Y(p+a)^2(\omega/g_\mathrm{o}) + \frac{2}{3}(\delta Y)^3(\omega/g_\mathrm{o}) + \frac{4}{3}p(\delta Y)^3 \,)\sin(2g_\mathrm{o}z) \\
C^{\text{e.p.}}_{21} = {} & 2\delta Y - 4\delta Y(p^2+a^2) - \frac{4}{3}(\delta Y)^3 \\
& + (\, -2p(g_\mathrm{o}z)(\omega/g_\mathrm{o})^2 - (g_\mathrm{o}z)(\omega/g_\mathrm{o})^3 \,)\cos^2(g_\mathrm{o}z) \\
& + (\, +2p(g_\mathrm{o}z)(\omega/g_\mathrm{o})^2 + (g_\mathrm{o}z)(\omega/g_\mathrm{o})^3 - 8p\delta Y(\omega/g_\mathrm{o}) - 4\delta Y(\omega/g_\mathrm{o})^2 \,)\sin^2(g_\mathrm{o}z) \\
& + (\, -2p - (\omega/g_\mathrm{o}) + \frac{1}{2}(\omega/g_\mathrm{o})^3 + \frac{2}{3}(p-a)^3 + \frac{2}{3}(p+a)^3 + p(\omega/g_\mathrm{o})^2 \\
& + (p+a)^2(\omega/g_\mathrm{o}) + (p-a)^2(\omega/g_\mathrm{o}) + 2(\delta Y)^2(\omega/g_\mathrm{o}) + 4p(\delta Y)^2 \,)\sin(2g_\mathrm{o}z) \\
C^{\text{e.p.}}_{12} = {} & (\, -2(p+a)(g_\mathrm{o}z)(\omega/g_\mathrm{o})^2 \,)\cos^2(g_\mathrm{o}z) \\
& + (\, 2(p+a)(g_\mathrm{o}z)(\omega/g_\mathrm{o})^2 + 4\delta Y - 8\delta Y(p^2+a^2) \\
& -4\delta Y(\omega/g_\mathrm{o})^2 - 8p\delta Y(\omega/g_\mathrm{o}) - \frac{8}{3}(\delta Y)^3 \,)\sin^2(g_\mathrm{o}z) \\
& + (\, -2(p+a) + (p+a)(\omega/g_\mathrm{o})^2 + \frac{4}{3}(p+a)^3 \\
& +2\delta Y(g_\mathrm{o}z)(\omega/g_\mathrm{o})^2 + 4p(\delta Y)^2 \,)\sin(2g_\mathrm{o}z)
\end{aligned}$$

$$
\begin{aligned}
C_{22}^{\text{e.p.}} &= (\,4-8(p^2+a^2)-8p(\omega/g_\circ)-4(\omega/g_\circ)^2-8(\delta Y)^2\,)\sin^2(g_\circ z)\\
&\quad+(\,8p\delta Y+2(g_\circ z)(\omega/g_\circ)^2\,)\sin(2g_\circ z)\\
C_{31}^{\text{e.p.}} &= 1-2(p^2+a^2)-2(\delta Y)^2\\
&\quad+(\,-4p(\omega/g_\circ)-2(\omega/g_\circ)^2\,)\sin^2(g_\circ z)\\
&\quad+(\,2\delta Y(\omega/g_\circ)+4p(\delta Y)\,)\sin(2g_\circ z)\\
C_{13}^{\text{e.p.}} &= (\,4-8(p^2+a^2)-4(p-a)(\omega/g_\circ)-4(\omega/g_\circ)^2-8(\delta Y)^2\,)\sin^2(g_\circ z)\\
&\quad+(\,2(g_\circ z)(\omega/g_\circ)^2+4p(\delta Y)\,)\sin(2g_\circ z)\\
C_{23}^{\text{e.p.}} &= -16\delta Y\sin^2(g_\circ z)+4p\sin(2g_\circ z)\\
C_{32}^{\text{e.p.}} &= -8\delta Y\sin^2(g_\circ z)+4p\sin(2g_\circ z)\\
C_{41}^{\text{e.p.}} &= -\frac{4}{3}\delta Y+(\,\frac{2}{3}(\omega/g_\circ)+\frac{4}{3}p\,)\sin(2g_\circ z)\\
C_{14}^{\text{e.p.}} &= -10\frac{2}{3}\delta Y\sin^2(g_\circ z)+\frac{4}{3}(p+a)\sin(2g_\circ z)\\
C_{24}^{\text{e.p.}} &= -10\frac{2}{3}\sin^2(g_\circ z)\\
C_{42}^{\text{e.p.}} &= -\frac{8}{3}\sin^2(g_\circ z)\\
C_{33}^{\text{e.p.}} &= -8\sin^2(g_\circ z)\\
C_{51}^{\text{e.p.}} &= -\frac{1}{3}\\
C_{15}^{\text{e.p.}} &= -\frac{16}{3}\sin^2(g_\circ z)
\end{aligned}
$$

All other elements of $C_{(5X5)}^{\text{e.p.}}$ are zero.

List of symbols

Symbol	**Defining relation**	**Description**
a		ellipticity of light polarised by analyser
$\boldsymbol{A}$		Jones vector describing the analyser
$\boldsymbol{C}^{\text{e.p.}}_{(5\times5)}$		matrix defining the HAUP intensity formula, derived with respect to an eigenpolarisation as origin for the polariser reading and up to fourth order terms in the parameters $\Theta, Y, \delta Y, p, a$ and ω
$\boldsymbol{C}^{\Theta_o}_{(4\times4)}$		matrix defining the HAUP intensity formula, derived with respect to an extinction direction as origin for the polariser reading and up to third order terms in the parameters $\Theta, Y, \delta Y, p, a$ and ω
$\boldsymbol{C}_{(n\times n)}$		matrix containing the fitting-parameters for a fit up to n-th order terms in the angles Θ and Y
Δ	$= 2z\sqrt{g_o^2 + \omega^2}$	total retardation
$\Delta\kappa$	$= \kappa_1 - \kappa_2$	linear dichroism
Δn	$= n_1 - n_2$	linear birefringence
$\Delta\Theta$		correction to polariser position reading
$\delta\Theta_{\text{indicatrix}}$		rotation of the optical indicatrix
ΔY		correction to analyser position reading
δY		systematic error, describing a small deviation of the analyser from its supposed position
$\boldsymbol{g}$		the gyration tensor
G	$= \tilde{n}(n_r - n_l)$	
	$= g_{ij}s_i s_j$	the gyration in a certain direction $\boldsymbol{s}$
g_o	$= \frac{\pi}{\lambda}\Delta n$	reprensentation for linear birefringence in Jones calculus
γ	$= p - a$	

Γ_0		intensity of light incident on the polariser
Γ		intensity of light emerging from the analyser
k	$= \frac{\omega}{2g_o}$	a measure for the ellipticity of the eigenpolarisations
κ_1		absorption coefficient for the first (linear) eigenpolarisation
κ_2		absorption coefficient for the second (linear) eigenpolarisation
λ		wavelength of the light
Λ		angle defining analyser position
n_1		refractive index belonging to one (linear) eigenpolarisation
n_2		refractive index belonging to the other (linear) eigenpolarisation
$\tilde{n}$		average of all main refractive indices
n_r		refractive index belonging to a right circular eigenpolarisation
n_l		refractive index belonging to a left circular eigenpolarisation
$n_r - n_l$		circular birefringence
ω	$= \frac{\pi}{\lambda}(n_r - n_l)$	representation for circular birefringence in Jones calculus
p		ellipticity of light polarised by polariser
$\bar{p}$		ellipticity p considered to be an apparatus constant
p_o	$= \frac{\pi}{\lambda}\Delta\kappa$	representation for linear dichroism in Jones calculus
$\boldsymbol{P}$		Jones vector describing the polariser
$\boldsymbol{S}$		Jones matrix describing the sample
$\boldsymbol{s}$		unit wave vector of the light
Θ		angle defining polariser position
Θ_0		position of polariser defining an extinction direction
Y	$= \Lambda - \Theta$	alternative reading system for the analyser
z		thickness of the crystal platelet

Chapter 3

Application of the High Accuracy Universal Polarimeter to magnetic and absorbing crystals

Application of the High Accuracy Universal Polarimeter to magnetic and absorbing crystals

M. Kremers and H. Meekes

Abstract

In this paper we show that the High Accuracy Universal Polarimeter can be used to investigate the optical properties of (almost) any crystal through which light can be transmitted. The only extra condition is that the reciprocal linear birefringence (or the reciprocal linear dichroism) of the sample is large with respect to the other optical effects that are present. The sample is allowed to exhibit reciprocal linear birefringence and reciprocal circular birefringence. This is the situation for which the High Accuracy Universal Polarimeter was originally intended. We show, however, that also reciprocal linear dichroism and reciprocal circular dichroism may be present. The method can, therefore, be applied to (weakly) absorbing crystals. Furthermore, optical effects are taken into account that are related to the breaking of time-reversal symmetry. These are the non-reciprocal circular birefringence, non-reciprocal circular dichroism, non-reciprocal linear birefringence and non-reciprocal linear dichroism. This means that, under some conditions, each (weakly) absorbing, magnetic crystal can be investigated with the High Accuracy Universal Polarimeter. We derive a unified formula for the intensity change of the light that propagates through the polarimeter. This expression can be used to determine the (complex) eigenpolarisations of an arbitrary sample. Moreover, it is shown how this unified formula can be translated to a formula in terms of the different birefringent and dichroic optical effects. The relevant formula for a specific case can, therefore, directly be given. The method is demonstrated by means of measurements on samples of $NiSO_4 \cdot 6H_2O$. This material shows reciprocal linear birefringence, reciprocal linear dichroism, reciprocal circular birefringence and reciprocal circular dichroism, simultaneously.

3.1 Introduction

The study of optical properties of single crystals has a long tradition. Nowadays, it is still very important. The main reason for this lies in the fact that optical effects in crystals are symmetry-dependent, tensorial properties. Whenever new crystalline phases are discovered that have interesting physical properties, optical studies are often performed in order to study the symmetry. In addition, the occurrence of a phase transition into such a phase can be detected by means of optical measurements, because optical properties depend on the order parameter. Also fluctuations of the order parameter may be detected (Ferré and Gehring, 1984). Furthermore, optical properties can be related to the bandstructure of a material, especially in the case of absorbing crystals.

The (new) crystalline phases that are currently of interest often have involved structures. In advance, the symmetry of these phases is not always clear. Consider, for example, the high-T_c superconductors that are subject of many investigations. It has been proposed that so-called anyons, being excitations that obey fractional statistics, exist in these materials (Kalmeyer and Laughlin (1987), Laughlin (1988a), Laughlin (1988b)). The anyons are supposed to break both the spatial inversion and the time reversal symmetry (Wen and Zee (1989), Halperin et al. (1989), Kitazawa (1990), Dzyaloshinskii (1991)). Many optical experiments have been performed (Fabre and Boccara, 1992 and references therein) with the aim of detecting this symmetry breaking. The relevant optical effects that were (supposedly) observed were very small. Therefore, a lot of dispute remained and, to our knowledge, the situation has not yet been clarified.

A second example of crystals with an involved structure is formed by the magneto-electric crystals. In these crystals an electric polarisation can be induced by an applied magnetic field and a magnetisation can result from the action of an applied electric field (O'Dell, 1970). It has been predicted (Brown et al., 1963) that a new optical effect can exist in these magneto-electric crystals, even when no external field is applied. It is a result of the coupling between the electric and magnetic field of the light itself. The effect is called gyrotropic- or non-reciprocal- or Jones-birefringence (Hornreich and Shtrikman (1968), Graham and Raab (1992)). Throughout this paper we use the name non-reciprocal linear birefringence. It can give rise to a shift of the principal axes of linear birefringence and a change in the propagation velocity of plane electromagnetic waves. Hornreich and Shtrikman (1968) have estimated that the shift of the principal axes is in the order of 10^{-6} rad, which is extremely small. As far as we know, the only experimental indication for the existence of non-reciprocal linear birefringence has been reported by Pisarev et al. (1991).

As a last example, we want to discuss the case of incommensurately modulated crystals (de Wolff (1974), Janner and Janssen (1977), de Wolff et al. (1981), Janner et al. (1983)). In these crystals an extra periodicity, the modulation, is present which is incommensurate with the basic 3-dimensional translation lattice. Therefore, the corresponding 3-dimensional lattice translational symmetry is broken. It has been suggested that, for example, spatial inversion symmetry can be broken due to the presence of the modulation (Uesu and Kobayashi (1985), Kobayashi et al. (1986), Meekes and Janner (1988)). This has been tested by measuring the optical activity (i.e. reciprocal circular birefringence) of these crystals (see, for the most recent results Kobayashi et al., 1994 and references therein). Optical activity can not exist in a centrosymmetric medium. In a number of cases, it has been claimed that a very small, but non-zero optical activity was measured in these incommensurately modulated crystals that are, on the average, centrosymmetric. However, also for these measurements, there remains a lot of dispute (Ortega et al. (1994), Kremers and Meekes (1994a), Kremers et al. (1994b)).

There are clear resemblances between the just described examples. In all cases, one searches for very subtle optical effects. Their measurement is usually complicated considerably by the presence of other, much larger optical effects. The crystals are mostly optically anisotropic and in many cases also absorbing. Therefore, the subtle effects have to be separated from birefringent as well as dichroic properties in an appropriate way. Unfortunately, many experiments are still performed in which the contribution of these optical effects is conveniently neglected or wrongly taken into account. In this paper, we investigate how the High Accuracy Universal Polarimeter can be put to use for the correct measurement of subtle optical effects in crystals that are both birefringent and dichroic.

The High Accuracy Universal Polarimeter (HAUP) has been introduced by Kobayashi and Uesu (1983) for the measurement of small reciprocal circular birefringence in the presence of considerably larger reciprocal linear birefringence. One of the important principles of this polarimetric method is that the optical system is kept very simple. In fact, it only consists of a polariser, the sample and a second polariser, called analyser. In this way, the number of systematic errors that have to be taken into account is kept minimal. Furthermore, the rotation angles of both polarisers are restricted to a small range. This allows for the derivation of the so-called HAUP intensity formula, which expresses the intensity of the light, propagated through the optical system, as a function of the rotation angles of the polarisers, the properties of the sample and the intrinsic systematic errors. By fitting the intensities, measured at different combinations of polariser angles, to the HAUP intensity formula one is able to detect values of reciprocal circular birefringence that are smaller than the magnitudes of the systematic errors. Simultaneously, the reciprocal linear birefringence is found. Moreover, the rotation of the principal axes of this birefringence can also be obtained. It has been shown by Moxon and Renshaw (1990) that the HAUP method can also be applied to detect small reciprocal linear and reciprocal circular dichroism in the presence of considerably larger reciprocal linear birefringence (see also, Moxon et al., 1991).

With this paper, we extend the HAUP method, so that it can be applied to absorbing crystals of all (magnetic) symmetry classes. First, it is explained how the optical properties of such a crystal can be described both in terms of material tensors and in terms of parameters that were given by Jones (1948). It is shown that the latter description is more convenient. Therefore, we want to derive the HAUP intensity formula in terms of the Jones parameters. It is realised, however, that there are many cases in which either the reciprocal linear birefringence or the reciprocal linear dichroism is large with respect to the additional optical effects. The most important goal of this paper is to show that these cases can be unified in one HAUP intensity formula. This formula is expressed in terms of the eigenpolarisations of a general sample. Subsequently, specific examples are discussed. The crystal is taken to be linearly birefringent and dichroic for all examples. The principal axes of both effects are assumed to be the same. The use of HAUP is discussed for the case that, in addition, small reciprocal circular birefringence and reciprocal circular dichroism are present. This case is demonstrated by means of measurements on $NiSO_4 \cdot 6H_2O$. Furthermore, the case is studied in which the principal axes of reciprocal linear dichroism and reciprocal linear birefringence do not coincide. Finally, it is shown, that it should be possible to detect the non-reciprocal linear birefringence in magneto-electric crystals.

3.2 The description of linear optical properties of crystals

The study of the linear optical properties of crystals usually starts with the investigation of the so-called proper waves. These are plane waves that can propagate in the crystal without a change of their polarisation. The proper waves are found by solving the Fresnel equations; the combination of the Maxwell equations and the constitutive equations for plane waves (see for example Ramachandran and Ramaseshan, 1961). The linear optical properties of a crystal depend, therefore, on the material tensors in the constitutive equations. In case that the frequency of the light is far from natural magnetic resonance frequencies, the magnetic permeability tensor $\boldsymbol{\mu}$ can be approximated very well with the unit tensor. The constitutive equations then become:

$$\begin{aligned} D_i(\boldsymbol{r}) &= \varepsilon_{ij} E_j(\boldsymbol{r}) + \gamma_{ijk} \frac{\delta E_j(\boldsymbol{r})}{\delta r_k} \\ B_i(\boldsymbol{r}) &= H_i(\boldsymbol{r}). \end{aligned} \tag{3.1}$$

This is the case that we treat in this paper. The tensor $\boldsymbol{\varepsilon}$ specifies the local response and the tensor $\boldsymbol{\gamma}$ specifies the *non*local response of the medium. The wavelength λ of the light is long with respect to typical lattice constants a of crystals. The effects originating from the non-local response, therefore, have a magnitude in the order of a/λ with respect to the effects caused by the local response (Agranovich and Ginzburg, 1984).

A classification of optical effects can be given by separating the tensors $\boldsymbol{\varepsilon}$ and $\boldsymbol{\gamma}$ in real, imaginary, symmetric and antisymmetric parts:

$$\begin{aligned} \boldsymbol{\varepsilon} &= \boldsymbol{\varepsilon}^s + \boldsymbol{\varepsilon}^a &= \boldsymbol{\varepsilon}'^s + \boldsymbol{\varepsilon}'^a + i\left(\boldsymbol{\varepsilon}''^s + \boldsymbol{\varepsilon}''^a\right) \\ \boldsymbol{\gamma} &= \boldsymbol{\gamma}^s + \boldsymbol{\gamma}^a &= \boldsymbol{\gamma}'^s + \boldsymbol{\gamma}'^a + i\left(\boldsymbol{\gamma}''^s + \boldsymbol{\gamma}''^a\right), \end{aligned}$$

where a single prime denotes the real part and a double prime the imaginary part. The symbols s and a denote that the tensor is, respectively, symmetric or antisymmetric in its first two indices.

In table 3.1 the possible optical effects are associated with the different parts of the tensors $\boldsymbol{\varepsilon}$ and $\boldsymbol{\gamma}$. Each of the optical effects can be described by two proper waves that

nr.	optical effect	material tensor	occurrence in non-absorbing crystals	occurrence in non-magnetic crystals	corresponding parameter in Jones calculus
1	R. Linear Birefringence	ε'^{s}	+	+	$g_o = \frac{\pi}{\lambda}(n_1 - n_2)$
2	R. Linear Dichroism	ε''^{s}	−	+	$p_o = \frac{\pi}{\lambda}(\kappa_1 - \kappa_2)$
3	N.R. Circular Birefringence	ε''^{a}	+	−	$\omega = \frac{\pi}{\lambda}(n_r - n_l)$
4	N.R. Circular Dichroism	ε'^{a}	−	−	$\delta = \frac{\pi}{\lambda}(\kappa_r - \kappa_l)$
5	R. Circular Birefringence	γ'^{a}	+	+	$\omega = \frac{\pi}{\lambda}(n_r - n_l)$
6	R. Circular Dichroism	γ''^{a}	−	+	$\delta = \frac{\pi}{\lambda}(\kappa_r - \kappa_l)$
7	N.R. Linear Birefringence	γ''^{s}	+	−	$g_{45} = \frac{\pi}{\lambda}(n_{-45} - n_{45})$
8	N.R. Linear Dichroism	γ'^{s}	−	−	$p_{45} = \frac{\pi}{\lambda}(\kappa_{-45} - \kappa_{45})$

Table 3.1 Descriptions of optical effects that can occur in transmission optical measurements; R. = Reciprocal, N.R. = Non-Reciprocal. Both the description in terms of specific parts of material tensors and in terms of Jones parameters is given. Furthermore, the occurrence (+) or absence (−) of the effects is indicated for non-absorbing crystals and for non-magnetic crystals.

have different polarisations and that propagate with different velocities, for each direction in the crystal. The polarisations of the proper waves are orthogonal in case that the crystal is non-absorbing. Moreover, the propagation velocities are real in that case. They become complex, however, if the crystal does absorb light, in which case the polarisations of the proper waves are no longer necessarily orthogonal.

In magnetic crystals the effects associated with ε^a or with γ^s are allowed, contrary to non-magnetic crystals. These effects are non-reciprocal; the (complex) velocities of the proper waves change if the light path is reversed. However, without changing the propagation direction of the light with respect to the sample, it is still possible to separate non-reciprocal linear birefringence from reciprocal linear birefringence and non-reciprocal linear dichroism from reciprocal linear dichroism. On the other hand, the non-reciprocal circular birefringence can not be distinguished from reciprocal circular birefringence and non-reciprocal circular dichroism can not be distinguished from reciprocal circular dichroism in this way.

The tensor ε has, in principle, 9 different complex elements, whereas the tensor γ can have 27 different complex elements. This means, that the optical properties of a general absorbing and magnetic crystal are determined by 2×36 different numbers. It is obvious, therefore, that a description which uses the full tensors ε and γ is not convenient for the interpretation of optical experiments. In an experiment, usually one sample is present which is traversed by the light in a specific direction. For this orientation, one wants to measure the values of each of the eight possible optical effects in table 3.1. A description that is very well suited for such an approach is the Jones matrix calculus (Jones, 1948). It must be emphasised that this calculus was derived by Jones using a superposition method. In most cases this gives the same solutions as those that follow from solving the Fresnel equations. Sometimes, however, the Jones calculus gives different results. An example is the case of light propagating in the neighbourhood of an optic axis (direction of zero reciprocal linear birefringence) in an optically active, biaxial crystal (Ramachandran and Ramaseshan, 1961). In this paper we use the Jones matrix calculus, but we consider only those cases for which either the reciprocal linear birefringence or the reciprocal linear dichroism is relatively large, so that the superposition method is valid (Ramachandran and Ramaseshan, 1961).

The parameters that were introduced by Jones (1948) for the various optical effects have also been given in table 3.1. They can all be expressed in terms of a difference of two indices. At the end of this paper a list of symbols has been added in which the meaning of all these indices is explained. Both the symbol ω and the symbol δ appear twice in the table. This indicates that in case of the circular optical effects it is not possible to separate reciprocal effects from non-reciprocal effects if only one direction of light propagation is used.

In case of a general sample and light entering at normal incidence, the electric field $\boldsymbol{E}(z)$ at distance z from the entrance surface is determined by the Jones matrix $\boldsymbol{S}$ according to $\boldsymbol{E}(z) = \boldsymbol{S}\boldsymbol{E}(0)$. The Jones matrix $\boldsymbol{S}$ can be written in terms of the Jones parameters (Jones, 1948):

$$\boldsymbol{S} = \exp(T_N z) \times \tag{3.2}$$

$$\begin{pmatrix} \cosh(Q_N z) + (p_o + i g_o)\sinh(Q_N z)/Q_N & ((p_{45} + i g_{45}) - (\omega + i\delta))\sinh(Q_N z)/Q_N \\ ((p_{45} + i g_{45}) + (\omega + i\delta))\sinh(Q_N z)/Q_N & \cosh(Q_N z) - (p_o + i g_o)\sinh(Q_N z)/Q_N \end{pmatrix},$$

where

$$T_N = -\frac{2\pi}{\lambda}(\tilde{\kappa} + i\tilde{n}),$$

$$\tilde{n} = \frac{n_1 + n_2}{2}$$

$$\tilde{\kappa} = \frac{\kappa_1 + \kappa_2}{2}$$

and

$$Q_N^2 = (p_o + i g_o)^2 + (p_{45} + i g_{45})^2 - (\omega + i\delta)^2.$$

The proper waves of a sample can be represented by the eigenvectors of the corresponding Jones matrix $\boldsymbol{S}$. If the crystal is non-absorbing p_o, δ and p_{45} equal zero. The Jones matrix is then unitary. Consequently, the eigenvectors are orthogonal (Jones, 1942). In case that the crystal is absorbing, the eigenvectors can be non-orthogonal.

Before using, however, the Jones matrix of equation (3.2) for several specific cases we construct another Jones matrix $\boldsymbol{S}$ in terms of the parameters that define two general eigenpolarisations (i.e. proper waves), according to the procedure given by Jones (1942). The advantage of this approach is that the HAUP intensity formula that is derived from the latter Jones matrix unifies many of the specific cases that can be described with the matrix (3.2), as is derived.

3.3 The derivation of the HAUP intensity formula

The HAUP method is a polarimetric method. Normally incident, monochromatic, circularly polarised light propagates successively through a polariser, the sample and a second polariser that is called analyser. The intensity of the emerging light is measured for different settings of the polarisers. The measured intensities are subsequently fitted to the HAUP intensity formula that describes the intensity change Γ/Γ_0 of the light traversing the optical system. In order to make the method as sensitive as possible, the systematic errors that are known to be present are included in the description. The values of the systematic errors are, therefore, simultaneously determined during the fitting procedure.

The basic HAUP set-up that is used in our laboratory has been described by Dijkstra et al. (1991). Several changes were made in this set-up, which have been reported by Kremers and Meekes (1994a). In the latter reference the HAUP intensity formula was rederived for the case of small reciprocal circular birefringence in the presence of considerably larger reciprocal linear birefringence. Here, the HAUP intensity formula is derived in a similar way.

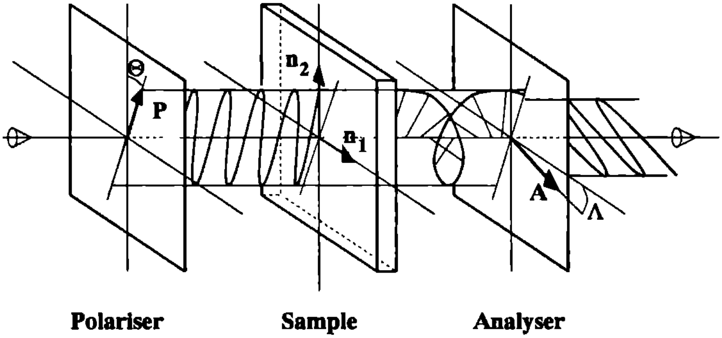

Figure 3.1 The optical system of HAUP, consisting only of a polariser, the sample and an analyser. The vectors ($\boldsymbol{n}_1$, $\boldsymbol{n}_2$) and the angles (Θ, Λ) are referred to in the text.

In figure 3.1 the basic optical system of HAUP is presented. The vectors $\boldsymbol{n}_1$ and $\boldsymbol{n}_2$ indicate the principal axes of the linear birefringence. If the crystal is non-absorbing, these coincide with the main axes of the (elliptic) polarisations of the proper waves. The polariser is represented by a Jones vector $\boldsymbol{P}$. The polarisation direction of the light emerging from the polariser is represented by the angle Θ. This angle is measured with respect to one of the directions $\boldsymbol{n}_{i=1,2}$. The angle Λ denotes, in a similar way, the polarisation direction of the analyser with respect to the other direction $\boldsymbol{n}_{i=2,1}$. Consequently, the polarisers are crossed when $\Theta = \Lambda$. A HAUP measurement with the origin for Θ close to $\boldsymbol{n}_1$ is called the measurement of the first extinction direction. If the sample is rotated over $\frac{1}{2}\pi$ rad, Θ is measured with respect to $\boldsymbol{n}_2$ as in figure 3.1. The second extinction direction can then be measured.

Even very high quality polarisers do not perfectly polarise light. The polarisation of the light emerging from them is still slightly elliptical. The corresponding ellipticities, denoted p and a respectively, have a magnitude in the order of 10^{-4}. These are two of the systematic errors that are taken into account in the HAUP method. The Jones vectors of these non-ideal polarisers are (Dijkstra et al., 1991):

$$\begin{aligned} \boldsymbol{P} &= \begin{pmatrix} P_1 \\ P_2 \end{pmatrix} = \begin{pmatrix} \cos\Theta\cos p - i\sin\Theta\sin p \\ \sin\Theta\cos p + i\cos\Theta\sin p \end{pmatrix} \\ \boldsymbol{A} &= \begin{pmatrix} A_1 \\ A_2 \end{pmatrix} = \begin{pmatrix} -\sin\Lambda\cos a - i\cos\Lambda\sin a \\ \cos\Lambda\cos a - i\sin\Lambda\sin a \end{pmatrix} . \end{aligned} \tag{3.3}$$

The intensity change Γ/Γ_0 can be calculated if the Jones matrix $\boldsymbol{S}$ is specified:

$$\Gamma/\Gamma_0 = |\boldsymbol{A}^\dagger \boldsymbol{S}\boldsymbol{P}|^2 . \tag{3.4}$$

In some cases (see Dijkstra et al., 1991) it is possible to derive an explicit expression $\Gamma/\Gamma_0(\Theta,\Lambda)$ for arbitrary positions of both polariser and analyser. Nevertheless, that expression can not be used as such in order to extract the desired information by fitting the measured intensities.

It was realised by Kobayashi and Uesu (1983), however, that it is nowadays possible to set polarisers at positions with an accuracy of about $5\cdot10^{-6}$ rad. Therefore, the angles Θ and Λ can be restricted to values within a range that is comparable with the magnitude of the systematic errors ($\mathcal{O}(10^{-4})$) that are present. Consequently, it is possible to expand the HAUP intensity formula (3.4) up to low order terms in the angles Θ and Λ, in the systematic errors and in any optical parameter in the Jones matrix $\boldsymbol{S}$ that is expected to be small. The thus obtained HAUP intensity formula can then be used to fit intensities that have been measured for a set of different polariser angles within the above mentioned small range.

In the next section, we first derive a HAUP intensity formula in terms of the parameters that describe two general complex eigenpolarisations. The result can be considered to be the unified HAUP intensity formula. It can be used to determine, for any sample, the complex ellipticities of the eigenpolarisations simultaneously with the (complex) birefringence. Usually, however, one is interested in measuring the values of specific optical effects as they have been given in table 3.1. Therefore, the HAUP intensity formula is subsequently derived by using the Jones matrix (3.2). It is shown that the result is analogous to the unified HAUP intensity formula. Therefore, it is possible to give expressions for the complex ellipticity angles of the eigenpolarisations in terms of the Jones parameters. The shapes of the eigenpolarisations that one finds in this way for specific examples, agree with those that can be derived from the corresponding material tensors $\boldsymbol{\varepsilon}$ and $\boldsymbol{\gamma}$ by means of the Fresnel equations.

3.3.1 The unified HAUP intensity formula

A general polarisation state of light is represented by figure 3.2. It is characterised by the azimuth angle $\psi \in [0, \pi)$ and the ellipticity angle $\chi \in [-\pi/4, \pi/4]$. The azimuth angle ψ is the angle between the major axis of the ellipse of vibration and the positive direction of the x-axis of the reference coordinate system. The ellipticity angle χ is the arctangent of the ellipticity e. This ellipticity is defined as the ratio of the minor axis length and the major axis length. Its sign is positive for right-handed polarised light and negative for left-handed polarised light. The polarisation state in figure 3.2 can be represented by a two-dimensional complex vector $\boldsymbol{J}$ in the Jones matrix calculus:

$$\boldsymbol{J} = \begin{pmatrix} \cos\psi\cos\chi - i\sin\psi\sin\chi \\ \sin\psi\cos\chi + i\cos\psi\sin\chi \end{pmatrix}. \tag{3.5}$$

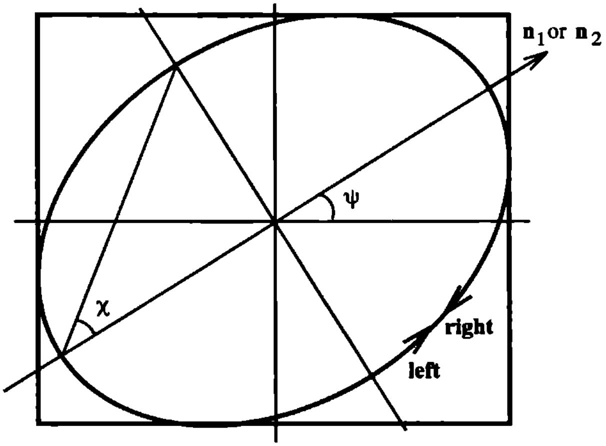

Figure 3.2 The polarisation state of light. The propagation direction is towards the reader. A counter-clockwise rotation in time is called a left-handed polarisation state. A clockwise rotation in time is called a right-handed polarisation state. The parameters are addressed in the text.

In principle, two independent eigenpolarisations exist for light propagating in a certain direction in a crystal, but for all cases that we consider the major axes of the two corresponding ellipses of vibration are orthogonal to each other. We do take, however, arbitrary ellipticities for both eigenpolarisations:

$$\begin{aligned}\chi_1 &= k_s - k_a \\ \chi_2 &= k_s + k_a.\end{aligned}$$

The first eigenpolarisation ($\boldsymbol{n}_1$ in figure 3.1) is given azimuth angle $\psi = 0$. The second eigenpolarisation ($\boldsymbol{n}_2$ in figure 3.1) has, therefore, azimuth angle $\psi = \pi/2$. Thus, on a Cartesian basis, the Jones vectors of the eigenpolarisations are:

$$\boldsymbol{J}_1 = \begin{pmatrix} \cos(k_s - k_a) \\ i\sin(k_s - k_a) \end{pmatrix} \text{ and } \boldsymbol{J}_2 = \begin{pmatrix} i\sin(-k_s - k_a) \\ \cos(-k_s - k_a) \end{pmatrix}. \tag{3.6}$$

From the eigenpolarisations we construct the coordinate transformation matrix $\boldsymbol{R}$:

$$\boldsymbol{R} = \begin{pmatrix} \cos(k_s - k_a) & i\sin(-k_s - k_a) \\ i\sin(k_s - k_a) & \cos(-k_s - k_a) \end{pmatrix}. \tag{3.7}$$

The propagation velocities of the eigenpolarisations are taken to be c/n_1 and c/n_2, where n_1 and n_2 are the (complex) refractive indices and c is the light velocity in vacuum. The response of the sample on its eigenvector basis $\{\boldsymbol{J}_1, \boldsymbol{J}_2\}$ is then

$$\boldsymbol{W}_0 = \begin{pmatrix} e^{i\Delta/2} & 0 \\ 0 & e^{-i\Delta/2} \end{pmatrix}, \tag{3.8}$$

where

$$\Delta = \frac{2\pi z}{\lambda}(n_1 - n_2) \tag{3.9}$$

and z is the thickness of the sample platelet. The Jones matrix $\boldsymbol{S}$ of the sample on the Cartesian basis is calculated in the following way:

$$\begin{aligned}\boldsymbol{S} &= \boldsymbol{R}\boldsymbol{W}_0\boldsymbol{R}^{-1} \\ &\approx \begin{pmatrix} \cos(\Delta/2) + i\sin(\Delta/2) & -2(k_s + k_a)\sin(\Delta/2) \\ -2(k_s - k_a)\sin(\Delta/2) & \cos(\Delta/2) - i\sin(\Delta/2) \end{pmatrix}.\end{aligned} \tag{3.10}$$

In the actual calculation we have included terms up to third order in the ellipticity angles, which were assumed to be small. This assumption is valid for light propagating not too close to an optic axis. In the final result, however, only first order terms in the ellipticity angles remained. In this paper, therefore, we have omitted quadratic or higher order terms in these angles. It is shown later, that the ellipticity angles can be expressed in terms of the Jones parameters. The relevant parameters can, in turn, be related to the tensor γ of equation (3.1). The corresponding ellipticity angles are, therefore, small ($\mathcal{O}(\frac{a}{\lambda})$) with respect to Δ, provided that Δ is not too small.

Using the Jones matrix $\boldsymbol{S}$ of equation (3.10) we now demonstrate how one calculates the HAUP intensity formula (3.4). For this, it is necessary to calculate $\boldsymbol{A}^\dagger\boldsymbol{SP}$. This has been done in the following way:

$$\begin{aligned}\boldsymbol{A}^\dagger\boldsymbol{SP} &= \cos(\Delta/2)\,(P_1A_1^* + P_2A_2^*)\\ &+ \; i\sin(\Delta/2)\,(P_1A_1^* - P_2A_2^*)\\ &+ \; +2k_a\sin(\Delta/2)\,(P_1A_2^* - P_2A_1^*)\\ &+ \; -2k_s\sin(\Delta/2)\,(P_1A_2^* + P_2A_1^*)\,. \end{aligned} \tag{3.11}$$

In appendix C the expansions for the terms $P_1A_1^* + P_2A_2^*$, $P_1A_1^* - P_2A_2^*$, $P_1A_2^* - P_2A_1^*$ and $P_1A_2^* + P_2A_1^*$ are given up to third order in Θ, Λ, p and a. It has been shown by Kremers and Meekes (1994a) that this is sufficient for the angles Λ and Θ that are used in the experiments.

Note, that all parameters Δ, k_a and k_s are complex numbers in absorbing crystals. Therefore, we substitute

$$\begin{aligned} \Delta - iE &\quad \text{for} \quad \Delta,\\ k_a' + ik_a'' &\quad \text{for} \quad k_a\\ \text{and} \quad k_s' + ik_s'' &\quad \text{for} \quad k_s. \end{aligned} \tag{3.12}$$

Before calculating $\boldsymbol{A}^\dagger\boldsymbol{SP}$ it must be noted that the angle Λ is usually not used in HAUP experiments. Instead, the position of the analyser is read with respect to the situation in which both polarisers are crossed (Kobayashi and Uesu, 1983). In this alternative reading system the position of the analyser is indicated with the angle Y, in such a way that for $Y = 0$ the polarisers are crossed. Furthermore, it is necessary to discuss another systematic error, δY, that is encountered in HAUP measurements. This systematic error describes a small deviation of the actual analyser position from its supposed position. The origin of this error can, for a large part, be found in mechanical inaccuracies in the system that is used to rotate the polarisers (Kremers and Meekes (1994a) and reference therein). One can change to the new reading system for the analyser by substituting $\Theta + Y + \delta Y$ for Λ in all terms in appendix C. Indeed, in this way one has that $\Lambda - \Theta = Y + \delta Y$. The systematic error δY is small ($\mathcal{O}(10^{-3})$) and is therefore treated in the same way as the other small parameters.

The HAUP intensity formula, derived up to third order terms in δY, Y, Θ, p and a, can then be written in the following form (Moxon and Renshaw, 1990):

$$\Gamma/\Gamma_0 = \begin{pmatrix} 1 & Y & Y^2 \end{pmatrix} C^{\text{e.p.}}_{(3\times3)} \begin{pmatrix} 1 \\ \Theta \\ \Theta^2 \end{pmatrix}. \tag{3.13}$$

The matrix elements of $C^{\text{e.p.}}_{(3\times3)}$ are given in appendix D. The superscript e.p. means eigenpolarisation, referring to the fact that the angles Θ in this expression are supposed to be read with respect to a major axis of an eigenpolarisation.

Experimentally, the exact position of such an eigenpolarisation is difficult to find. Therefore, it is better to use a reference for the angle Θ that can be found more accurately. An extinction direction is chosen for this reference. It corresponds to that orientation of the sample between crossed polarisers for which the transmitted intensity is minimal. In our set-up the extinction direction is found by rotating both polarisers simultaneously, while keeping them crossed, until the intensity is minimal. The position of the polariser at an extinction direction is denoted Θ_0. This position can be calculated from equation (3.13). It is the value of Θ for which:

$$\left.\frac{\delta\Gamma}{\delta\Theta}\right|_{Y=0} = 0. \tag{3.14}$$

This gives the following expression for Θ_0:

$$\Theta_0 = -\frac{1}{2}\delta Y + \frac{(p+a)\sin(\Delta) - \delta Y \sinh(E)}{2\cosh(E) - 2\cos(\Delta)} + (k_a'' - k_s''). \tag{3.15}$$

Note, that Θ_0 differs from the position of the eigenpolarisation ($\Theta = 0$). This difference is not only caused by the optical properties of the sample, but also, for a large part, by the systematic errors, p, a, and δY. This shows the importance of taking these systematic errors appropriately into account. The value of Θ_0 is measured with respect to an arbitrary origin in a HAUP experiment. Nevertheless, if the behaviour of Θ_0 can be recorded as a function of Δ or E it is still possible to use Θ_0 for the determination of changes in $(k_a'' - k_s'')$.

It will be clear that the position Θ_0 can be found very accurately. Therefore, it is used as origin for the reading of polariser angles. The corresponding HAUP intensity formula for this reading system is obtained by substituting $\Theta + \Theta_0$ for Θ and expression (3.15) for Θ_0 in equation (3.13).

Finally, the *unified* HAUP intensity formula is obtained:

$$\Gamma/\Gamma_0 = \begin{pmatrix} 1 & Y & Y^2 \end{pmatrix} C^{\Theta_0}_{(3\times3)} \begin{pmatrix} 1 \\ \Theta \\ \Theta^2 \end{pmatrix}, \tag{3.16}$$

where

$$\begin{aligned}
C^{\Theta_0}_{21} &= (2(k_s' - k_a') - (p-a))\sin(\Delta) + \frac{(p+a)\sinh(E) + \delta Y \sin(\Delta)}{\cosh(E) - \cos(\Delta)}\sin(\Delta) \\
C^{\Theta_0}_{22} &= 2e^{E} - 2\cos(\Delta) \\
C^{\Theta_0}_{31} &= e^{E} \\
C^{\Theta_0}_{13} &= 2(\cosh(E) - \cos(\Delta)) \\
C^{\Theta_0}_{12} &= 0.
\end{aligned} \tag{3.17}$$

All other elements of $C^{\Theta_0}_{(3\times3)}$ are zero, except for $C^{\Theta_0}_{11}$. This term has not explicitly been worked out, because it is not used to extract optical parameters from a measurement. The superscript Θ_0 indicates that, for this HAUP intensity formula, an extinction direction has to be used as origin for the reading of the angles Θ. Note, that we have found a different sign for E in the expression for $C^{\Theta_0}_{22}$ as Dijkstra et al. (1991). More important, though, is the fact that we have not used the assumption that E is small with respect to Δ, as opposed to Moxon and Renshaw (1990) and Dijkstra et al. (1991).

The unified formula (3.16) corresponds to the measurement of the first extinction direction. The polarisation of the light emerging from the polariser has a direction close to $\boldsymbol{n}_1$. The same formula can, nevertheless, be used when the second extinction direction is measured. The polarisation direction of the polariser is then close to $\boldsymbol{n}_2$. In the derivation of the HAUP intensity formula one only has to interchange the ellipticity angles χ_1 and χ_2. This comes down to changing the signs of k'_a and k''_a. The same formula (3.16) can, therefore, be used for the second extinction direction if the signs of k'_a, k''_a, Δ and E are reversed. It is important, however, to determine the values of the systematic errors for each extinction direction separately (see Kremers and Meekes, 1994a), because they can behave in an unpredictable way.

Considering the form of the HAUP intensity formula (3.17), we fit the intensities, that are measured in a HAUP experiment, against a polynomial equation of the form:

$$\Gamma = \begin{pmatrix} 1 & Y & Y^2 \end{pmatrix} C_{(3\times3)} \begin{pmatrix} 1 \\ \Theta \\ \Theta^2 \end{pmatrix}. \tag{3.18}$$

Note, that Γ_0 is included in the fitting-parameters C_{ij}. The fitting procedure that we use is a linear least squares method (Deming and Morgan, 1979). Not all elements of $C_{(3\times3)}$, which are the actual fitting-parameters, need to be free in the fit. We only allow for C_{11}, C_{21}, C_{12}, C_{22}, C_{31} and C_{13} to be non-zero. C_{12} is allowed to be non-zero, because this fitting-parameter indicates how well the position of the extinction direction has been determined. It can even be used to improve the results by means of the so-called $\Delta\Theta$-correction (see for a detailed analysis Kremers and Meekes, 1994a). The thus obtained fitting-parameters C_{ij} give the values of the expressions for the corresponding matrix elements $C^{\Theta_0}_{ij}$ of equation (3.17). It is clear that both E and $\cos(\Delta)$ can simply be calculated from C_{22} and C_{31}.

At this point one is left with the problem of finding the values of k'_a, k'_s, k''_a and k''_s. These have to be extracted from the fitting-parameter C_{21} and the measured value for the extinction direction Θ_0. The measurement of a single extinction direction is not sufficient to do this. Two extinction directions have to be measured to separate k_a from k_s. The procedure of extracting these ellipticity angles is treated explicitly for the case of measurements on $NiSO_4 \cdot 6H_2O$ in section 3.4. Here, we proceed with the derivation of the HAUP intensity formula, using the Jones matrix of equation (3.2). In fact, the same equations (3.17) are found and k'_a, k'_s, k''_a and k''_s can be expressed in terms of Jones parameters.

3.3.2 HAUP intensity formulae in terms of optical effects

With this paper we want to show that HAUP can have a much wider application in crystal optics than the simultaneous measurement of small reciprocal circular birefringence and large reciprocal linear birefringence. We consider those cases in which the Jones parameters g_{45}, p_{45}, ω and δ can be considered small with respect to g_o and p_o.

We expand the matrix elements of (3.2) up to first order in the small parameters g_{45}, p_{45}, ω and δ. The small optical effects only appear up to first order in the final expressions, even if one derives the HAUP intensity formula up to third order in all small parameters. This has been checked explicitly for all cases. Therefore, the following expansions can be used:

$$\begin{aligned} \cosh(Q_N z) &= \cosh\left[(p_o + i g_o)z\right] + \mathcal{O}(2) &&= \cos\left[(g_o - i p_o)z\right] + \mathcal{O}(2) \\ \frac{\sinh(Q_N z)}{Q_N} &= \frac{\sinh\left[(p_o + i g_o)z\right]}{(p_o + i g_o)} + \mathcal{O}(2) &&= \frac{g_o + i p_o}{p_o^2 + g_o^2} \sin\left[(g_o - i p_o)z\right] + \mathcal{O}(2). \end{aligned} \qquad (3.19)$$

With these expansions the Jones matrix (3.2) becomes:

$$\boldsymbol{S} \approx \exp\left(-(\tilde{\kappa} + i\tilde{n})\tfrac{2\pi z}{\lambda}\right) \times$$

$$\begin{pmatrix} \cos\left[(g_o - i p_o)z\right] + i \sin\left[(g_o - i p_o)z\right] & \begin{array}{l} \{\ (g_o p_{45} - p_o g_{45} - g_o\omega + p_o\delta) \\ +i(g_o g_{45} + p_o p_{45} - g_o\delta - p_o\omega)\ \} \times \\ \dfrac{\sin\left[(g_o - i p_o)z\right]}{p_o^2 + g_o^2} \end{array} \\ \begin{array}{l} \{\ (g_o p_{45} - p_o g_{45} + g_o\omega - p_o\delta) \\ +i(g_o g_{45} + p_o p_{45} + g_o\delta + p_o\omega)\ \} \times \\ \dfrac{\sin\left[(g_o - i p_o)z\right]}{p_o^2 + g_o^2} \end{array} & \cos\left[(g_o - i p_o)z\right] - i \sin\left[(g_o - i p_o)z\right] \end{pmatrix}. \qquad (3.20)$$

The only Jones parameters that do *not* change their sign upon a change of the extinction direction are δ and ω. Therefore, it follows that, given the substitutions of equation (3.12), the matrix (3.20) has the same form as the matrix (3.10) except for the factor $\exp\left(-(\tilde{\kappa} + i\tilde{n})\frac{2\pi z}{\lambda}\right)$. The relation between the parameters is given in table 3.2. The HAUP intensity formula for this case is, consequently, given by:

$$\Gamma/\Gamma_0 = \exp\left(-2\tilde{\kappa}\frac{2\pi z}{\lambda}\right) \begin{pmatrix} 1 & Y & Y^2 \end{pmatrix} C^{\Theta_0}_{(3\times3)} \begin{pmatrix} 1 \\ \Theta \\ \Theta^2 \end{pmatrix}, \qquad (3.21)$$

where the matrix elements $C^{\Theta_0}_{ij}$ are obtained by substitutions in equation (3.17) according to the scheme given in table 3.2.

Moreover, the expression for Θ_0 is found from the same substitutions in equation (3.15).

HAUP parameters	Δ	E	k'_a	k'_s	k''_a	k''_s
Jones parameters	$2g_o z$	$2p_o z$	$\frac{1}{2}\frac{g_o\omega - p_o\delta}{p_o^2 + g_o^2}$	$-\frac{1}{2}\frac{g_o p_{45} - p_o g_{45}}{p_o^2 + g_o^2}$	$\frac{1}{2}\frac{g_o\delta + p_o\omega}{p_o^2 + g_o^2}$	$-\frac{1}{2}\frac{g_o g_{45} + p_o p_{45}}{p_o^2 + g_o^2}$

Table 3.2 The relation between the description of the HAUP method in terms of eigen-polarisations and in terms of Jones parameters

In most experiments not all optical effects of table 3.1 have to be taken into account. Several specific cases will now be addressed that can be expected to be of interest.

3.3.2.1 Uniaxial or orthorhombic biaxial crystals that are absorbing and non-magnetic

First, we study the case in which non-reciprocal linear birefringence and non-reciprocal linear dichroism are absent; $g_{45} = p_{45} = 0$. Furthermore, we suppose that the crystal is uniaxial or orthorhombic biaxial, so that the reciprocal linear birefringence and reciprocal linear dichroism have mutual principal axes. This is accounted for by means of the parameters g_o and p_o. There are many non-magnetic, coloured crystals that belong to this case.

The optical effects of such a sample can be found by fitting the measured intensities in the HAUP experiment to the polynomial equation (3.18). The obtained fitting-parameters C_{ij} give the values of the corresponding elements $C_{ij}^{\Theta_0}$. It is seen that the determination of both the reciprocal linear dichroism, $\Delta\kappa = \frac{\lambda}{2\pi z}E$, and the value of $\cos(\Delta)$ is independent of the presence of small reciprocal circular birefringence or small reciprocal circular dichroism. From $\cos(\Delta)$ the value of Δ can usually be constructed if the reciprocal linear birefringence is known for a certain temperature and wavelength λ (Kremers and Meekes, 1994a). An alternative method for the simultaneous measurement of reciprocal linear birefringence and reciprocal linear dichroism has been reported by Rivera (1992) for measurements with a polarising microscope. Sometimes one is certain that for a part of the measurements k'_a is zero. The value of $(p - a)$ can then be determined from the values of the fitting-parameter C_{21} by means of a linear least squares fit for this part, because Δ and E are known. Subsequently, k'_a can be calculated from C_{21} for the other part.

Suppose that one has been able, in this or another way, to extract the value of $2k'_a$ from the fitting-parameter C_{21} and the value of $2k''_a$ from the measured Θ_0. The circular birefringence and the circular dichroism can then be calculated using:

$$n_r - n_l = (Ek''_a + \Delta k'_a)\frac{\lambda}{\pi z} \quad (3.22)$$

$$\kappa_r - \kappa_l = (\Delta k''_a - Ek'_a)\frac{\lambda}{\pi z}. \quad (3.23)$$

In many practical cases the reciprocal linear dichroism is also small. Then, one has:

$$n_r - n_l = (\Delta k'_a)\frac{\lambda}{\pi z} \quad (3.24)$$

$$\kappa_r - \kappa_l = (\Delta k''_a)\frac{\lambda}{\pi z}, \quad (3.25)$$

if second order terms in the small parameters can be neglected.

3.3.2.2 Linear Birefringence and Linear Dichroism with different principal axes, biaxial crystals, no circular effects

The principal axes for reciprocal linear birefringence and reciprocal linear dichroism were taken to have the same directions in the previous subsection . Here, we want to demonstrate that these effects can also be measured simultaneously in non-orthorhombic biaxial crystals. Their principal axes do not necessarily coincide then. For the time being, we do not consider any circular optical effects: $\delta = 0$ and $\omega = 0$.

We assume that the principal axes of the reciprocal linear dichroism make a small angle, α_{pg}, with the principal axes of the reciprocal linear birefringence. The latter are taken to be the coordinate axes. The reciprocal linear birefringence is, therefore, described by the parameter g_o. To account for the fact that the reciprocal linear dichroism has different principal axes one must include both p_o and p_{45}. The parameter p_{45} is small with respect to p_o and g_o because we have assumed that the angle α_{pg} is small. This angle can be calculated from p_o and p_{45} (Jones, 1948):

$$\tan(2\alpha_{pg}) = \frac{p_{45}}{p_o}. \quad (3.26)$$

From table 3.2 it can be seen that, in this case, the (small) angle $\tan(2\alpha_{pg})$ gives rise to eigenpolarisations that have equal ellipticity. This means that they have the same handedness. Therefore, the eigenpolarisations are non-orthogonal, contrary to the case presented in section 3.3.2.1. By measuring two successive extinction directions in a HAUP experiment it is, therefore, possible to discriminate between that case and the present one.

In case that also circular birefringence and circular dichroism are present it is still possible to extract all optical effects from the HAUP measurement. Again, this is done by measuring two extinction directions. From the polynomial fits of both measurements one calculates the symmetric and antisymmetric parts k_s and k_a. After that, all optical parameters can be obtained by a comparison with the expressions in table 3.2. Of course, it is necessary to know the value of $p-a$. This value is usually determined by measurements in circumstances where k'_a and k'_s are known to be zero.

The HAUP method can also be used in cases where the angle α_{pg} is large. For this, however, it is necessary that also p_o is small with respect to g_o. For many coloured biaxial crystals this is still a valid approximation. The angle α_{pg} can take any value if p_o and p_{45} have the same order of magnitude. Moreover, because p_o is small the equations (3.17) can correspondingly be expanded.

3.3.2.3 The measurement of non-reciprocal effects: non-reciprocal linear birefringence and non-reciprocal linear dichroism

In this section we demonstrate the way in which HAUP can be used to measure the non-reciprocal linear birefringence or the non-reciprocal linear dichroism. Again, a crystal is considered that is both linearly birefringent and linearly dichroic. In addition, we include non-reciprocal linear birefringence by means of the Jones parameter g_{45} and we take p_{45} equal to zero. Later, we discuss the case where non-reciprocal linear dichroism is present. The rotation α_{gg} of the principal axes of the linear birefringence is given by (Jones, 1948):

$$\tan(2\alpha_{gg}) = \frac{g_{45}}{g_o}. \tag{3.27}$$

As explained before, it is expected that the non-reciprocal linear birefringence is very small ($\mathcal{O}(10^{-6}$ rad), see Hornreich and Shtrikman, 1968).

The HAUP intensity formula that is obtained in this way, is very analogous to the one found in section 3.3.2.2 for dichroic, biaxial crystals. It will not be surprising, that the latter also represents the case of non-reciprocal linear dichroism. Suppose that in a crystal the principal axes of reciprocal linear dichroism and reciprocal linear birefringence would be symmetry restricted to the same directions if the magnetic ordering were neglected. It is possible that the actual symmetry of the magnetically ordered crystal allows for non-reciprocal linear dichroism. This, in turn, causes the existence of a (small) angle between the principal axes of linear dichroism and linear birefringence, which is exactly the situation treated in section 3.3.2.2. The difference between the two situations is, however, that in case of non-reciprocal linear dichroism the Jones matrix would change if the direction of light propagation through the crystal were reversed. In non-magnetic crystals, on the other hand, the Jones matrix is always invariant under a reversal of the light path.

The experiment that we suggest for the measurement of non-reciprocal linear birefringence or non-reciprocal linear dichroism is, therefore, a temperature dependent HAUP measurement of a uniaxial or biaxial orthorhombic crystal that undergoes at some temperature a phase transition into a magnetically ordered state. The symmetry of this state must, of course, allow for non-reciprocal linear birefringence or non-reciprocal linear dichroism. Unfortunately, both spatial inversion symmetry and time reversal symmetry must then be broken (Brown et al., 1963). This implies that the crystal can also be circularly birefringent and circularly dichroic. Therefore, one has to take these effects into account, but they can be separated if two extinction directions are measured. Another possibility to detect non-reciprocal effects is to perform an additional HAUP measurement in which the orientation of the sample with respect to the direction of light propagation is reversed.

3.4 Experimental results

3.4.1 The example of $NiSO_4 \cdot 6H_2O$

In order to demonstrate how one can separate the parameters that represent small optical effects from a HAUP intensity formula we have chosen the example of the greenishly coloured $NiSO_4 \cdot 6H_2O$. This crystal is interesting for several reasons. It is a uniaxial crystal, space group $P4_12_12$ that exhibits reciprocal linear birefringence (Stadnicka et al., 1987), reciprocal linear dichroism (Moxon et al., 1991), reciprocal circular birefringence (Underwood et al., 1938) and reciprocal circular dichroism (Grinter et al., 1970). All of these optical effects, except the linear birefringence, show a clear variation with wavelength. In case of the cited references, the circular birefringence and the circular dichroism were determined by means of measurements along the optic axis. Both the linear birefringence and the linear dichroism are then zero. The advantage of HAUP is that circular birefringence and circular dichroism can also be measured in directions where linear birefringence and linear dichroism are non-zero.

Crystals of $NiSO_4 \cdot 6H_2O$ are further interesting, because at low temperatures they are paramagneto-electric (Hou and Bloembergen, 1965). This means that the crystal can be considered to be magneto-electric if it is placed in an external magnetic field. In this sense it can be described as a quasi-moving dielectric crystal (O'Dell, 1970). We are planning to build a HAUP set-up that can operate in high magnetic fields. With this set-up it is then possible to study the optical properties of magneto-electric crystals using paramagneto-electric $NiSO_4 \cdot 6H_2O$.

Previous HAUP experiments by Moxon et al. (1991) have shown that for $NiSO_4 \cdot 6H_2O$ it is possible to measure linear and circular dichroism, using the assumption that the linear dichroism is small. They were unable, however, to detect the circular birefringence. Moreover, the behaviour of the circular dichroism as a function of wavelength was shown, but only in arbitrary units. Unfortunately, they did not specify the orientation of the sample that was used in their experiment.

Here, we present the results of HAUP measurements on $NiSO_4 \cdot 6H_2O$ for two different sample orientations. In the first sample, thickness z = 0.70 mm, the light propagates in a direction that makes an angle of 15°40′ with the optic axis. In the second sample, thickness $z = 0.10$ mm, the light propagates in a direction perpendicular to the optic axis. For both samples we have determined the values of linear birefringence, linear dichroism, circular birefringence and circular dichroism as a function of wavelength. In each case, two extinction directions were measured.

3.4.2 The HAUP intensity formula for $NiSO_4 \cdot 6H_2O$

In case of $NiSO_4 \cdot 6H_2O$ it is safe to assume, for visible light, that the linear dichroism is small with respect to the linear birefringence (Moxon et al., 1991). Therefore, we conveniently expand the expressions for $C_{21}^{\Theta_0}$ and Θ_0 for small linear dichroism. The other expressions are used in their original form. Thus, we get the following HAUP intensity formula:

$$\Gamma/\Gamma_0 = \exp\left(-2\tilde{\kappa}\frac{2\pi z}{\lambda}\right)\begin{pmatrix} 1 & Y & Y^2 \end{pmatrix} C^{\Theta_0}_{(3\times 3)} \begin{pmatrix} 1 \\ \Theta \\ \Theta^2 \end{pmatrix}, \tag{3.28}$$

where the matrix elements $C_{ij}^{\Theta_0}$ are given by equation (3.17) if we substitute:

$$k_a' \approx \frac{\pi z}{\lambda}\frac{n_r - n_l}{\Delta}$$

and

$$k_s' = 0.$$

The expanded expression for Θ_0 is:

$$\Theta_0 \approx -\frac{1}{2}\delta Y + \frac{1}{2}(p + a)\cot(\Delta/2) - \frac{\pi z}{\lambda}\frac{\kappa_r - \kappa_l}{\Delta}. \tag{3.29}$$

3.4.3 Determination of the optical properties of $NiSO_4 \cdot 6H_2O$

The intensities measured in the HAUP experiments have been fitted to the polynomial equation (3.18). During this fitting procedure the so-called $\Delta\Theta$-correction (see Kremers and Meekes, 1994a) has been performed. From the fitting-parameters C_{ij} one has to determine the optical properties.

First the factor $\Gamma_0 \exp\left(-2\tilde{\kappa}\frac{2\pi z}{\lambda}\right)$ is determined:

$$\Gamma_0 \exp\left(-2\tilde{\kappa}\frac{2\pi z}{\lambda}\right) = \sqrt{C_{31}\left(C_{13} - \left(C_{22} - C_{31}\right)\right)} \tag{3.30}$$

and all fitting-parameters are divided by this factor. Then, the linear birefringence $\Delta n = \frac{\lambda}{2\pi z}\Delta$ is constructed from $\cos^2(\Delta/2)$:

$$\cos^2(\Delta/2) = \frac{1}{2}\left(1 + C_{31}\right) - \frac{1}{4}C_{22}. \tag{3.31}$$

At $\lambda = 500$ nm the linear birefringence is $n_o - n_e = 1.517 - 1.493 = 0.024$ (Stadnicka et al., 1987). Using this information, the linear birefringence as a function of wavelength can be derived from the $\cos^2(\Delta/2)$ values. In figure 3.3 the result is shown for both samples.

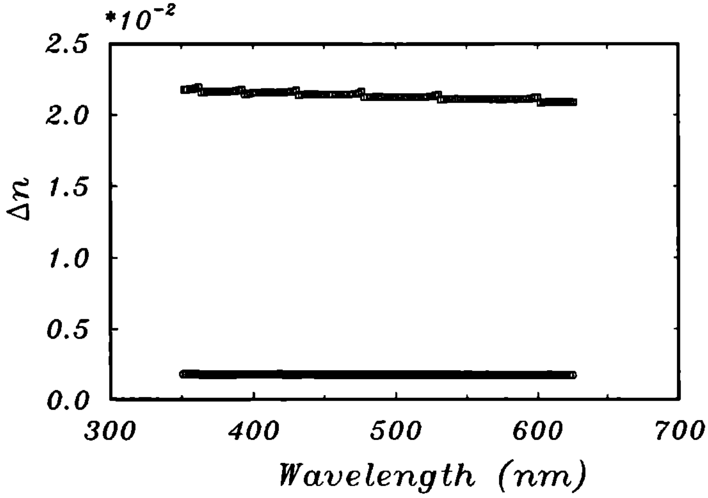

Figure 3.3 The linear birefringence $\Delta n = n_1 - n_2$ of $NiSO_4 \cdot 6H_2O$ for light propagating at two different angles ϕ with respect to the optic axis; ○ (lower curve) corresponds to $\phi = 15^o 40'$, □ (upper curve) corresponds to $\phi = 90^o$.

The linear dichroism$\Delta\kappa = \frac{\lambda}{2\pi z} E$ is calculated from:

$$E = \ln(C_{31}). \tag{3.32}$$

The results have been plotted in figure 3.4. It is clear that at right angles to the optic axis both the linear birefringence and the linear dichroism are largest. This is as expected, because for light propagating along the optic axis both optical effects are necessarily zero for a uniaxial crystal. The results show that the linear dichroism can, indeed, be taken small with respect to the linear birefringence. Therefore, we can use the expansions made above (section 3.4.2). The linear dichroism shows a peak at $\lambda = 400$ nm. The onset of another peak is observed at $\lambda = 625$ nm. This agrees with the results of Moxon et al. (1991).

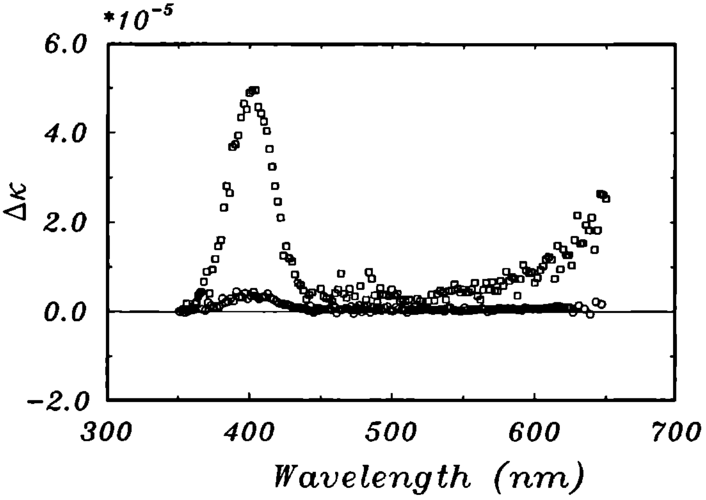

Figure 3.4 The linear dichroism $\Delta\kappa = \kappa_1 - \kappa_2$ of $NiSO_4 \cdot 6H_2O$ for light propagating at two different angles ϕ with respect to the optic axis; ○ corresponds to $\phi = 15°40'$, □ corresponds to $\phi = 90°$.

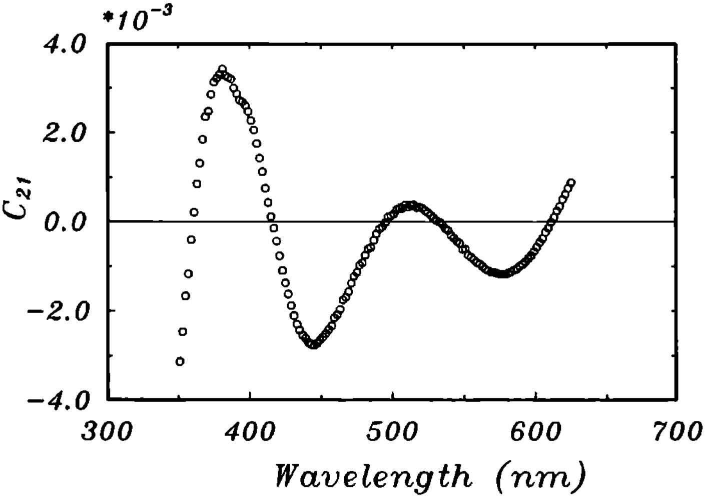

Figure 3.5 The fitting-parameter C_{21} as a function of the wavelength for the sample in which the light propagates at an angle $\phi = 15°40'$ with respect to the optic axis.

The obtained fitting-parameters C_{21}, as a function of the wavelength of the light, are given in the figures 3.5 and 3.6. There is a much larger variation in the maxima (and minima) in figure 3.5 than in figure 3.6. This indicates that the wavelength variation of k'_a is largest for the sample of figure 3.5.

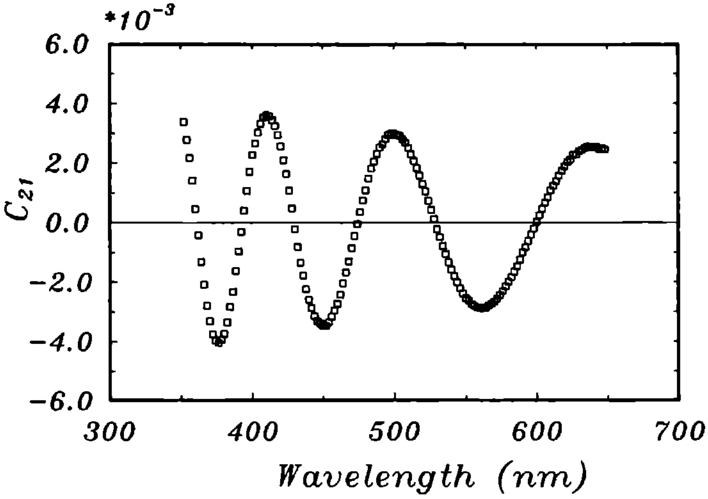

Figure 3.6 The fitting-parameter C_{21} as a function of the wavelength for the sample in which the light propagates at an angle $\phi = 90^o$ with respect to the optic axis.

Consider, now, the expression for this fitting-parameter C_{21}. The value of $2\delta Y$ can be found if there is a wavelength at which $\sin(\Delta) = 0$ and $E \approx 0$. Thus, we find $2\delta Y(\lambda = 611\text{nm}) = -1.1 \cdot 10^{-5}$ from figure 3.5 and $2\delta Y(\lambda = 530\text{nm}) = -2.2 \cdot 10^{-4}$ from figure 3.6. The value of $p + a$ is obtained by plotting the measured values of Θ_0 against $\cot(\Delta/2)$ in a region where the circular dichroism can be neglected. In this case, this is the same region as where the linear dichroism is small (Moxon et al., 1991). The plot is then a straight line, because:

$$\Theta_0 \approx \frac{1}{2}(p + a)\cot(\Delta/2) - \frac{1}{2}\delta Y. \tag{3.33}$$

The slope of this line equals $\frac{1}{2}(p + a)$. The intercept of the line with the Θ_0-axis can not be used to determine δY, because the values of Θ_0 are measured with respect to some arbitrary origin. Thus, we have found $p + a = -2.3 \cdot 10^{-4}$ for the sample in which the light propagates at an angle $\phi = 15^o40'$ to the optic axis. For the other sample we have found $p + a = 2.8 \cdot 10^{-3}$.

At this point of the interpretation the linear birefringence, the linear dichroism, the value of δY and the value of $p + a$ are all known. Therefore, it is possible to calculate

$2k'_a - (p-a)$ from the fitting-parameter C_{21}. It is known that the optical activity changes sign at $\lambda = 503$ nm for light propagating along the optic axis. Therefore, we have taken values of $p-a$ such, that $2k'_a + (p-a) \approx 0$ at this wavelength. In the figures 3.7 and 3.8 we show the values of k'_a that were obtained in this way.

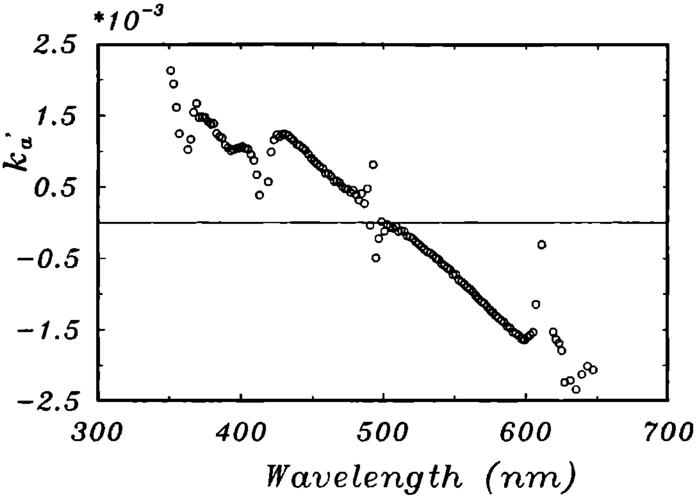

Figure 3.7 k'_a as a function of the wavelength for the sample in which the light propagates at an angle $\phi = 15°40'$ with respect to the optic axis.

The discontinuities in the figures arise at those wavelengths where $\sin(\Delta/2) = 0$. The first reason for this is that the assumptions made in deriving the HAUP intensity formula are not valid when Δ equals an integer times 2π (Kremers and Meekes, 1994a). Secondly, it is very difficult to subtract exactly the correct contributions $2\delta Y \cos(\Delta/2)$ and $E(p+a)\cot(\Delta/2)$ from the fitting-parameter C_{21}. Therefore, terms can remain in k'_a that behave as $(\sin(\Delta/2))^{-1}$ and $(\sin(\Delta/2))^{-2}$. These terms are singular whenever $\Delta/2$ is equal to an integer times π. The observed discontinuities are, therefore, no sample properties. We have to conclude that the results of the HAUP method must be evaluated very carefully in regions where $\sin(\Delta/2)$ is close to zero.

From k'_a the circular birefringence $n_r - n_l$ is calculated in the following way:

$$n_r - n_l = \frac{\lambda}{\pi z} \Delta k'_a. \tag{3.34}$$

The circular birefringence of the sample with an orientation of $\phi = 15°40'$ to the optic axis is given in figure 3.9. In the same way this could have been done, for the other sample. The obtained circular birefringence is then, approximately, of the same magnitude. Nevertheless, the determination of the circular birefringence in directions perpendicular

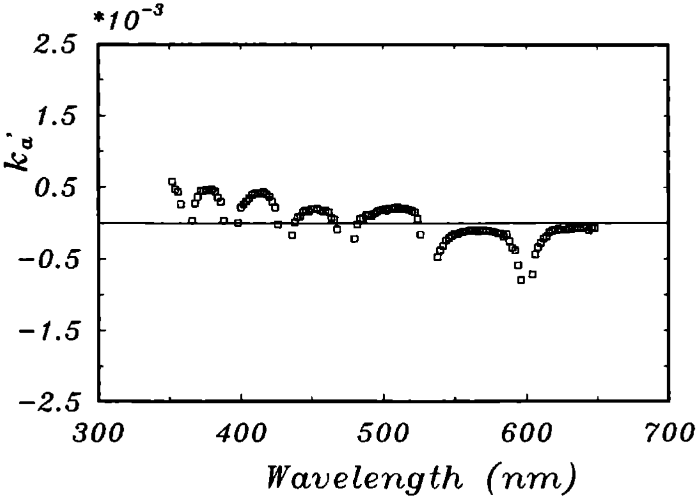

Figure 3.8 k_a' as a function of the wavelength for the sample in which the light propagates at an angle $\phi = 90°$ with respect to the optic axis.

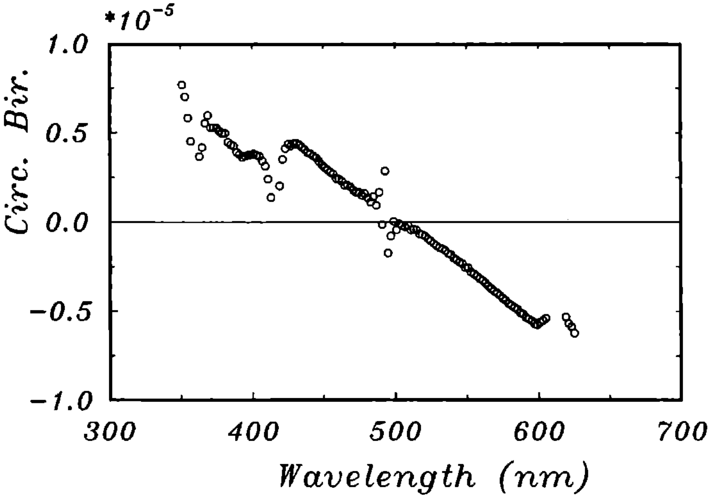

Figure 3.9 The circular birefringence $n_r - n_l$ as a function of the wavelength for the sample in which the light propagates at an angle $\phi = 15°40'$ with respect to the optic axis.

to the optic axis is more difficult, because the linear birefringence is very large there. As a result, k'_a becomes very small for this direction, so that it is difficult to measure it. Moreover, it is not easy to make the sample so thin that the number of times that $\Delta/2$ becomes equal to an integer times π is limited. In this case, the thickness was only 0.10 mm, but, still, six discontinuities are observed in the measured wavelength interval (see figure 3.8). The circular birefringence of figure 3.9 has, except for the discontinuities, a wavelength dependence as can be expected from the measurements along the optic axis (Underwood et al., 1938).

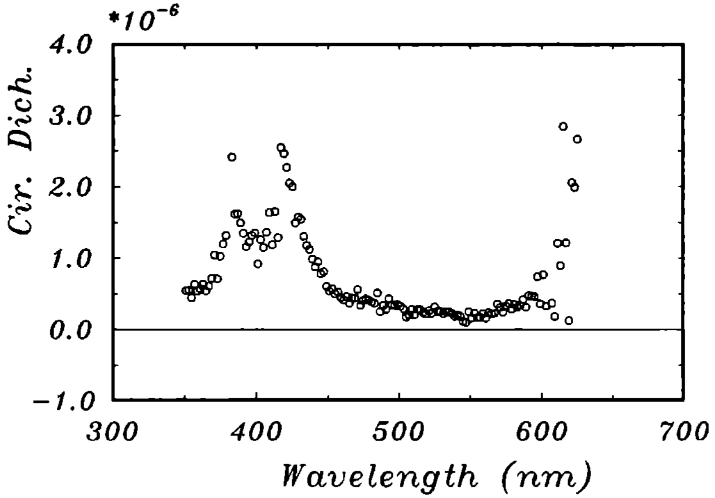

Figure 3.10 The circular dichroism $\kappa_r - \kappa_l$ as a function of the wavelength for the sample in which the light propagates at an angle $\phi = 15^o 40'$ with respect to the optic axis.

The only optical property that still has to be determined is the circular dichroism. It is calculated by comparing the values of Θ_0 of the first and the second extinction direction. For the first extinction direction there is a contribution $-\frac{\pi z}{\lambda}\frac{\kappa_r - \kappa_l}{\Delta}$ to Θ_0 and for the second extinction direction there is a contribution $+\frac{\pi z}{\lambda}\frac{\kappa_r - \kappa_l}{\Delta}$. The values of Θ_0 are measured with respect to some arbitrary origin. Nevertheless, one knows that the two extinction directions differ by an angle $\pi/2$, except for the contributions $\frac{1}{2}\left((p+a)\cot(\Delta/2) - \delta Y\right)$. The values of the latter terms are already known. Therefore, these are subtracted from Θ_0. Furthermore, $\pi/2$ is subtracted from the values of Θ_0 of the second extinction direction. The difference that is left between the two extinction directions is then $\frac{2\pi z}{\lambda}\frac{\kappa_r - \kappa_l}{\Delta} + \delta\Theta$. At this point we take the additional systematic error $\delta\Theta$ into account. This error exists for the same reason as the δY-error. The actual orientation of the polariser can differ from its supposed position due to, for example, mechanical inaccuracies in the driver system. The systematic error $\delta\Theta$ can be determined if there is some region, where the circular dichroism is zero. After having removed the $\delta\Theta$-error one calculates the circular dichroism $\kappa_r - \kappa_l$. For the sample with an orientation of $\phi = 15^\circ 40'$ to the optic axis we have plotted the circular dichroism in figure 3.10. In this case, we have neglected $\delta\Theta$ so that the circular dichroism approaches zero at $\lambda = 545$ nm.

A peak in the circular dichroism is observed at $\lambda = 400$ nm. The structure within this peak is probably caused by the fact that there is a wavelength there for which $\Delta/2$ equals $n\pi$. A measurement with another sample thickness could be used to check this. The onset of a second circular dichroism peak is observed at $\lambda = 625$ nm. The circular dichroism for the sample with the other orientation gave a more or less horizontal line, without structure. One can expect the circular dichroism to be extremely small for that orientation, because it will be even smaller than the circular birefringence. We have seen above that the latter is already very difficult to measure.

3.5 Discussion and Conclusions

In this paper we have shown that the HAUP method can be applied to a wide variety of crystals of any symmetry. The method allows for a precise separation of small optical effects (even non-reciprocal ones) from relatively large reciprocal linear birefringence and reciprocal linear dichroism, but also from systematic errors. The latter must always be taken into account for accurate measurements. The small optical effects have been shown to be responsible for the (complex) ellipticities of the eigenpolarisations that can propagate in the crystal. The HAUP intensity formula can be given in a unified form in terms of these eigenpolarisations. It can then be used to measure the complex ellipticities of an arbitrary sample. On the other hand, it is possible to translate the unified HAUP intensity formula directly into the corresponding expression in terms of the Jones parameters. Then, one can measure the magnitude of the optical effects that are expected to be present in the sample.

The presence or absence of optical effects can give information about the breaking of spatial-inversion symmetry (e.g. in incommensurately modulated crystals), of time-reversal symmetry (e.g. in high-T_c superconductors), or of both (e.g. in magneto-electrics). In all cases, there is a large interest for this information, but the optical effects that might occur are expected to be very small. Therefore, it is important to have an idea of the sensitivity of HAUP for such effects. It has been explained by Kremers and Meekes (1994a) that this sensitivity is, approximately, equal to the accuracy with which polarisers can be set at a certain position. It is, therefore, reasonable to assume a sensitivity of $1 \cdot 10^{-5}$ rad for the measurement of the ellipticity angles k_s', k_a', k_s'' and k_a''. It must be noted, though, that the sensitivity can be reduced to a large extent if the reciprocal linear birefringence and the sample thickness are such that the value of $\Delta/2$ is in the neighbourhood of an integer times π.

Often, an interesting optical effect is found from the ellipticity angles by multiplying with the magnitude of the reciprocal linear birefringence, see equations (3.24) and (3.25). In case of $NiSO_4 \cdot 6H_2O$, for example, the linear birefringence is in the order of 10^{-2} rad. The (maximum) sensitivity for the small optical effects will, therefore, be 10^{-7} rad. This agrees with the estimated sensitivity for the circular dichroism that was plotted in figure 3.10.

We believe that with this sensitivity HAUP must be regarded as a powerful instrument in crystal optics and can be applied to investigate many interesting problems.

3.6 Acknowledgments

We would like to express our gratitude to Prof. Dr. P. Bennema, Prof. Dr. T. Janssen and Prof. Dr. A. Janner for all the support. This work is part of the research program of the Stichting voor Fundamenteel Onderzoek der Materie (Foundation for Fundamental Research on Matter).

References

Agranovich, V. M., and Ginzburg, V. L.,
Crystal Optics with Spatial Dispersion, and Excitons (Berin: Springer-Verlag, 1984).

Brown, W. F., Shtrikman. S., and Treves, D., *J. Appl. Phys.* **34**, 1233 (1963).

Deming, S. N. and Morgan, S. L., *Clin. Chem.* **25**, 840 (1979).

Dijkstra, E., Meekes, H. and Kremers, M., *J. Phys. D: Appl. Phys* **24**, 1861 (1991).

Dzyaloshinskii, I. E., *Physics Letters A* **155**, 62 (1991).

Fabre, J. C., and Boccara, A. C., *Optics Communications* **93**, 306 (1992).

Ferré, J., and Gehring, A., *Rep. Prog. Phys.* **47**, 513 (1984).

Graham, E. B., and Raab, R. E., *Philosophical Magazine B* **66**, 269 (1992).

Grinter, R., Harding, J., and Mason, S. F., *J. Chem. Soc. (A)*, 667 (1970).

Halperin, B. I., March-Russell, J., and Wilczek, F., *Phys. Rev. B* **40**, 8726 (1989).

Hornreich, R. M. and Shtrikman, S., *Phys. Rev.* **171**, 1065 (1968).

Hou, S. L., and Bloembergen, N., *Phys. Rev.* **138**, A1218 (1965).

Janner, A., Janssen, T., and de Wolff, P. M., *Acta Cryst. A* **39**, 671 (1983).

Janner, A., and Janssen, T., *Phys. Rev. B* **15**, 643 (1977).

Jones, R. C., *J. Opt. Soc. Am.* **32**, 486 (1942).

Jones, R. C., *J. Opt. Soc. Am.* **38**, 671 (1948).

Kalmeyer, V. and Laughlin, R. B., *Phys. Rev. Lett.* **59**, 2095 (1987).

Kitazawa, Y., *Phys. Rev. Lett.* **65**, 1275 (1990).

Kobayashi, J., and Uesu, Y, *J. Appl. Cryst.* **16**, 204 (1983).

Kobayashi, J., Kumomi, H., and Saito, K., *J. Appl. Cryst.* **19**, 377 (1986).

Kobayashi, J., Saito, K., and Utsumi, H.,
Phys. Rev. B: Condensed Matter **50**, 2766 (1994).

Kremers, M., and Meekes, H., *submitted to J. Phys. D: Appl. Physics*, (1994a).

Kremers, M., Dijkstra, E., and Meekes, H., *submitted to Phys. Rev. B*, (1994b).

Laughlin, R. B., *Science* **242**, 525 (1988).

Laughlin, R. B., *Phys. Rev. Lett.* **60**, 2677 (1988).

Meekes, H. and Janner, A., *Phys. Rev. B* **38**, 8075 (1988).

Moxon, J. R. L. and Renshaw, A. R., *J. Phys: Condens. Matter* **2**, 6807 (1990).

Moxon, J. R. I., Renshaw, A. R., and Tebbutt, I. J., *J. Phys. D: Appl. Physics* **24**, 1187 (1991).

O'Dell, T. H., *The electrodynamics of magneto-electric media*
(Amsterdam: North-Holland, 1970).

Ortega, J., Etxebarria, J., Folcia, C.L. and Breczewski, T.,
submitted to Phys. Rev. B (1994).

Pisarev, R. V., Krichevtsov, B. B., and Pavlov, V. V., *Phase Transitions* **37**, 63 (1991).

Ramachandran, G. N. and Ramaseshan, S.,
Crystal Optics, Handbuch der Physik, Band XXV/1
(Berlin: Springer, 1961).

Rivera, J. P., *Ferroelectrics* accepted for publication (1992).

Stadnicka, K., Glazer, A. M., and Koralewski, M., *Acta Cryst.* B**43**, 319 (1987).

Uesu, Y., and Kobayashi, J., *Ferroelectrics* **64**, 115 (1985).

Underwood, N., Slack, F. G., and Nelson, E. B., *Phys. Rev.* **54**, 355 (1938).

Wen, X. G. and Zee, A., *Phys. Rev. Lett.* **62**, 2873 (1989).

de Wolff, P. M., *Acta Cryst. A* **30**, 777 (1974).

de Wolff, P. M., Janssen, T., and Janner, A., *Acta Cryst. A* **37**, 625 (1981).

Appendix C

The expansions of the terms $P_{\mathrm{i}}A_{\mathrm{j}}^* \pm P_{\mathrm{k}}A_{\mathrm{l}}^*$ up to third order in Θ, Λ, p and a

$$
\begin{aligned}
P_1A_1^* + P_2A_2^* = & \quad \left\{i(p+a) - \frac{1}{6}i(p+a)^3\right\} \\
+ & \quad (\Lambda - \Theta)\left\{-1 + \frac{1}{2}(p-a)^2\right\} \\
+ & \quad \Lambda\Theta\left\{i(p+a)\right\} - \left(\Lambda^2 + \Theta^2\right)\left\{\frac{1}{2}i(p+a)\right\} \\
+ & \quad \left(\Lambda\Theta^2 - \Theta\Lambda^2\right)\left\{\frac{1}{2}\right\} + \left(\Lambda^3 - \Theta^3\right)\left\{\frac{1}{6}\right\} + \mathcal{O}(4) \\
P_1A_1^* - P_2A_2^* = & \quad \left\{-i(p-a) + \frac{1}{6}i(p-a)^3\right\} \\
+ & \quad (\Lambda + \Theta)\left\{-1 + \frac{1}{2}(p+a)^2\right\} \\
+ & \quad \Lambda\Theta\left\{i(p-a)\right\} + \left(\Lambda^2 + \Theta^2\right)\left\{\frac{1}{2}i(p-a)\right\} \\
+ & \quad \left(\Lambda\Theta^2 + \Theta\Lambda^2\right)\left\{\frac{1}{2}\right\} + \left(\Lambda^3 + \Theta^3\right)\left\{\frac{1}{6}\right\} + \mathcal{O}(4) \\
P_1A_2^* - P_2A_1^* = & \quad \left\{1 - \frac{1}{2}(p-a)^2\right\} \\
+ & \quad (\Lambda - \Theta)\left\{i(p+a)\right\} \\
+ & \quad \Lambda\Theta\left\{1\right\} + \left(\Lambda^2 + \Theta^2\right)\left\{-\frac{1}{2}\right\} + \mathcal{O}(4) \\
P_1A_2^* + P_2A_1^* = & \quad \left\{1 - \frac{1}{2}(p+a)^2\right\} \\
+ & \quad (\Lambda + \Theta)\left\{-i(p-a)\right\} \\
+ & \quad \Lambda\Theta\left\{-1\right\} + \left(\Lambda^2 + \Theta^2\right)\left\{-\frac{1}{2}\right\} + \mathcal{O}(4)
\end{aligned}
$$

Appendix D

The unified HAUP intensity formula for Θ read with respect to an eigenpolarisation

$$\Gamma/\Gamma_0 = \begin{pmatrix} 1 & Y & Y^2 \end{pmatrix} C^{\mathrm{e.p.}}_{(3\times3)} \begin{pmatrix} 1 \\ \Theta \\ \Theta^2 \end{pmatrix}, \tag{D.1}$$

where

$$\begin{aligned}
C^{\mathrm{e.p.}}_{11} &= -2\left(k'_s - k'_a\right)\left(pe^{-E} - ae^{E}\right) \\
&+ \cos(\Delta)\left\{2pa + 2\left(k'_s - k'_a\right)(p-a) - 2\delta Y\left(k''_s - k''_a\right)\right\} \\
&+ \sin(\Delta)\left\{-2(p+a)\left(k''_s - k''_a\right) - 2p\delta Y + 2\delta Y\left(k'_s - k'_a\right)\right\} \\
&+ e^{E}\left\{a^2 + \left(k''_s - k''_a\right)\delta Y + (\delta Y)^2\right\} \\
&+ e^{-E}\left\{p^2\right\} \\
C^{\mathrm{e.p.}}_{21} &= \cos(\Delta)\left\{-2\left(k''_s - k''_a\right)\right\} \\
&+ \sin(\Delta)\left\{2\left(k'_s - k'_a\right) - 2p\right\} \\
&+ e^{E}\left\{2\left(k''_s - k''_a\right) + 2\delta Y\right\} \\
C^{\mathrm{e.p.}}_{12} &= \cos(\Delta)\left\{-4\left(k''_s - k''_a\right) - 2\delta Y\right\} \\
&+ \sin(\Delta)\left\{-2(p+a)\right\} \\
&+ \left\{2\delta Y\right\}e^{E} \\
&+ \cosh(E)\left\{+4\left(k''_s - k''_a\right)\right\} \\
C^{\mathrm{e.p.}}_{22} &= 2\left(\cosh(E) - \cos(\Delta)\right) + 2\sinh(E) \\
C^{\mathrm{e.p.}}_{31} &= e^{E} \\
C^{\mathrm{e.p.}}_{13} &= 2\left(\cosh(E) - \cos(\Delta)\right).
\end{aligned}$$

All other elements of $C^{\mathrm{e.p.}}_{(3\times3)}$ are zero.

List of symbols

Symbol	**Defining relation**	**Description**
a		ellipticity of light polarised by analyser
$\boldsymbol{A}$		Jones vector describing the analyser
α_{pg}		the angle between the principle axes of linear dichroism and linear birefringence
α_{gg}		the rotation of the principle axes of linear birefringence due to non-reciprocal linear birefringence
$C^{\mathrm{e.p.}}_{(3\times3)}$		matrix defining the HAUP intensity formula, derived with respect to an eigenpolarisation as origin for the polariser reading and up to third order terms in the parameters $\Theta, Y, \delta Y, p$ and a
$C^{\Theta_0}_{(3\times3)}$		matrix defining the HAUP intensity formula, derived with respect to an extinction direction as origin for the polariser reading and up to third order terms in the parameters $\Theta, Y, \delta Y, p$ and a
$C_{(3\times3)}$		matrix containing the fitting-parameters for a fit up to third order terms in the angles Θ and Y
χ		arctangent of the ellipticity of a polarisation state of light
χ_1		ellipticity angle of the first eigenpolarisation
χ_2		ellipticity angle of the second eigenpolarisation
δ	$= \frac{\pi}{\lambda}(\kappa_r - \kappa_l)$	representation for circular dichroism in Jones calculus
Δ	$= \frac{2\pi z}{\lambda}(n_1 - n_2)$	
$\Delta\kappa$	$= \kappa_1 - \kappa_2$	reciprocal linear dichroism
Δn	$= n_1 - n_2$	reciprocal linear birefringence
$\delta\Theta$		systematic error, describing a small deviation of the polariser from its supposed position
$\Delta\Theta$		correction to polariser position reading
δY		systematic error, describing a small deviation of the analyser from its supposed position

ΔY		correction to analyser position reading
Γ		intensity of light emerging from the analyser
Γ_0		intensity of light incident on the polariser
g_o	$= \frac{\pi}{\lambda}\Delta n$	reprensentation for reciprocal linear birefringence in Jones calculus
g_{45}	$= \frac{\pi}{\lambda}(n_{-45} - n_{45})$	representation for non-reciprocal birefringence in Jones calculus
$\boldsymbol{J}$		Jones vector of an eigenpolarisation
k_s		symmetric part of the ellipticity angles χ_1 and χ_2
k_a		antisymmetric part of the ellipticity angles χ_1 and χ_2
κ_1		extinction coefficient for the first (linear) eigenpolarisation
κ_2		extinction coefficient for the second (linear) eigenpolarisation
κ_r		extinction coefficient belonging to a right circular eigenpolarisation
κ_l		extinction coefficient belonging to a left circular eigenpolarisation
$\kappa_r - \kappa_l$		circular dichroism
$\tilde{\kappa}$	$= \frac{\kappa_1+\kappa_2}{2}$	average extinction coefficient
κ_{-45}		extinction coefficient for a linear polarisation bisecting the positive x- and negative y-axis
κ_{45}		extinction coefficient for a linear polarisation bisecting the positive x- and positive y-axis
λ		wavelength of the light
Λ		angle defining analyser position
$\tilde{n}$	$= \frac{n_1+n_2}{2}$	average index of refraction
n_1		refractive index belonging to the first eigenpolarisation
n_2		refractive index belonging to the second eigenpolarisation

n_r		refractive index belonging to a right circular eigenpolarisation
n_l		refractive index belonging to a left circular eigenpolarisation
$n_r - n_l$		circular birefringence
n_{-45}		refractive index for a linear polarisation bisecting the positive x- and negative y-axis
n_{45}		refractive index for a linear polarisation bisecting the positive x- and positive y-axis
ω	$= \frac{\pi}{\lambda}(n_r - n_l)$	representation for circular birefringence in Jones calculus
p		ellipticity of light polarised by polariser
p_o	$= \frac{\pi}{\lambda}\Delta\kappa$	representation for reciprocal linear dichroism in Jones calculus
p_{45}	$= \frac{\pi}{\lambda}(p_{-45} - p_{45})$	representation for non-reciprocal linear dichroism in Jones calculus
ψ		azimuth angle of a polarisation state of light
$\boldsymbol{P}$		Jones vector describing the polariser
$\boldsymbol{S}$		Jones matrix describing the sample
Θ		angle defining polariser position
Θ_0		position of polariser defining an extinction direction
Y	$= \Lambda - \Theta$	alternative reading system for the analyser
z		thickness of the crystal platelet

Chapter 4

Optical Activity in the Incommensurate Phase of $((CH_3)_4N)_2ZnCl_4$: a Controversy

Optical Activity in the Incommensurate Phase of $((CH_3)_4N)_2ZnCl_4$: a Controversy

M. Kremers, E. Dijkstra and H. Meekes

Abstract

This paper reports on measurements with a high accuracy universal polarimeter of the optical activity of tetramethylammonium tetrachloro-zincate. This compound has an incommensurately modulated phase that is centrosymmetric if one averages the effect of the modulation. Therefore, the question arises whether this phase is optically active or not. For the three components of the gyration tensor (g_{11}, g_{13} and g_{33}) that have been measured with a thoroughly tested set-up, we present results which were always zero. On the contrary, results reported by others are clearly non-zero. The possible reasons for this controversy are discussed.

4.1 Introduction

In the displacively modulated phase of tetramethylammonium tetrachloro-zincate $((CH_3)_4N)_2ZnCl_4$, the lattice translational symmetry is broken, due to the incommensurate nature of the modulation. The occurrence of such an incommensurately modulated phase is a common feature of different members of the family of A_2BX_4 type crystals, having a $\beta-K_2SO_4$ structure (Cummins , and references therein, 1990). Despite the fact that the lattice translational symmetry is broken, the symmetry of the incommensurately modulated phase can still be described, using a $(3+d)$ dimensional, (centrosymmetric) superspace group, where d is the dimension of the modulation (Janssen and Janner, 1987). In case of $((CH_3)_4N)_2ZnCl_4$ $d = 1$ and the superspace group is Pcmn$(00\gamma)(1s\bar{1})$. The actual crystal can be viewed as a particular three-dimensional section of a $(3 + 1)$-dimensional, lattice translationally invariant, centrosymmetric structure embedded in superspace. The fact that the three-dimensional section has no lattice translational symmetry implies that, along the incommensurate direction, there can be at most one inversion center belonging to the embedded structure. Thus, strictly speaking, the ideal incommensurately modulated phase will not be centrosymmetrical. Moreover, a normal space group description is not possible. On the other hand, the so-called average structure of the incommensurate phase of $((CH_3)_4N)_2ZnCl_4$, obtained by averaging the effect of the modulation, has the same centrosymmetric space group symmetry, Pcmn, as the non-modulated, high-temperature, paraelectric phase. Consequently, it is very interesting to investigate to what extent the symmetry of the incommensurate phase differs from the symmetry of the average structure.

A very sensitive test for the symmetry of the incommensurate phase can be provided by the measurement of optical activity (i.e. optical gyration), which is a third-rank-tensorial property of crystals. In essence, it is caused by spatial dispersion due to the finiteness of the wavelength of the light in the optical region. In other words, optical activity arises from a non-local dependence of the displacement field $\boldsymbol{D}$ on the electric field vector $\boldsymbol{E}$. Since it is a tensorial property, optical activity can be used to test for the presence of symmetry elements in the crystal. Moreover, this test is sensitive for symmetries on the scale of the wavelength of the light. This can be considered to be a semi-macroscopical scale, because the wavelength of the light, λ, is large with respect to usual lattice constants a (in non-modulated crystals), but small with respect to the dimensions of macroscopic samples. The magnitude of the optical activity can be estimated to be in the order of a/λ. In incommensurately modulated crystals, structural periodicities are present, however, that are much larger than a. Therefore, one expects that optical activity in (non-centrosymmetric) incommensurately modulated crystals can even be larger than in non-modulated crystals.

In the classical approach for non-modulated crystals one only considers a constant Fourier component ($\boldsymbol{k} = 0$) for the tensors that describe the optical properties. This is a purely macroscopic description for which it is sufficient to use space averaged tensors. Furthermore, in that case it is the point group of the crystal that imposes symmetry restrictions on the macroscopic physical properties. Due to the presence of large structural periodicities in incommensurately modulated crystals, this approach can no longer be considered as adequate. One has to allow for spatial dependent optical tensors. This has been worked out by Meekes and Janner (1988). These authors have demonstrated how to find symmetry restrictions from the superspace group on (long-wavelength) Fourier components of both dielectric and gyration tensors. They concluded that even for a centrosymmetric superspace group, the presence of such long-wavelength Fourier components, that are absent in non-modulated crystals, may lead to non-vanishing elements of the gyration tensor. A description of the optical properties using the point group of the average structure and even using the point group of the superspace group, on the other hand, leads to a constant gyration tensor with all elements zero, caused by the presence of the inversion center (Nye (1985), Meekes and Janner (1988)).

It will be clear that an accurate measurement of gyration tensor elements in incommensurately modulated phases with a centrosymmetric superspace group, would provide useful information for the selection of the proper symmetry description. Unfortunately this is very difficult due to the, often simultaneously present, linear birefringence. As optical activity (i.e. the gyration) is usually considerably smaller than the linear birefringence, the measurement of optical activity was, in the past, mostly restricted to crystal sections with zero linear birefringence. If optical activity is allowed in incommensurately modulated crystals with a centrosymmetric superspace group, it may be even smaller than it is in classical, gyrotropic crystals, because the deviation with respect to the centrosymmetric average structure can be rather small.

Fortunately, the invention of the High Accuracy Universal Polarimeter (HAUP) by Kobayashi and Uesu (1983) opened the way to measuring very small values of optical activity in the presence of linear birefringence. An improvement to the HAUP method was reported by Kobayashi et al. (1986), that showed the importance of properly taking into account the relevant systematic errors for this method. Other descriptions of the HAUP method and the separation of systematic errors from the optical properties of the sample, have been given by Moxon and Renshaw (1990) and Dijkstra et al. (1991). Recently, Kremers and Meekes (1994) have critically reconsidered the working principles of the HAUP method and revealed several mistakes in the commonly used interpretation of HAUP measurements.

The incommensurate phase of $((CH_3)_4N)_2ZnCl_4$ has already been subject of several investigations using the HAUP method. First, Saito et al. (1985) measured the g_{13} component (according to the crystallographic setting used in the present paper) of the gyration tensor. The maximum value in the incommensurate phase was approximately $1.7 \cdot 10^{-7}$. The authors checked the value of g_{13} with an ordinary polarimeter for the temperature at which they had detected a zero linear birefringence with HAUP. They claimed that this value agreed with the g_{13} values obtained with the HAUP method.

The second report on optical activity in $((CH_3)_4N)_2ZnCl_4$ was made by Kobayashi et al. (1986). In this HAUP measurement an important additional systematic error (the so-called δY-error) was taken into account for the first time. The g_{13} component of the gyration tensor was found to become as large as $3 \cdot 10^{-7}$ in the incommensurate phase. However, the temperature at which a zero linear birefringence was found, differed considerably from the earlier reported value (Saito et al., 1985) and also the behaviour of g_{13} with temperature was clearly different. The origin of these differences might be attributed to the neglect of the δY-error by Saito et al. (1985).

The present authors measured all six components of the gyration tensor with HAUP (Dijkstra et al., 1992). It appeared that all of them, except g_{22}, were non-zero in the incommensurate phase, but also in the (non-modulated) paraelectric phase. However, recently Kremers and Meekes (1994) have reconsidered both the interpretation and the experimental set-up that were used in these experiments. It appeared that several improvements were necessary to both the set-up and the interpretation in order to get reliable results.

The next observation of optical activity in $((CH_3)_4N)_2ZnCl_4$ was made by Kushnir et al. (1993), using a different polarimetric method. These authors focussed their attention on the component g_{33} and found a non-zero result with a maximum value of $5 \cdot 10^{-7}$. Also, already in the paraelectric phase, optical activity was observed.

Folcia et al. (1993) also measured g_{33}, using the HAUP method, but concluded that there was no detectable optical activity $|g_{33}| < 1.5 \cdot 10^{-7}$. They argued that the symmetry restrictions in the incommensurate phase are the same as in a normal centrosymmetric phase and that therefore optical activity is forbidden.

In view of the contradicting results, Kobayashi et al. (1993) performed new HAUP measurements on $((CH_3)_4N)_2ZnCl_4$. All components g_{ij} of the gyration tensor were found to be zero, except for g_{13}, becoming maximally $2 \cdot 10^{-7}$ in the incommensurate phase.

Recently, however, the interpretation of HAUP data, used by Kobayashi et al., has been questioned by Ortega et al. (1994). The latter authors report on g_{13} measurements of Rb_2ZnCl_4, an incommensurately modulated crystal expected to have the same superspace group symmetry as $((CH_3)_4N)_2ZnCl_4$. An essentially zero g_{13} component, $|g_{13}| < 5 \cdot 10^{-6}$, has been obtained by these authors, everywhere in the incommensurate phase. They have also re-processed previously reported measurements of Kobayashi et al. (1988), again obtaining a negligible g_{13}. Surprisingly, the original interpretation of Kobayashi et al. (1988), using the same data, gave a five times larger g_{13} than the values obtained from the re-processing.

In view of all these controversial results, we have decided to perform new measurements of the elements g_{11}, g_{33} and g_{13} of the gyration tensor of $((CH_3)_4N)_2ZnCl_4$ with HAUP, in the incommensurate phase as well as in the paraelectric phase. In our opinion the obtained results are very reliable, since both an improved experimental set-up and an improved, correct, interpretation of the data have been used, according to our recently presented reconsideration of the HAUP method (Kremers and Meekes, 1994).

This paper is organised in the following manner. First a description is given of the crystal structure of $((CH_3)_4N)_2ZnCl_4$, in order to make clear which gyration tensor elements may be important in the different phases. Then, after describing the samples that have been used (section 4.3) and how the measurements have been performed (section 4.4) we will clarify in section 4.5 our way of interpreting the measurements. Subsequently, the results are presented in section 4.6 and 4.7. We have added a special section about the possible influence of the crystal growth method (section 4.8). After that, our results are compared with those of other authors in the discussion, section 4.9, and the conclusions are given in section 4.10.

4.2 The crystal structure of $((CH_3)_4N)_2ZnCl_4$ as a function of temperature

In the tables 4.1 and 4.2, the phase transitions occurring in $((CH_3)_4N)_2ZnCl_4$ are presented and the different phases are characterised. The corresponding gyration tensors are also shown. The incommensurate phase (II) has not been specified in table 4.1, but is described in table 4.2. In the present section the contents of both tables (4.1 and 4.2) will be clarified.

At temperatures higher than $T_i = 297.6$ K (see table 4.1), the space group symmetry of $((CH_3)_4N)_2ZnCl_4$ is Pcmn ($|\boldsymbol{a}| = 15.525\text{Å}$, $|\boldsymbol{b}| = 8.946\text{Å}$ and the pseudo-hexagonal axis $|\boldsymbol{c}| = 12.268 Å$). This is a centrosymmetric space group and therefore, all elements of the gyration tensor are zero (Nye, 1985). There exists, however, a disorder of the $[ZnCl_4]^{2-}$ tetrahedra in this phase, actually breaking the mirror symmetry parallel to the (010) plane (Wiesner et al., 1967). Such a disorder appears to be a common feature of the $\beta - K_2SO_4$ type paraelectric phase of A_2BX_4 crystals with an incommensurate phase (see, for example, Kazuyuki Itoh et al., 1983).

Upon decreasing the temperature below $T_i = 297.6$ K the paraelectric phase of $((CH_3)_4N)_2ZnCl_4$ undergoes a phase transition to an incommensurately modulated structure, in which an extra periodicity with wave vector $\boldsymbol{q} = \gamma \boldsymbol{c}^*$ develops (Cummins , and references therein, 1990). This periodicity is incommensurate with the lattice of the paraelectric phase. In the incommensurate phase, the value of γ changes continuously (therefore taking irrational values) with temperature (see table 4.2).

Phase	VI	V	IV	III	II	I
Temp (K)	< 161	< 181	$< 276.5 (= T_m)$	$< 280 (= T_c)$		$> 297.6 (= T_i)$
Symmetry	$P2_12_12_1$	$P2_1/c11$	$P112_1/n$	$Pc2_1n$		Pcmn
Type			ferroelastic ε_{xz}	ferroelectric $\boldsymbol{P}_y$		paraelectric
γ	1/3	0	1/3	2/5		0
System	Orthorh.	Monocl.	Monocl.	Orhorh.		Orthorh.
gyration tensor $\boldsymbol{g}$	$\begin{pmatrix} g_{11} & 0 & 0 \\ 0 & g_{22} & 0 \\ 0 & 0 & g_{33} \end{pmatrix}$	0	0	$\begin{pmatrix} 0 & 0 & g_{13} \\ 0 & 0 & 0 \\ g_{13} & 0 & 0 \end{pmatrix}$		0

Table 4.1 Crystal phases and gyration tensors of $((CH_3)_4N)_2ZnCl_4$. Phase II is the incommensurate phase, which is described in table 4.2.

It has been observed by several authors (Bziouet et al. (1987), Sveleba et al. (1993), Vogels et al. (1994)) that, in the incommensurate phase, in a small temperature interval ($290.8 < T < 292.8$ K), γ is locked at a rational value of $\frac{5}{12}$ and it is believed that this locking is intrinsic. In the investigations of Vogels et al. (1994), $((CH_3)_4N)_2ZnCl_4$ crystals have been used that were grown with the same equipment and comparable conditions, as the crystals that were used for the measurements presented here. We therefore have to take into account that such a locking of the modulation wave vector can occur in the samples used for the present investigations. The symmetries of the commensurate structures that can result from a rational value of γ have been derived by, for example, Janssen (1986) for the superspace group Pcmn$(00\gamma)(1s\bar{1})$. In case of $\gamma = \frac{5}{12}$ the three possible space group symmetries are $P12_1/c1$, $P2_1cn$ and P1c1. Which of these three is realised, depends on the exact phase of the modulation wave. This phase can be determined very locally in a

	II: Incommensurate Phase				
Temp (K)	$< \approx 290.8$	$< \approx 292.8$			< 297.6
Symmetry	Pcmn(00γ)(1s$\bar{1}$)	P12$_1$/c1	or P2$_1$cn	or P1c1	Pcmn(00γ)(1s$\bar{1}$)
γ	$0.408 < \gamma < \frac{5}{12}$	$\frac{5}{12}$			$\frac{5}{12} < \gamma < 0.42$
gyration tensor g	?	$\emptyset$	$\begin{pmatrix} 0 & 0 & 0 \\ 0 & 0 & g_{23} \\ 0 & g_{23} & 0 \end{pmatrix}$	$\begin{pmatrix} 0 & g_{12} & 0 \\ g_{12} & 0 & g_{23} \\ 0 & g_{23} & 0 \end{pmatrix}$	?

Table 4.2 Specification of the incommensurate phase of $((CH_3)_4N)_2ZnCl_4$ and the possible gyration tensors that correspond to the commensurate value $\gamma = \frac{5}{12}$.

crystal, due to the pinning to all kind of defects. As one can see in table 4.2, none of the three possible space groups allows for a non-zero g_{11}, g_{13} or g_{33}. These, however, are the three gyration tensor elements that we study in this paper. A non-zero result can thus not be caused by the locking of γ to $\frac{5}{12}$.

At a temperature of $T_c = 280$ K (see table 4.1), a lock-in transition to a ferroelectric phase occurs. There, γ takes the rational value 2/5 and the crystal has a five-fold superstructure. The only non-zero component of the gyration tensor is g_{13}. A further decrease of temperature results in three more commensurate phases. The measurements presented in this paper, however, were only performed in the paraelectric phase and in the incommensurately modulated phase.

4.3 The Samples

Totally transparent $((CH_3)_4N)_2ZnCl_4$ crystals of about 1 cm^3, containing no observable inclusions, have been grown by a thermal convection method (Arend et al., 1986). The large natural faces on the crystals were indexed, using an optical goniometer. Three crystal

Sample	Sample Surface	Thickness (mm)	Linear Birefringence Δn	Gyration $G = g_{ij}s_is_j$
1	(100)	1.50	$\Delta n_{11} = n_c - n_b$	$G_{11} = g_{11}$
2	(001)	1.66	$\Delta n_{33} = n_a - n_b$	$G_{33} = g_{33}$
3	(101)	0.91	$\Delta n_{13} \approx 0.62\Delta n_{33} + 0.38\Delta n_{11}$	$G_{13} = 0.39g_{11} + 0.62g_{33} + 0.97g_{13}$

Table 4.3 The three samples of $((CH_3)_4N)_2ZnCl_4$ used in the present experiments and the optically relevant parameters detected by a HAUP measurement. n_a, n_b and n_c are the main refractive indices. g is the gyration tensor and s is the unit wave vector of the incident light with respect to the crystallographic axes.

platelets, parallel to the natural (100), (101) and (001) crystallographic faces, were cut with a wire saw. Both sides of the platelets have been polished on felt, with diamond paste down to 1 μm size. Special care was taken to keep the two polished faces of each sample as plane-parallel as possible. In table 4.3, the optical parameters that determine the propagation of light in a HAUP measurement (linear birefringence and gyration) are presented for each sample.

4.4 Measurements

All measurements have been performed with the HAUP apparatus built in our laboratory as described by Dijkstra et al. (1991). This original version of the apparatus appeared to be inadequate to perform reliable measurements and therefore, some essential improvements were carried out (Kremers and Meekes, 1994).

Since the centrosymmetry of the paraelectric phase may be broken by a disorder of the $[ZnCl_4]^{2-}$ tetrahedra and because of the suggested possible gyration effect in this phase by several authors (Dijkstra et al. (1992), Kushnir et al. (1993)) each of the three samples was subjected to a HAUP measurement as a function of the wavelength λ of the light at constant temperature T = 320 K. The measurement procedure is described by Kremers and Meekes (1994). The sensitivity of the set-up can be derived from the results in case we find that the paraelectric phase is indeed non-gyratory. Thus, we can then decide whether measurements in the incommensurate phase should reveal the magnitude of the gyration previously reported by others (Saito et al. (1985), Kobayashi et al. (1986), Kushnir et al. (1993), Kobayashi et al. (1993)).

Subsequently, the three samples have been subjected to a HAUP measurement as a function of temperature, at constant wavelength λ, in the paraelectric phase and the incommensurately modulated phase. In these measurements four extinction directions were measured (see, Kremers and Meekes, 1994). The measurement of one extinction direction takes about a quarter of an hour. Thus, before the measurement of the fourth extinction direction, the temperature had been stable for three quarters of an hour and before the measurement of the third extinction direction two quarters of an hour, etc. By measuring four extinction directions, we can therefore study the effect of temperature stabilisation. This is important, because, from measurements of the dielectric properties, it is well known (Le Van Hong , and references therein, 1990) that several relaxation processes occur in A_2BX_4 type incommensurately modulated crystals. These processes may be associated with, for example, the motion of discommensurations or the motion of domain walls, possibly related to the coexistence of incommensurate and commensurate regions in the crystal and pinning due to defects. As an example, we would like to refer to measurements by Hiroyuki Mashiyama and Hirohumi Kasatani (1987) and Hideaki Sakata et al. (1990). These authors report on a time evolution of the dielectric constant, in the incommensurate phase of K_2ZnCl_4, changing over more than 10 hours, at a constant temperature. This time evolution was associated with the nucleation and annihilation of discommensurations near the phase transition from the incommensurate phase to a lock-in phase.

4.5 Extraction of the systematic errors

The fitting procedures used for the measurements presented in this paper have been described extensively by Kremers and Meekes (1994). In all cases, the possible presence of small linear dichroism, caused by anisotropic surface scattering, has been taken into account. The absolute values of the linear dichroism $|\Delta\kappa|$ were never larger than $5 \cdot 10^{-7}$. Also the so-called $\Delta\Theta$-correction, described by these authors, has been performed for all measurements.

Here, we want to give a brief outline of the way the typical systematic errors of HAUP measurements have been extracted, using the measurement on the (101) sample, as a function of the temperature, as an example. From a fit (up to second order in the polariser angles) of the measured intensities to the HAUP intensity formula one obtains the parameter:

$$4\sin^2(\pi z\, \Delta n/\lambda) \tag{4.1}$$

from which the linear birefringence Δn must be calculated (z is the thickness of the sample)
and the parameter:

$$C_{21} = 2\delta Y \cos^2(\pi z\, \Delta n/\lambda) - ((p-a)+2k)\sin(2\pi z\, \Delta n/\lambda) + \frac{2z\pi\, \Delta\kappa}{\lambda}(p+a)\cot(\pi z\, \Delta n/\lambda) \tag{4.2}$$

with $k = G/(2\tilde{n}\Delta n)$ in which $\tilde{n}$ is the average refractive index and G is the gyration, in which we are interested. p and a represent the small parasitic ellipticities of light polarised by the polariser and analyser respectively. The systematic error δY describes a small uncertainty in the reading of the analyser position.
Furthermore, one obtains the extinction direction from the fit:

$$\Theta_0 = \frac{1}{2}(p+a)\cot(\pi\; z\; \Delta n/\lambda) - \frac{1}{2}\delta Y + \delta\Theta_{\mathrm{indicatrix}} \tag{4.3}$$

where $\delta\Theta_{\mathrm{indicatrix}}$ is the possible rotation of the optical indicatrix.

From $4\sin^2(\pi\; z\; \Delta n/\lambda)$, C_{21} and Θ_0, one has to extract the systematic errors p, a, and δY in order to be able to obtain the gyration G.

4.5.1 A total fit to C_{21}

For all measurements, it has been checked whether a total fit to the C_{21} (eqn. (4.2)), inserting Δn from (4.1), as a function of temperature or wavelength, was possible. An example is given in figure 4.1 for the (101) sample as a function of the temperature in the paraelectric phase and the incommensurate phase. An almost perfect fit can be observed, implying that the parameter $k = G/(2\tilde{n}\Delta n)$ is practically a constant independent of temperature. For all the samples that have been measured, this procedure of fitting C_{21} showed k to be constant in all cases.

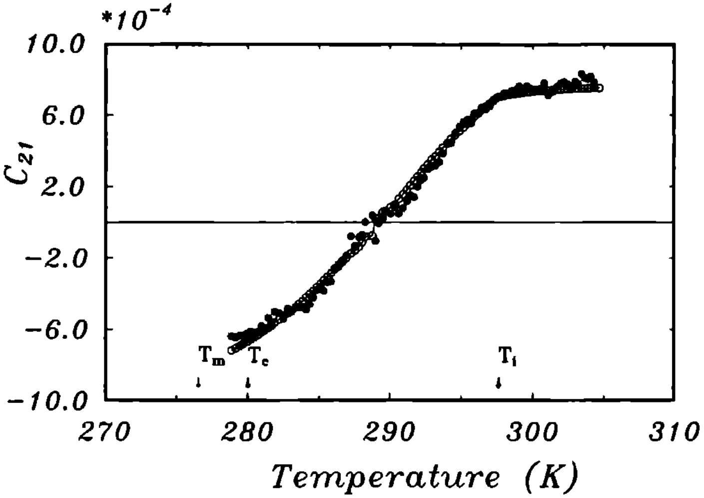

Figure 4.1 A total fit to C_{21} (eqn. (4.2)) for the (101) sample as a function of the temperature in the paraelectric phase and the incommensurate phase. The full circles are the C_{21} data and the open circles represent the fit to these data.

4.5.2 Elimination of the δY-error

As shown by Kremers and Meekes (1994), the origin of the δY-error mainly lies in the fact that there is a deviation ΔY of the analyser from its supposed position, due to the eccentricities of the rotation stages on which the polarisers are mounted or due to other mechanical inaccuracies. These authors, however, proposed a method to eliminate this contribution to the δY-error almost completely. During the first step of the fitting procedures, in which the measured intensities are fitted to the HAUP intensity formula, one corrects the analyser positions with the value of ΔY. Subsequently one can obtain the remaining contribution of δY by plotting $C_{21}/\sin(2\pi z\ \Delta n/\lambda)$ against $\cot(\pi z\ \Delta n/\lambda)$, in case that k is a constant. The slope of a straight line fitted through these points, equals δY.

In figure 4.2 this has been done for the (101) sample and the measurement as a function of temperature. The results are shown both with and without the ΔY-correction. Without the ΔY-correction a value $\delta Y = -9.26 \cdot 10^{-4}$ was obtained. The remaining contribution of δY is only $2.86 \cdot 10^{-7}$ after the ΔY-correction.

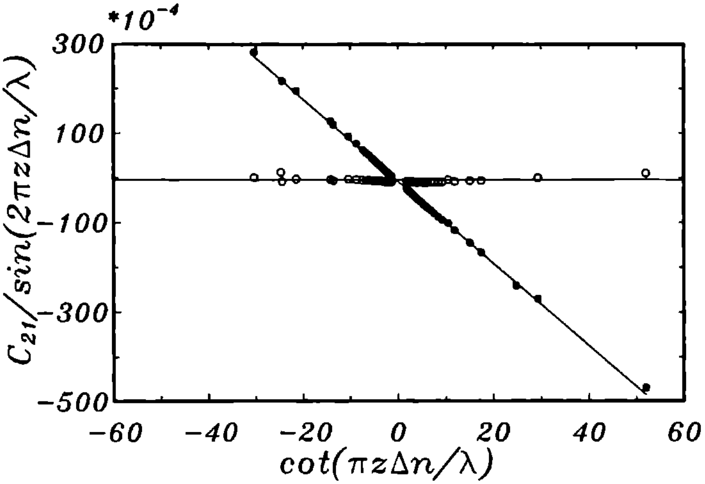

Figure 4.2 A plot of $C_{21}/\sin(2\pi z\ \Delta n/\lambda)$ versus $\cot(\pi z\ \Delta n/\lambda)$ for the measurement of the (101) sample as a function of temperature. The full circles represent the data obtained without the ΔY-correction and the open circles represent the data obtained with ΔY-correction. The straight lines are least squares fits to these data.

For all measurements, the ΔY-correction resulted in a similar large reduction of the δY-error, but there was practically no change in the values of the other systematic errors p and a, nor in the values of the optical parameters Δn and G. This shows that the ΔY-correction worked perfectly well.

4.5.3 The systematic errors *p* and *a*

After the determination of δY, the value of $p + a$ was obtained by plotting Θ_0 against $\cot(\pi z\ \Delta n/\lambda)$. The result for the (101) sample is given in figure 4.3. It is clear that there is a perfect straight line behaviour, implying that $-\frac{1}{2}\delta Y + \delta\Theta_{\text{indicatrix}}$ is a constant, independent of temperature. The orientation of the indicatrix is fixed in the paraelectric phase, due to the orthorhombic symmetry. Therefore, we conclude, that there is no indicatrix rotation in the incommensurate phase. Also, in the (100) and (001) samples, no indicatrix rotation could be observed.

It follows from equation (4.3), that the slope of the straight line fitted through the data in figure 4.3, equals $\frac{1}{2}(p + a)$. Thus, we found $(p + a) = 1.01 \cdot 10^{-3}$.

As discussed earlier, for all measurements it was concluded that the value of $k = G/(2\bar{n}\Delta n)$ was practically constant, independent of temperature or wavelength. The paraelectric phase of $((CH_3)_4N)_2ZnCl_4$ is centrosymmetric and not modulated. From the measurements as a function of wavelength in the paraelectric phase, we thus have concluded that there $k = 0$. The value of $\gamma \equiv (p - a)$ can therefore be obtained as the intercept at the ordinate axis of a fitted straight line in a $C_{21}/\sin(2\pi z\ \Delta n/\lambda)$ against $\cot(\pi z\ \Delta n/\lambda)$ plot, see equation (4.2).

Also, in case of the measurements as a function of temperature, only the results in the paraelectric phase were used to find the value of $\gamma = (p - a)$. In other words, γ was obtained by averaging over the paraelectric phase, in order to use the same method as Kobayashi et al. (1993).

After the determination of both $(p + a)$ and $\gamma = (p - a)$, one can calculate p and a separately. For all measurements as a function of the temperature, four extinction directions have been measured. As noted before, by Kremers and Meekes (1994), the obtained p and a errors only agreed between the first and the third extinction direction and between the second and the fourth extinction direction. It has thus again been shown, that neither p nor a can be taken as an apparatus constant. Both systematic errors p and a depend on the actual position of the polarisers, though a rotation of π rad gives the same values.

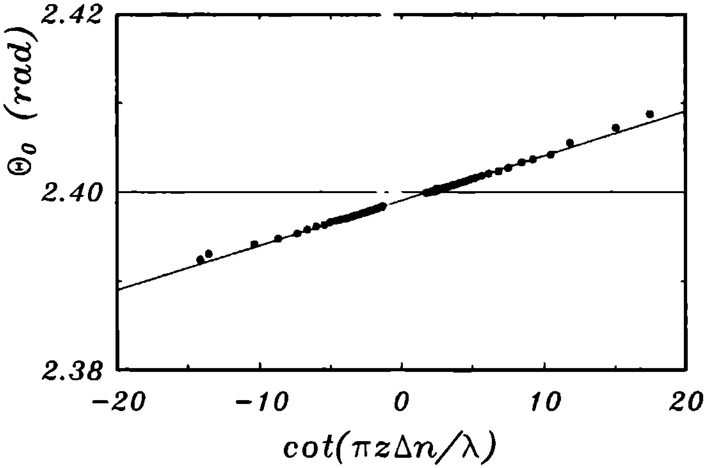

Figure 4.3 A plot of Θ_0 versus $\cot(\pi z\ \Delta n/\lambda)$ for the measurement, as a function of temperature, of the (101) sample. The straight line represents the result of a least squares fit.

4.6 Wavelength dependence in the paraelectric phase

All three samples (see table 4.3), have been measured at constant temperature T = 320 K as a function of the wavelength λ of the light. The obtained values of the linear birefringence Δn are plotted in figure 4.4. Indeed, from the three data sets it follows that $\Delta n_{13} \approx 0.62\Delta n_{33} + 0.38\Delta n_{11}$. Vlokh et al. (1987) also have reported on measurements of the linear birefringence as a function of wavelength for $((CH_3)_4N)_2ZnCl_4$ crystals. Although these authors do not give the crystallographic setting they used, we conclude from comparison that it must be Pmcn and that they have reversed the sign of Δn_b (setting Pmcn).

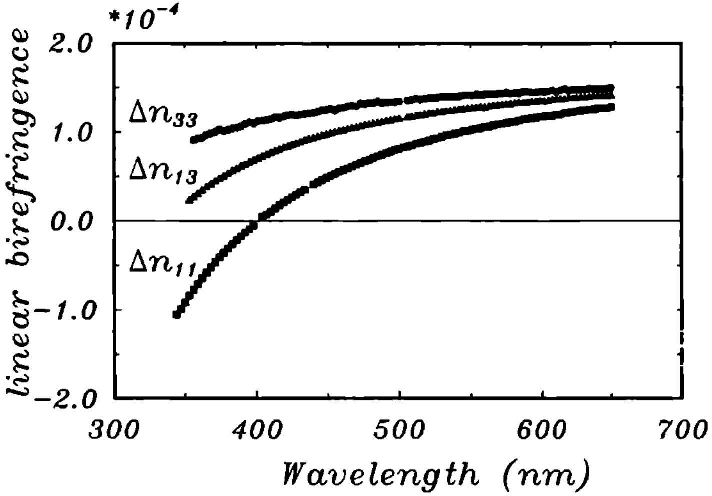

Figure 4.4 The linear birefringences Δn_{33} (full circles), Δn_{13} (full triangles) and Δn_{11} (full squares)in the paraelectric phase of $((CH_3)_4N)_2ZnCl_4$ as a function of the wavelength λ, at a temperature T = 320 K

The average refractive index $\tilde{n}$ does not follow from a HAUP measurement. It may change with wavelength and with temperature. In order to avoid extensive additional measurements, we prefer to give the circular birefringence $(n_r - n_l)$ instead of the gyration G. In figures 4.5, 4.6 and 4.7 the obtained circular birefringences $(n_r - n_l)_{ij} = G_{ij}/\tilde{n}$ have been plotted.

Though the noise in $G_{33}/\tilde{n}$ of figure 4.7 is somewhat larger than the noise in $G_{11}/\tilde{n}$ of figure 4.5 and in $G_{13}/\tilde{n}$ of figure 4.6, it is clear that for all three samples a zero gyration has been found. We can safely conclude that, in the case of $((CH_3)_4N)_2ZnCl_4$, our HAUP equipment can discriminate circular birefringence values $G/\tilde{n}$ of $3 \cdot 10^{-8}$ from zero. The most recent report on optical activity in the incommensurate phase of $((CH_3)_4N)_2ZnCl_4$

has been made by Kobayashi et al. (1993). These authors claim to have measured a maximum value of $2 \cdot 10^{-7}$ for g_{13}. As the average refractive index of $((CH_3)_4N)_2ZnCl_4$ crystals is about 1.527 (Dijkstra et al., 1992), this corresponds to a circular birefringence of $1.3 \cdot 10^{-7}$. If such an effect is present, it can certainly be detected with our HAUP.

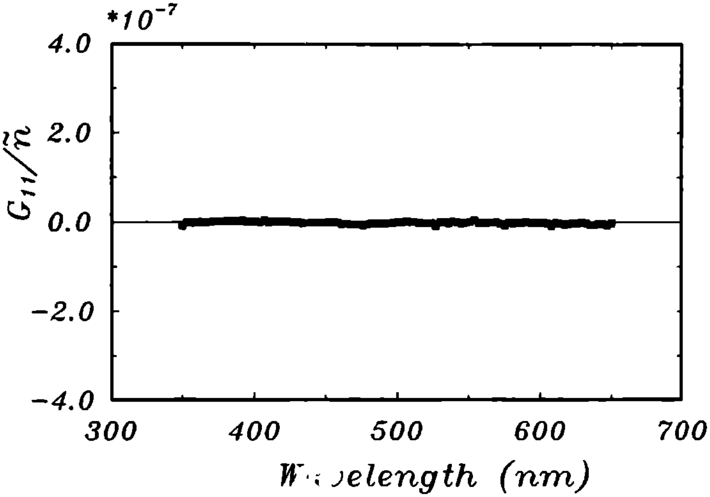

Figure 4.5 The circular birefringence $G_{11}/\bar{n}$ of $((CH_3)_4N)_2ZnCl_4$ in the paraelectric phase at a temperature of T = 320 K.

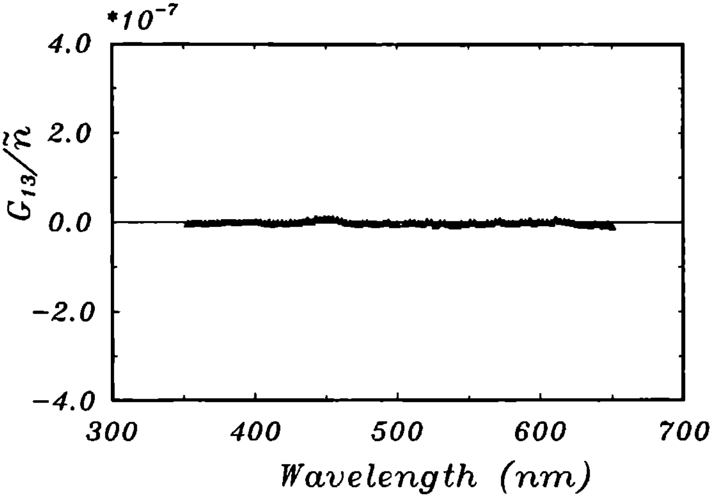

Figure 4.6 The circular birefringence $G_{13}/\tilde{n}$ of $((CH_3)_4N)_2ZnCl_4$ in the paraelectric phase at a temperature of T = 320 K.

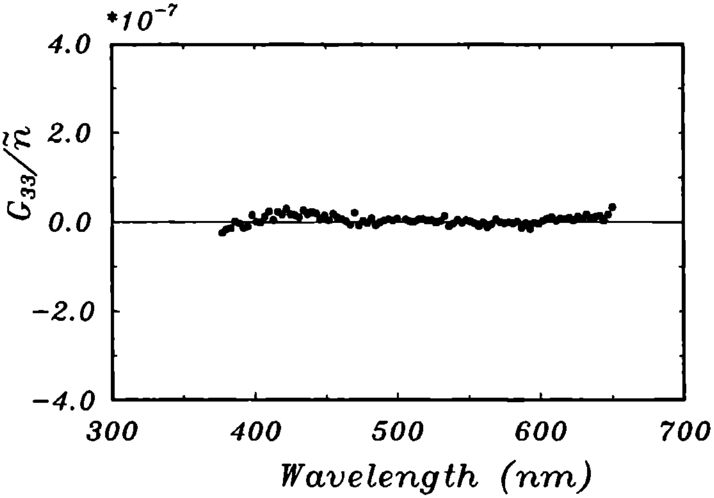

Figure 4.7 The circular birefringence $G_{33}/\tilde{n}$ of $((CH_3)_4N)_2ZnCl_4$ in the paraelectric phase at a temperature of T = 320 K.

4.7 Temperature dependence

In figure 4.8 the linear birefringence Δn_{13} has been plotted for the first and the fourth extinction direction at a constant wavelength $\lambda = 600$ nm. The first extinction direction has been measured each time directly after the change of temperature, but the temperature had been stable for about three quarters of an hour when the fourth extinction direction was measured. Nevertheless, the absolute values of both curves agree very well at all temperatures. No effect of temperature stabilisation can thus be detected in the linear birefringence. In the figures 4.9 and 4.10 the linear birefringences $\Delta n_{11}(\lambda = 632.8$ nm) and $\Delta n_{33}(\lambda = 600$ nm) have been plotted.

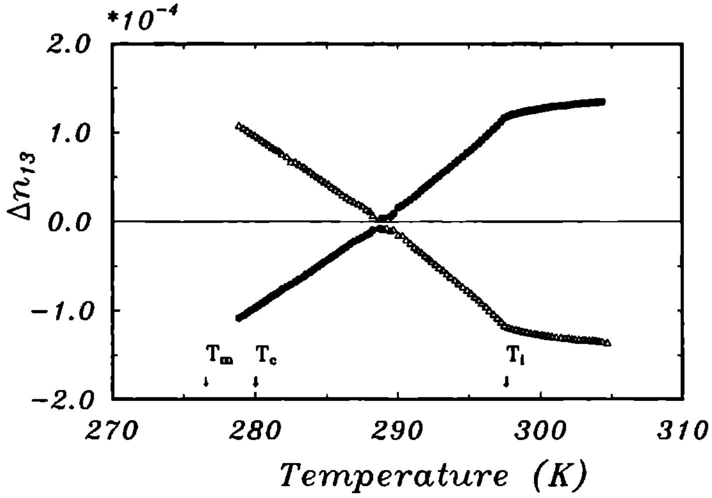

Figure 4.8 The linear birefringence Δn_{13} of $((CH_3)_4N)_2ZnCl_4$ in the paraelectric and incommensurate phase. The wavelength of the light is $\lambda = 600$ nm. Full circles (●) correspond to the first extinction direction and open triangles (△) to the fourth extinction direction.

The circular birefringence $G_{13}/\tilde{n}$ resulting from the measurements of the fourth extinction direction of the (101) sample is presented in figure 4.11. The absolute value of the circular birefringence is everywhere smaller than $1{\cdot}10^{-8}$ as opposed to the $g_{13}/\tilde{n} \approx 1.3{\cdot}10^{-7}$ found by Kobayashi et al. (1993). We conclude from figure 4.11 that the gyration g_{13} is zero, or too small to be measured with HAUP, in the paraelectric and incommensurate phase of $((CH_3)_4N)_2ZnCl_4$. Unfortunately, Kobayashi et al. (1993) do not specify the time that the temperature was stabilised in their measurements. Therefore, we have plotted in figure 4.12 the circular birefringence $G_{13}/\tilde{n}$, obtained from the measurement of the first extinction direction (no temperature stabilisation) of the (101) sample. In this case one can see a very small, possibly non-zero circular birefringence, having some temperature dependence. Already in the paraelectric phase there is a deviation from zero. However, the maximum value of the circular birefringence is $G_{13}/\tilde{n} = 3 \cdot 10^{-8}$ at T_c, which is still considerably smaller than the $g_{13}/\tilde{n} \approx 1.3 \cdot 10^{-7}$ found by Kobayashi et al. (1993). Furthermore, we have concluded in section 4.6, that a circular birefringence for $((CH_3)_4N)_2ZnCl_4$ should be larger than $3 \cdot 10^{-8}$ in order to be safely discriminated from zero. It is therefore questionable, whether the circular birefringence $G_{13}/\tilde{n}$ in figure 4.12 should be considered as significant.

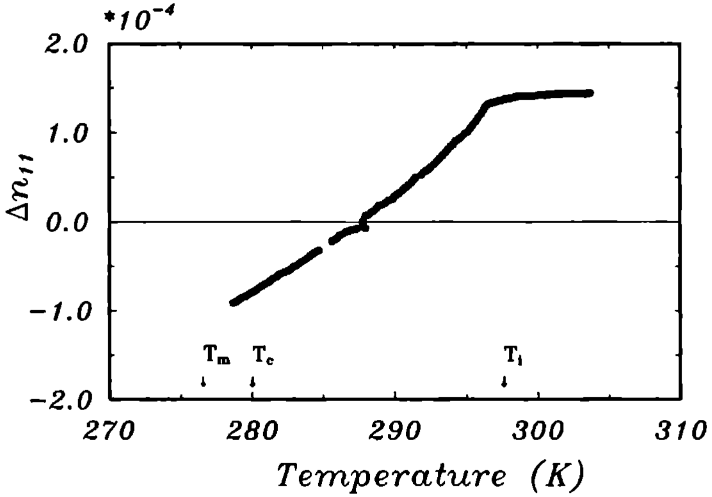

Figure 4.9 The linear birefringence Δn_{11} of $((CH_3)_4N)_2ZnCl_4$ in the paraelectric and incommensurate phase. The wavelength of the light is $\lambda = 632.8$ nm.

The circular birefringences $G_{11}/\tilde{n}$ and $G_{33}/\tilde{n}$ (fourth extinction direction) are shown in figures 4.13 and 4.14. In both figures, the noise around zero in the circular birefringence is maximally $3 \cdot 10^{-8}$. So both $G_{11}/\tilde{n}$ and $G_{33}/\tilde{n}$ are zero in the incommensurate (and paraelectric) phase, or too small to be detected. The results for G_{33} are consistent with those obtained by Folcia et al. (1993), but disagree with the report of Kushnir et al. (1993), who found a value of $g_{33}/\tilde{n} = 3.3 \cdot 10^{-7}$. Since the latter authors used a polarimetric technique, different from HAUP, we are not in the position to discuss the possible influence of wrongly taking into account systematic errors in their measurements. Nevertheless, one can expect that systematic errors also play an important role in their case and that one should treat them with great care.

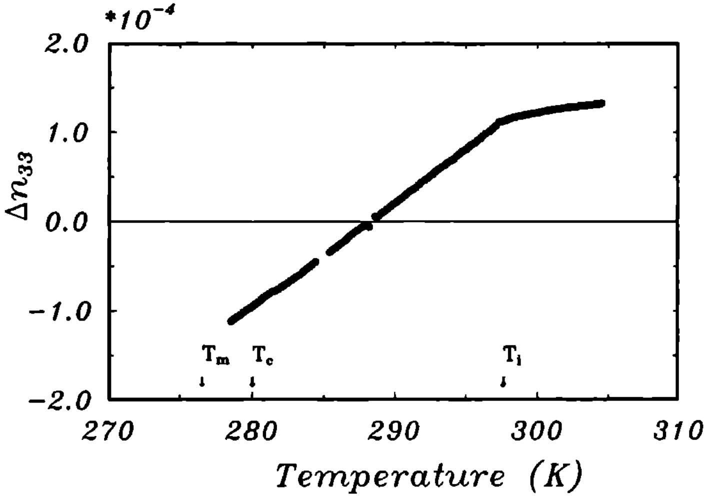

Figure 4.10 The linear birefringence Δn_{33} of $((CH_3)_4N)_2ZnCl_4$ in the paraelectric and incommensurate phase. The wavelength of the light is $\lambda = 600$ nm.

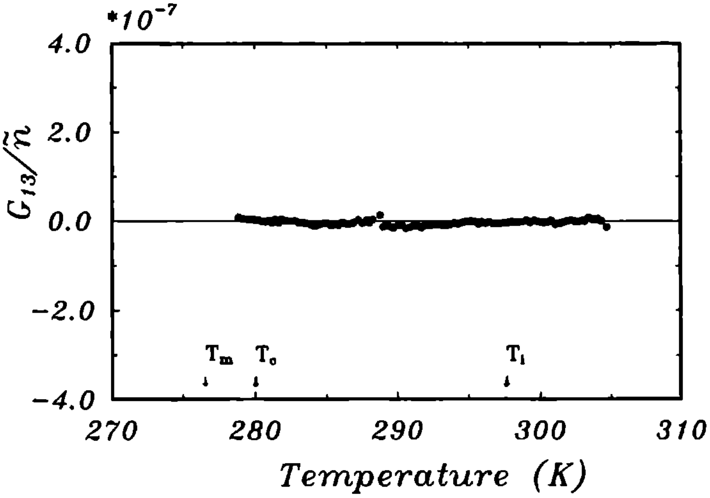

Figure 4.11 The circular birefringence $G_{13}/\tilde{n}$ of $((CH_3)_4N)_2ZnCl_4$ in the paraelectric and incommensurate phase, obtained from the measurement of the fourth extinction direction. The temperature has each time been stabilised for about three quarters of an hour. The wavelength of the light was $\lambda = 600$ nm.

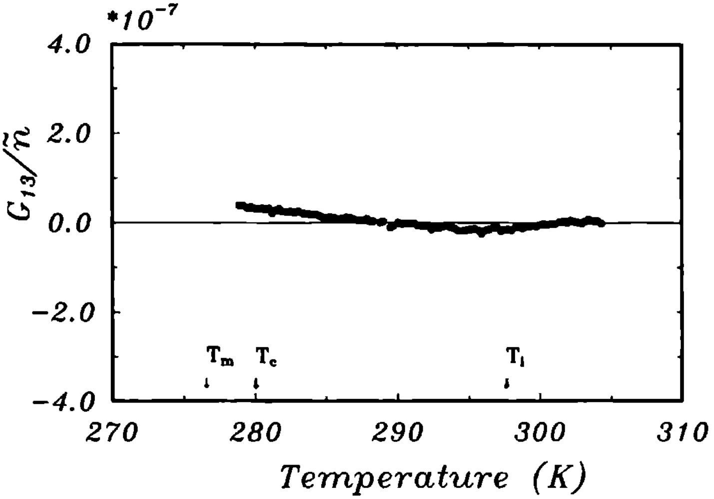

Figure 4.12 The circular birefringence $G_{13}/\tilde{n}$ of $((CH_3)_4N)_2ZnCl_4$ in the paraelectric and incommensurate phase, obtained from the measurement of the first extinction direction. The temperature was not stabilised. The wavelength of the light was $\lambda = 600$ nm.

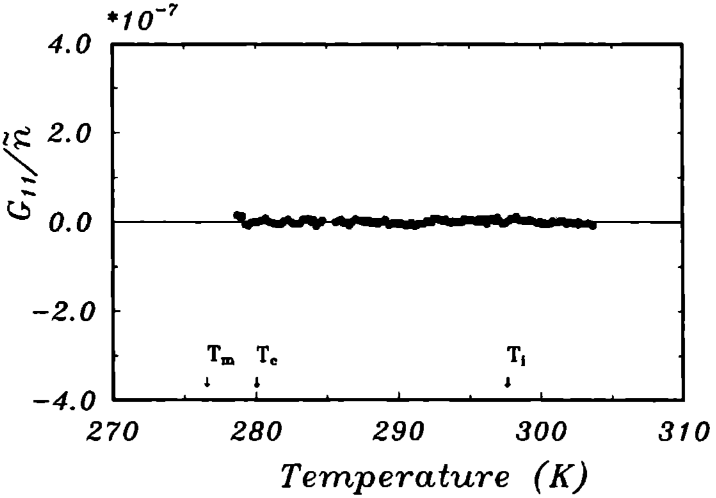

Figure 4.13 The circular birefringence $G_{11}/\tilde{n}$ of $((CH_3)_4N)_2ZnCl_4$ in the paraelectric and incommensurate phase, obtained from the measurement of the fourth extinction direction. The temperature has each time been stabilised for about three quarters of an hour. The wavelength of the light was $\lambda = 632.8$ nm.

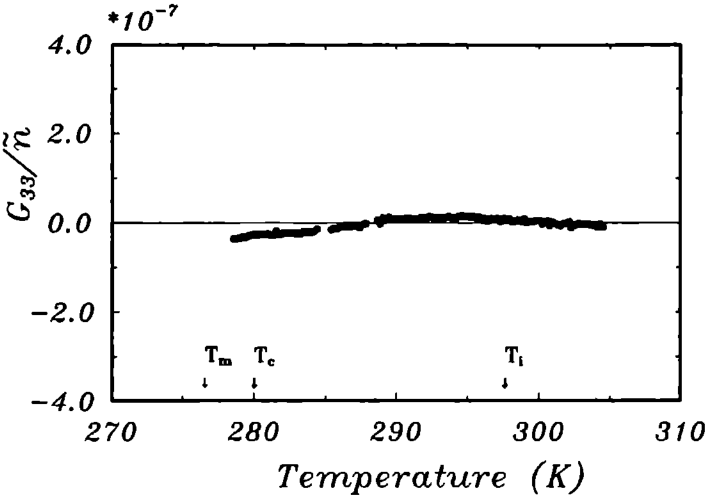

Figure 4.14 The circular birefringence $G_{33}/\tilde{n}$ of $((CH_3)_4N)_2ZnCl_4$ in the paraelectric and incommensurate phase, obtained from the measurement of the fourth extinction direction. The temperature has each time been stabilised for about three quarters of an hour. The wavelength of the light was $\lambda = 600$ nm.

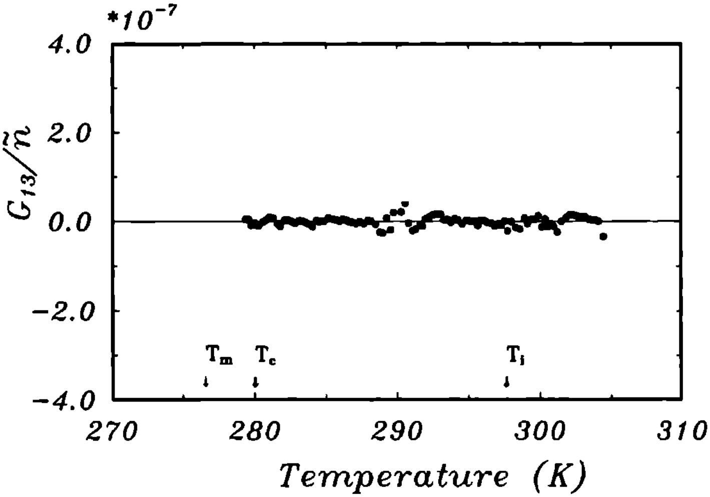

Figure 4.15 The circular birefringence $G_{13}/\tilde{n}$ of $((CH_3)_4N)_2ZnCl_4$ in the paraelectric and incommensurate phase, obtained from the measurement of the fourth extinction direction. The crystal from which the sample was cut, has been grown by a slow cooling method. During the measurement, the temperature has each time been stabilised for about three quarters of an hour. The wavelength of the light was $\lambda = 550$ nm.

4.8 The influence of the crystal growth method

It is well known that the quality of crystals (for example represented by the number and kind of defects) can depend on the crystal growth method. Furthermore, the properties of A_2BX_4 type incommensurately modulated crystals can be influenced strongly by the crystal quality (Katsumi Hamano et al. (1980), Kapustianik et al. (1992), Hiroyuki Mashiyama and Hirohumi Kasatani (1987), Unruh (1984), Bziouet et al. (1987), Kushnir et al. (1993b)). It has even been suggested by Kushnir et al. (1993c) that defects are precisely the cause for the observation of a non-zero circular birefringence in these crystals.

Therefore, we will present here some additional results of HAUP measurements on $((CH_3)_4N)_2ZnCl_4$ crystals that have been obtained from different growth methods than the thermal convection method, that was used for the samples of table 4.3. It should be clear, however, that we realise that these measurements are by no means a thorough investigation of the role of the crystal growth method or the role of defects.

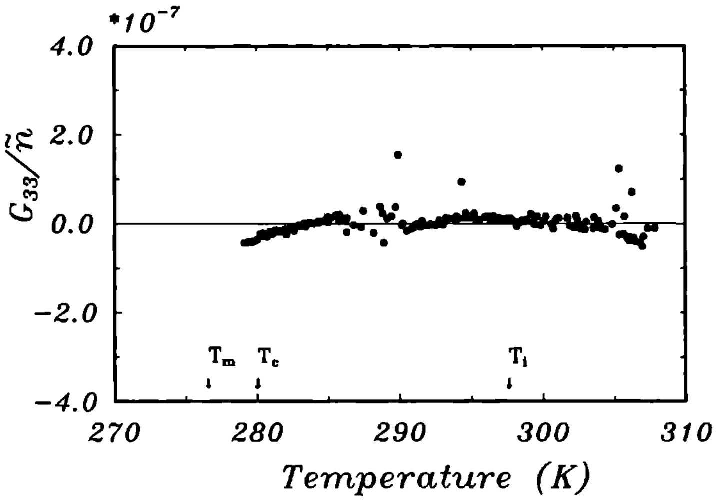

Figure 4.16 The circular birefringence $G_{33}/\tilde{n}$ of $((CH_3)_4N)_2ZnCl_4$ in the paraelectric and incommensurate phase. The crystal from which the sample was cut, has been grown by slow evaporation of a solution of $((CH_3)_4N)_2ZnCl_4$ in a water-methanol mixture. The noise is large, because of the fact that a photon counting system was used with a limited resolution. The wavelength of the light was $\lambda = 595$ nm.

The crystals in which Kobayashi et al. (1993) detected a non-zero gyration g_{13} were grown at the university of Halle by means of a slow cooling method. In figure 4.15 we show the circular birefringence $G_{13}/\tilde{n}$ of a (101) sample cut from a crystal that also was grown by a slow cooling method. The absolute value of the circular birefringence $G_{13}/\tilde{n}$

is smaller than $3 \cdot 10^{-8}$. Thus, again we have been unable to detect a non-zero gyration, in contrast with Kobayashi et al. (1993). The possible reasons for this controversy will be addressed in the discussion, section 4.9.

The non-zero g_{33} (maximally $5 \cdot 10^{-7}$), reported by Kushnir et al. (1993) was found in crystals grown by slow evaporation of an aqueous solution (see, Kushnir et al., 1993b). We have grown a $((CH_3)_4N)_2ZnCl_4$ crystal by slowly evaporating a saturated solution of $((CH_3)_4N)_2ZnCl_4$ in a water-methanol mixture at a temperature $T \approx 292.5$ K in the incommensurate phase. The obtained circular birefringence $G_{33}/\tilde{n}$ from a HAUP measurement on a (001) sample is shown in figure 4.16. This particular experiment was performed with the old set-up, in which the photon counting system had a limited resolution, causing the noise to be rather large (Kremers and Meekes, 1994). Nevertheless it is clear that, excluding the temperature region in the neigbourhood of zero linear birefringence, the circular birefringence does even not exceed a value of $\pm 5 \cdot 10^{-8}$. This result thus disagrees with the findings of Kushnir et al. (1993).

4.9 Discussion

The HAUP measurements presented in this paper were intended to study the symmetry of the incommensurate phase of $((CH_3)_4N)_2ZnCl_4$ by means of the gyration tensor elements g_{11}, g_{13} and g_{33}. These measurements have been performed with a thoroughly tested apparatus. Moreover, the optical parameters of the sample have been extracted from the HAUP data with a method that has resulted from a very critical reconsideration of the interpretation of HAUP measurements. We have found that all three elements g_{11}, g_{13} and g_{33} must have values that are smaller than the resolution of our apparatus. Therefore, it is our opinion, that the (possibly non-zero) elements of Fourier components of the gyration tensor must be considered to be very small in the case of $((CH_3)_4N)_2ZnCl_4$. Of course, these results do not exclude the possibility that detectable gyration effects can be found in other incommensurately modulated crystals that have a centrosymmetric superspace group. At present, careful measurements on such members of the A_2BX_4 family are in progress in our laboratory.

There is a group of workers in Spain, that also have performed HAUP measurements on several incommensurate crystals of the A_2BX_4 family (Ortega et al. (1992), Folcia et al. (1993), Ortega et al. (1994)). These authors report that they could not detect a non-zero gyration effect in any of these crystals, within the resolution of their apparatus. As a consequence, they conclude that it is the point group of the average structure that imposes symmetry restrictions on the optical properties. In our view, such a conclusion may be premature. The non-zero gyration tensor elements that can be expected to result from the presence of an incommensurate modulation, may be very small for the cases that have been investigated, but they need not be necessarily zero. Moreover, it is possible that detectable gyration effects are present in other crystals that have not yet been studied. It would be very useful, of course, to have a microscopic model with which the magnitude of optical effects could be estimated for incommensurately modulated crystals. Unfortunately, such a model still has to be developed.

On the other hand, the HAUP experiments themselves deserve careful attention, because of the controversy that exists between the results presented in this paper and those reported on by Kobayashi et al. (1993). These authors claim to measure a clearly non-zero g_{13} for $((CH_3)_4N)_2ZnCl_4$, whereas the present investigations show that g_{13} must be, at least, ten times smaller. We can think of only few reasons that would explain this controversy.

For example, though we have been unable to detect a non-zero gyration in a crystal grown by slow cooling, such a growth method, as used by Kobayashi et al. (1993) might produce crystals of specific (high or low) quality, that are gyratory. In $((CH_3)_4N)_2ZnCl_4$ crystals with a large defect concentration the modulation wave vector $\boldsymbol{q} = \gamma \boldsymbol{c}^*$ can be locked at several rational values of γ (Bziouet et al., 1987). As shown by Janssen (1986), one could obtain in this way local structures with a point group symmetry that allows for optical activity. However, in view of our own results from different growth methods, this explanation does not seem very likely.

Another reason for the controversy may be found in a different thermal treatment of the samples, during or before a HAUP measurement. In our measurements, a stabilisation at each temperature of about three quarters of an hour seems to have no influence on the linear birefringence. It does, however, have a small influence on the circular birefringence. Nevertheless, the values obtained without stabilisation are still much smaller than the ones reported by Kobayashi et al. (1993). Also, the temperature at which the crystals are grown and/or stored after growth may be important, since it is well known that memory effects can play a role in incommensurately modulated crystals (see for example Folcia et al. (1986) and Folcia et al. (1989)).

Finally, the controversy between our results and those of Kobayashi et al. (1993), can perhaps be explained by a different way of interpreting the data obtained from a HAUP experiment. Ortega et al. (1994) expressed some doubts regarding the interpretation of Kobayashi et al. (1988) for the case of Rb_2ZnCl_4 . It can however be considered as strange, that an incorrect interpretation would only lead to one non-zero gyration tensor element, as there is in principle no difference in interpretation for different sample orientations.

Of course, the non-zero $g_{33} \approx 5 \cdot 10^{-7}$ reported by Kushnir et al. (1993) also disagrees with the result of our measurements. However, all other HAUP experiments (except Dijkstra et al., 1992) on $((CH_3)_4N)_2ZnCl_4$ (Folcia et al. (1993), Kobayashi et al. (1993)) give an essentially zero g_{33}, consistent with our results. The result of Dijkstra et al. (1992) was incorrect. As the HAUP method is studied more extensively than the polarimetric method used by Kushnir et al. (1993), we are confident that g_{33} indeed is zero, or too small to be experimentally accessible.

4.10 Conclusions

From HAUP measurements in the paraelectric and incommensurately modulated phase of $((CH_3)_4N)_2ZnCl_4$ we conclude that the gyration tensor elements g_{11}, g_{13} and g_{33} are too small to be detected, in both phases. Crystals grown by using different methods show the same results. A very small circular birefringence may have been found, however, in the case that the temperature was not stabilised before the measurement.

Previous HAUP measurements on the same compound, presented by Dijkstra et al. (1992) revealed non-zero gyration tensor elements, but were incorrect due to an inadequate set-up and mistakes in the interpretation, leading to detectable non-zero values for almost al gyration tensor components.

Nevertheless, measurements of other authors result in clearly non-zero gyration tensor elements, sometimes even in the paraelectric phase. The controversy concerning the existence of gyration in the incommensurate phase of $((CH_3)_4N)_2ZnCl_4$, therefore, remains. We feel that it should be solved by a cooperation of the workers in this field. Therefore, we would like to suggest that a set of samples of $((CH_3)_4N)_2ZnCl_4$ is selected that is measured with the techniques of several groups. In this way, one can check whether these measurements all give the same results. Subsequently, the influence of sample quality and sample treatment can be studied.

4.11 Acknowledgments

The authors would like to thank H. Hempel, University of Halle, for kindly providing the crystal grown by a slow cooling method. This work is part of the research program of the Stichting voor Fundamenteel Onderzoek der Materie (Foundation for Fundamental Research on Matter).

References

Arend, H., Perret, F., Wüest, H. and Kerkoc, P., *Journ. of Cryst. Growth* **74**, 321 (1986).

Bziouet, M., Almairac, R. and Saint-Grégoire, P., *J. Phys. C: Solid State Phys.* **20**, 2635 (1987).

Cummins, H. Z., *Phys. Rep.* **185**, 211 (1990).

Dijkstra, E., Meekes, H. and Kremers, M., *J. Phys. D: Appl. Phys* **24**, 1861 (1991).

Dijkstra, E., Kremers, M. and Meekes, H., *J. Phys.: Condens. Matter* **4**, 715 (1992).

Folcia, C. L., Tello, M. J., Pérez-Mato, J. M. and Zubillaga, J. A., *Solid State Commun.* **60**, 581 (1986).

Folcia, C. L., Zúniga, F. J., Madariaga, G., Pérez-Mato, J. M. and Tello, M. J., *Phys. Rev. B* **40**, 11037 (1989).

Folcia, C. L., Ortega, J. and Etxebarria, J., *Phys. Rev. B* **48**, 695 (1993).

Hideaki Sakata, Katsumi Hamano, Xiaoqing Pan and Unruh, H. G., *J. Phys. Soc. Jpn.* **59**, 1079 (1990).

Hiroyuki Mashiyama and Hirohumi Kasatani, *J. Phys. Soc. Jpn.* **56**, 3347 (1987).

Le Van Hong, Gen Li, Tao, N. and Cummins, H. Z., *Phys. Rev. B* **41**, 6050 (1990).

Janssen, T., *Ferroelectrics* **66**, 203 (1986)

Janssen, T. and Janner, A., *Adv. Phys.* **36**, 519 (1987).

Kapustianik, V. B., Polovinko, I. I., Sveleba, S. A., Vlokh, O. G. and Zhmurko, V. S., *Europhys. Lett.* **19**, 429 (1992).

Katsumi Hamano, Yoshito Ikeda, Takayauki Fujimoto, Kenji Ema and Shunsuke Hirotsu, *J. Phys. Soc. Jpn.* **49**, 2278 (1980).

Kazuyuki Itho, Akinori Hinasada, Hironori Matsunaga and Eiji Nakamura, *J. Phys. Soc. Jpn.***52**, 664 (1983).

Kobayashi, J. and Uesu, Y., *J. Appl. Cryst.* **16**, 204 (1983).

Kobayashi, J., Kumomi, I. and Saito, K., *J. Appl. Cryst.* **19**, 377 (1986).

Kobayashi, J., Saito, K., Fukase, H. and Matsuda, K., *Phase Transitions* **12**, 225 (1988).

Kobayashi, J., *Condensed Matter News* **1**, 17 (1992).

Kobayashi, J., Saito, K., Takahashi, N. and Kamiya, I., *Phys. Rev. B* **48**, 10038 (1993).

Kremers, M. and Meekes, H., *submitted to J. Phys. D: Appl. Phys* (1994).

Kushnir, O. S., Shopa, Y. I. and Vlokh, O. G., *Europhys. Lett.* **22**, 389 (1993).

Kushnir, O. S., Shopa, Y. I., Vlokh, O. G., Polovinko, I. I. and Sveleba, S. A., *J. Phys.: Condens. Matter* **5**, 4759 (1993b).

Kushnir, O. S. and Vlokh, O. G., *J. Phys.: Condens. Matter* **5**, 7017 (1993c).

Meekes, H. and Janner, A., *Phys. Rev. B* **38**, 8075 (1988).

Moxon, J. R. L. and Renshaw, A. R., *J. Phys: Condens. Matter* **2**, 6807 (1990).

Nye, J. F., *Physical properties of crystals* (Oxford: Oxford University Press, 1985).

Ortega, J., Etxebarria, J., Zubillaga, J., Breczewski, T. and Tello, M.J., *Phys. Rev. B* **45**, 5155 (1992).

Ortega, J., Etxebarria, J., Folcia, C.L. and Breczewski, T., *submitted to Phys. Rev. B* (1994).

Saito, K, Kunishima, I., Kobayashi, J. and Uesu, Y., *Ferroelectrics* **64**, 137 (1985).

Sveleba, S., Zhmurko, V., Polovinko, I., Trybula, Z., Kempiński, W. and Zuk, T., *Physica B* **183**, 183 (1993).

Unruh, H. G., *Ferroelectrics* **53**, 319 (1984).

Vlokh, O. G., Kityk, A. V. and Polovinko, I. I., *Opt. Spektrosk.* **62**, 221 (1987).

Vogels, L. J. P., Meekes, H. and de Boer, J. L., *submitted to J. Phys CM* (1994).

Wiesner, J. R., Srivastava, R. C., Kennard, C. H. L., DiVaira, M. and Lingafelter, E. C., *Acta Cryst.* **23**, 565 (1967).

Chapter 5

Influence of the incommensurate modulation on the optical properties of $((CH_3)_4N)_2CuCl_4$

Influence of the incommensurate modulation on the optical properties of $((CH_3)_4N)_2CuCl_4$

M. Kremers and H. Meekes

Abstract

This paper reports on the measurement of the optical properties of incommensurately modulated $((CH_3)_4N)_2CuCl_4$ by using the High Accuracy Universal Polarimeter. With this technique it is possible to measure, simultaneously, linear birefringence, linear dichroism, circular birefringence, circular dichroism and the rotation of the optical indicatrix. Two different samples are used. The orientation of the first sample allows for the measurement of the gyration tensor element g_{33}. In the other sample g_{13} can be measured. The optical effects are studied as a function of temperature, both in a region of zero linear dichroism and in a region of finite linear dichroism. The measurements reveal that the crystals have a low defect concentration. The presence of the incommensurate modulation is clearly revealed by the linear birefringence. The linear dichroism, on the other hand appears to be unaffected by the modulation. It is interesting that if one averages the effect of the incommensurate modulation a crystal structure is obtained that is believed to be orthorhombic and centrosymmetric. Two effects are observed that are forbidden by the symmetry of this average structure. One of them is the rotation of the optical indicatrix, which contradicts an orthorhombic symmetry. The other is the onset of non-zero optical activity, approximately halfway the incommensurate phase. In centrosymmetric media this effect is not allowed to occur. The observed temperature dependence of the optical activity g_{13} differs from the behaviour measured by other authors. It is discussed whether the observed effects can be attributed to a symmetry breaking by the incommensurate modulation.

5.1 Introduction

Tetramethylammonium tetrachloro-cuprate $((CH_3)_4N)_2CuCl_4$ (Morosin and Lingafelter (1961), Clay et al. (1975)) is a member of the family of A_2BX_4 type crystals that show a phase transition from a $\beta-K_2SO_4$ structure into an incommensurately modulated phase. The modulation wave vector of $((CH_3)_4N)_2CuCl_4$, $\boldsymbol{q} = (2+\delta)\boldsymbol{c}^*/3$ with $\delta \approx 0.02$, is approximately constant in the incommensurate phase (Gesi and Iizumi, 1980). Due to the incommensurateness of the modulation wave vector the 3-dimensional lattice translational symmetry is broken in the incommensurate phase. This phase is often considered to be an intermediate phase between the $\beta-K_2SO_4$ type phase and a so-called lock-in phase. In the latter, the modulation becomes commensurate with the lattice. Therefore a superstructure is formed. The resulting structure has, again, 3-dimensional lattice translational symmetry and is usually ferroelectric. In the case of $((CH_3)_4N)_2CuCl_4$, however, the lock-in phase is ferroelastic (Sawada et al., 1980). Another lock-in phase exists at lower temperatures (Sugiyama et al., 1980).

Due to the broken lattice translational symmetry it is not possible to use a normal space group description for the incommensurate phase. The crystal can, however, be embedded in a so-called superspace, where the lattice translational symmetry is restored. The symmetry can, consequently, be described by means of a so-called superspace group (de Wolff (1974), Janner and Janssen (1977), de Wolff et al. (1981), Janner et al. (1983)). Often, it is even possible to use the same superspace group for the embedding of the other (commensurate) phases (Janssen, 1986). To our knowledge, the superspace group symmetry of the incommensurate phase of $((CH_3)_4N)_2CuCl_4$ has not been determined experimentally. Nevertheless, it is believed that the only superspace group that allows for the, known, normal space group symmetries of the other phases is $Pcmn(00\gamma)(1s\bar{1})$ (Hogervorst (1986), Ortega et al. (1992)). Note that this superspace group is equivalent to $Pcmn(00\gamma)(ss\bar{1})$ with the modulation wave vector $\boldsymbol{c}^* - \boldsymbol{q}$ instead of $\boldsymbol{q}$. If, in the incommensurate phase, the effect of the modulation is averaged one has an orthorhombic and centrosymmetric structure. For the related compound $((CH_3)_4N)_2CuBr_4$ the superspace group is known to be $Pcmn(\alpha 00)(\bar{1}s1)$ (Madariaga et al., 1990). The average structure of this crystal is also orthorhombic and centrosymmetric. It is the aim of this paper to investigate whether optical effects can be observed in the incommensurate phase of $((CH_3)_4N)_2CuCl_4$ that are not allowed by the symmetry of the average structure. These effects then have to be caused by the presence of the incommensurate modulation.

Recently, we have investigated the optical properties of another member of the A_2BX_4 family, $((CH_3)_4N)_2ZnCl_4$ (Kremers et al., 1994a), which also has the superspace group symmetry $Pcmn(00\gamma)(1s\bar{1})$. We searched for the presence of optical activity in the incommensurate phase, because this effect is a sensitive test for the symmetry. Due to the finiteness of the wavelength of the light in the optical region, (weak) spatial dispersion contributes to the propagation of light in crystals. It is understood that this causes optical activity. It is a third-rank-tensorial property that can be used to test for the presence of symmetry elements on the scale of the wavelength of the light. This wavelength, λ, is large with respect to usual lattice constants, a, of non-modulated crystals. The optical activity is estimated to have a magnitude in the order of a/λ. The structural periodicities that are present in incommensurately modulated crystals, however, are much larger than a. The spatial dispersion is, therefore, not necessarily weak. Thus, a relatively large optical activity might result, under the condition that it is allowed by symmetry. It was shown by Meekes and Janner (1988) that one can take the large structural periodicities into account by considering also $\boldsymbol{k} \neq 0$ Fourier components of both dielectric and gyration tensors. Moreover, the symmetry restrictions imposed by the superspace group were evaluated by these authors. It was found that the gyration tensor can have non-vanishing elements for a centrosymmetric superspace group, whereas the point group of the average structure, but also the point group of the superspace group do not allow for non-zero gyration tensor elements (Nye (1985), Meekes and Janner (1988)). In the case of $((CH_3)_4N)_2ZnCl_4$ we could not detect any non-zero gyration, or any other effect caused by a symmetry breaking due to the modulation (Kremers et al., 1994a). In this paper, we pursue the search for the influence of the incommensurate modulation on optical properties for the case of $((CH_3)_4N)_2CuCl_4$. This material is interesting for several reasons.

The crystals of $((CH_3)_4N)_2CuCl_4$ have an orange colour due to the absorption edge at $\lambda \approx 500$ nm. The position of this edge depends (weakly) on the temperature and shows characteristic behaviour at the phase transitions (Vlokh et al., 1988). By means of band structure calculations (Blokh et al., 1990) it was found that the $[CuCl_4]^{2-}$ tetrahedra play the dominant role in the formation of the absorption band. It is well known that the modulation influences the orientations of these tetrahedra in $((CH_3)_4N)_2MCl_4$ (M = Zn, Fe, Co, Ni, and Mn) crystals. We want to point out that there is an important Jahn-Teller distortion (Clay et al., 1975) in the M = Cu compound. It is interesting, therefore, to investigate the influence of the modulation on the dichroic optical properties. We report on measurements of both the linear and the circular dichroism of $((CH_3)_4N)_2CuCl_4$. The latter effect is forbidden by symmetry in centrosymmetric media, in the same way as optical activity is. Furthermore, it is well known that refractive indices n can increase considerably at an absorption edge (Agranovich and Ginzburg, 1984). The wavelength of the light in the crystal, $\lambda = \lambda_0/n$, is then considerably reduced (λ_0 is the wavelength of the light in vacuum). This leads to an increase of the optical activity, because the size of the effect behaves as a/λ. It is interesting, therefore, to measure optical activity in incommensurately modulated crystals, with an average centrosymmetric structure, using wavelengths near an absorption edge. In this paper we report on such measurements. The compound $((CH_3)_4N)_2CuCl_4$ is further interesting because it has a monoclinic and centrosymmetric lock-in phase. The optical activity is, therefore, necessarily zero in this phase. On the other hand, the optical indicatrix can rotate around the unique axis of the monoclinic structure. Therefore, it is interesting to search for an indicatrix rotation already in the incommensurate phase. Such a rotation is forbidden if the incommensurate phase has the orthorhombic symmetry of the average structure.

The simultaneous measurement of linear birefringence, linear dichroism, circular birefringence (i.e. optical activity), circular dichroism and indicatrix rotation is by no means straightforward. It can be accomplished with the High Accuracy Universal Polarimeter (HAUP). This instrument was introduced by Kobayashi and Uesu (1983) for the simultaneous measurement of linear birefringence, optical activity and indicatrix rotation. Recently, we have shown (Kremers and Meekes, 1994c) how HAUP can be used for absorbing and magnetic crystals, so that dichroic effects can also be measured.

The HAUP technique has already been used to investigate $((CH_3)_4N)_2CuCl_4$. In these investigations the wavelength $\lambda = 632.8$ nm was used, which is above the absorption edge. The dichroic effects are then negligible. The first HAUP measurements on $((CH_3)_4N)_2CuCl_4$ were reported by Uesu and Kobayashi (1985). At the phase transition from the incommensurate to the lock-in phase a large thermal hysteresis (about 7 K) was observed in the results for the gyration tensor element g_{13} (for the settings used in this paper). The measured gyration was clearly non-zero only in the incommensurate phase. The thermal hysteresis was also detected in the linear birefringence of the sample. Sawada et al. (1980) observed a thermal hysteresis of about 10 K at the same phase transition in measurements of the dielectric constant. The cause of such a hysteresis is often found in the role played by defects (see for example Hamano et al., 1980). The width of the hysteresis can therefore be used as an indication of the quality of $((CH_3)_4N)_2CuCl_4$ crystals. It is clear that HAUP measurements on a $((CH_3)_4N)_2CuCl_4$ sample with a smaller thermal hysteresis are desirable. In this paper we report on such measurements.

The HAUP measurements of Uesu and Kobayashi (1985) showed, in addition, a rotation of the optical indicatrix in the incommensurate phase around the axis that is the unique axis in the first commensurate lock-in phase. Both the observation of a non-zero gyration and the rotation of the indicatrix imply that the point group symmetry of the incommensurate phase can not be mmm. The measurement of g_{13} was later repeated by Saito et al. (1990) and again a clearly non-zero result was obtained in the incommensurate phase. In this paper we also report on measurements of the gyration g_{13} of $((CH_3)_4N)_2CuCl_4$ for the same wavelength $\lambda = 632.8$ nm as used by Uesu and Kobayashi (1985). We wanted to repeat these measurements, because, contrary to the group of Kobayashi, we found that optical activity was too small to be detected in the case of $((CH_3)_4N)_2ZnCl_4$ (see Kremers et al., 1994a). For that case a controversy still exists.

Ortega et al. (1992) also performed HAUP measurements on $((CH_3)_4N)_2CuCl_4$ crystals. These authors measured the gyration tensor element g_{33}. The direction of light propagation is then parallel to the modulation wave vector. The gyration in the incommensurate phase was found to be smaller than the experimental error. The rotation of the optical indicatrix was not studied by these authors. Their measurements were performed at the wavelength $\lambda = 632.8$ nm, where dichroic effects can be neglected. We report on HAUP measurements of the gyration tensor element g_{33} both for that wavelength and for a wavelength near the absorption edge. Moreover, the rotation of the optical indicatrix and dichroic effects are studied.

This paper is organised in the following way. First, we describe the crystal structure for the successive phases of $((CH_3)_4N)_2CuCl_4$ in order to clarify the optical effects that can be expected. Then, the sample preparation is treated and the most important details of the measuring method are given. Subsequently, the interpretation of the measurements is discussed, because this is an essential part of the HAUP technique. After this, we present the obtained results, which are then discussed.

5.2 The crystal structure of $((CH_3)_4N)_2CuCl_4$ as a function of temperature

The four successive phases that occur in $((CH_3)_4N)_2CuCl_4$ upon changing the temperature are characterised in table 5.1. The temperatures T_i and T_c are those that we observe in our measurements. The value $T_i = 299$ K agrees with that of Ortega et al. (1992), though it is often claimed that $T_i = 297$ K. The high-temperature paraelastic phase (I) is centrosymmetric and orthorhombic ($|\boldsymbol{a}| = 15.155$ Å, $|\boldsymbol{b}| = 9.039$ Å and the pseudo-hexagonal axis $|\boldsymbol{c}| = 12.127$ Å). The gyration tensor is, therefore, necessarily zero and the indicatrix has a fixed orientation. The HAUP measurements in the paraelastic phase can, therefore, be used as a reference for the results in the incommensurate phase (II) and the lock-in phase (III).

Phase	IV	III	II	I
Temp (K)	$< 263 (= T_{c2})$	$< 292.4 (= T_c)$	$< 299 (= T_i)$	$> 299 (= T_i)$
Symmetry	$P112_1/n$	$P2_1/c11$	$Pcmn(00\gamma)(1s\bar{1})$?	Pcmn
γ	0	2/3	$(2+\delta)/3$	0
Type	ferroelastic	ferroelastic	incommensurate	paraelastic
Domain Walls	(100)	(001)		
System	Monocl.	Monocl.	Orthorh. ?	Orthorh.
Gyration Tensor $\boldsymbol{g}$	0	0	?	0
Indicatrix Rotation	around $\boldsymbol{c}$	around $\boldsymbol{a}$	?	none

Table 5.1 Successive phase transitions in $((CH_3)_4N)_2CuCl_4$. The parameter γ determines the modulation wave vector according to the relation $\boldsymbol{q} = \gamma \boldsymbol{c}^*$. It is important to note that the superspace group symmetry of the incommensurate phase has not been checked experimentally. The indicatrix rotation is given with respect to the orthorhombic structure of the paraelastic phase I.

Vlokh et al. (1988) showed by means of precise birefringence measurements that the modulation wave vector $\boldsymbol{q}$ shows some variation with temperature in the incommensurate phase (II). In the same paper, the authors showed that there is a large influence of (X-rays induced) defects on both the temperature behaviour of the modulation wave vector and on the value of T_c. The lock-in phase transition temperature T_c increases with the defect concentration. Therefore, one can state that the temperature width of the incommensurate phase is an indication of the quality of the crystal.

Below T_c the modulation wave vector of $((CH_3)_4N)_2CuCl_4$ locks in at $\boldsymbol{q} = \frac{2}{3}\boldsymbol{c}^*$. The crystal then has a three-fold superstructure. Ferroelastic domains are formed in this monoclinic lock-in phase with twin planes parallel to (001) (Sawada et al., 1980). The indicatrix can rotate up to approximately $4 \cdot 10^{-2}$ rad around the $\boldsymbol{a}$ axis in a single domain (Sugiyama et al., 1980). Although each of the domains is centrosymmetric it is still expected that the multi-domain state of the sample is optically active (Dijkstra et al. (1992), Kushnir and Vlokh (1993)).

A third phase transition takes place at $T_{c2} = 263$ K (Sugiyama et al., 1980). The value of γ becomes zero and the structure is monoclinic with the **c** axis as unique axis. The twin planes between the domains are parallel to (100). Again, each domain is centrosymmetric, but a multi-domain sample is expected to be optically active.

5.3 The Samples

The growth of good quality crystals is more difficult for $((CH_3)_4N)_2CuCl_4$ than for the related compound $((CH_3)_4N)_2ZnCl_4$. We have grown $((CH_3)_4N)_2CuCl_4$ crystals by the thermal convection method as described by Arend et al. (1986). The stoichiometric solution of $((CH_3)_4N)Cl$ and $CuCl_2$ in water has a dark green colour. If the thermal convection is too large, one can easily observe many solution inclusions in the orange crystals. According to our experience, nicely faceted, inclusion-free crystals of about 0.5 cm^3 can be grown in several months if a small thermal convection is used ($\Delta T = 1.5$K). With an optical goniometer it is easy to identify the natural crystal faces. The thus grown $((CH_3)_4N)_2CuCl_4$ crystals are often platelike with large (001) faces or they are extended along the **c**-direction and have large (110) and $(1\bar{1}0)$ faces. The (010) faces are usually very small, contrary to the (100) faces.

Sample Surface	Thickness z (mm)	Linear Birefringence Δn	Gyration $G(s) = g_{ij}s_is_j$
(001)	0.14	$\Delta n_{33} = n_b - n_a$	$G_{33} = g_{33}$
(101)	0.22	$\Delta n_{13} \approx 0.61(n_b - n_a) + 0.39(n_c - n_b)$	$G_{13} = 0.39g_{11} + 0.61g_{33} + 0.98g_{13}$

Table 5.2 The two samples of $((CH_3)_4N)_2CuCl_4$ used in the present experiments. n_a, n_b and n_c are the main refractive indices of the crystal. g is the gyration tensor and s is the unit wave vector of the incident light with respect to the crystallographic axes of the paraelastic phase.

From these crystals we have cut two platelets with a wire saw. One was parallel to the natural (001) face and the other was parallel to the (101) face. Both sides of these plates were polished on felt with diamond paste down to $\frac{1}{4}$ μm size. It was checked with a polarising microscope that both polished faces of each sample were plane-parallel. Due to the large linear birefringence one observes thickness changes of the sample as a change in colour of the transmitted light. Within the spot of the light beam the variation in thickness is less than 5 μm.

The linear birefringence and gyration of the two samples is given in table 5.2.

5.4 Measurements

All measurements have been performed with the HAUP apparatus built in our laboratory as described by Dijkstra et al. (1991). This original version of the apparatus appeared to be inadequate to perform reliable measurements and some essential improvements were, therefore, carried out (Kremers and Meekes, 1994b).

In table 5.3 an overview is given of the measurements that have been performed on the two samples. There were two reasons for performing the wavelength dependent HAUP measurements. As explained in the introduction, it is interesting to measure the optical properties of an incommensurately modulated crystal near an absorption edge as a function of temperature. The measurement as a function of the wavelength reveals the position of the absorption edge. In this way we found that $\lambda \approx 511$ nm is a good choice for the HAUP measurement near the absorption edge. Moreover, the value of the linear birefringence must be known at a certain combination of temperature and wavelength that is used in the measurement. This is necessary for the determination of the behaviour of the linear birefringence with changing temperature or wavelength. The temperature dependence of the linear birefringences Δn_{13} and Δn_{33} for the wavelength $\lambda = 632.8$ nm were given by, respectively, Saito et al. (1990) and Ortega et al. (1992). Using these values, the linear birefringences as a function of wavelength were derived at a constant temperature from the wavelength dependent HAUP measurement. Subsequently, the linear birefringence could be determined for the HAUP measurement at the wavelength $\lambda = 511$ nm.

Sample	Measurement I: λ dependence	Measurement II: T dependence	Measurement III: T dependence
(001)	T=296 K	$\lambda = 632.8$ nm	$\lambda = 511$ nm
(101)	T=296.8 K	$\lambda = 632.8$ nm	$\lambda = 511$ nm

Table 5.3 Specification of the three HAUP measurements that have been performed on each of the two samples.

At least two extinction directions (Kremers and Meekes, 1994b) were measured in each of the performed HAUP experiments. This is necessary for the separation of circular dichroism from indicatrix rotation (see also Kremers and Meekes, 1994c). Both of these effects are of interest. The temperature was left to stabilise for about half an hour after each change of its value. In case of shorter stabilisation times it was sometimes observed that, for example, the optical activity showed a definite change with temperature in the paraelastic phase. Optical activity is, however, symmetry forbidden in this phase. After a temperature stabilisation of about half an hour the results of the measurements were as expected.

5.5 Interpretation of the measurements

In a HAUP experiment first the position Θ_0 of an extinction direction is determined with respect to an arbitrary, but fixed, origin. In our case, we rotate both polarisers to a position of minimal intensity, while keeping them crossed. Subsequently, intensities are measured at different polariser positions. The angle Θ of the polariser, measured with respect to Θ_0, is kept within $2 \cdot 10^{-2}$ rad. Also the angle Y of the analyser, measured with respect to the crossed polarisers position, is kept within the same small range. This allows for the fitting of the measured intensities to the so-called HAUP intensity formula. Recently, we have derived a unified formula for absorbing crystals (Kremers and Meekes, 1994c). For the case that we consider here this formula reduces to:

$$\Gamma/\Gamma_0 = \exp\left(-2\tilde{\kappa}\frac{2\pi z}{\lambda}\right) \begin{pmatrix} 1 & Y & Y^2 \end{pmatrix} C^{\Theta_0}_{(3\times3)} \begin{pmatrix} 1 \\ \Theta \\ \Theta^2 \end{pmatrix}, \tag{5.1}$$

with

$$\begin{aligned}
C^{\Theta_0}_{21} &= -(2k + (p-a))\sin(\frac{2\pi z}{\lambda}\Delta n) + 2\delta Y\cos^2(\frac{\pi z}{\lambda}\Delta n) + \frac{2\pi z}{\lambda}\Delta\kappa(p+a)\cot(\frac{\pi z}{\lambda}\Delta n) \\
C^{\Theta_0}_{12} &= 0 \\
C^{\Theta_0}_{22} &= 2\exp\left(\frac{2\pi z}{\lambda}\Delta\kappa\right) - 2\cos(\frac{2\pi z}{\lambda}\Delta n) \\
C^{\Theta_0}_{31} &= \exp\left(\frac{2\pi z}{\lambda}\Delta\kappa\right) \\
C^{\Theta_0}_{13} &= 2\left(\cosh(\frac{2\pi z}{\lambda}\Delta\kappa) - \cos(\frac{2\pi z}{\lambda}\Delta n)\right)
\end{aligned} \tag{5.2}$$

and z is the thickness of the sample platelet. All other coefficients $C^{\Theta_0}_{ij}$ are zero, except for $C^{\Theta_0}_{11}$. This term has not been worked out specifically, because it is not used to extract optical parameters from the measurement. The expression for Θ_0, defining the position of the extinction direction, is:

$$\Theta_0 = -\frac{1}{2}\delta Y + \frac{1}{2}(p+a)\cot(\frac{2\pi z}{\lambda}\Delta n) - k' + \delta\Theta_{\text{indicatrix}}. \tag{5.3}$$

Here, $\Delta n = n_1 - n_2$ is the *linear birefringence* and $\Delta\kappa = \kappa_1 - \kappa_2$ is the *linear dichroism*. The *circular birefringence* $n_r - n_l$ is related to the parameter k:

$$k = \frac{n_r - n_l}{2\Delta n} \tag{5.4}$$

and the *circular dichroism* $\kappa_r - \kappa_l$ is related to k':

$$k' = \frac{\kappa_r - \kappa_l}{2\Delta n}. \tag{5.5}$$

The gyration G and the circular birefringence are related in the following way:

$$n_r - n_l = \frac{G}{\tilde{n}}, \tag{5.6}$$

where $\bar{n}$ is the average of the two refractive indices n_1 and n_2 that determine the linear birefringence. In the same way, $\bar{\kappa}$ in equation (5.1) is the average of the two extinction coefficients κ_1 and κ_2 that determine the linear dichroism. The parameter $\delta\Theta_{\mathrm{indicatrix}}$ in equation (5.3) describes the rotation of the optical indicatrix. Note, that in the expressions for $C_{21}^{\Theta_0}$ and Θ_0 the linear dichroism has been considered to be small with respect to the linear birefringence.

In the fit of the intensities to the HAUP intensity formula both the so-called ΔY-correction and the $\Delta\Theta$-correction are performed (Kremers and Meekes, 1994b). By means of the ΔY-correction the contribution of the systematic error δY is reduced to a large extent. The $\Delta\Theta$-correction improves the values of all fitting-parameters C_{ij} and gives a correction to the value of Θ_0.

Besides δY two other systematic errors, p and a, must be extracted from the fitting-parameters in order to determine the circular birefringence, the circular dichroism and the indicatrix rotation. The linear birefringence and the linear dichroism can be calculated without a knowledge of the systematic errors. The errors p and a describe the parasitic ellipticities of the light polarised by, respectively, the polariser and the analyser. In short, the systematic errors are extracted by studying the fitting-parameters as a function of temperature (or wavelength) in a region of small linear dichroism where there is no circular birefringence, no circular dichroism and no indicatrix rotation. In the case of $((CH_3)_4N)_2CuCl_4$ we use for this the orthorhombic and centrosymmetric paraelastic phase. The value of δY is found as the slope of a straight line fitted to a plot of $C_{21}^{\Theta_0}/\sin\left(\frac{2\pi z}{\lambda}\Delta n\right)$ against $\cot\left(\frac{\pi z}{\lambda}\Delta n\right)$. The value of $p+a$ is obtained in the same way by plotting Θ_0 against $\cot\left(\frac{\pi z}{\lambda}\Delta n\right)$. We take the value of $p-a$ such that the average value of k becomes zero in the centrosymmetric paraelastic phase. If the systematic errors are known, one can calculate the optical properties of the sample from the fitting-parameters. For a detailed description of the used procedure we refer to Kremers and Meekes (1994b)(1994c).

5.6 Results

5.6.1 Sample quality

All temperature dependent measurements were performed by cooling down from the paraelastic phase (I) to the lock-in phase (III). For the (101) sample and the wavelength $\lambda = 632.8$ nm we subsequently performed an additional measurement by increasing the temperature. The corresponding behaviour of the fitting-parameter C_{21} is plotted in figure 5.1. It shows a sharp change at the phase transition temperature $T_c = 292.4$ K. The thermal hysteresis (about 0.6 K) at this phase transition is very small with respect to the sometimes observed values of 10 K. Moreover, the temperature width of the incommensurate phase, here 6.6 K, is as can be expected for a crystal with a very low defect concentration (Vlokh et al., 1988). We conclude, therefore, that our $((CH_3)_4N)_2CuCl_4$

crystals are of very good quality.

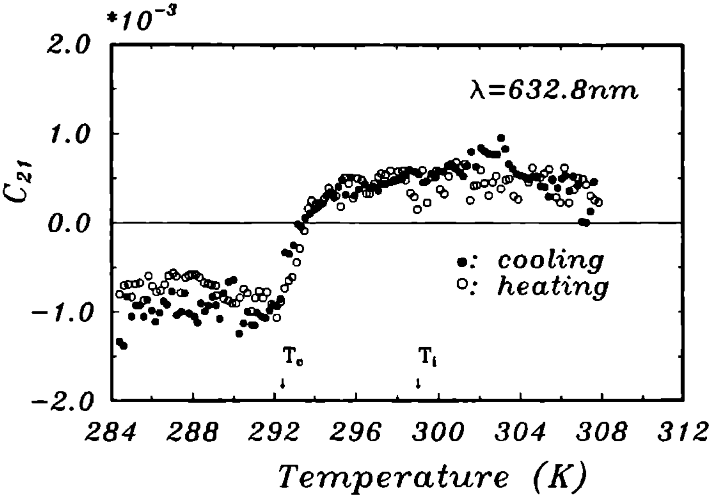

Figure 5.1 The fitting-parameter C_{21} for the (101) sample and a wavelength $\lambda = 632.8$ nm. A very small thermal hysteresis is observed at T_c. The values of T_i and T_c have been derived from the results for the linear birefringence, which are presented further on.

5.6.2 The linear birefringence Δn_{33} and the linear dichroism $\Delta\kappa_{33}$

In figure 5.2 the linear birefringence Δn_{33} is shown as found for the wavelength $\lambda = 632.8$ nm. There is a reasonable agreement with the results of Ortega et al. (1992), although our values are about 2 % lower. This may be caused by an inaccurate measurement of the sample thickness. In order to derive the linear birefringence from a HAUP experiment it is necessary to know its value for a single value of the parameter (e.g. temperature, wavelength) that is varied during the measurement.

The result of figure 5.2 has been used, therefore, to derive the wavelength dependence of the linear birefringence at the temperature T = 296 K from the corresponding HAUP measurement. The results are given in figure 5.3. Thus, it can be seen by extrapolation that the value of Δn_{33}(T = 296 K, λ = 632.8 nm) agrees between the results of figures 5.2 and 5.3.

The temperature dependence of the linear birefringence at a wavelength $\lambda = 511$ nm is given in figure 5.4. This has been done in such a way that it gives the best agreement with the data in figure 5.3 at $\lambda = 511$ nm. Both phase transitions at T_i and T_c can clearly be observed. The linear birefringence Δn_{33} shows a discontinuity at $T_c = 292.4$ K.

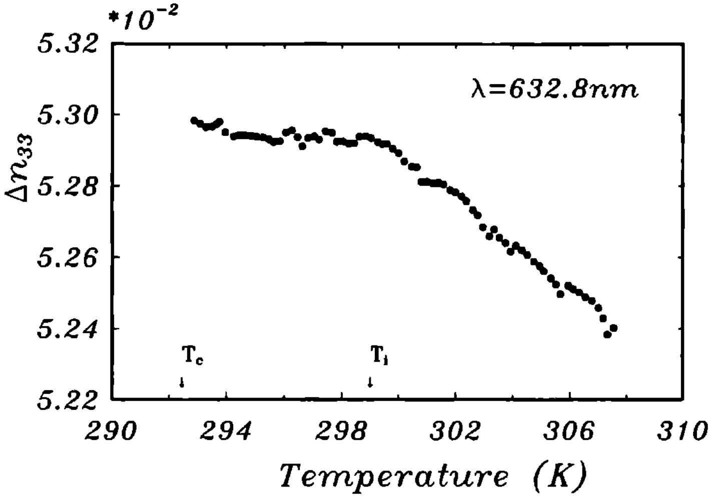

Figure 5.2 The linear birefringence Δn_{33} as a function of temperature in the paraelastic and incommensurate phase of $((CH_3)_4N)_2CuCl_4$ The wavelength of the light is $\lambda = 632.8$ nm

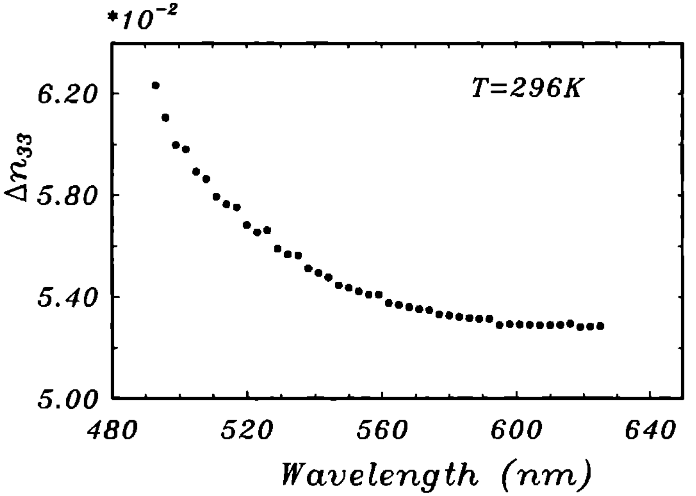

Figure 5.3 The linear birefringence Δn_{33} of $((CH_3)_4N)_2CuCl_4$ as a function of the wavelength λ of the light at the temperature T = 296 K The discontinuities in this figure are a result of the fact that HAUP gives inaccurate results whenever $\sin\left(\frac{\pi z}{\lambda}\Delta n\right) = 0$

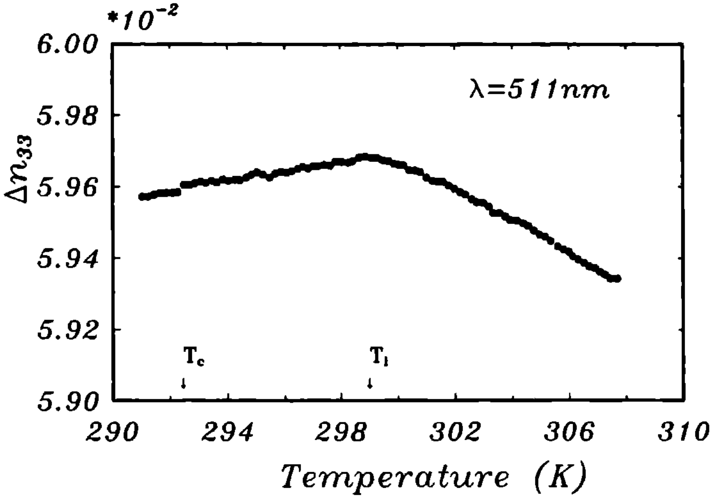

Figure 5.4 The linear birefringence Δn_{33} of $((CH_3)_4N)_2CuCl_4$ as a function of temperature in the paraelastic, incommensurate and (partly) in the first lock-in phase of $((CH_3)_4N)_2CuCl_4$. The wavelength of the light is 511 nm

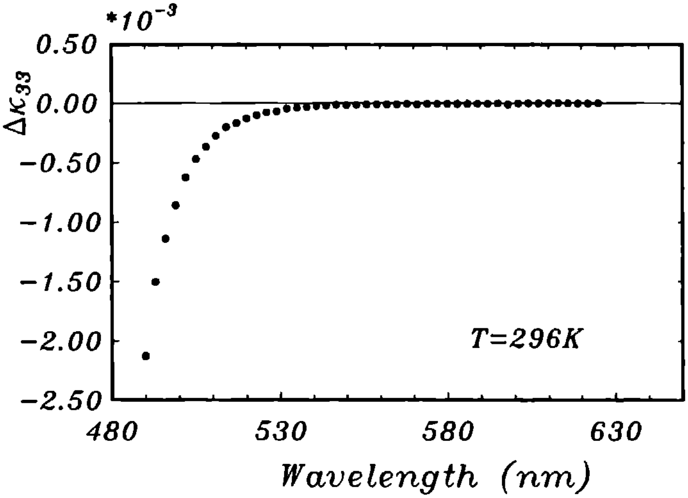

Figure 5.5 The linear dichroism $\Delta\kappa_{33}$ of $((CH_3)_4N)_2CuCl_4$ as a function of the wavelength λ of the light The temperature is T = 296 K

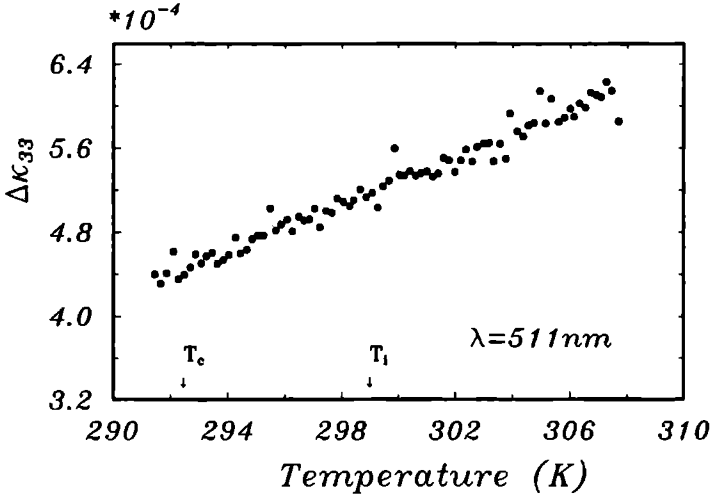

Figure 5.6 The linear dichroism $\Delta\kappa_{33}$ of $((CH_3)_4N)_2CuCl_4$ as a function of the temperature. The wavelength of the light is $\lambda = 511$ nm.

It is interesting to see that the linear birefringence has a smoother behaviour in the paraelastic phase for the measurements in figure 5.4 than those in figure 5.2, although both figures are for the same sample. This difference may be related to the thermal history of the sample. The choice for the measurement at the wavelength $\lambda = 511$ nm was made by considering the wavelength dependence of the linear dichroism, which is presented in figure 5.5. For wavelengths larger than 570 nm the linear dichroism $\Delta\kappa_{33}$ is negligible. The linear dichroism shows a sharp increase at the absorption edge. It was impossible to measure at wavelengths smaller than $\lambda = 490$ nm, because the light was absorbed too strongly there. At $\lambda = 511$ nm the linear dichroism is clearly non-zero. On the other hand it is still small with respect to the linear birefringence. Therefore, the HAUP intensity formula (5.2) can be used for the interpretation of the measurements. It was explained in the introduction that the temperature dependence of the linear dichroism $\Delta\kappa_{33}$ for such a wavelength near the absorption edge could be sensitive to the incommensurate modulation. The result is shown in figure 5.6. Unfortunately, only a linear decrease of $\Delta\kappa_{33}$ is seen with decreasing temperature. Even at the phase transition temperatures T_i and T_c no structure is observed. The sign of $\Delta\kappa_{33}$ is different in figure 5.6 than in figure 5.5. This is caused by the fact that the, arbitrarily chosen, first extinction direction differed by $\frac{1}{2}\pi$ between these measurements.

5.6.3 The linear birefringence Δn_{13} and the linear dichroism $\Delta\kappa_{13}$

In the figures 5.7 and 5.8 we show the temperature dependence of the linear birefringence Δn_{13} at, respectively, λ = 632 8 nm and λ = 511 nm. Both are in good agreement with the wavelength dependence of the linear birefringence Δn_{13}, which is presented in figure 5.9, at the temperature T = 296.8 K. The temperature dependence of Δn_{13} is in reasonable agreement with the results of Saito et al. (1990), although our values are, also for this case, about 2 % lower. It is interesting that at T $\approx$ 305 K a clear change in slope is observed for both wavelengths used. The reason for this change is unclear to us. Moreover, the linear birefringence Δn_{33} in the figures 5.2 and 5.4 do not show a change of slope at this temperature.

In figure 5.10 we present the wavelength dependence of the linear dichroism $\Delta\kappa_{13}$ at the temperature T = 296.8 K. Again, it is seen that at λ = 511 nm a clearly non-zero linear dichroism is present that is still small with respect to the linear birefringence. The result for the temperature dependence of the linear dichroism $\Delta\kappa_{13}$ at this wavelength is plotted in figure 5.11. Also in this case, only a linear dependence on temperature is observed with no structure at the phase transitions. The temperature dependence of $\Delta\kappa_{33}$ is larger than that of $\Delta\kappa_{13}$.

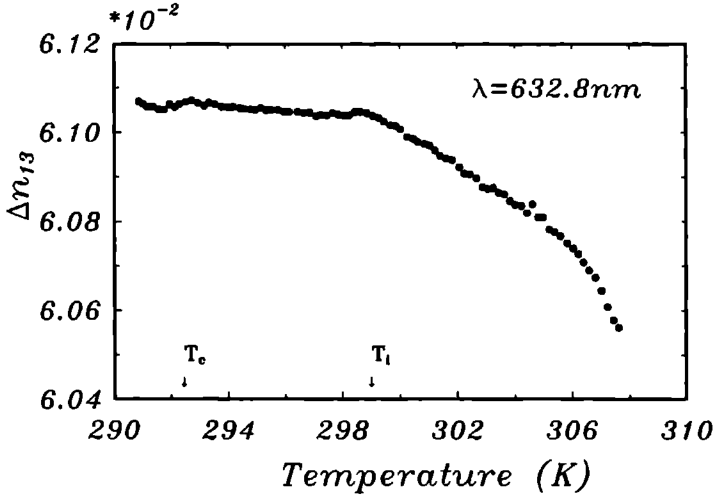

Figure 5.7 The linear birefringence Δn_{13} of $((CH_3)_4N)_2CuCl_4$ as a function of temperature in the paraelastic, incommensurate and (partly) in the first lock-in phase of $((CH_3)_4N)_2CuCl_4$ The wavelength of the light is λ = 632 8 nm

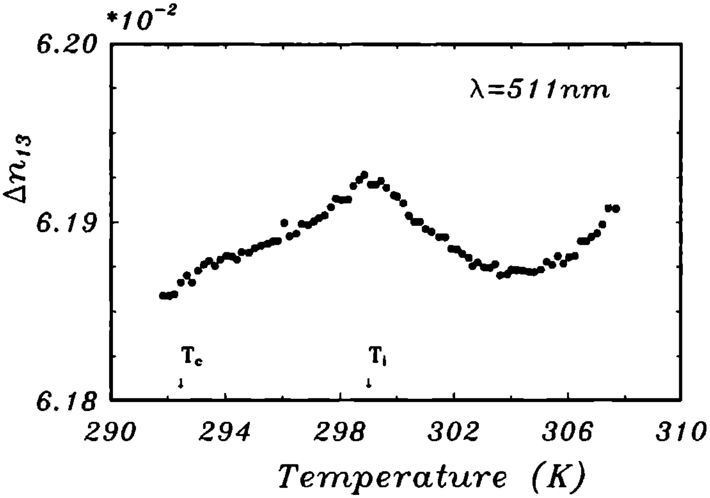

Figure 5.8 The linear birefringence Δn_{13} of $((CH_3)_4N)_2CuCl_4$ as a function of temperature in the paraelastic, incommensurate and (partly) in the first lock-in phase of $((CH_3)_4N)_2CuCl_4$. The wavelength of the light is 511 nm.

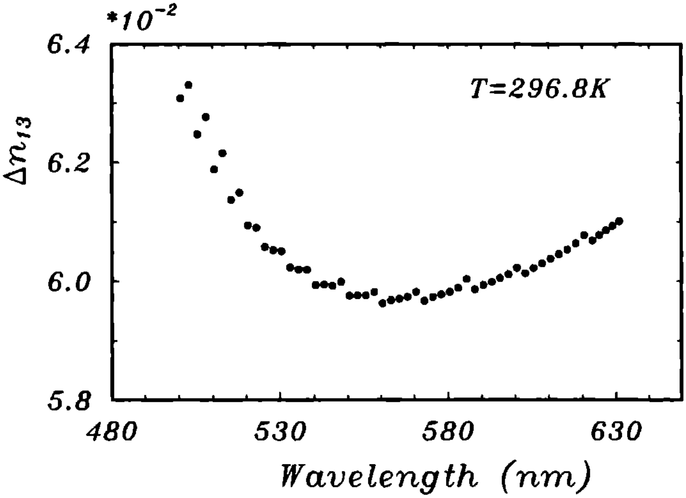

Figure 5.9 The linear birefringence Δn_{13} of $((CH_3)_4N)_2CuCl_4$ as a function of the wavelength λ of the light at the temperature T = 296.8 K.

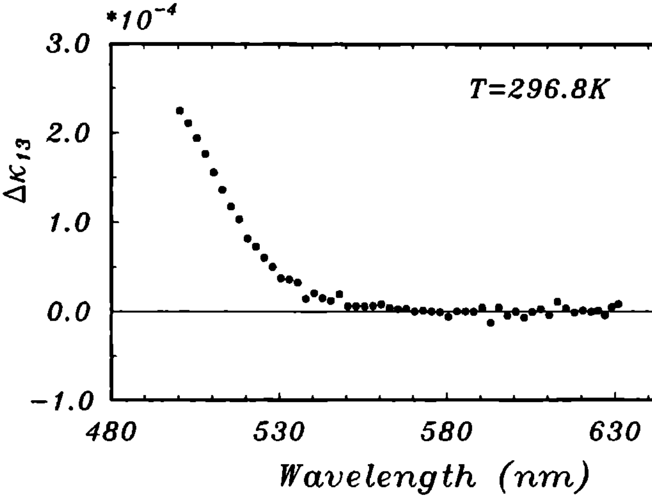

Figure 5.10 The linear dichroism $\Delta\kappa_{13}$ of $((CH_3)_4N)_2CuCl_4$ as a function of the wavelength λ of the light. The temperature is T = 296.8 K.

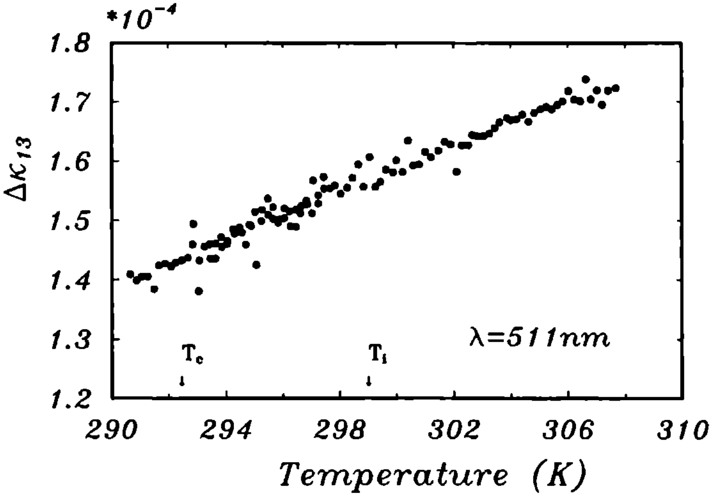

Figure 5.11 The linear dichroism $\Delta\kappa_{13}$ of $((CH_3)_4N)_2CuCl_4$ as a function of the temperature. The wavelength of the light is λ = 511 nm.

5.6.4 Optical Activity

As expressed by equation (5.4), the circular birefringence $n_r - n_l$ is determined by the ellipticity k and the linear birefringence. In the figures 5.12 and 5.13 the temperature dependence of k is presented for the (001) sample.

In case of the measurement with $\lambda = 632.8$ nm, figure 5.12, we observe that $|k| < 1.5 \cdot 10^{-4}$ for the majority of points. Moreover, the results scatter around zero in both the paraelastic and the incommensurate phase. These results agree with those of Ortega et al. (1992). We have to conclude that the gyration G_{33} in the incommensurate phase is zero or too small to be detected at the wavelength $\lambda = 632.8$ nm. It has been explained in the introduction, though, that optical activity, if present, may be more pronounced for wavelengths near the absorption edge. The results for the corresponding measurement using $\lambda = 511$ nm, figure 5.13, show that $|k| < 1 \cdot 10^{-4}$ for nearly all points. It is, therefore, not possible to detect optical activity G_{33} in the incommensurate phase, even not for this wavelength.

Nevertheless, a non-zero gyration G_{13}, measured with HAUP, has been reported by both Uesu and Kobayashi (1985) and Saito et al. (1990). In figure 5.14 we show our results for the same wavelength, $\lambda = 632.8$ nm, as used by these authors. In general, the value of $|k|$ is smaller than $1 \cdot 10^{-4}$ for temperatures higher than T = 295 K. Nevertheless, a systematic deviation from zero is observed. Below T = 295 K a clear onset of the gyration G_{13} is observed. Moreover, the ferroelastic phase III shows a large gyration, $k \approx -8 \cdot 10^{-4}$, though this phase is centrosymmetric. In our opinion, this effect is inevitable, because the sample enters a multi-domain state. The gyration is a result of the change in orientation of the optical indicatrix from one domain to the next. Our results are clearly different from those obtained by Uesu and Kobayashi (1985) and Saito et al. (1990). This difference is addressed in the discussion.

The ellipticity k at the wavelength $\lambda = 511$ nm near the absorption edge for the same (101) sample has been plotted in figure 5.15. The open circles are the results obtained for a measurement with a stabilisation time of only 15 minutes at each temperature. The ellipticity k is, then, not even constant in the centrosymmetric paraelastic phase. Therefore, we have used a stabilisation time of about 30 minutes for all temperature dependent measurements. The thus obtained results are represented by the full circles. Again, it is observed that at a temperature T = 295 K there is an onset of gyration G_{13} in the incommensurate phase.

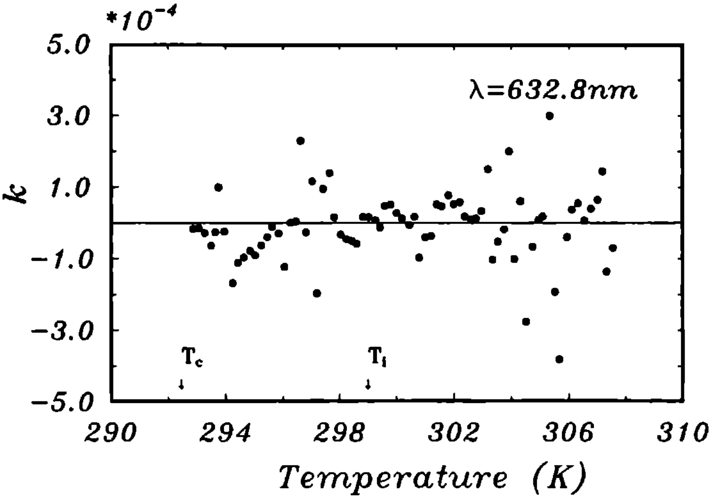

Figure 5.12 The ellipticity $k = \frac{n_r - n_l}{2\Delta n}$ for the (001) sample of $((CH_3)_4N)_2CuCl_4$ as a function of temperature. The wavelength of the light is $\lambda = 632.8$ nm.

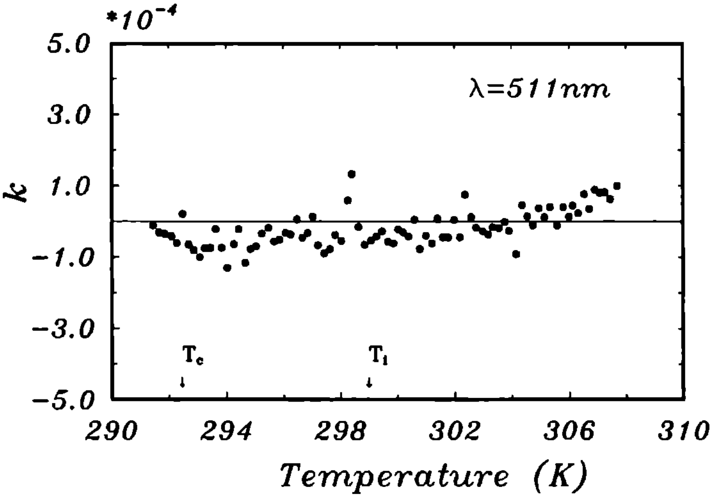

Figure 5.13 The ellipticity $k = \frac{n_r - n_l}{2\Delta n}$ for the (001) sample of $((CH_3)_4N)_2CuCl_4$ as a function of temperature. The wavelength of the light is $\lambda = 511$ nm.

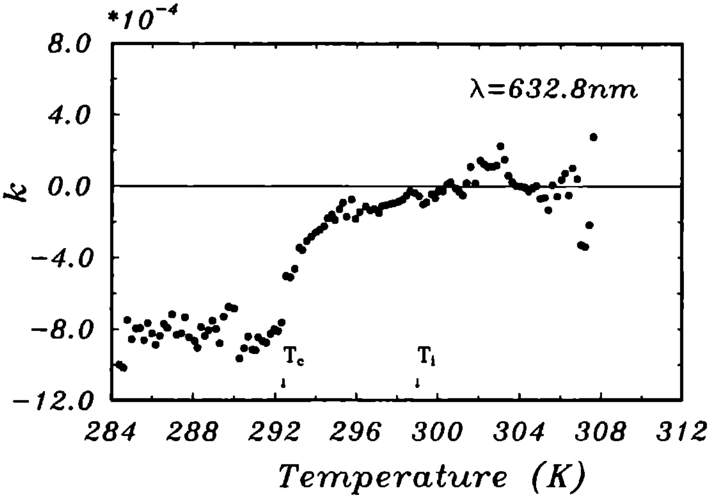

Figure 5.14 The ellipticity $k = \frac{n_r - n_l}{2\Delta n}$ for the (101) sample of $((CH_3)_4N)_2CuCl_4$ as a function of temperature. The wavelength of the light is $\lambda = 632.8$ nm.

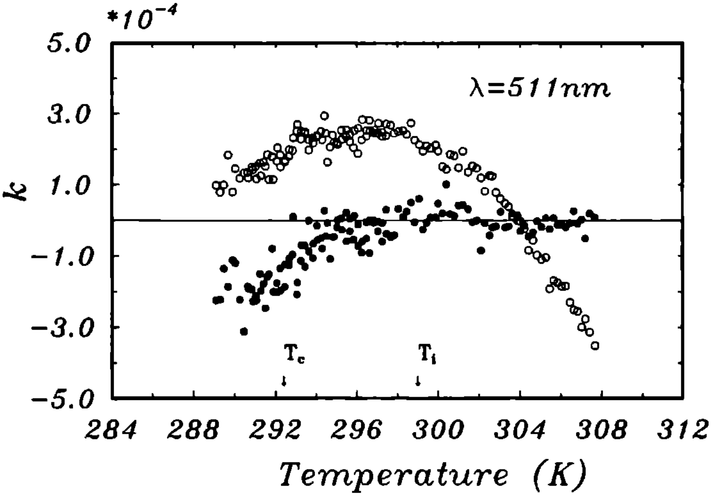

Figure 5.15 The ellipticity $k = \frac{n_r - n_l}{2\Delta n}$ for the (101) sample of $((CH_3)_4N)_2CuCl_4$ as a function of temperature. The wavelength of the light is $\lambda = 511$ nm. The open circles give the result with a temperature stabilisation of 15 minutes. The full circles represent the results obtained with a stabilisation time of 30 minutes.

5.6.5 The circular dichroism and indicatrix rotation

In order to calculate the circular dichroism and the indicatrix rotation one must measure two extinction directions. After the determination of the systematic errors separately for both extinction directions and the linear birefringence one subtracts the contribution $-\frac{1}{2}\delta Y + \frac{1}{2}(p+a)\cot\left(\frac{\pi z}{\lambda}\Delta n\right)$ from the measured values of Θ_0. In addition, an amount of $\frac{1}{2}\pi$ is subtracted from Θ_0 for the second extinction direction. The resulting values are plotted in figure 5.16 for the temperature dependent measurement of the (001) sample at the wavelength $\lambda = 511$ nm.

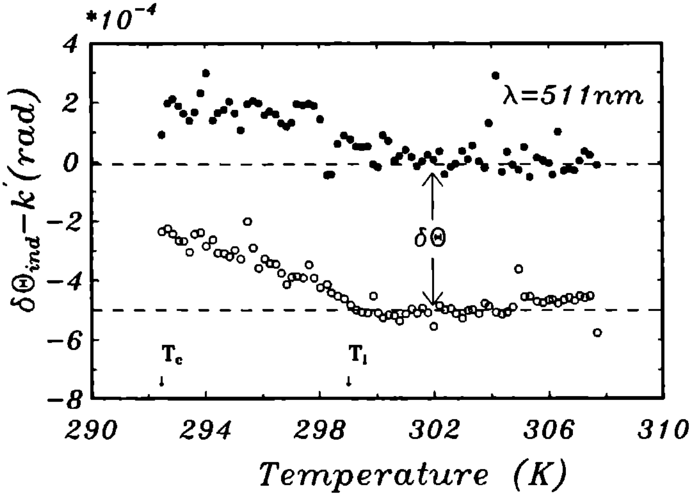

Figure 5.16 The values of $\delta\Theta_{\mathrm{ind}} - k'$ for the two extinction directions as obtained for the measurement on the (001) sample. The wavelength of the light is $\lambda = 511$ nm.

The paraelastic phase is orthorhombic and centrosymmetric. Therefore, there can be no indicatrix rotation and no circular dichroism in this phase. The curves in figure 5.16 should coincide, therefore. Nevertheless, there is a difference caused by the so-called $\delta\Theta$-error (Kremers and Meekes, 1994c). For this measurement $\delta\Theta = 5.57 \cdot 10^{-4}$ rad.

Both curves in figure 5.16 show the expected constant behaviour in the paraelastic phase. At T_i, however, there is a deviation from this behaviour. This can be caused by both circular dichroism and indicatrix rotation. These effects can, however, be separated, because the circular dichroism has different signs for both extinction directions, whereas the indicatrix rotation has equal signs (Kremers and Meekes, 1994c).

In figure 5.17 we present the thus obtained values of the indicatrix rotation $\delta\Theta_{\mathrm{indicatrix}}$. There is no absolute scale on the ordinate axis, because the Θ_0 values are measured with respect to an arbitrary origin. Nevertheless, a definite rotation of the optical indicatrix is observed in the incommensurate phase with a maximum of about $2 \cdot 10^{-4}$ rad.

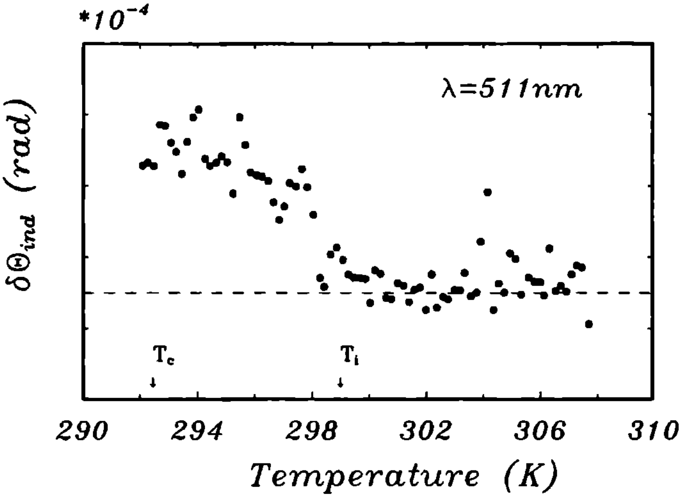

Figure 5.17 Rotation of the optical indicatrix in the (001) sample for the wavelength λ = 511 nm. The distance between tick marks on the ordinate axis equals $1 \cdot 10^{-4}$. There is no absolute scale, because Θ_0 can only be measured with respect to an arbitrary origin.

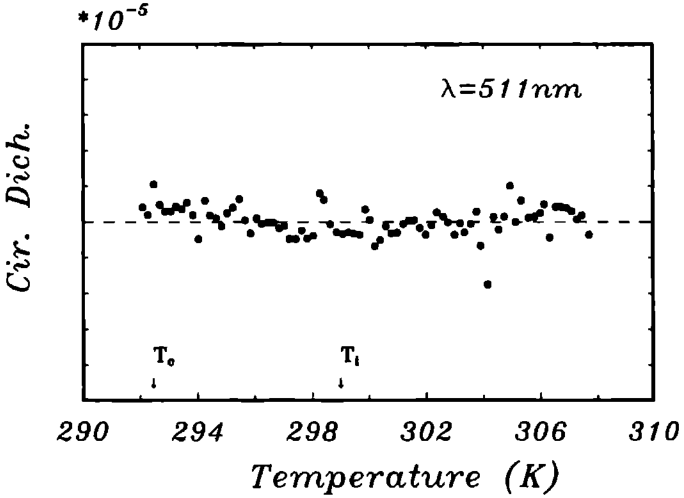

Figure 5.18 The circular dichroism $\kappa_r - \kappa_l$ of the (001) sample for the wavelength λ = 511 nm. The distance between tick marks on the ordinate axis equals $1 \cdot 10^{-5}$.

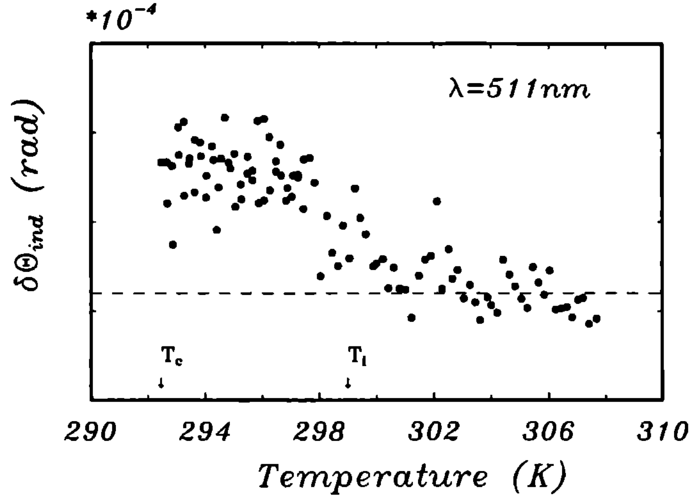

Figure 5.19 Rotation of the optical indicatrix in the (101) sample for the wavelength $\lambda =$ 511 nm. The distance between tick marks on the ordinate axis equals $1 \cdot 10^{-4}$.

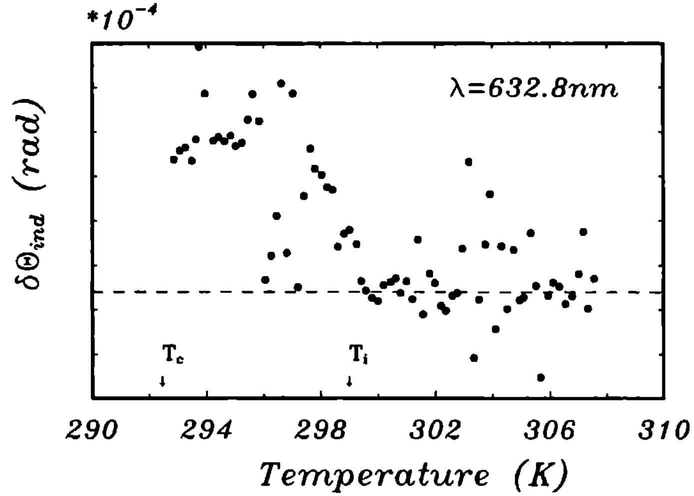

Figure 5.20 Rotation of the optical indicatrix in the (001) sample for the wavelength $\lambda =$ 632.8 nm. The distance between tick marks on the ordinate axis equals $1 \cdot 10^{-4}$.

The circular dichroism is obtained by taking the difference of the two curves in figure 5.16 and multiplying the result with $2\Delta n$ according to equation (5.5). The thus obtained values are plotted in figure 5.18. It is seen that, with respect to the experimental error, there is no detectable circular dichroism in the incommensurate phase. The same conclusion had to be drawn for all other measurements. A rotation of the indicatrix, however, was observed in all cases, having the same order of magnitude. We have plotted the corresponding results in the figures 5.19 and 5.20. The result for the (101) sample at the wavelength $\lambda = 632.8$ nm has not been given, because the value of $\delta\Theta_{\mathbf{indicatrix}}$ was not constant in the paraelastic phase. The reason for this is, at present, unclear to us.

5.7 Discussion and Conclusions

The measurements in this paper have been performed in order to search for optical effects in the incommensurate phase of $((CH_3)_4N)_2CuCl_4$ that are not allowed by the symmetry of the average structure. The temperature dependence of the optical effects has been studied for $\lambda = 632.8$ nm and $\lambda = 511$ nm. The latter wavelength is near the absorption edge. A sample platelet parallel to (001) and one parallel to (101) have been used for the investigations. We used the recently extended HAUP method (Kremers and Meekes, 1994c). Also dichroic effects could, therefore, be measured reliably simultaneously with the other effects.

Only a very small thermal hysteresis at T_c was observed in our samples. This, together with the width of the incommensurate phase, indicates that the samples were of high quality. It has been found, that a temperature stabilisation time of about 30 minutes is sufficient to give reliable results for all measurements.

The measured values of the linear birefringence were found to be in reasonable agreement with those of other authors. In addition, an unexplained change in the linear birefringence Δn_{13} has been observed at $T \approx 305$ K in the paraelastic phase. The phase transition from this phase to the incommensurate phase is clearly revealed by the linear birefringence. The phase transition temperature that we observed was $T_i = 299(\pm 0.25)$ K. It is unclear to us why this value disagrees with the often reported value $T_i = 297$ K. The measured linear birefringence showed typical structures in the incommensurate phase. This agrees with the results of Vlokh et al. (1988), who concluded that the modulation wave vector must show a variation with temperature in this phase. The first order character of the phase transition from the incommensurate to the first ferroelastic lock-in phase showed up as a discontinuity in the linear birefringence at the phase transition temperature.

In advance, it was expected that the influence of the incommensurate modulation on the $[CuCl_4]^{2-}$ tetrahedra would be reflected by the temperature dependence of the linear dichroism $\Delta\kappa$. However, both $\Delta\kappa_{13}$ and $\Delta\kappa_{33}$ only showed a linear dependence on the temperature. Even at the phase transition temperatures the linear dichroism was structureless. Also the circular dichroism was measured, but in all cases it was zero, or too small to be detected.

The measured gyration G_{33} agrees with the results of Ortega et al. (1992) for the wavelength $\lambda = 632.8$ nm. It is zero or too small to be detected. We have checked whether the gyration G_{33}, if non-zero, could be enhanced for a wavelength near an absorption edge, $\lambda = 511$ nm. However, also for this wavelength it was impossible to detect any gyration.

In addition, we have measured the gyration G_{13} at two different wavelengths, because a clearly non-zero G_{13} in the incommensurate phase was reported by Uesu and Kobayashi (1985) and Saito et al. (1990). These authors find a zero gyration in the first lock-in phase. In our measurements, however, a non-zero gyration was found in this phase. We believe that this is a result of the multi-domain state of the sample, which is difficult to avoid without applying external forces. Also the behaviour with temperature of the gyration G_{13} that we measured in the incommensurate phase clearly differs from the results of Uesu and Kobayashi (1985) and Saito et al. (1990). These authors find a gyration G_{13} that starts deviating from zero below T_i. It becomes maximal halfway the incommensurate phase and then decreases, until it is zero at T_c. In our case, however, the gyration is very small for temperatures above T = 295 K and a steady increase is observed below this temperature. This was found for both wavelengths used. The reason for a non-zero gyration in the incommensurate phase may be found in a symmetry breaking caused by the incommensurate modulation with respect to the average centrosymmetric structure. It is, however, important to realise that also a coexistence of commensurate and incommensurate domains is often observed in the incommensurate phase (see for example Hedoux et al., 1989). The observed gyration in the incommensurate phase can then be attributed to a steady increase of the number of commensurate domains until only commensurate domains are left at T_c. From our measurements of the linear birefringence, and also those of others (see for example Vlokh et al., 1988), it is expected that the (length of the) modulation wave vector is not constant in the incommensurate phase. Unfortunately, the exact behaviour of the modulation wave vector $\boldsymbol{q}$ has not been measured very accurately by means of diffraction experiments. Moreover, the superspace group has not yet been determined experimentally, as far as we know. It is, therefore, even not certain that the average structure of the incommensurate phase is centrosymmetric and orthorhombic. It is clear that a very careful, temperature dependent investigation of the incommensurate phase of $((CH_3)_4N)_2CuCl_4$ by means of X-ray diffraction would be of great help in the interpretation of our results. This may be a topic of further research.

Finally, we discuss the observed rotation of the optical indicatrix in the incommensurate phase that contradicts an orthorhombic symmetry. Contrary to the results of Uesu and Kobayashi (1985) we have detected a rotation around the c-axis of about $2 \cdot 10^{-4}$ rad in the incommensurate phase. There is no indicatrix rotation in the paraelastic phase. According to the analysis presented by Meekes and Janner (1988), a long wavelength Fourier component of the dielectric tensor with wave vector $\boldsymbol{h} = l\boldsymbol{c}^* + m\boldsymbol{q}$ and l, m both odd, can give rise to such a rotation if the superspace group is Pcmn$(00\gamma)(1s\bar{1})$. In case that also wave vectors $\boldsymbol{h}$ with l even and m odd are important, a rotation around the

$\boldsymbol{a}$-axis can be expected. Unfortunately, the orientation of our samples was not suited for identifying this rotation. Uesu and Kobayashi (1985) did observe a rotation of about $5 \cdot 10^{-3}$ rad around the $\boldsymbol{a}$-axis, however none around the $\boldsymbol{b}$- or $\boldsymbol{c}$-axes. Unfortunately, their sample showed a very large thermal hysteresis, contrary to our samples. It is not unlikely that this hysteresis is related to the behaviour of the modulation wave vector. Therefore, we think that it is difficult to compare the results.

At present, it is still unclear if the different results that are obtained by different authors are caused by differences in the (quality) of the samples or by the method of measurement. We would like to suggest, therefore, that a specific set of samples of incommensurately modulated crystals are measured by different groups that work in this field. Moreover, the quality of these samples should be checked by means of additional measurements.

5.8 Acknowledgments

We would like to acknowledge Prof. Dr. P. Bennema, Prof. Dr. T. Janssen and Prof. Dr. A. Janner for their support and contributions. This work is part of the research program of the Stichting voor Fundamenteel Onderzoek der Materie (Foundation for Fundamental Research on Matter).

References

Agranovich, V. M., and Ginzburg, V. L., *Crystal Optics with Spatial Dispersion, and Excitons* (Berlin: Springer-Verlag, 1974).

Arend, H., Perret, F., Wüest, H. and Kerkoc, P., *Journ. of Cryst. Growth* **74**, 321 (1986).

Blokh, O. G., Dutsyak, G. Z., Kityk, A. V., and Kityk, I. V., *Journal of Applied Spectroscopy* **53**, 746 (1990).

Clay, R., Murray-Rust, J., and Murray-Rust, P., *Acta Crystallogr.* B**31**, 289 (1975).

Dijkstra, E., Meekes, H. and Kremers, M., *J. Phys. D: Appl. Phys* **24**, 1861 (1991).

Dijkstra, E., Janner, A., and Meekes, H., *J. Phys.: Condens. Matter* **4**, 693 (1992).

Gesi, K., and Iizumi, M., *J. Phys. Soc. Japan* **48**, 1775 (1980).

Hamano, K., Ikeda, Y., Fujimoto, T., Ema, K., and Hirotsu, S., *J. Phys. Soc. Japan* **49**, 2278 (1980).

Hedoux, A., Grebille, D., Lefebvre, J., and Perret, R., *Phase transitions* **14**, 177 (1989).

Hogervorst, A. C. R., *Comparative study of the modulated structures in Rb_2ZnCl_4 and in related compounds*, Ph.D. thesis Delft (1986).

Janner, A., Janssen, T., and de Wolff, P. M., *Acta Cryst. A* **39**, 671 (1983).

Janner, A., and Janssen, T., *Phys. Rev. B* **15**, 643 (1977).

Janssen, T., *Ferroelectrics* **66**, 203 (1986).

Kobayashi, J. and Uesu, Y., *J. Appl. Cryst.* **16**, 204 (1983).

Kremers, M., Dijkstra, E., and Meekes, H., *submitted to Phys. Rev.* (1994a).

Kremers, M., and Meekes, H., *submitted to J. Phys. D: Appl. Phys* (1994b).

Kremers, M., and Meekes, H., *submitted to J. Phys. D: Appl. Phys* (1994c).

Kushnir, O. S., and Vlokh, O. G. *J. Phys.: Condens. Matter* **5**, 7017 (1993).

Madariaga, G., Zúñiga, F.J., Paciorek, W. A., and Bocanegra, E. H., *Acta Cryst.* B**46**, 620 (1990).

Meekes, H. and Janner, A., *Phys. Rev. B* **38**, 8075 (1988).

Morosin, B., and Lingafelter, E. C., *J. Phys. Chem.* **65**, 50 (1961).

Nye, J. F., *Physical properties of crystals* (Oxford: Oxford University Press, 1985).

Ortega, J., Etxebarria, J., Zubillaga, J., Breczewski, T., and Tello, M. J., *Phys. Rev.* B**45**, 5155 (1992).

Saito, K., Sugiya, H., and Kobayashi, J., *J. Appl. Phys.* **68**, 732 (1990).

Sawada, A., Sugiyama, J., Wada, M., and Ishisbashi, Y., *J. Phys. Soc. Japan* **48**, 1773 (1980).

Sugiyama, J., Wada, M., Sawada, A., and Ishibashi, Y., *J. Phys. Soc. Japan* **49**, 1405 (1980).

Uesu, Y., and Kobayashi, J., *Ferroelectrics* **64**, 115 (1985).

Vlokh, O. G., Polovinko, I. I., and Sveleba, S. A., *Opt. Spektrosk.* **65**, 751 (1988).

Vlokh, O. G., Zhmurko, V. S., Polovinko, I.I., and Sveleba, S. A., *Sov. Tech. Phys. Lett.* **16**, 900 (1990).

de Wolff, P. M., *Acta Cryst. A* **30**, 777 (1974).

de Wolff, P. M., Janssen, T., and Janner, A., *Acta Cryst. A* **37**, 625 (1981).

Chapter 6

Influence of the incommensurate modulation on the optical properties of the solid solution $((CH_3)_4N)_2ZnCl_{2.8}Br_{1.2}$

Influence of the incommensurate modulation on the optical properties of the solid solution $((CH_3)_4N)_2ZnCl_{2.8}Br_{1.2}$

M. Kremers and H. Meekes

Abstract

This paper reports on measurements with a High Accuracy Universal Polarimeter of the birefringence, optical activity and indicatrix rotation in incommensurately modulated $((CH_3)_4N)_2ZnCl_{2.8}Br_{1.2}$ crystals. It is shown that in this solid solution the inversion symmetry is broken already in the paraelastic phase, due to the inhomogeneous distribution of Cl and Br over the zinc-halide tetrahedra. This, however, allows one to study the influence of the incommensurate modulation on a non-zero optical activity. This influence is clearly shown for a sample in which, moreover, the modulation wave vector is believed to lock at several commensurate values.

6.1 Introduction

Crystals of the solid solution $((CH_3)_4N)_2ZnCl_{4-x}Br_x$, $0 < x < 4$, can be considered to be members of the family of A_2BX_4 type crystals that have a $\beta-K_2SO_4$ structure at high temperatures. In the neighbourhood of room temperature a phase transition occurs to an incommensurately modulated structure with modulation wave vector $\boldsymbol{q} = \gamma \boldsymbol{c}^*$ for the crystals with $x < 3$ (Colla et al., 1984). It is important to realise that a description in terms of the $\beta-K_2SO_4$ structure (Colla et al., 1987) neglects the difference between Cl and Br. Each zinc-halide tetrahedron in the crystal can only contain an integral number, n, of bromine atoms. For a general value of x there is, therefore, a distribution of these tetrahedra $ZnCl_{4-n}Br_n$ with different values n, such that the average value of n is equal to x. The corresponding relative concentrations ρ_n were determined from Raman scattering experiments by van Loosdrecht and Janner (1991). Thus, if one takes the difference between Cl and Br into account all lattice translational symmetry and point group symmetry is generally lost already in the high temperature phase. Although this has only subtle effects on X-ray diffraction experiments (Colla et al., 1987) we show in this paper that it has definite consequences for the optical properties of these crystals.

Our interest in A_2BX_4 type crystals with an average $\beta-K_2SO_4$ structure lies in the occurrence of an incommensurately modulated phase. In a broader context it is our aim to investigate the influence of an (incommensurate) modulation on the physical properties of such crystals. It is not possible to use a normal space group description for the incommensurate phase, because the presence of the modulation breaks the lattice translational symmetry. Such a symmetry can, however, be recovered if the crystal is embedded in a so-called superspace which has a dimension larger than 3. The symmetry of the structure can accordingly be described by means of a superspace group (de Wolff (1974), Janner and Janssen (1977), de Wolff et al. (1981), Janner et al. (1983)). Many members of the A_2BX_4 family, considered here, have superspace group symmetry $Pcmn(00\gamma)(1s\bar{1})$. The point group of the structure that is obtained by averaging the effect of the modulation in the incommensurate phase is mmm. The average structure is, therefore, orthorhombic and centrosymmetric. If one is able to detect optical properties that are symmetry forbidden by the point group mmm, a clear influence of the incommensurate modulation has been found. We have recently investigated the optical properties of $((CH_3)_4N)_2ZnCl_4$ and $((CH_3)_4N)_2CuCl_4$ crystals (Kremers et al. (1994a), Kremers and Meekes (1994d)). This was done with a High Accuracy Universal Polarimeter (HAUP) that is very well suited for this purpose (Kobayashi and Uesu (1983), Dijkstra et al. (1991), Kremers and Meekes (1994b), Kremers and Meekes (1994d)). In the case of $((CH_3)_4N)_2CuCl_4$ a rotation of the optical indicatrix was detected in the incommensurate phase, which contradicts an orthorhombic symmetry. In addition, (small) optical activity was found which contradicts the presence of an inversion center (Nye, 1985). For the case of $((CH_3)_4N)_2ZnCl_4$, however, no macroscopic symmetry breaking with respect to the average structure could be detected.

In this paper we report on similar HAUP measurements on $((CH_3)_4N)_2ZnCl_{2.8}Br_{1.2}$ crystals. These have been performed for the following reasons. As explained above, one can expect that in this solid solution deviations can occur from the macroscopic point group symmetry mmm of the average structure. The crystal can, therefore, show non-zero optical activity and indicatrix rotation even in the high temperature phase. Instead of searching for a deviation from zero in the incommensurate phase as has been done for $((CH_3)_4N)_2ZnCl_4$ it is possible, therefore, to study the deviation from a non-zero behaviour in the case of $((CH_3)_4N)_2ZnCl_{2.8}Br_{1.2}$. Though there is still disagreement on the presence of optical activity in in the incommensurate phase of $((CH_3)_4N)_2ZnCl_4$ (Kremers et al., 1994a), the results presented in this paper for $((CH_3)_4N)_2ZnCl_{2.8}Br_{1.2}$ show, undoubtedly, that optical activity can be affected by the modulation. Moreover, one can consider the Br atoms to be (intrinsic) defects of a perfect $((CH_3)_4N)_2ZnCl_4$ crystal, although the number of these defects is then relatively large in the case of $((CH_3)_4N)_2ZnCl_{2.8}Br_{1.2}$. Nevertheless, one may get an idea, in this way, of the role played by defects in an incommensurately modulated crystal.

We have organised this paper as follows. First, the temperature dependence of the crystal structure of $((CH_3)_4N)_2ZnCl_{2.8}Br_{1.2}$ is described. After that, we describe the sample treatment and the most important details of the measuring method. Then, we discuss the interpretation of the HAUP data. Subsequently, the results are presented and discussed.

6.2 The crystal structure of $((CH_3)_4N)_2ZnCl_{2.8}Br_{1.2}$ as a function of temperature

The x-T phase diagram of $((CH_3)_4N)_2ZnCl_{4-x}Br_x$ crystals was determined by Colla et al. (1984). In table 6.1 we present the successive phases that can be identified if one disregards the difference between Cl and Br .

Phase	V	IV	III	II	I
Temp (K)	$< 223 (= T_{c3})$	$< 240 (= T_{c2})$	$< 280 (= T_c)$	$< 294 (= T_i)$	$> 294 (= T_i)$
Symmetry	$P12_1/c1$		$P112_1/n$	$Pcmn(00\gamma)(1s\bar{1})$?	Pcmn
γ	1/2	1/3 and 1/2	1/3	0.36 – 0.39	0
System	Monocl.		Monocl.	Orthorh. ?	Orthorh.
Gyration Tensor $\boldsymbol{g}$	0		0	?	0
Indicatrix Rotation	around $\boldsymbol{b}$		around c	?	none

Table 6.1 Successive phase transitions in $((CH_3)_4N)_2ZnCl_{2.8}Br_{1.2}$. The structural data represent the case in which one disregards the difference between Br and Cl . The parameter γ determines the modulation wave vector according to the relation $\boldsymbol{q} = \gamma \boldsymbol{c}^*$.

Phase I is a paraelastic phase with space group Pcmn ($|\boldsymbol{a}| = 15.67$Å, $|\boldsymbol{b}| = 9.07$ Å and the pseudo-hexagonal axis $|\boldsymbol{c}| = 12.39$ Å). At T_i a phase transition into an incommensurate phase occurs. From our birefringence measurements we find the value $T_i = 294$ K that differs from the value $T_i = 290$ K given by Colla et al. (1987). The behaviour of the modulation parameter γ in the incommensurate phase has been investigated by Vogels et al. (1992)(1994). It was found that the modulation wave vector $\boldsymbol{q}$ locks at several commensurate values of γ in the incommensurate phases of $((CH_3)_4N)_2ZnCl_{4-x}Br_x$ crystals ($x > 0$). The exact temperature behaviour of γ can, however, differ from one crystal to another (Vogels et al., 1994). The locking behaviour can also be expected from the point of view that the Br atoms are intrinsic defects. It was shown by Bziouet et al. (1987) that a large (X-rays induced) defect concentration in crystals of $((CH_3)_4N)_2ZnCl_4$ ($x = 0$) also causes the modulation wave vector to lock at several rational values.

At $T_c = 280$ K a lock-in phase transition into a ferroelastic phase takes place. The crystal has then a three-fold superstructure and evolves into a multi-domain state. Two other phase transitions are known to occur at lower temperatures. We have only performed measurements in the phases I and II.

6.3 The Samples

Colourless crystals of about 1 cm^3 with large natural faces have been grown by means of a thermal convection method (Arend et al., 1986) from a stoichiometric aqueous solution of $((CH_3)_4N)Hal$ and $ZnHal_2$ (Hal = Br ,Cl) for the value $x = 1$. The value of x for the crystals growing from such a solution is always somewhat larger (Colla, 1987b), being $x = 1.2$ in this case. The directions of the crystallographic axes $\boldsymbol{a}$, $\boldsymbol{b}$ and $\boldsymbol{c}$ were determined with the help of an optical goniometer. Two crystal platelets, one parallel to the natural (001) face and another parallel to the (101) face, were cut with a wire saw. The faces of these platelets were polished with diamond paste down to 1 μm size. In table 6.2 we give the optical parameters that determine the light propagation in these samples.

Sample Surface	Thickness (mm)	Linear Birefringence Δn	Gyration $G = g_{ij}s_is_j$
(001)	1.80	$\Delta n_{33} = n_a - n_b$	$G_{33} = g_{33}$
(101)	2.05	$\Delta n_{13} \approx 0.62(n_a - n_b) + 0.38(n_b - n_c)$	$G_{13} = 0.39g_{11} + 0.62g_{33} + 0.97g_{13}$

Table 6.2 The two samples that have been used in the present experiments and the optical parameters that are relevant. n_a, n_b, and n_c are the main refractive indices. The gyration tensor $\boldsymbol{g}$ and the unit wave vector $\boldsymbol{s}$ of the light determine the gyration G that is observed. The indices of G indicate the gyration tensor element that gives the largest contribution to the total gyration for the direction $\boldsymbol{s}$. The corresponding linear birefringence and other optical properties are labeled with the same indices.

The (001) sample was chosen, because the direction of light propagation is parallel to the modulation wave vector in such a sample. The (101) sample was selected because previous HAUP measurements on several members of the A_2BX_4 family have shown interesting and controversial results for this sample orientation (Kremers et al., 1994a).

6.4 Measurements

The measurements presented in this paper were carried out with a HAUP apparatus built in our laboratory. A description of this apparatus has been given by Dijkstra et al. (1991). Some essential improvements were made in this set-up, which have been discussed by Kremers and Meekes (1994b).

In case of the (001) sample measurements were performed as a function of the temperature for two different wavelengths $\lambda = 632.8$ nm and $\lambda = 500$ nm. The same sample was also subjected to measurements as a function of wavelength at two different temperatures $T = 305$ K and $T = 290$ K. The (101) sample was measured only as a function of temperature for the wavelength $\lambda = 632.8$ nm. We want to point out that we have checked the obtained linear birefringences by measurements on two additional samples that were prepared with different thicknesses. In this way it is possible to determine the value of the linear birefringence without doubt.

In the measurements as a function of temperature at least two extinction directions (Kremers and Meekes, 1994b) were measured, in order to determine the rotation of the indicatrix with a large accuracy (Kremers and Meekes, 1994c). The temperature was left to stabilise for about half an hour after each change of its value, because we have learned from previous experiments that shorter stabilisation times can lead to irreproducible results. It has been shown by Colla et al. (1987) that the modulation wave vector has a larger tendency to lock at rational values of γ as the temperature is varied more slowly. In our case one can consider the temperature variation to be very slow in this respect.

6.5 Interpretation of the measurements

The results presented in this paper were obtained with the interpretation that has been presented by Kremers and Meekes (1994b). Both the so-called $\Delta\Theta$-correction and the ΔY-correction were carried out. The latter reduces the magnitude of the δY-error, typical in the HAUP method, to the order of 10^{-5} or smaller. The $\Delta\Theta$-correction improves all results, but is especially important for an accurate determination of the rotation of the optical indicatrix. Although the crystals of $((CH_3)_4N)_2ZnCl_{4-x}Br_x$ are totally transparent for visible light, we have taken the possible presence of small linear dichroism $\Delta\kappa$ into account. This effect may be caused by anisotropic surface scattering. The absolute value of of the linear dichroism $|\Delta\kappa|$ never exceeded $1 \cdot 10^{-6}$.

The optical properties of a sample that determine the propagation of light with unit wavevector $\boldsymbol{s}$ are extracted from the intensities measured in the HAUP experiment by fitting these intensities to the so-called HAUP intensity formula. In this way one finds the value of $4\sin^2(\pi z\Delta n/\lambda)$ from which the linear birefringence Δn has to be calculated (z is the thickness of the sample). From one of the fitting-parameters one also obtains the value of

$$2\delta Y\cos^2(\pi z\Delta n/\lambda) - ((p-a)+2k)\sin(2\pi z\Delta n/\lambda)\,, \tag{6.1}$$

where $k = G/(2\tilde{n}\Delta n)$ in which $\tilde{n}$ is the average refractive index and G is the gyration. The parameters p and a are the small parasitic ellipticities of the light polarised by, respectively, the polariser and the analyser. We have determined the value of the systematic error δY from expression (6.1) at that temperature or wavelength where $\sin(2\pi z\Delta n/\lambda)$ equals 0. The value of expression (6.1) is equal to $2\delta Y$ at such a point. Subsequently one can calculate the behaviour of $(p-a)+2k$. The parameter $(p-a)$ gives a constant contribution to this behaviour, which can only be determined if one is certain that k is equal to zero for part of the measurements. This is not the case for our measurements. However, it is well-known from other experiments that $(p-a)$ has a magnitude in the order of 10^{-4}. One can, therefore, estimate the gyration by neglecting $(p-a)$ in case that the value of

$(p-a)+2k$ is much larger than 10^{-4}.

Furthermore, the measurements provide the values of

$$\Theta_0 = \frac{1}{2}(p+a)\cot(\pi z\Delta n/\lambda) - \frac{1}{2}\delta Y + \delta\Theta_{\text{indicatrix}}.$$

The parameter $\delta\Theta_{\text{indicatrix}}$ represents a possible rotation of the optical indicatrix. An equal contribution $\delta\Theta_{\text{indicatrix}}$ is found in the measurement of the other extinction direction, whereas Δn changes sign for the latter. By comparing the values of Θ_0 for both extinction directions and subtracting the corresponding contributions $\frac{1}{2}(p+a)\cot(\pi z\Delta n/\lambda) - \frac{1}{2}\delta Y$ it is possible to find the rotation of the optical indicatrix with a large accuracy (Kremers and Meekes, 1994c). In order to do this, however, the value of $p+a$, which does depend on the extinction direction, must be determined. We have done this by plotting Θ_0 against $\cot(\pi z\Delta n/\lambda)$ for a small part of the measurements where $\delta\Theta_{\text{indicatrix}}$ is (nearly) constant.

6.6 Results

6.6.1 The linear birefringence

The linear birefringence Δn_{33} of the (001) sample as a function of temperature has been plotted in figure 6.1. A clear change of slope is observed at $T_i = 294$ K. This temperature is, therefore, believed to indicate a (second order) phase transition. A straight line behaviour of the linear birefringence is observed below T_i. The discontinuities are a result of the inaccuracy of the HAUP method in those cases that $\sin(\pi z\Delta n/\lambda)$ equals zero. The behaviour of the linear birefringence as a function of wavelength is presented in figure 6.2. The lock-in phase transition at $T = T_c$ is faintly visible in the measurement at $\lambda = 632.8$ nm. The results of figures 6.1 and 6.2 agree nicely. We want to recall that the temperature dependence of Δn_{33} has been checked by measuring another (001) sample with a different thickness.

In figure 6.3 we present the linear birefringence Δn_{13} for the (101) sample as a function of the temperature. Also in this case we have checked the result by measurements on another (101) sample with a different thickness. Again change of slope is observed at $T_i = 294$ K, but now also at approximately $T = 297$ K. In addition, the birefringences changes slope at several temperatures in the incommensurate phase, contrary to the results in figure 6.1. It is explained in the discussion that these deviations can be attributed to the behaviour of the modulation wave vector with temperature.

Note, that compared to the case of $x = 0$ (Kremers et al., 1994a) the behaviour of Δn_{33}, as a function of temperature at $\lambda = 632.8$ nm, is comparable, whereas the behaviour of Δn_{13} is very different. Thus, in the latter case, a clear influence of the substitution of Cl for Br is observed.

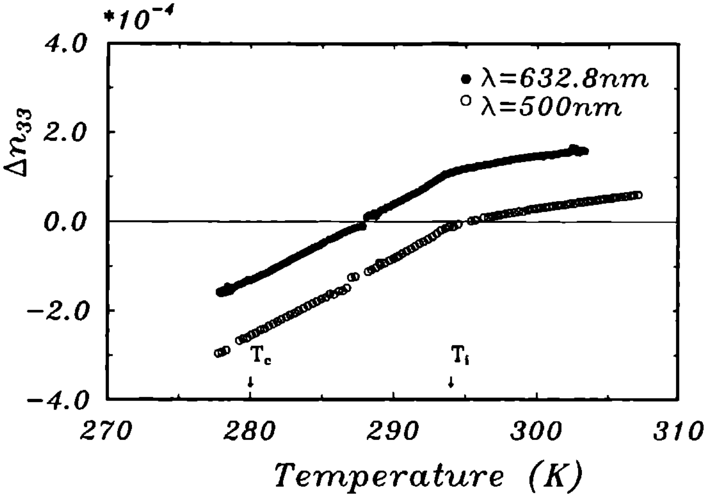

Figure 6.1 The linear birefringence Δn_{33} of $((CH_3)_4N)_2ZnCl_{2\ 8}Br_{1\ 2}$ at two different wavelengths as a function of temperature in the paraelastic and incommensurate phase.

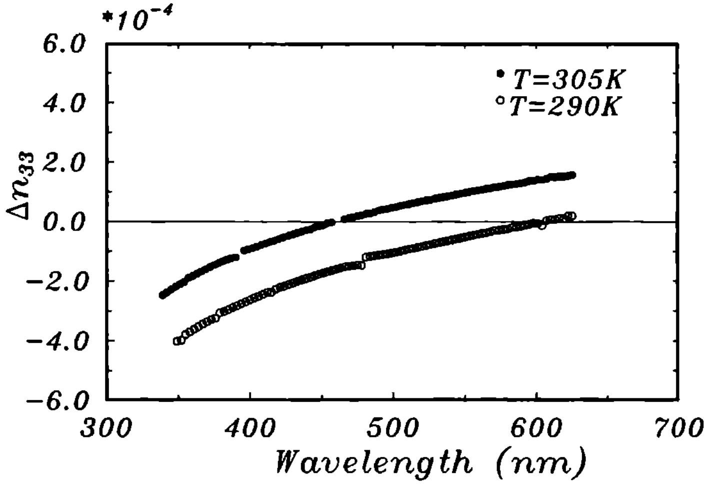

Figure 6.2 The linear birefringence Δn_{33} of $((CH_3)_4N)_2ZnCl_{2\ 8}Br_{1\ 2}$ at two different temperatures as a function of the wavelength of the light.

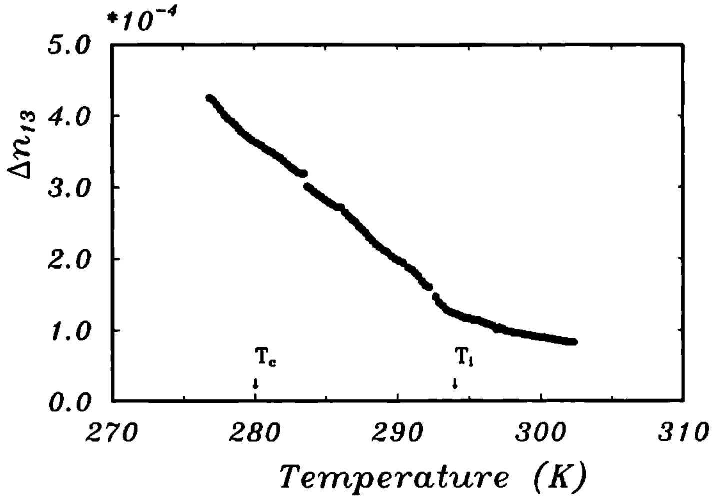

Figure 6.3 The linear birefringence Δn_{13} of $((CH_3)_4N)_2ZnCl_{2\ 8}Br_{1\ 2}$ as a function of temperature. The wavelength of the light is $\lambda = 632.8$ nm.

6.6.2 The gyration

It has been explained in section 6.5 that it is possible to determine the value of $(p-a)+2k$ from the measurements. The parameter k represents the ellipticity angle of the elliptical eigenpolarisations of the light that propagates in the sample. We have plotted in figure 6.4 the temperature dependence of $k+\frac{1}{2}(p-a)$ for the (001) sample and the two different wavelengths used. Note, that $(p-a)$ is a constant with a magnitude in the order of 10^{-4}. Therefore, it is clear that k, and consequently G_{33}, is non-zero already in the paraelastic phase. It has been explained in the introduction that one can expect this, because the centrosymmetry is broken by the complete miscibility of Br and Cl . Crystals of $((CH_3)_4N)_2ZnCl_{4-x}Br_x$ are, therefore, indeed optically active. This gives the possibility of studying the influence of the presence of the modulation wave vector on a non-zero optical activity.

In figure 6.5 we show the the temperature dependence of $k + \frac{1}{2}(p - a)$ for the (101) sample. Also in this case there is non-zero optical activity both in the paraelastic and in the incommensurate phase. The ellipticity angle k, however, shows a remarkable behaviour. Several plateaus of constant k are observed. We have drawn horizontal dashed line segments through these plateaus. Even above T_i a plateau is present. The origin of this remarkable behaviour is addressed in the discussion.

The structure in the ellipticity angle k may be caused by the structure that is present in the linear birefringence, because of the relation $k = \frac{G}{2\Delta n \bar{n}}$. In order to get an idea about the temperature dependence of the gyration G_{13}, we have neglected the contribution of $p - a$ in figure 6.5. For a first approximation this is reasonable, because the value of $p - a$ is small with respect to the observed values of $2k + (p - a)$. The circular birefringence $G_{13}/\bar{n}$ can then be calculated. The results are presented in figure 6.6 which shows that the structure in k is not only due to the behaviour of the linear birefringence. Also the gyration G_{13} shows a very characteristic behaviour.

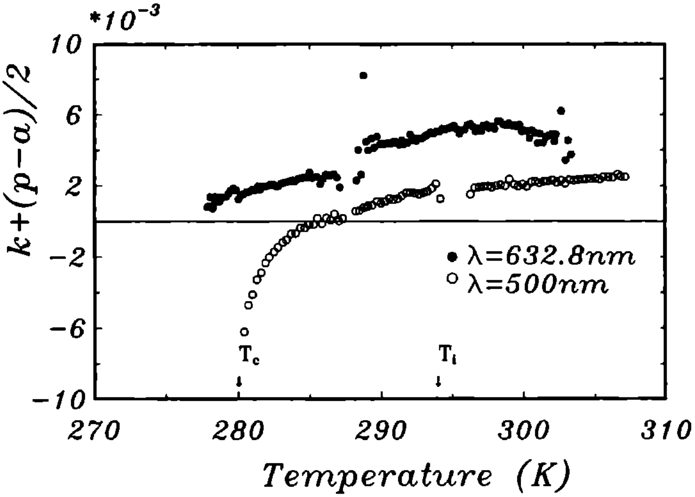

Figure 6.4 The temperature dependence of $k + \frac{1}{2}(p - a)$ for the (001) sample at two different wavelengths.

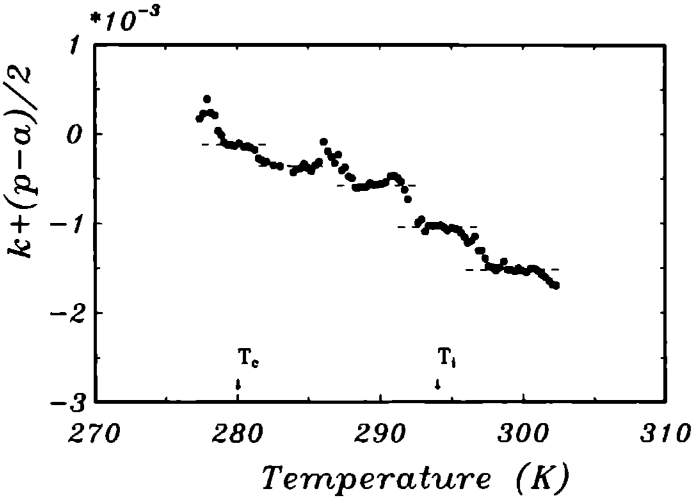

Figure 6.5 The temperature dependence of $k+\frac{1}{2}(p-a)$ for the (101) sample The dashed horizontal line segments have been drawn as a guide to the eye The wavelength of the light is $\lambda = 632\ 8$ nm

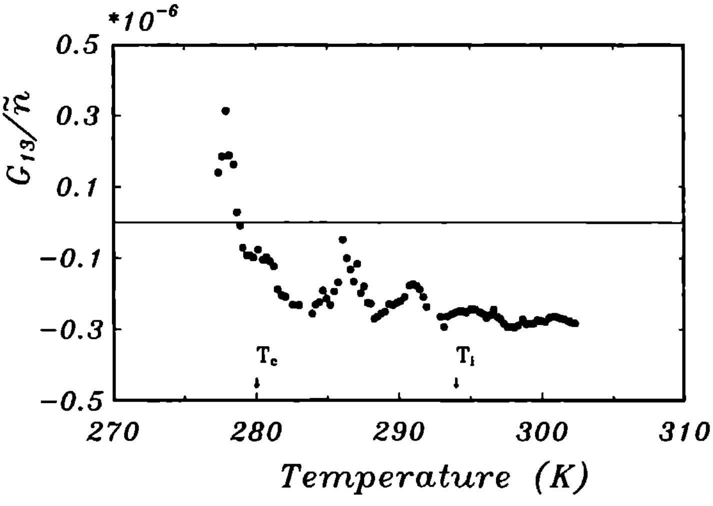

Figure 6.6 The temperature dependence of the circular birefringence $G_{13}/\tilde{n}$, obtained by neglecting the contribution of $p-a$ The wavelength of the light is $\lambda = 632\ 8$ nm

6.6.3 Rotation of the optical indicatrix

In figure 6.7 we have plotted the rotation of the optical indicatrix as derived for the (101) sample. In a truly orthorhombic crystal indicatrix rotation is forbidden by symmetry. The non-constant behaviour in the paraelastic phase of $((CH_3)_4N)_2ZnCl_{2.8}Br_{1.2}$ again demonstrates the fact that a point group symmetry mmm is not present. In the incommensurate phase a rotation of approximately $2 \cdot 10^{-3}$ rad is observed.

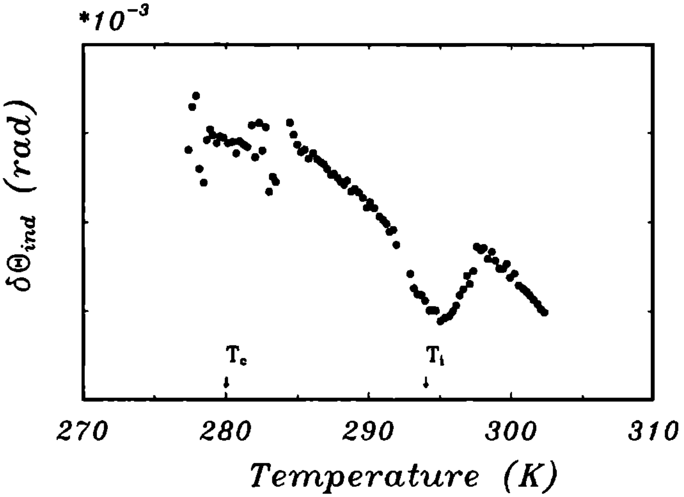

Figure 6.7 Rotation of the optical indicatrix in the (101) sample for the wavelength λ = 632.8 nm. The distance between the tick marks on the ordinate axis equals $1 \cdot 10^{-3}$. There is no absolute scale, because Θ_0 can only be measured with respect to an arbitrary origin.

6.7 Discussion

From the measured birefringences Δn_{33} and Δn_{13} we have concluded that the phase transition from the paraelastic phase to the incommensurate phase occurs in $((CH_3)_4N)_2ZnCl_{2.8}Br_{1.2}$ crystals at the temperature T_i = 294 K. Vogels et al. (1992) observed satellite faces on the morphology of these crystals up to exactly the same temperature. The transition temperature derived by Colla et al. (1987) from differential scanning calorimetry, on the other hand, was T_i = 290 K. This difference may be caused by the fact that a much larger cooling rate was used by Colla et al. (1987). Another reason may be found in the differences that are observed for different individual crystals. The birefringence Δn_{13} presented in figure 6.3, for example, shows several deviations from a straight line behaviour in the incommensurate phase. In other samples, however, we did observe a perfectly linear dependence on temperature of the birefringence Δn_{13}. It is our opinion that the behaviour of the modulation wave vector is very sensitive to the presence of defects in $((CH_3)_4N)_2ZnCl_{2.8}Br_{1.2}$ crystals, but more importantly that the behaviour of the modulation wave vector clearly influences the optical properties. A strong indication for the latter is given by the results in figure 6.5. One observes five plateaus of more or less constant ellipticity angle k in this figure. In other $((CH_3)_4N)_2ZnCl_{2.8}Br_{1.2}$ samples, having the same orientation, we also observed a clearly non-zero k having, however, a smooth temperature dependence without plateaus. The results in figure 6.5 are, nevertheless, very interesting.

As mentioned before, it is known that large defect concentrations can cause the modulation wave vector to lock at several commensurate values in $((CH_3)_4N)_2ZnCl_4$ crystals. Moreover, such a locking behaviour seems to be a characteristic intrinsic property of $((CH_3)_4N)_2ZnCl_{4-x}Br_x$ crystals (Vogels et al., 1994). Therefore, we attribute the plateaus in figure 6.5 to regions of different commensurate modulation wave vectors. Note, that this implies that here the modulation wave vector already has a certain temperature dependence above $T_i = 294$ K, which also effects the rotation of the optical indicatrix at $T \approx 297$ K. It is striking that at the latter temperature the phase transition to the incommensurate phase occurs for $((CH_3)_4N)_2ZnCl_4$ (x=0). At present we can not say whether this is a coincidence. Another explanation for the observed plateaus might be found in the temperature dependence of the amplitude of the modulation. However, one only expects a steady increase of the amplitude with decreasing temperature. This can not explain the observed behaviour of k. Also the unit cell parameters of the average lattice are known to show a smooth temperature dependence.

Thus, we believe that in figure 6.5 one can, indirectly, observe a locking of $\boldsymbol{q}$ at different commensurate values. Between the plateaus the modulation wave vector may be incommensurate, changing continuously with temperature. It is also possible, however, that there are many different plateaus that are too small to be distinguished. Nevertheless, it is evident that the presence of the modulation influences the ellipticity angle k. The results presented in figure 6.6 demonstrate that also the optical activity is undoubtedly influenced by the presence of the modulation.

In the incommensurate phase the behaviour of the rotation of the optical indicatrix resembles the behaviour that was observed for $((CH_3)_4N)_2CuCl_4$ (Kremers and Meekes, 1994d). It is interesting that this effect does not show plateaus in the incommensurate phase. It is possible that indicatrix rotation has a stronger dependence on the modulation amplitude than on the length of the modulation wave vector.

6.8 Conclusions

We have demonstrated that the difference between Cl and Br is essential for the optical properties of $((CH_3)_4N)_2ZnCl_{4-x}Br_x$ crystals. Due to the complete miscibility of Cl and Br the crystal can not be considered to be orthorhombic, as has been proven by a non-zero indicatrix rotation in the paraelastic phase. Furthermore, the crystal can not be considered to be centrosymmetric, as was proven by the measurement of non-zero optical activity in the paraelastic phase.

The measurements on a characteristic (101) sample have shown that the presence of the modulation wave vector has a definite influence on the birefringence, on the rotation of the optical indicatrix and on the optical activity. The latter may provide an important impulse for the search of non-zero optical activity in the incommensurate phase of crystals that are not optically active in the high temperature phase I.

It is our opinion that a more complete investigation of $((CH_3)_4N)_2ZnCl_{4-x}Br_x$ crystals with varying defect concentrations could be very fruitful if it were combined with the determination of the temperature dependence of the modulation by means of, for example, X-ray diffraction experiments.

6.9 Acknowledgments

We are indebted to Prof. Dr. P. Bennema, Prof. Dr. T. Janssen and Prof. Dr. A. Janner for their support. This work is part of the research program of the Stichting voor Fundamenteel Onderzoek der Materie (Foundation for Fundamental Research on Matter).

References

Arend, H., Perret, F., Wüest, H. and Kerkoc, P., *Journ. of Cryst. Growth* **74**, 321 (1986).

Bziouet, M., Almairac, R. and Saint-Grégoire, P., *J. Phys. C: Solid State Phys.* **20**, 2635 (1987).

Colla, E., Muralt, P., Arend, H., Perret, R., Godefroy, G., and Dumas, C., *Solid St. Commun.* **52**, 1033 (1984).

Colla, E., Gramlich, V., and Petter, W., *Acta Cryst. C* **43**, 1070 (1987).

Colla, E., *PhD thesis*, ETH Zürich, Switzerland (1987b).

Dijkstra, E., Meekes, H. and Kremers, M., *J. Phys. D: Appl. Phys* **24**, 1861 (1991).

Janner, A., Janssen, T., and de Wolff, P. M., *Acta Cryst. A* **39**, 671 (1983).

Janner, A., and Janssen, T., *Phys. Rev. B* **15**, 643 (1977).

Kobayashi, J. and Uesu, Y., *J. Appl. Cryst.* **16**, 204 (1983).

Kremers, M., Dijkstra, E., and Meekes, H., *submitted to Phys. Rev.* (1994a).

Kremers, M., and Meekes, H., *submitted to J. Phys. D: Appl. Phys* (1994b).

Kremers, M., and Meekes, H., *submitted to J. Phys. D: Appl. Phys* (1994c).

Kremers, M., and Meekes, H., *submitted to Phys. Rev.* (1994d).

van Loosdrecht, P. H. M., and Janner, A., *J. Phys.: Condens. Matter* **3**, 8113 (1991).

Nye, J. F., *Physical properties of crystals* (Oxford: Oxford University Press, 1985).

Vogels, L. J. P., Verheijen, M. A., Meekes, H., and Bennema, P., *J. Cryst. Growth* **121**, 697 (1992).

Vogels, L. J. P., Meekes, H., and de Boer, J. L., *J. Phys.: Condens. Matter* **6**, 8205 (1994).

de Wolff, P. M., *Acta Cryst. A* **30**, 777 (1974).

de Wolff, P. M., Janssen, T., and Janner, A., *Acta Cryst. A* **37**, 625 (1981).

Part II

Morphological Aspects of Incommensurate Crystals

Chapter 7

Introduction to (incommensurate) crystal morphology

Introduction to (incommensurate) crystal morphology

M. Kremers

Introduction

In part II of this thesis we turn to morphological aspects of incommensurate crystals. It is known from experiments that the morphology of incommensurate crystals differs essentially from that of classical crystals. In the case of incommensurately modulated crystals, for example, additional flat faces occur that can directly be related to the presence of the modulation (see for a review Bennema et al., 1991). If the modulation wave vector changes as a function of some external variable (e.g. temperature or pressure) also the orientation of these new, so-called satellite faces changes, if allowed to grow under the changed conditions. For classical crystals one expects that the (ideal) morphology has the same point group symmetry as the microscopic crystal structure according to the principle of Neumann. The shapes of quasi-crystals, however, often show icosahedral symmetries (see, for example, Beeli and Nissen, 1993) that are non-crystallographic in the sense that they are not compatible with 3-dimensional lattice translational symmetry. A detailed experimental study of the morphology of incommensurate composite crystals has not yet been made, but also for this type of incommensurate crystals a non-classical behaviour can be expected. Before starting, however, with an attempt to give a theoretical foundation for the morphology of incommensurate crystals, we want to summarise the development of the theory that is nowadays used to predict the morphology of classical crystals. Then, we extend a part of this theory to the case of incommensurate crystals. The rest is left to future research.

In the development of the theory for the prediction of the morphology of classical crystals several stages can be identified. Crystal shapes are usually polyhedra. The first stage, therefore, consisted of determining whether the orientations of crystal faces are free or restricted to some laws. The latter was found to be the case and the most important result was the law of rational indices (Haüy, 1784, 1801). After that, one studied the possibility of predicting the relative morphological importance (MI) of crystal faces. The MI can be expressed in terms of the relative average sizes of faces or as the relative average frequency of appearance, considering a large enough number of crystals. One was able to derive trends for the relative MI's from the lattice parameters with some restrictions given by the space group symmetry. This result is known as the Bravais-Friedel-Donnay-Harker law (Friedel (1907), Donnay and Harker (1937)). It was realised, however, that a connection with the actual microscopic structure was necessary for a better description. This connection was made by the theory of Hartman and Perdok (Hartman and Perdok, 1955), which predicts crystal shapes at $T = 0$ K in a vacuum surrounding. It was discovered, however, that crystal faces can become rough at finite temperatures and finite driving forces.Rough faces, in a sense, have zero MI if a crystal is allowed to grow long enough. Currently, one investigates the role played by the mother phase from which the crystal grows and the influence of additives. Moreover, the prediction of classical crystal morphology is transferred from the minds of experts to sophisticated computer programs. Here we proceed by briefly summarising the just mentioned stages.

7.1 The law of rational indices by Haüy

A classical crystal has a lattice with three basis vectors of length a, b and c that make angles α, β and γ with respect to each other. The orientation of a crystal face is subsequently characterised by the intercepts a', b' and c' at which the face intersects the axes or, alternatively, by the direction angles α', β' and γ'. The law of rational indices then implies that

$$\frac{a}{a'} : \frac{b}{b'} : \frac{c}{c'} = \frac{\cos\alpha'}{\cos\alpha} : \frac{\cos\beta'}{\cos\beta} : \frac{\cos\gamma'}{\cos\gamma} = h : k : l, \tag{7.1}$$

where h, k and l are integral, so-called Miller indices of the crystal face.

7.2 The Bravais-Friedel-Donnay-Harker law

From the work of Bravais (1850) it is known that each crystal face is parallel to a lattice plane of the reciprocal lattice. Friedel used this result in the formulation of the Bravais-Friedel law. It states that a crystal face is more important on the crystal shape when the set of corresponding lattice planes has a larger interplanar distance, denoted d_{hkl}.

$$d_{hkl} > d_{h'k'l'} \Rightarrow \mathrm{MI}_{hkl} > \mathrm{MI}_{h'k'l'} \tag{7.2}$$

Later, it was recognised by Donnay and Harker that the space group symmetry is also relevant for the morphology. The law of Donnay and Harker, in fact, expresses that the morphological importance of a crystal face must be expressed in terms of the interplanar distance defined by the smallest (symmetry) allowed reciprocal vector in the direction of the face normal. This means that lattice planes defined by reciprocal lattice vectors for which a systematic extinction occurs in the diffraction pattern have zero MI. Due to the presence of, for example, a glide plane $\{m_z|\frac{1}{2}00\}$ in a non-symmorphic space group it is possible that a (100) face has zero MI, whereas a (200) face can be relatively important.

7.3 The Hartman-Perdok theory

The connection of the macroscopic morphology with the microscopic structure has been developed by Hartman and Perdok. The basic ideas are as follows. It is realised that a crystal grows from a mother phase in which some kind of growth units are present. These are assemblies of atoms that will be incorporated as such in the crystal when it is forced to grow. Then, one represents the microscopic crystal structure by a graph in which the vertices correspond to the growth units and the edges correspond to the chemical bonds between them. Subsequently, one searches for so-called connected nets. These correspond to slices with average thickness d_{hkl} (in correspondence with the space group) and with average orientation given by the Miller indices (hkl) in which all vertices (growth units) are connected by all kinds of arbitrary uninterrupted paths of edges (bonds). It is believed that the crystal can grow with the layers that are represented by the connected nets. One often searches for so-called periodic bond chains in order to find a connected net. A periodic bond chain (PBC) is the periodic repetition of an uninterrupted path of bonds between to translationally equivalent growth units. A connected net is defined by two interconnected PBC's.

Suppose that all connected nets have been identified. The (bond)energy per growth unit needed to cut a corresponding slice (hkl) from the crystal graph is the so-called attachment energy E^{att}_{hkl}. The (bond)energy per growth unit within the resulting slice is the so-called slice energy E^{slice}_{hkl}. The sum of these two energies gives the crystallisation energy E^{cr}_{hkl}, which is the (bond)energy per growth unit of all bonds in the infinite crystal

$$E^{\text{cr}}_{hkl} = E^{\text{att}}_{hkl} + E^{\text{slice}}_{hkl}. \tag{7.3}$$

Another important parameter is the surface free energy per unit area Γ_{hkl} of such a slice. This is related to E^{att}_{hkl} in the following way

$$\Gamma_{hkl} = N\frac{E^{\text{att}}_{hkl}}{M_{hkl}}, \tag{7.4}$$

where N is the number of growth units per unit cell and M_{hkl} is the so-called mesh area of the face. The latter is calculated from the interplanar distance d_{hkl} and the volume V of the unit cell

$$M_{hkl} = \frac{V}{d_{hkl}}. \tag{7.5}$$

It is clear that all these parameters can be calculated from the structural data and a sensible estimate of the energies of the bonds that occur in the crystal graph. In a first approximation one expects the following behaviour:

$$E^{\text{att}}_{hkl} < E^{\text{att}}_{h'k'l'} \Rightarrow E^{\text{slice}}_{hkl} > E^{\text{slice}}_{h'k'l'} \Rightarrow \text{MI}_{hkl} > \text{MI}_{h'k'l'}. \tag{7.6}$$

The calculated parameters can, however, more sophisticatedly be used to derive both growth and equilibrium forms of crystals.

The equilibrium form is defined as the shape that minimises the total of surface free energy and internal crystal free energy for a constant number of growth units. The equilibrium form of a crystal can be constructed from the surface free energies Γ_{hkl} by means of the so-called Wullf plot construction. It must be noted that in this procedure only flat faces are considered. One draws radii vectors $\boldsymbol{\Gamma}_{hkl}$ that have a length Γ_{hkl} in the directions of the face normals. Planes are then drawn at the end-points of these vectors and perpendicular to them. The body formed by all points reachable from the origin without crossing any of the planes is the equilibrium form. If one uses the surface free energies as calculated from equation (7.4) the equilibrium form of the crystal is obtained at the temperature $T = 0$.

The growth form of a crystal can not be constructed from the surface free energies. Instead the rates of growth R_{hkl} should be used. It is often assumed that one can take these rates of growth proportional to the values E^{att}_{hkl} (Hartman and Bennema, 1980).

7.4 Thermal and kinetic roughening

Thermal roughening (Leamy and Gilmer, 1974) can be understood in terms of the order-disorder phase transition that can be shown to exist in a two-dimensional Ising lattice (Onsager, 1944). The physical idea behind this effect is that below the transition temperature, called roughening temperature, the crystal grows with flat layers, because the edge free energy of a step on the surface has a finite value. A finite amount of energy is, therefore, involved in creating a step on the surface. Above the roughening temperature, however, the edge free energy is zero. Steps can then be created without cost of energy and the surface actually roughens up.

The second mechanism for the roughening of a crystal face is that the driving force (supersaturation) is too large. The activation energy for the formation of a critical nucleus becomes roughly equal to the thermal energy kT. The tendency to grow with a layer mechanism is then absent and the surface will roughen up.

In general one can state that rough faces grow faster than flat faces. The roughened faces will, therefore, not be present on a grow form if it is allowed to grow long enough. Only the flat faces survive. Faces that are rough at the growth conditions are, therefore, excluded from the Wulff plot construction.

7.5 Mother phase and additives

The morphologies that are predicted by the method that has been summarised thus far do often still not agree satisfactorally with the ones that are experimentally obtained. It is believed that this is due to the role played by the mother phase from which the crystal grows. The structure of solid-fluid interfaces is, therefore, currently under investigation (see, for example, Liu and Bennema).

On the other hand, one currently studies whether it is possible to influence the growth forms of crystals by additives. For this purpose one may use computer programs based on molecular mechanics and molecular dynamics.

7.6 Incommensurate crystal morphology

The above summarises the present status of the prediction of the morphology of classical crystals. It is clear that 3-dimensional lattice translational symmetry is one of the most important tools. It is essential for the law of rational indices, the Bravais-Friedel-Donnay-Harker rules, but also for the Hartman-Perdok theory and the calculation of order-disorder transitions from Ising models. In order to be able to predict the morphology of incommensurate crystals one can, therefore, not use the presently known theory for classical crystals. Moreover, the incommensurateness can not be neglected as it has definite consequences for the morphology. Therefore, an alternative approach is needed. In this part of the thesis we show that it is possible to use a superspace approach for the calculation of surface free energies that can be used to construct equilibrium forms of incommensurate crystals. The influence of the growth conditions, mother phase and/or additives is not taken into account, but left to future investigations.

The second part of this thesis is organised in the following way. First, the case of an incommensurately modulated 1-dimensional crystal is treated. This analysis helps to understand the theory for incommensurately modulated 3-dimensional crystals that is presented in the subsequent chapter. Finally, the last chapter of this thesis is concerned with the calculation of equilibrium forms for the case of quasi-crystals.

References

Beeli, C., and Nissen, H. -U., *Philosophical Magazine* **68**, 487 (1993).

Bennema, P., Balzuweit, K., Dam, B., Meekes, H., Verheijen, M.A., and Vogels, L.J.P., *J. Phys. D* **24**, 186 (1991).

Bravais, A., *J. Ecole Polytech., Paris* **19**, 1 (1850).

Donnay, G.D.H., and Harker, D., *Amer. Miner.* **22**, 446 (1937).

Friedel, G., *Bull. Soc. fr. Minéral* **30** 326 (1907).

Hartman, P., and Perdok, W. G.,
Acta Crystallogr. **8**, 49 (1955)
Acta Crystallogr. **8**, 521 (1955)
Acta Crystallogr. **8**, 525 (1955).

Hartman, P., and Bennema, P., *J. Crys. Growth* **49**, 145 (1980).

Haüy, R.J., *Essai d'une théorie sur la structure des cristaux* Paris (1784), *Traité de cristallographie* Paris (1801).

Leamy, H.J., and Gilmer, G. H., *J. Cryst. Growth* **24/25**, 499 (1974).

Onsager, L., *Phys. Rev.* **65**, 117 (1944).

Liu, X. Y., and Bennema, P., *submitted to Phys. Rev. B* (1994).

Chapter 8

A superspace description for the morphology of modulated crystals

an explanation for the occurrence of faces (hklm)

A superspace description for the morphology of modulated crystals

– an explanation for the occurrence of faces (hklm)* –

M. Kremers, H. Meekes, P. Bennema, K. Balzuweit
and M. A. Verheijen

Abstract

A theory is presented for the explanation of equilibrium forms of modulated crystals. In this theory crystallographic concepts are generalised to a superspace description of these crystals. The aim is to be able to deal with the case of incommensurately modulated crystals and consequently explain the occurrence of satellite faces. The case of a modulated one-dimensional crystal is treated.

8.1 Introduction

Non-modulated crystals show lattice translational periodicity in three independent directions. They have a lattice spanned by three vectors $\boldsymbol{a}_1$, $\boldsymbol{a}_2$ and $\boldsymbol{a}_3$. Modulated crystals have an extra periodicity. In commensurately modulated crystals this extra periodicity is commensurate with the lattice. The crystal can then be described by choosing a different lattice with another unit cell. In incommensurately modulated crystals there is no integral combination of $\boldsymbol{a}_1$, $\boldsymbol{a}_2$ and $\boldsymbol{a}_3$ that is commensurate with the extra periodicity. The crystal loses its translational symmetry in at least one direction. However, since the modulation is periodic, the average structure can still be described by the original lattice.

A typical macroscopic property of crystals is their morphology. Crystals are often bounded by flat faces. These faces are perpendicular to reciprocal lattice vectors

$$\boldsymbol{H}_{hkl} = h\boldsymbol{a}_1^* + k\boldsymbol{a}_2^* + l\boldsymbol{a}_3^* \tag{8.1}$$

and can thus be characterised by three integral numbers (hkl). This corresponds to the law of rational indices. Morphological theories for the explanation of the stability of crystal faces, with respect to faces perpendicular to arbitrary vectors from reciprocal space, already exist (Bennema and van der Eerden, 1987). The modern morphological theory is based on an integration of the crystallographic Hartman Perdok theory (Hartman and Perdok, 1955) and statistical mechanical theory of roughening transition (Bennema

---

[*] appeared in *Phil. Mag. B* **69**, 69 (1994)

(1991), Bennema et al. (1993)). A crystallographic face (hkl) can be constructed by cutting 1/h of $\boldsymbol{a}_1$, 1/k of $\boldsymbol{a}_2$ and 1/l of $\boldsymbol{a}_3$ and taking the plane through these points. It follows that in each such face a two-dimensional lattice can be defined, which is a periodic repetition of a planar elementary cell. In the calculation of stability of crystal faces this fact is very useful, since only this planar cell, called the mesh area M_{hkl}, has to be considered.

Modulated crystals are also bounded by flat faces. A striking example is the mineral calaverite ($AuTe_2$). Its very rich morphology has puzzled crystallographers for a long time until a very satisfying description was eventually given by Dam et al. (1985). When the modulation is one-dimensional, it has been found (Bennema et al. (1991), Janner et al. (1980), Dam et al. (1983), Dam et al. (1985)) that these faces are perpendicular to vectors which are integral linear combinations of four vectors from reciprocal space and can therefore be characterised by four integral numbers ($hklm$). Three of these vectors, $\boldsymbol{a}_1^*$, $\boldsymbol{a}_2^*$ and $\boldsymbol{a}_3^*$, span the reciprocal lattice of the average structure and the fourth is the modulation wave vector $\boldsymbol{q}$. Suppose that this vector is $\boldsymbol{q} = \alpha\boldsymbol{a}_1^* + \beta\boldsymbol{a}_2^* + \gamma\boldsymbol{a}_3^*$. The face ($hklm$) is then perpendicular to the vector

$$\boldsymbol{H}_{hklm} = h\boldsymbol{a}_1^* + k\boldsymbol{a}_2^* + l\boldsymbol{a}_3^* + m\boldsymbol{q} \tag{8.2}$$

It cuts the $\boldsymbol{a}_1$ axis at 1/(h $+\alpha$m), the $\boldsymbol{a}_2$ axis at 1/(k $+\beta$m) and the $\boldsymbol{a}_3$ axis at 1/(l $+\gamma$m). If at least one of the three numbers α, β or γ is irrational, we speak of an incommensurate modulation and it is not always possible to define a planar elementary cell on this surface, because the translational symmetry can be broken. Therefore, in calculating the stability of such a face in a traditional way (Vogels et al., 1992), it would be necessary to consider the complete face instead of just one planar elementary cell. Moreover, the exact surface structure can be very complicated due to the modulation and calculations using this structure will at least be very involved. Furthermore, because ($hklm$) faces do show up as stable faces on modulated crystals we are led to the question in what respect such a face ($hklm$) differs from a face perpendicular to any vector from reciprocal space that can not be described by equation 8.2.

In this paper we approach this problem in the following manner. There exists a clear relationship between crystallographic faces and the crystal's X-ray diffraction pattern. Faces are perpendicular to reciprocal lattice vectors and diffraction spots are found in the directions of these vectors. In crystals, X-ray reflections are found in directions $\boldsymbol{k} = h\boldsymbol{a}_1^*+k\boldsymbol{a}_2^*+l\boldsymbol{a}_3^*+m\boldsymbol{q}$. They are called satellite reflections when $m \neq 0$, because they usually have smaller intensities than main reflections ($m = 0$) and are in the neighbourhood of the latter. Faces ($hklm$) are therefore called satellite faces when $m \neq 0$. It has been shown (Janssen and Janner, 1987) that the vectors $\boldsymbol{k}$ can be considered as projections of lattice vectors in a reciprocal superspace (of dimension higher than three) on the physical three-dimensional reciprocal space. This corresponds to an embedding of the modulated crystal in this superspace, where it has full lattice translational symmetry. The physical crystal is then a three-dimensional section of the superspace. Therefore crystal faces are generalised to hyperfaces in superspace as suggested by Janner (1983). Also other crystallographic concepts will be generalised. In this paper we give the example of a modulated one-dimensional crystal embedded in a 1+1-dimensional superspace. A preliminary result of this approach has been published earlier (Bennema et al., 1993).

8.2 The embedding of a modulated one-dimensional crystal

Here, a set of displacively modulated one-dimensional crystals is treated instead of just one. The atomic positions are given by:

$$r(n,\phi) = na + f \sin 2\pi(qna + \phi) \tag{8.3}$$

n labels the cell and f is the modulation amplitude. All crystals from the set have the same average lattice determined by a and the same modulation wavelength q. The phase factor ϕ determines the phase of the modulation wave with respect to the origin. Each crystal from the set is characterised by a different phase ϕ modulo 1.

The modulation wavelength q, is given by

$$q = \alpha a^*,\ 0 \leq \alpha \leq 1 \tag{8.4}$$

where a^* defines the reciprocal lattice of the average structure.

In order to embed the modulated crystal in a 1+1-dimensional superspace a lattice must be defined in this space. On an orthonormal basis, this lattice is spanned by the vectors:

$$\begin{aligned} \boldsymbol{a}_s &= (a, -\alpha d) \\ \boldsymbol{d}_s &= (0, d) \end{aligned}$$

The reciprocal lattice is defined by:

$$\begin{aligned} \boldsymbol{a}_s^* &= (a^*, 0) \\ \boldsymbol{d}_s^* &= (q, d^*), \end{aligned}$$

where a^*, d and d^* are chosen such that

$$aa^* = dd^* = 1.$$

Therefore, (with Eq. 4), we have

$$\begin{aligned} \boldsymbol{a}_s \cdot \boldsymbol{a}_s^* = \boldsymbol{d}_s \cdot \boldsymbol{d}_s^* = 1 \\ \boldsymbol{a}_s \cdot \boldsymbol{d}_s^* = \boldsymbol{a}_s^* \cdot \boldsymbol{d}_s = 0. \end{aligned}$$

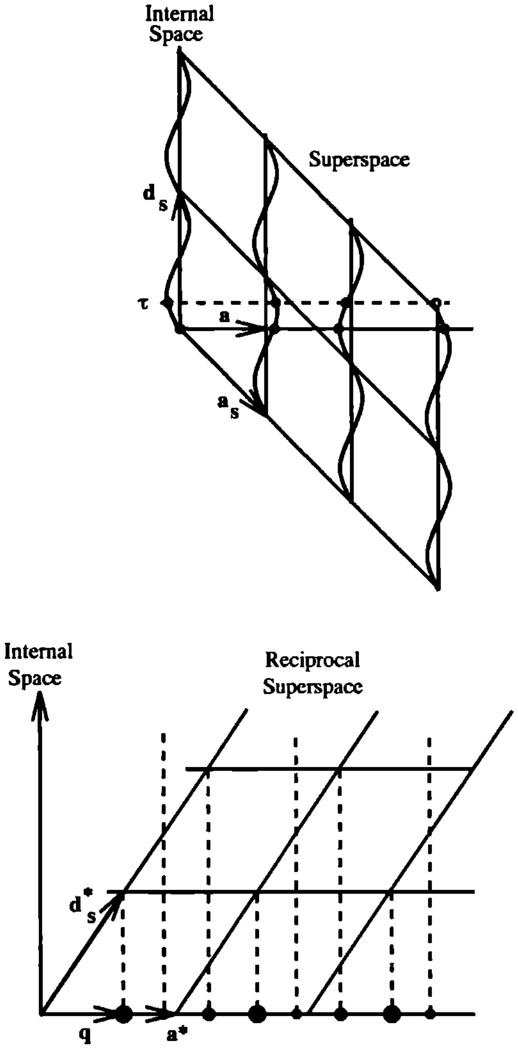

Figure 8.1 The 1+1-dimensional superspace construction for a modulated one-dimensional structure. The atoms embedded in this superspace are shown (a) and the lattice in reciprocal superspace is given (b).

In principle there are no further restrictions on the vector d. However, we require that the unit of length in the internal space has the same periodicity length as the modulation wave in real space, which is a natural choice (Janner, 1983):

$$d = |\boldsymbol{d}_s| = 1/q.$$

The vector $\boldsymbol{a}_s$ then becomes $(a, -a)$ and consequently the angle between $\boldsymbol{a} = (a, 0)$ and $\boldsymbol{a}_s$ has to be

$$\rho = \pi/4$$

The two periodicities a and $1/q$ present in the crystal are thus represented in superspace by respectively $\boldsymbol{a}$ and $\boldsymbol{d}_s$. From here on, we will only consider incommensurate modulations, so only irrational values for $\alpha = qa$.

The atoms embedded in 1+1-dimensional superspace (see figure 8.1) are described by:

$$\boldsymbol{r}_s(n, \tau) = (na + f \sin(2\pi(qna + \tau + \tau_0), \tau) = (r(n, \tau + \tau_0), \tau) \qquad (8.5)$$

and it is clear that a physical crystal is a section at $\tau + \tau_0 = \phi$. The parameter τ can thus be considered as a phase which runs along the $\boldsymbol{d}_s$ axis, called internal axis, perpendicular to the space of the physical crystal, denoted as external space. A section at a different phase τ gives another modulated one-dimensional crystal with the same average lattice and the same, though shifted with respect to the origin, modulation wave. It is important to realise that the embedding therefore represents an infinite number of these modulated crystals.

8.3 Generalisation of crystallographic concepts to superspace

8.3.1 Chemical bonds

A crystal can be considered to be a collection of atoms in a lattice where the atoms are bound to each other by chemical bonds. An often used interpretation of a chemical bond is that the corresponding binding energy is the energy needed to take the two atoms and bring them infinitely far apart. The bond is represented by a line segment connecting the atoms and it is assumed that the energy is a function of the bond length. Normally a longer bond corresponds to a lower energy. We generalise this concept and connect at each phase τ in equation 8.5, thus for each crystal, the atoms in superspace with each other. Instead of a finite number of bonds per unit internal axis length, we thus obtain a bond density in superspace, as is shown in appendix E. The bonds are taken to be parallel to the physical space. At this point it is not clear which meaning a binding component in the internal direction could have. Also, by defining bonds in this way, it is guaranteed that a generalised Wulff plot construction, that we will introduce, yields the physical crystal, as we will explain later.

8.3.2 Crystallographic planes

The generalisation of a crystallographic plane (hm) is straightforward (Janner, 1983). A crystallographic hyperplane is taken to be perpendicular to the vector

$$\boldsymbol{H}_{(hm),s} = h\boldsymbol{a}_s^* + m\boldsymbol{d}_s^*. \tag{8.6}$$

It can be constructed by cutting the $\boldsymbol{a}_s$ axis at $1/h$ and the $\boldsymbol{d}_s$ axis at $1/m$ and taking the plane through these points. In our 1+1-dimensional case this will be a line.

8.3.3 Interplanar distances

Now a grid of netplanes $(hm)_s$ can be constructed in superspace with interplanar distance

$$d_{(hm),s} = \frac{1}{|\boldsymbol{H}_{(hm),s}|} = \frac{a}{((h+m\alpha)^2 + m^2\alpha^2)^{\frac{1}{2}}}. \tag{8.7}$$

This is essentially different from the result obtained when the notion of interplanar distance would be generalised for satellite planes in physical space. In that case one would find

$$d_{(hm)} = \frac{1}{|\boldsymbol{H}_{(hm)}|} = \frac{a}{|h+m\alpha|}. \tag{8.8}$$

It is important to realise that this interplanar distance becomes infinite when $h = -m\alpha$, which can not have a physical meaning. However, if α is a true irrational number h never equals $-m\alpha$.

8.3.4 Mesh area

In close connection with the idea of interplanar distance is that of mesh area M. It is formally defined as the surface area of the planar elementary cell of a lattice plane and therefore fulfills the relation

$$M_{(hm)}d_{(hm)} = V, \tag{8.9}$$

where V is the volume of the unit cell of the lattice. We generalise this concept to

$$M_{(hm),s}d_{(hm),s} = V_s, \tag{8.10}$$

so that the mesh area in 1+1-dimensional superspace is given by

$$M_{(hm),s} = V_s\frac{((h+m\alpha)^2 + m^2\alpha^2)^{\frac{1}{2}}}{a}. \tag{8.11}$$

The generalisation in physical space would give:

$$M_{(hm)} = V\frac{|h+m\alpha|}{a}. \tag{8.12}$$

It is clear that for the case $h = -m\alpha$ the definition in physical space is again useless since the mesh area then becomes equal to zero.

8.4 The principle of selective cuts in superspace

One of the ways of calculating the stability of crystal faces is to consider the surface free energy Γ (Bennema and van der Eerden, 1987). A face is more stable when its surface free energy is lower. In a chemical bond model, as described above, the surface free energy is taken to be the energy per unit area necessary to create this surface by cutting bonds. The surface free energy thus corresponds to the broken bond energy per unit area involved in dividing an infinite crystal over the plane, in two semi-infinite halves. The equilibrium form of a crystal will then be such that the total surface free energy is minimal. The equilibrium form of a crystal can differ substantially from its growth form. The calculation of growth forms is more complicated and will not be considered in this paper.

The generalisation of several crystallographic concepts in the previous section, now allows for the calculation of surface energies using superspace. The broken bond energy per unit area is calculated for a crystallographic hyperplane cutting the embedded 1+1-dimensional crystal. Since we are now dealing with a bond density, we have to integrate the broken bond energy over a generalised mesh area $M_{(hm),s}$. The surface free energy is then obtained by dividing this result by the mesh area.

It is very important to see that in the intersection of one hyperplane with the 1+1-dimensional embedded crystal (described by equation 8.5) the same bonds are cut as in the intersection of a grid of these planes (with interplanar distance $d_{(hm),s}$) with the physical crystal. This is illustrated in figure 8.2 for the (01) plane. Traveling along the $\boldsymbol{a}$ axis, the relation in bond length between successive bonds cut by the grid in the physical crystal is very complicated. The bond density cut in superspace, indicated by the hatched area in the figure, is mathematically clearly much more convenient for calculations.

From the foregoing it is clear that the generalisation of calculating broken bond energies per mesh area to superspace for one $(hm)_s$ plane is equivalent to taking the physical crystal and cutting it at its intersections with all planes $(hm)_s$ of the grid. These planes intersect the physical crystal at distances $d_{(hm)}$ apart.

If the crystal is not modulated each such cut gives the same result and it is sufficient to consider a constant energy over the whole mesh area of a plane. Now one can see that in the case that there is a modulation, in fact a bond average over the grid of planes is taken. We will assume that this average determines the equilibrium form of the modulated crystal. This assumption will be addressed in the discussion.

The described procedure has a further striking aspect, which will be referred to as the principle of selective cuts, which is essential for the stability of satellite faces on modulated crystals. At first instance it might seem that in the grid of planes each possible modulated bond is encountered since there is no periodicity. However, from figure 8.2 it is, already by inspection, obvious that only a fraction of all possible bonds is found. This fraction is indicated for the (01) plane in the figure by depicting a finite number of its bonds. The energy of a bond is taken to be lower when the bond is longer. Therefore, it is obvious that the surface free energy of a hyperplane can be lower than the free energy obtained if we average over all possible bonds. This means that the average bond length in the fraction is then larger than a.

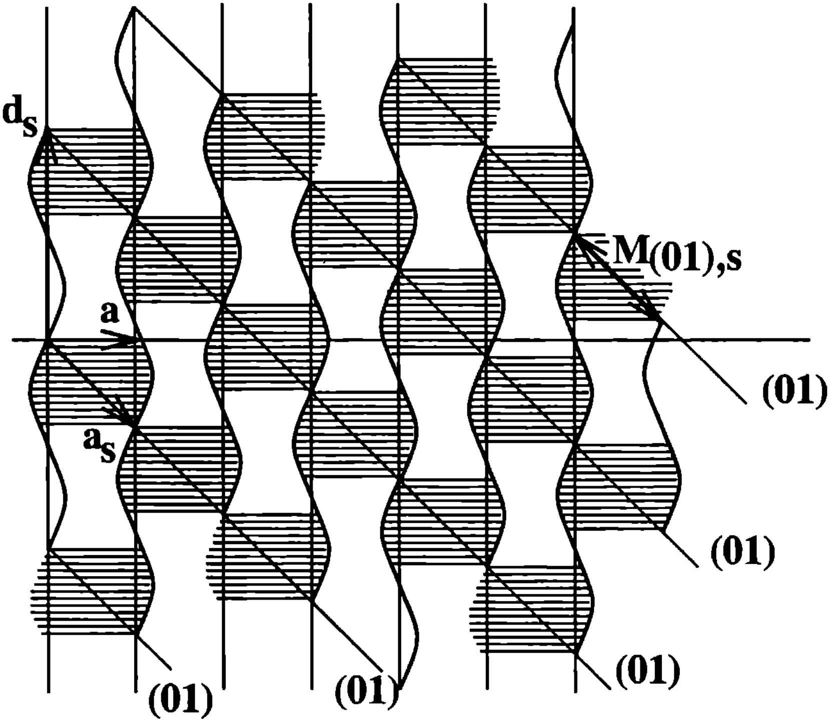

Figure 8.2 The principle of selective cuts demonstrated for the (01) plane. The mesh area $M_{(01),s}$ is indicated.

One must realise that for hyperplanes of which the indices h and m have some common divisor (other than 1) not every plane from the grid of planes $(hm)_s$ cuts the same set of bonds. (The same problem occurs for (hkl) faces with common divisors in non-modulated three-dimensional crystals.) We will not consider such planes in this paper, but they could be taken into account by averaging over all bonds cut by all the planes from the grid within one unit cell of the superspace lattice. For hyperplanes of which the indices have no common divisor (except 1) this procedure gives exactly the same result as integrating over a generalised mesh area.

As mentioned before, each phase τ along the internal $\boldsymbol{d}_s$ axis corresponds to a modulated crystal with the same two periodicities a and $1/q$. Therefore we assume that it is a legitimate procedure to minimise the surface free energy individually for each plane $(hm)_s$ by varying the phase at which the hyperplane intersects the $\boldsymbol{d}_s$ axis. That is equivalent to varying the phase τ_0 in equation 8.5. This assumption will also be addressed in the discussion.

We have thus obtained the very important result that the principle of selectivity gives rise to stabilised satellite faces. One already expects that for large mesh areas (roughly corresponding to high index planes) it is more difficult to let the selectivity principle work favourably. So, as a rule of thumb, high index planes will be less stable than low index planes.

8.5 Extension of the Wulff plot construction according to Herrring

The construction of an equilibrium form of a crystal from calculated surface energies has been treated by Herring (Herring (1951), Herring (1953)). In short, one draws a radius vector, with the surface free energy Γ as a measure for its length, in the direction of the face normal. Then a plane is constructed through the tip of each radius vector perpendicular to the vector. The shape of the equilibrium form is the body formed by all points reachable from the origin without crossing any of these planes. Cusps in the polar Γ plot can thus give planes on the equilibrium form. We will show that performing the same procedure in superspace can give a modulated one-dimensional crystal with satellite faces.

Since only bonds parallel to the physical space are considered, a crystallographic hyperplane parallel to this space will never cut a bond. Its surface free energy must therefore be zero. Let's now consider an arbitrary direction of a face normal which makes an angle θ with the $\boldsymbol{a}$ axis and assume that for this direction there is no selectivity. This latter assumption for example always holds when the modulation amplitude is zero. The surface free energy then fulfills the following relation:

$$\Gamma(\theta) = \Gamma_{max} \left|\cos\theta\right| . \tag{8.13}$$

The $\cos\theta$ dependence is simply the area along the $\boldsymbol{d}_s$ axis of the cut bond density, divided by the corresponding mesh area. Making a polar plot of Γ thus yields two circles. All constructed planes at tips of radial vectors of the Γ plot intersect the $\boldsymbol{a}$ axis in the same point corresponding to Γ_{max} in physical space. In figure 8.3 the Wulff plot of a model calculation is shown. The details will be treated in the next section, but at this point the figure is already illustrative for the two circles in superspace. The infinitely sharp cusp for $\theta = \pm\frac{\pi}{2}$ corresponds to the face $h = -m\alpha$, which strictly speaking never occurs due to the irrationality of α. This cusp, however, actually reduces the dimension of the equilibrium form by one. In this way, the equilibrium form becomes one-dimensional as required, since we consider a modulated one-dimensional crystal. It is important to realise that the generalisation of bonds with no internal component is essential for this reduction. If bonds also had an internal component, the obtained equilibrium form would be 1+1-dimensional. The notion of a crystal form in superspace was introduced by Janner (1983).

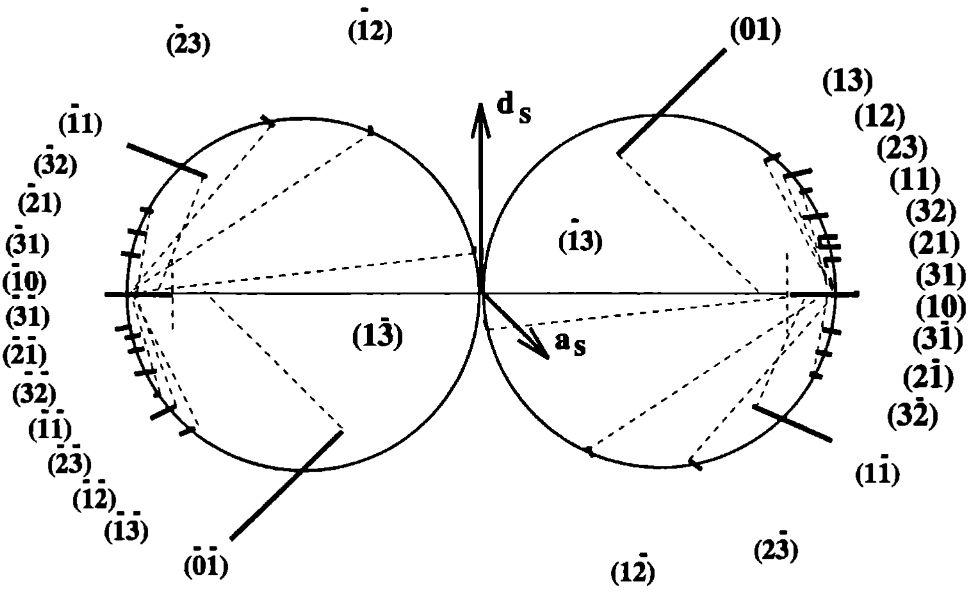

Figure 8.3 Generalised Wulff plot construction in superspace for the case $\alpha = 0.3$ and $f = 0.2a$. Faces with indices up to 3 have been plotted.

As we have derived, (hm) planes can be stabilised due to the principle of selectivity. They therefore give cusps in the two-circle Wulff plot and the planes constructed at the minimum energy vectors in principle do not cut the $\boldsymbol{a}$ axis at the same point any longer. The intersection closest to the origin will determine the morphology and this may very well correspond to a satellite face. The distance γ, between the origin and the intersection of a plane with the $\boldsymbol{a}$ axis, thus determines the morphological importance of the plane. The surface free energy Γ and the distance γ are related in the following way:

$$\gamma = \Gamma / \left|\cos\theta\right|.$$

8.6 A model calculation

A calculation of surface energies has been performed for 200 different values of α in $q = \alpha a^*$, $0 \leq \alpha \leq 1$ and a constant amplitude $f = 0.2a$. Crystallographic planes (hm) have been considered for which $-4 \leq h, m \leq 4$. For the minimisation the phase τ_0 was varied over 750 different values, in order to find the spreading between maximal and minimal surface energies.

The length of a bond at phase τ in cell n along the $\mathbf{a}$ axis is given by

$$l(n,\tau) = a + f(\sin 2\pi(\alpha(n+1) + \tau + \tau_0) - \sin 2\pi(\alpha n + \tau + \tau_0)), \tag{8.14}$$

where we assume that $2f < a$. The energy of a bond as function of its length is taken to be

$$\Phi(l(n,\tau)) = \frac{\chi}{l(n,\tau)}. \tag{8.15}$$

The surface free energy Γ is then calculated according to

$$\Gamma_{(hm)} = \frac{\sigma\,|\cos\theta|}{M_{(hm),s}} \int_{M_{(hm),s}} dM\, \Phi(l(n(M),\tau(M))) \tag{8.16}$$

where σ is the bond density in superspace, which we take to be equal to 1 m^{-1}.

The integration only runs over one generalised mesh area, since the remainder of the plane is just a periodic repetition of this mesh area.

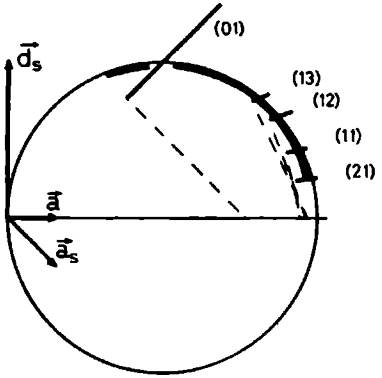

Figure 8.4 Part of the generalised Wulff plot construction of figure 8.3 for indices up to 40. It clearly shows the singular shape of the cusps.

In figure 8.3 the results for $q = 0.3a^*$ and $f = 0.2a$ are represented in the Wulff plot for $-3 \leq h, m \leq 3$. The line segments intersecting the circles represent the spreading of the surface energies found for the 750 values of τ. The figure shows that cusps indeed occur for (hm) planes. In this case the modulated one-dimensional crystal is bounded by (01) faces. It is interesting to know what the exact shape of the cusps is. Therefore, the calculation has been repeated for all faces with indices $-40 \leq h, m \leq 40$, which have their face normals in some restricted part of the two-circle Wulff plot.

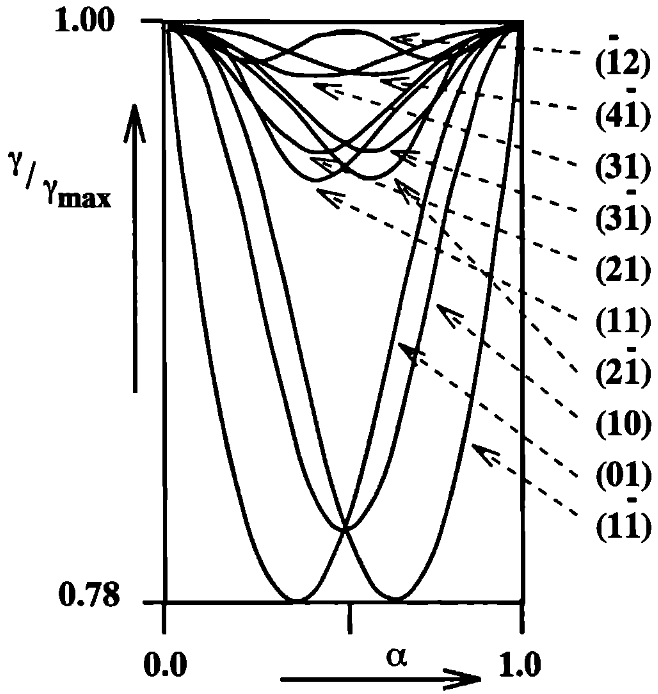

Figure 8.5 Normalised $\gamma = \Gamma / |\cos\theta|$ values for 200 α points, calculated by minimising over 750 phases. The smallest value of γ corresponds to the highest morphological importance. A representative set of crystallographic planes has been plotted. $f = 0.2a$.

The results are shown in figure 8.4, from which it is clear that the spreading in energy is definitely much larger for the low index planes already present in figure 8.3, than for any other crystallographic plane in their neighbourhood. It is clear that the cusps in the extended Wulff plot have a singular character.

Figure 8.5 shows the results of the $\gamma = \Gamma / |\cos\theta|$ values, that determine the morphological importance, calculated for the 200 different α values. In order to keep this figure surveyable not all calculated crystallographic planes have been plotted; instead, it has been tried to give a representative picture. As explained before, the surface free energy is, per construction, zero when α is exactly $-h/m$. These singular points are therefore not drawn. From the figure it becomes clear that the order in stability of faces is strongly dependent on α. Consider for example the $(1\bar{1})$ plane. It is very stable for large values of α, but less stable, with respect to other planes, for small values of α. One can also observe that in general the surface free energy of low index planes is stabilised more than that of high index planes. Looking more closely to this figure one can see that it has a mirror symmetry in $\alpha = 0.5$. The origin of this symmetry is explained in appendix F.

8.7 Discussion

In this section we will discuss the essential assumptions made in this paper in more detail.

One of these assumptions is that the average energy of all bonds cut by a mesh area of one hyperplane determines the presence of this face on the equilibrium form of the modulated crystal. This may seem strange for a modulated one-dimensional crystal, because its equilibrium form is determined by merely two faces. Only two bonds have to be cut in order to create the faceted crystal from the infinite crystal. However, for a modulated three-dimensional crystal (and even for a modulated two-dimensional one), it does make sense to average over all bonds cut by the mesh area. In order to create a satellite face $(hklm)$ from an infinite crystal, in general not only one, but an infinite number of modulated bonds must be cut. All of these cut modulated bonds can be represented by sets of bonds intersected by mesh areas in superspace. This will be worked out in a forthcoming paper.

Now, consider a very large equilibrium form. Then, in creating a face from the infinite crystal so many bonds must be cut, that adding or subtracting one bond will have no influence on the overall free energy of the equilibrium form. On a face of such a very large crystal, many complete mesh areas $M_{(hm),s}$ will be present. With respect to this, the number of non complete mesh areas present on the face will be negligible. In other words we approximate the surface free energy as if an integer number of mesh areas determines the free energy.

Closely connected to the averaging procedure is the assumption that the phase of the modulation can be adjusted for each face independently, in order to minimise the free energy of the face. Again we will discuss the relevance of this assumption for the modulated three-dimensional crystal. For an ideal modulated crystal all bonds on all faces in principle change when the phase of the modulation is varied. This implies that varying the phase, in order to minimise the surface free energy of one face, automatically changes the free energy of all other faces. Nevertheless, we have used independent phases for each face. The reason for this is the following. Adding a single layer of atoms to one particular face, clearly changes the phase of the modulation at that surface, but there is no change in the phases of the modulation at the other faces. In the case of a very large crystal, adding this layer to the face hardly changes the size of the surface. However, the surface free energy may change considerably due to the selectivity principle. Thus, the total surface free energy of a large crystal can, even for a fixed number of particles, be minimised by adding and removing layers on different faces. Thereby not so much the surface area is changed, but to a larger extent the phase of the modulation at each individual face and therefore its surface free energy.

In real, non ideal, crystals this minimising process will certainly be influenced by the presence of defects that locally alter (pin) the modulation phase in such a way that the bulk energy is minimal. A crystal surface is an intrinsic defect of a finite crystal and will therefore tend to minimise the surface free energy. We think that our assumption of using independent phases in the minimising procedure is therefore a realistic one.

8.8 Conclusions

It has been shown that the well known procedure for calculating the stability of faces from surface energies can be extended to superspace for modulated crystals.

It is very well possible to generalise concepts as chemical bonds, crystallographic planes, interplanar distances and mesh areas. Also a Wulff plot can be drawn in superspace yielding the equilibrium form of the physical crystal.

Due to the principle of selectivity, satellite faces indeed get a chance of appearing, which is not a priori obvious. Satellite faces can even be more stabilised than main faces and the shape of cusps in the generalised Wulff plot is singular.

In order to demonstrate the selectivity principle the situation has been outlined for a modulated one-dimensional crystal. There are however no limitations for the extension of the presented method to higher dimensions. Results of calculations for modulated three-dimensional cases will be published in the near future.

In the one-dimensional case it has been demonstrated that the order in stability of faces is strongly dependent on the modulation parameter α. In general low index faces will be more stable than high index faces. Further, it has become clear that with a larger modulation amplitude, in general, more stabilisation can be obtained.

Our analysis shows that the superspace construction is not only relevant for a structural description, but also for the analysis of physical properties of modulated crystals, the example in this paper being the morphology.

Acknowledgments

The authors would like to thank Prof. J. van der Eerden and Dr. L. J. P. Vogels for stimulating discussions during the first developments of the presented theory. We are indebted to Prof. A. Janner for his suggestions, enthousiastic support and critical reading of the manuscript. We would like to mention that S. van Smaalen has independently studied the same subject as treated in this paper (van Smaalen 1993), however on a different footing.

References

Bennema, P., *Sir Charles Frank, an eightieth birthday tribute*, edited by R. G. Chambers, J. E. Enderby, A. Keller, A. R. Lang and J. W. Steeds (Philadelphia and New York: Adam Hilger Bristal, 1991).

Bennema, P., *Handbook of crystal growth* Ch. 7, edited by Hurle, D. T. J. (Elsevier, 1993).

Bennema, P., Balzuweit, K., Dam, B., Meekes, H., Verheijen, M. A., and Vogels, L.J.P., *J. Phys. D: Appl. Phys.* **24**, 186 (1991).

Bennema, P., and van der Eerden, J.P. *Morphology of Crystals Part A*, edited by I. Sunagawa (Tokyo: Terra Scient., Dordrecht: Reidel Publ.,1987).

Bennema, P., Kremers, M., Meekes, H., Balzuweit, K., and Verheijen, M. A., *Discuss. Faraday. Soc.* **95**, 2 (1993).

Dam, B., Janner, A., Bennema, P., v.d. Linden, W. H., and Rasing, Th., *Phys. Rev. Lett.* **50**, 849 (1983).

Dam, B., Janner, A., and Donnay, J. D. H., *Phys. Rev. Lett.* **55**, 2301 (1985).

Hardy, G. H., and Wright, E. M., *An introduction to the theory of numbers* (Oxford: Clarendon Press, 1954).

Hartman, P., Perdok, W. G., *Acta Cryst.* **8**, 525 (1955).

Herring, C., *Phys. Rev.* **82**, 87 (1951).

Herring, C., *Structure and Properies of Solid Surfaces* edited by Gomer, R., and Smith, C. S., 5 (University of Chicago Press, 1953).

Janner, A., *Studies in Physical and Theoretical Chemistry* **23**, 461 (Amsterdam: Elsevier, 1983).

Janner, A., Rasing, Th., Bennema, P., and v.d. Linden, W. H., *Phys. Rev. Lett.* **45**, 1700 (1980).

Janssen, T., and Janner, A., *Adv. Phys.* **36**, 519 (1987).

van Smaalen, S., *Phys. Rev. Lett.* **70**, 2419 (1993).

Vogels, L.J.P., Balzuweit, K., Meekes, H., and Bennema, P., *J. Crystal Growth* **116**, 397 (1992).

Appendix E

In this appendix we will show that the generalisation of chemical bonds, encountered in a modulated one-dimensional crystal, to bonds in superspace with only an external component, yields a uniform bond density. If one travels in the modulated one-dimensional crystal starting from the origin along the bonds, one encounters bonds in such a way that the n'th bond has phase $n\alpha + \phi$ as can be seen from equation 8.3. This means that for the generalisation we must draw successively bonds in superspace, each time separated along the $\boldsymbol{d}_s$ axis by a phase α. Since α is an irrational number, it is not so easy to see what the result of this procedure is. Therefore, we use the following approach. Every irrational number can be approximated by means of a continued fraction expansion (Hardy and Wright, 1954). Thus, the irrational number is approximated by a fraction p/q in which p and q are both integers. In every next approximation, which is a better one, q increases. The irrational number can be considered to be the approximation for which q becomes infinite. Now consider such a commensurate approximation $p/q \approx \alpha$. In this case we must draw bonds in superspace separated by a phase p/q. After drawing q bonds the total phase has increased by p which is an integer number. This combined with the periodicity along the $\boldsymbol{d}_s$ axis leads to the conclusion that there are q different bonds in every unit cell in superspace. It is easy to see that within each unit cell these bonds have a mutual constant distance in phase of $1/q$. In the limit that q goes to infinity, we get an infinite number of bonds in every unit cell and the constant distance in phase between two successive bonds becomes zero in this limit. So, we obtain a uniform bond density in superspace.

Appendix F

The reason for the mirror symmetry in figure 8.5 is the following. Let the atomic positions of a certain modulated one-dimensional crystal be given by equation 8.3 with fixed phase $\phi = \phi_1$.

$$r(n, \phi) = na + f \sin 2\pi(qna + \phi_1).$$

Then, there exists another modulation wave of the same type that gives the same displacements of the atoms from their average positions, but that is different between the atoms. This is the modulation wave with

$$q' = a^* - q = (1 - \alpha)a^*$$

and

$$\phi = \phi_2 = 1/2 - \phi_1.$$

Namely

$$\sin 2\pi(q'na + \phi_2) = \sin 2\pi(qna + \phi_1).$$

Since the atomic positions are the same for both modulation waves, also the chemical bonds must be the same, since in our model these depend only on the positions of the atoms.

A face (hm) for a certain α is equivalent to a $((h+m)\overline{m})$ face for $\alpha' = 1 - \alpha$, because

$$ha^* + mq$$

becomes

$$(h + m)a^* - mq'$$

in the new crystal upon substituting

$$q = a^* - q'.$$

This explains the observed symmetry in figure 8.5, which is reflected in the same relation between the indices h and m.

Chapter 9

Equilibrium morphology of incommensurately modulated crystals, a superspace description

Equilibrium morphology of incommensurately modulated crystals a superspace description

M. Kremers, H. Meekes, P. Bennema, M. A. Verheijen
and J.P. van der Eerden

Abstract

The theory for the explanation of equilibrium morphologies of incommensurately modulated 1-dimensional crystals, presented in a previous paper, is extended to the case of incommensurately modulated 3-dimensional crystals. It is shown that, concerning the morphology, there exists a one-to-one correspondence between faces on the physical crystal and crystallographic hyperplanes of the embedded crystal in superspace. This holds for both main faces and satellite faces. The occurrence of the latter, however, is unique for incommensurately modulated crystals. It is shown that the stability of satellite faces, as well as main faces, can be attributed to a principle of selective cuts. The superspace approach that is developed leads to a calculation method for surface free energies that, in principle, can be applied to incommensurately modulated structures of arbitrary complexity. Equilibrium morphologies are constructed from the calculated surface free energies by means of a standard Wulff plot. The dependence of the equilibrium morphology on several structural parameters is studied for an incommensurately modulated simple cubic model crystal. This study allows for a basic understanding of the differences in morphology of $AuTe_2$ crystals and $((CH_3)_4N)_2ZnCl_4$ crystals.

9.1 Introduction

It is well-known that the morphology of crystals is often determined by flat faces. The orientation of these faces is related to directions of Fourier wave vectors of the structure. Namely, the Fourier wave vectors are parallel to the face normals. Crystal faces can, therefore, perfectly be labeled by a set of three integral indices. In case of incommensurately modulated crystals, a $\mathbb{Z}$-module with a rank higher than its dimension is formed by the Fourier wave vectors (Janner and Janssen (1977), de Wolff et al. (1981)). In these crystals extra periodicities, modulations, are present in addition to the basic periodicities that define a 3-dimensional translation lattice. The rank of the $\mathbb{Z}$-module exceeds its dimension if the modulations are incommensurate with the basic lattice. A famous example is the mineral calaverite $Au_{1-x}Ag_xTe_2$. Its complex morphology has puzzled crystallographers for a long time (see for example Goldschmidt et al., 1931). A labeling of the crystal faces by three low indices did not seem to be possible, though many attempts were made. At present, it is known that there is a one-dimensional incommensurate modulation in this crystal (Sueno et al. (1979), van Tendeloo et al. (1983), Schutte and de Boer (1988)), so that the rank of the $\mathbb{Z}$-module is four. The Fourier wave vectors, therefore, can be labeled by four integral indices. This was the key to solving the, only partly understood morphology of $Au_{1-x}Ag_xTe_2$ crystals. The faces that determine the morphology of incommensurately modulated crystals are perpendicular to Fourier wave vectors of the $\mathbb{Z}$-module. It was shown that the faces of $Au_{1-x}Ag_xTe_2$ could be labeled, very satisfactorily, with four low integral indices (Dam et al. (1985), Janner and Dam (1989)). The same behaviour has been found for many other incommensurately modulated crystals (see Bennema et al., 1991). In figure 9.1 the result, as was given by Janner and Dam (1989), is reproduced for a typical twin crystal of $Au_{1-x}Ag_xTe_2$. A crystal face is called a main face if the fourth index is zero. Otherwise, it is called a satellite face. The investigation of many mineral crystals, but also of crystals grown in our laboratory, has revealed that satellite faces are very dominant for the morphology of $Au_{1-x}Ag_xTe_2$ crystals. This is

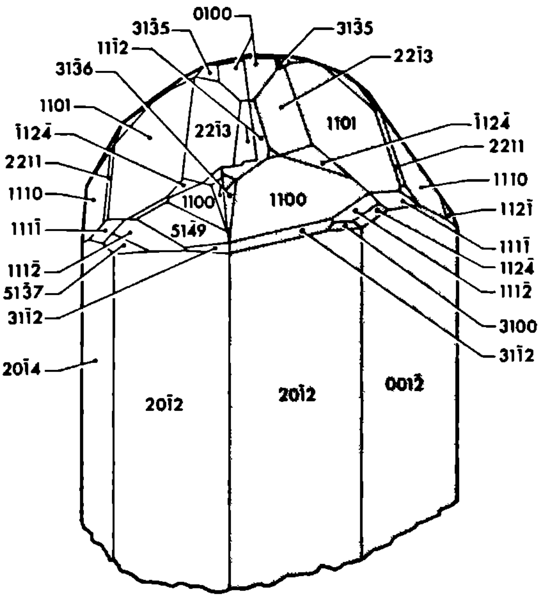

Figure 9.1 A typical twin crystal of the mineral $Au_{1-x}Ag_xTe_2$. This figure was reproduced from Janner and Dam (1989). The crystal faces are labeled with four integral indices, reflecting the presence of an incommensurate modulation. The faces with a non-zero fourth index are called satellite faces. It is clear that many, large satellite faces determine the morphology of $Au_{1-x}Ag_xTe_2$.

a clear example of a strong influence of the incommensurate modulation on the physical properties of a crystal. The beautiful description of the orientation of crystal faces, however, does not yet clarify the nature of this influence. In order to have a better understanding one would also like to be able to explain the stability of these faces. It is shown in this paper that it is not expected, in advance, that satellite faces can appear as stable crystal faces. In this paper we take on the challenge to find an explanation for the stability of (satellite) faces on incommensurately modulated crystals.

In two previous papers (Bennema et al. (1993), Kremers et al. (1994)), we have already outlined a superspace description for the morphology of an incommensurately modulated 1-dimensional model crystal. Here, we first want to recall the ideas that have been used in this superspace description. One adopts the view that the presence of a flat face on the equilibrium morphology of a crystal is determined by the surface free energy of that face, because the crystal will take such a shape in equilibrium, that the integrated surface free energy is minimal. Surface free energies are calculated by extending a broken-bond model to the embedding of the incommensurately modulated 1-dimensional crystal in a $1+1$-dimensional superspace. Thus, a uniform bond density is obtained in this superspace. In addition, several crystallographic concepts are generalised. In this way it is possible to show, in superspace, that the presence of an incommensurate modulation leads to a principle of selective cuts for the broken bonds. This principle implies that the average length of bonds intersected by a (satellite) face can be larger than the length that these bonds would have if there were no modulation. If a larger bond length corresponds to a lower bond energy, satellite faces (but also main faces) can be stabilised considerably and can appear on the equilibrium morphology of the crystal.

In the present paper, we treat equilibrium morphologies of incommensurately modulated 3-dimensional crystals. They are embedded in a $3+1$-dimensional superspace. In essence, the situation comes down to the same $1+1$-dimensional analysis as treated by Kremers et al. (1994). It is shown that (satellite) faces on the physical crystal correspond to crystallographic hyperplanes of the embedded crystal. An important result of this paper is, that this correspondence is one-to-one for the average energy of the (embedded) bonds broken by these planes. Consequently, it is in principle possible to calculate the equilibrium morphology of any incommensurately modulated crystal using a superspace approach. Also van Smaalen (1993) has reported on a theory for the explanation of the stability of satellite faces. This author was able to derive an expression for the surface free energy of faces, without making use of the superspace. We have agreed with van Smaalen (1994) to compare the results of both theories very carefully, in the near future. The benefits of using a superspace approach have been discussed by Bennema et al. (1994). Moreover, they become apparent in the present report.

This paper is organised in the following manner. In section 9.2 the model is presented for the description of an incommensurately modulated 3-dimensional crystal. In addition, several problems are outlined that arise if one wants to calculate surface free energies of faces within such a description. In the subsequent section, 9.3, the embedding of the crystal model in a 3 + 1-dimensional superspace is described. It is also explained how (chains of) bonds, as well as crystallographic hyperplanes, must be treated in this superspace. In section 9.4 we show that there exists a one-to-one correspondence between such crystallographic hyperplanes and faces on the physical crystal for the morphology. We would like to advise readers that are not interested in the details of this analysis to skip section 9.4 and to go directly to section 9.5. There, it is shown how this one-to-one correspondence can be used for the calculation of surface free energies and for the understanding of the principle of selective cuts. In the next section, 9.6, model calculations are presented by means of which the influence of several structural aspects on the equilibrium morphology is investigated. The basic assumptions that are used in this paper are critically discussed in section 9.7, where also the consequences of the obtained results for actually occurring incommensurately modulated crystals are evaluated. Finally, conclusions are presented in section 9.8.

9.2 The incommensurately modulated crystal

9.2.1 Structure

An incommensurate 3-dimensional displacively modulated crystal can be modeled in the following way. There are j kinds of point-like atoms in the 3-dimensional physical space. The positions of the atoms of kind j are given by position vectors $\boldsymbol{r}(\boldsymbol{n}, j)$:

$$\boldsymbol{r}(\boldsymbol{n},j) = \boldsymbol{n} + \boldsymbol{r}_j + \boldsymbol{f}_j u_j\left(\boldsymbol{q}\cdot[\boldsymbol{n}+\boldsymbol{r}_j] + \phi_j\right) \tag{9.1}$$

where the last term describes the effect of the modulation.
$\boldsymbol{n} = n_1\boldsymbol{a}_1 + n_2\boldsymbol{a}_2 + n_3\boldsymbol{a}_3$ with n_1, n_2 and $n_3 \in \mathbb{Z}$ and $\{\boldsymbol{a}_1, \boldsymbol{a}_2, \boldsymbol{a}_3\}$ forming the basis of a translation lattice Λ. The corresponding lattice translational symmetry is broken due to the modulation. In the 3-dimensional space of the crystal we define spatial positions

$$\boldsymbol{x} = x_1\boldsymbol{a}_1 + x_2\boldsymbol{a}_2 + x_3\boldsymbol{a}_3$$

by means of a set of three fractional coordinates (x_1, x_2, x_3) on the basis of Λ. The vector $\boldsymbol{r}_j$ gives for each atom-kind j a (different) shift with respect to the point $\boldsymbol{n}$.

The modulation is characterised by the modulation function u_j, the modulation amplitude vector $\boldsymbol{f}_j$ and the modulation wave vector $\boldsymbol{q}$. The modulation function u_j is periodic in its argument: $u_j(\phi) = u_j(\phi + 1)$. This argument contains a constant phase factor ϕ_j that determines the shift of the modulation wave with respect to the origin. We consider only one modulation wave vector $\boldsymbol{q}$ that is equal for all atoms, because this is the situation encountered for the majority of incommensurately modulated crystals known. The modulation wave vector is defined on the basis $\{\boldsymbol{a}_1^*, \boldsymbol{a}_2^*, \boldsymbol{a}_3^*\}$ of the reciprocal lattice Λ^*,

$$\boldsymbol{q} = q_1\boldsymbol{a}_1^* + q_2\boldsymbol{a}_2^* + q_3\boldsymbol{a}_3^*, \qquad q_1, q_2, q_3 \in \mathbb{R}. \tag{9.2}$$

A modulated crystal is called incommensurate if at least one of the numbers q_1, q_2 or q_3 is irrational. In that case $\boldsymbol{q}$ builds a $\mathbb{Z}$-module of rank four together with $\boldsymbol{a}_1^*$, $\boldsymbol{a}_2^*$ and $\boldsymbol{a}_3^*$. This $\mathbb{Z}$-module is used, for example, to describe the positions of spots in the X-ray diffraction patterns of incommensurately modulated crystals. It thus carries the Fourier transform of the structure. In equation (9.1) the phase $\phi = \boldsymbol{q} \cdot [\boldsymbol{n} + \boldsymbol{r}_j] + \phi_j$ is determined, for each atom, by the modulation wave vector $\boldsymbol{q}$. Due to the incommensurability, ϕ (mod.1) takes infinitely many different irrational values in the interval $[0, 1)$ for an infinite crystal. Therefore, there exist for each atom-kind j infinitely many different displacements from the positions $\boldsymbol{n} + \boldsymbol{r}_j$. This, actually, breaks the lattice translational symmetry.

Besides positions of atoms, a model for the morphology of crystals should further include (chemical) bonds. These are defined as line elements connecting any two different atomic positions. The bond energy depends on both the length of the bond and on the kinds of the atoms that are connected by the bond. It will be clear that, since the atomic positions are incommensurately modulated, there can also be infinitely many different bond lengths and corresponding bond energies.

9.2.2 Incommensurability of the modulation wave vector

It is important to discriminate between two possible types of modulation wave vectors $\boldsymbol{q}$ as defined by equation (9.2), because each type leads to a different (equilibrium) morphology. The two types correspond to the two ways in which $\boldsymbol{q}$ can be incommensurate with respect to the reciprocal lattice Λ^*.

In the first case, $\boldsymbol{q}$ has the same direction as some reciprocal lattice vector $\boldsymbol{H} \in \Lambda^*$. The ratio of their lengths $|\,\boldsymbol{q}\,| \;/\; |\,\boldsymbol{H}\,|$, however, is an irrational number. For this, it is necessary that at least one of the numbers q_1, q_2 or q_3 is irrational and that the ratio of any two of these numbers is rational. The modulation wave vector $\boldsymbol{q} = q_1\boldsymbol{a}_1^*$, with $q_1 \notin \mathbb{Q}$, is an example. We refer to this case as a modulation wave vector with an incommensurate *length.*

Alternatively, there may be no $\boldsymbol{H} \in \Lambda^*$ that points in the same direction as $\boldsymbol{q}$. In order to have this, the ratio of at least two of the three numbers q_1, q_2 and q_3 must be irrational. Certainly one of these two numbers is then irrational. An example is the modulation wave vector $\boldsymbol{q} = \cos\theta\; \boldsymbol{a}_1^* + \sin\theta \boldsymbol{a}_2^* \;|\boldsymbol{a}_1^*| \;/\; |\boldsymbol{a}_2^*|$ with $\tan\theta \notin \mathbb{Q}$and $\boldsymbol{a}_1^* \cdot \boldsymbol{a}_2^* = 0$, that has the same length as $\boldsymbol{a}_1^*$. To this case we refer as a modulation wave vector with an incommensurate *direction.*

Another classification of modulation wave vectors $\boldsymbol{q}$ is possible. Consider, in reciprocal space, all points $\boldsymbol{H} + m\boldsymbol{q}$ and let m run over all integral numbers and $\boldsymbol{H}$ over the reciprocal lattice Λ^*. Three different situations can be encountered. First, the points $\boldsymbol{H} + m\boldsymbol{q}$ can become dense on lines. The wave vector $\boldsymbol{q}$ then has an incommensurate *length.* Secondly, they can become dense on planes and the last possibility is that the points $\boldsymbol{H} + m\boldsymbol{q}$ become dense on the whole space. The modulation wave vector has an incommensurate *direction* in the latter two cases. It is not necessary to make a distinction between these cases for the analysis presented in this paper.

9.2.3 The intersection of bonds by crystallographic planes

It has been shown experimentally (Janner et al. (1980), Dam et al. (1983), Dam et al. (1985), Janner and Dam (1989), Bennema et al. (1991)) that the orientation of faces on incommensurately modulated crystals can be described very accurately with four integral indices h_1, h_2, h_3 and h_4. These indices define a vector $\boldsymbol{H}_{(h_1h_2h_3h_4)}$ perpendicular to the face.

$$\boldsymbol{H}_{(h_1h_2h_3h_4)} = h_1\boldsymbol{a}_1^*+h_2\boldsymbol{a}_2^*+h_3\boldsymbol{a}_3^*+h_4\boldsymbol{q} = (h_1+h_4q_1)\boldsymbol{a}_1^*+(h_2+h_4q_2)\boldsymbol{a}_2^*+(h_3+h_4q_3)\boldsymbol{a}_3^*. \quad (9.3)$$

Faces $(h_1h_2h_3h_4)$ for which $h_4 = 0$ are main faces and those with $h_4 \neq 0$ are satellite faces. The existence of the latter necessitates the use of four indices instead of three. Although this gives a satisfying description of the orientation of the faces that can occur, it does not explain why such (satellite) faces are stable. This is the reason that we want to be able to find the equilibrium morphology by means of a Wulff plot (Herring (1951) Herring (1953)), using calculated surface free energies $\Gamma_{(h_1h_2h_3h_4)}$.

In our model, the surface free energy $\Gamma_{(h_1h_2h_3h_4)}$ (at $T = 0$) is defined as the energy per unit area necessary to create the face $(h_1h_2h_3h_4)$ from an infinite crystal by cutting bonds. The energy necessary to cut one specific bond is exactly the bond energy. For incommensurately modulated crystals the calculation of $\Gamma_{(h_1h_2h_3h_4)}$ is not straightforward, however, because of the presence of infinitely many different bonds.

Consider a crystallographic plane $(h_1h_2h_3h_4)$. It can be constructed by positioning a plane such, that it cuts $1/(h_1 + h_4q_1)$ of the $\boldsymbol{a}_1$-axis, $1/(h_2 + h_4q_2)$ of the $\boldsymbol{a}_2$-axis and $1/(h_3 + h_4q_3)$ of the $\boldsymbol{a}_3$-axis. If the plane is not perpendicular to the modulation wave vector $\boldsymbol{q}$, there can be no 2-dimensional lattice translational periodicity on this plane. In non-modulated crystals, on the other hand, there exists for each plane $(h_1h_2h_3)$ a 2-dimensional unit cell, called mesh area $M_{(h_1h_2h_3)}$. The whole plane can then be covered by periodically repeating this mesh area. Consequently, for the calculation of the surface free energy of non-modulated crystals it is sufficient to consider precisely one mesh area. On the contrary, crystallographic planes $(h_1h_2h_3h_4)$ of incommensurately modulated crystals, not perpendicular to $\boldsymbol{q}$, have no such mesh area. In order to calculate a $\Gamma_{(h_1h_2h_3h_4)}$ one can only average over the infinite plane.

For the crystallographic planes that are perpendicular to $\boldsymbol{q}$, it is essential to distinguish between the two types of modulation wave vector discussed in section 9.2.2. If the modulation wave vector has an incommensurate *direction*, the only planes perpendicular to $\boldsymbol{q}$ are $(000h_4)$. There is again no mesh area on these planes, due to the incommensurate *direction* of $\boldsymbol{q}$ and one has to consider the whole plane. For a modulation wave vector with an incommensurate *length*, there is no unique set of indices for the plane perpendicular to it. Suppose that q_1 is non-zero. Then all planes $(h_1, h_1\frac{q_2}{q_1}, h_1\frac{q_3}{q_1}, h_4)$ with $h_1\frac{q_2}{q_1}$ and $h_1\frac{q_3}{q_1} \in \mathbb{Z}$ are perpendicular to $\boldsymbol{q}$ for any h_4. Moreover, on these planes there does exist a 2-dimensional unit cell.

However, also the latter, special situation differs from the case of a non-modulated crystal, despite the existence of a mesh area. This difference becomes apparent when we want to divide the crystal in identical slices. A face $(h_1h_2h_3)$ on a non-modulated crystal is assumed (Bennema, 1993) to grow with layers of thickness $d_{(h_1h_2h_3)} = |\boldsymbol{d}_{(h_1h_2h_3)}|$, where

$$\boldsymbol{d}_{(h_1h_2h_3)} = \frac{\boldsymbol{H}_{(h_1h_2h_3)}}{|\boldsymbol{H}_{(h_1h_2h_3)}|^2}. \tag{9.4}$$

Using this $d_{(h_1h_2h_3)}$ as interplanar distance, one can define a grid of netplanes. All planes of the grid are then equivalent, having the same surface free energy, unless the three indices h_1, h_2 and h_3 have a common divisor larger than 1. In case of an incommensurately modulated crystal an analogous construction gives a grid of netplanes with interplanar distance $d_{(h_1h_2h_3h_4)} = |\boldsymbol{d}_{(h_1h_2h_3h_4)}|$, where

$$\boldsymbol{d}_{(h_1h_2h_3h_4)} = \frac{\boldsymbol{H}_{(h_1h_2h_3h_4)}}{|\boldsymbol{H}_{(h_1h_2h_3h_4)}|^2}, \tag{9.5}$$

where $\boldsymbol{H}_{(h_1h_2h_3h_4)}$ is given by equation (9.3). For the special case of a modulation wave vector with an incommensurate *length*, however, we have seen that no unique grid can be defined perpendicular to $\boldsymbol{q}$. Furthermore, due to the intrinsic lack of translational symmetry along $\boldsymbol{q}$ it is a priori not clear whether for any one of these grids all its netplanes have equal surface free energy. For all other crystallographic planes $(h_1h_2h_3h_4)$, non-perpendicular to $\boldsymbol{q}$, a unique grid is defined by equation (9.5). It is however again unclear whether the individual members of the grid have equal surface free energy, unless the face $(h_1h_2h_3h_4)$ is parallel to $\boldsymbol{q}$. Also in the case that the modulation wave vector has an incommensurate *direction*, one does not know a-priori whether netplanes of a grid have equal surface free energy.

It will be clear that one is faced with many problems in understanding the stability of faces $(h_1h_2h_3h_4)$ using the description of the incommensurately modulated structure defined by equation (9.1). Fortunately, a more elegant description is possible by making use of a space that has a dimension higher than 3, the so-called superspace.

9.3 Embedding in superspace

9.3.1 Structure in superspace

The incommensurate crystal defined by equation (9.1) can be embedded (Janner and Janssen (1977), de Wolff et al. (1981), Janner et al. (1983)) in a $3+1$-dimensional superspace. Perpendicular to the physical space of the crystal, which is called external space, one defines a so-called internal space. In our model the internal space has dimension 1, because there is only one modulation wave vector. The atoms of equation (9.1) are represented in superspace by wavy lines $\boldsymbol{r}_s(\boldsymbol{n}, j, \tau)$ extended along the internal direction:

$$\boldsymbol{r}_s(\boldsymbol{n}, j, \tau) = \left(\boldsymbol{n} + \boldsymbol{r}_j + \boldsymbol{f}_j u_j\left(\boldsymbol{q}\cdot[\boldsymbol{n}+\boldsymbol{r}_j] + \phi_j + \tau\right), \tau\right). \tag{9.6}$$

The first three components of the right-hand side of equation (9.6) are in the external space and the fourth, τ, runs in the internal space. The wavy lines, obtained in this way, intersect the physical space ($\tau = 0$) exactly in the points defined by equation (9.1).

The advantage of this embedding is that the obtained structure has lattice translational symmetry in the superspace. There is a lattice Λ_s with basis $\{\boldsymbol{a}_{1s}, \boldsymbol{a}_{2s}, \boldsymbol{a}_{3s}, \boldsymbol{a}_{4s}\}$, where

$$\begin{aligned} \boldsymbol{a}_{1s} &= (\boldsymbol{a}_1, -q_1\boldsymbol{e}), \\ \boldsymbol{a}_{2s} &= (\boldsymbol{a}_2, -q_2\boldsymbol{e}), \\ \boldsymbol{a}_{3s} &= (\boldsymbol{a}_3, -q_3\boldsymbol{e}), \\ \boldsymbol{a}_{4s} &= (0, \boldsymbol{e}). \end{aligned} \tag{9.7}$$

Again the first three components are in the external space and the fourth is in the internal space. The reciprocal lattice Λ_s^* then has the basis $\{\boldsymbol{a}_{1s}^*, \boldsymbol{a}_{2s}^*, \boldsymbol{a}_{3s}^*, \boldsymbol{a}_{4s}^*\}$, where

$$\begin{aligned} \boldsymbol{a}_{1s}^* &= (\boldsymbol{a}_1^*, 0) \\ \boldsymbol{a}_{2s}^* &= (\boldsymbol{a}_2^*, 0) \\ \boldsymbol{a}_{3s}^* &= (\boldsymbol{a}_3^*, 0) \\ \boldsymbol{a}_{4s}^* &= (\boldsymbol{q}, \boldsymbol{e}^*). \end{aligned} \tag{9.8}$$

Furthermore, $\boldsymbol{a}_{is} \cdot \boldsymbol{a}_{js}^* = \delta_{ij}$ and $\boldsymbol{e} \cdot \boldsymbol{e}^* = 1$.

We denote spatial positions in superspace by a set of four fractional coordinates: $(x_{1s}, x_{2s}, x_{3s}, x_{4s})$. This set represents the position vector:

$$\boldsymbol{x}_s = x_{1s}\boldsymbol{a}_{1s} + x_{2s}\boldsymbol{a}_{2s} + x_{3s}\boldsymbol{a}_{3s} + x_{4s}\boldsymbol{a}_{4s}.$$

It follows from (9.7) that any point (x_1, x_2, x_3) with respect to the basis $\{\boldsymbol{a}_1, \boldsymbol{a}_2, \boldsymbol{a}_3\}$ in the physical space is equal to the point $(x_1, x_2, x_3, q_1x_1 + q_2x_2 + q_3x_3)$ with respect to the basis $\{\boldsymbol{a}_{1s}, \boldsymbol{a}_{2s}, \boldsymbol{a}_{3s}, \boldsymbol{a}_{4s}\}$ in superspace.

9.3.2 Modulated bond chains in superspace

Consider, in the structure defined by equation (9 1), two atoms of the same kind j that would be translationally equivalent if there were no modulation In that case they would be separated by a so-called bond-chain vector

$$b = (b_1, b_2, b_3), \quad b_1, b_2, b_3 \in \mathbb{Z} \tag{9 9}$$

In such a non-modulated crystal we have a so-called periodic bond chain (pbc) (Hartman and Perdok (1955), Bennema and van der Eerden (1987), Bennema (1993)) if it is possible to construct an uninterrupted path of (one or more) bonds that connects the two translationally equivalent atoms If a modulation is present, however, the pbc can be deformed, because the atoms may be displaced. We assume that, despite the deformation, all constituent bonds of the pbc still exist and that no extra bonds are formed. Only the bond energies have changed In this paper we actually consider these modulated pbc's We refer to them as modulated bond chains (mbc)

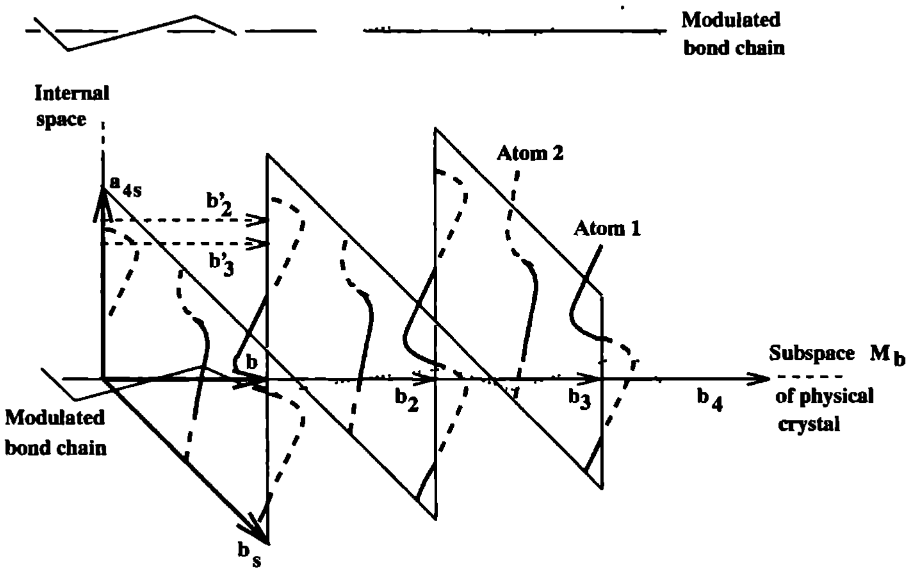

Figure 9.2 The embedding in the plane V_b, of a modulated bond chain (mbc) containing two kinds of atoms, 1 and 2 The mbc is represented by means of the physical subspace M_b Segments of the mbc can be represented by vectors b_i For each vector b_i there exists a translationally equivalent vector b'_i in the first unit cell of the lattice Λ_v on V_b. In this way a uniform bond density is constructed, because the modulation is incommensurate This is explained in the text

In figure 9.2 an example is given of the embedding of a mbc in superspace. The figure represents a view on the plane $V_{\boldsymbol{b},s}$ that is defined by the vectors $\boldsymbol{a}_{4s}$ and $\boldsymbol{b}_s$, where $\boldsymbol{b}_s$ is a lattice vector of Λ_s. One can construct $\boldsymbol{b}_s$ from the bond-chain vector $\boldsymbol{b}$ (equation (9.9)) in the following way:

$$\boldsymbol{b}_s = (b_1, b_2, b_3, 0). \tag{9.10}$$

The two vectors $\boldsymbol{b}_s$ and $\boldsymbol{a}_{4s}$ are basis vectors of a 2-dimensional lattice Λ_b that can be constructed on $V_{\boldsymbol{b},s}$. Therefore, it is possible to define positions in the plane $V_{\boldsymbol{b},s}$ by means of a set of two fractional coordinates, $(x_{b1}, x_{b2})_{V_{\boldsymbol{b},s}}$. Such a set represents the position vector:

$$\boldsymbol{x}_s = x_{b1}\boldsymbol{b}_s + x_{b2}\boldsymbol{a}_{4s}.$$

Each translation vector of Λ_b must have integral x_{b1} and x_{b2} in this notation.

The two kinds of wavy lines in figure 9.2 represent the embedding of two different atoms, 1 and 2. The corresponding modulation amplitude vectors $\boldsymbol{f}_1$ and $\boldsymbol{f}_2$ are taken to have arbitrary (different) components in the 3-dimensional physical space. This is depicted schematically in figure 9.2. The full line parts of the wavy lines suggest that the wavy line is in front of the plane $V_{\boldsymbol{b},s}$ and the dashed parts that it is behind the plane. In a 4-dimensional space, it is of course not unambiguously defined whether a point is behind or in front of a 2-dimensional plane. Therefore, the figure is only a schematic representation of the actual situation.

In the physical space all atoms 1 are connected by first nearest neighbour bonds with two atoms 2. Thus, a modulated bond chain is obtained, that has also been drawn schematically in figure 9.2.

The only part of the physical space present in the plane $V_{\boldsymbol{b},s}$ is a 1-dimensional subspace containing $\boldsymbol{b}$. It is denoted $M_{\boldsymbol{b}}$. The mbc winds its way everywhere in the close neighbourhood of this subspace. While traveling in $M_{\boldsymbol{b}}$ and starting from the origin, one enters after each distance $|\boldsymbol{b}|$ some new unit cell of the lattice Λ_b on $V_{\boldsymbol{b},s}$. In figure 9.2 this is demonstrated by means of the vectors $\boldsymbol{b}_2$ and $\boldsymbol{b}_3$, etc. all having length $|\boldsymbol{b}|$. It is possible to assign to each vector $\boldsymbol{b}_i$, $i = 1, 2, 3, \ldots$ a specific part of the mbc. One can take, for example, that part of the mbc that projects on $\boldsymbol{b}_i$ using orthogonal projections in the physical space. Using this construction one is certified that every point of the mbc is uniquely assigned to some vector $\boldsymbol{b}_i$.

It is important to realise that both $\boldsymbol{a}_{4s}$ and $\boldsymbol{b}_s$ are elements of the translation group of the whole embedded structure. Therefore, each vector $\boldsymbol{b}_i$ and its corresponding part of the mbc is translationally equivalent to a vector $\boldsymbol{b}'_i$ starting in the first unit cell of Λ_b, together with an equivalent mbc part. The vectors $\boldsymbol{b}'_2$ and $\boldsymbol{b}'_3$ have been drawn in figure 9.2. Due to the incommensurability all vectors $\boldsymbol{b}'_i$ intersect the $\boldsymbol{a}_{4s}$-axis at a different height in the first unit cell of Λ_b. The corresponding mbc parts, therefore, form a uniform bond density in superspace in the same way as derived for a 1-dimensional incommensurately modulated crystal by Kremers et al. (1994). This construction can, therefore, be considered to be a 1 + 1-dimensional embedding of a mbc. Since there is a lattice Λ_b on $V_{b,s}$ it is also possible to define 1 + 1-dimensional hyperplanes $(h_1, h_2)_s$ using the reciprocal lattice Λ_b^*. It is shown later that this is very useful.

9.3.3 Oblique bonds in superspace

In the construction of a modulated bond chain in section 9 3 2 only first nearest neighbours have been used. Although this is the approximation that is also often made for non-modulated crystals, it is interesting to brood on the consequences of including next nearest neighbour bonds. This may prove to be very useful, because there are several microscopic models (Selke (1984), Janssen (1986), Frenkel and Kontorova (1938)) in which the inclusion of (repulsive) next nearest neighbour interactions is essential for obtaining an incommensurate ground state.

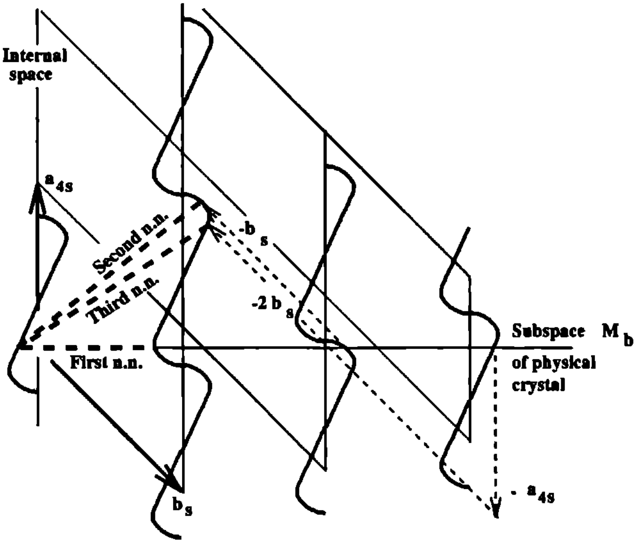

Figure 9.3 The 1 + 1-dimensional embedding of a mbc with only one kind of atom and modulation amplitude vector $\boldsymbol{f}$ parallel to $\boldsymbol{b}$ First nearest neighbour bonds are parallel to the physical space Second, third, etc nearest neighbour bonds can be represented in the first unit cell of the lattice Λ_b on $V_{b,s}$ by means of oblique bonds This is done by finding a point on the second wavy line that is translationally equivalent to the end point of the bond in case that the bond would have been defined parallel to the physical space For example, the end point of the (parallel) second nearest neighbour bond has been translated with the lattice vector $-\boldsymbol{b}_s$ and the end point of the (parallel) third nearest neighbour bond with the lattice vector $-(\boldsymbol{a}_{4s} + 2\boldsymbol{b}_s)$

One can, of course, construct mbc's with next nearest neighbour bonds following the same procedure as described in section 9.3.2. Then, however, all constituent bonds are again parallel to the physical space. Consequently, a hyperplane parallel to the physical space intersects no bonds. It, therefore, has zero surface free energy in the extension of a Wulff plot to superspace. It has been explained by Kremers et al. (1994), that this reduces the dimension of the equilibrium shape with 1 and gives, in any case, a morphology entirely in the physical space. However, in case that next nearest neighbour bonds are defined in the following alternative way, some interesting questions are raised.

In figure 9.3 we have again drawn a view on a $V_{\mathfrak{b},s}$ plane, but in this case, for sake of simplicity, there is only one kind of atom and the modulation amplitude vector $\boldsymbol{f}$ has been taken parallel to $\boldsymbol{b}$. In the physical subspace $M_{\mathfrak{b}}$ a first nearest neighbour bond is indicated by means of a thick dashed line element between the first and the second atom. In the same way a second nearest neighbour bond could have been drawn between the first and third atom in $M_{\mathfrak{b}}$, but instead the bond has been drawn between the first atom in the physical space and the point on the second wavy line that is translationally equivalent (using a translation $-\boldsymbol{b}_s$) to the third atom. Similarly, a third nearest neighbour bond has been constructed using the translation $-\boldsymbol{a}_{4s} - 2\boldsymbol{b}_s$. In each unit cell of the lattice $\Lambda_{\mathfrak{b}}$ one can construct such oblique nearest neighbour bonds following the same procedure. Furthermore, all oblique bonds thus obtained are translationally equivalent to oblique bonds in the first unit cell of $\Lambda_{\mathfrak{b}}$. In this way, again a uniform bond density is obtained in superspace, but the bonds need no longer be parallel to the physical space. A hyperplane that is parallel to the physical space then intersects these embedded oblique bonds. The implication of this construction is that it should be possible to obtain a morphological shape having the same dimension as the superspace by means of a Wulff plot construction in this superspace. The notion of a crystal form in superspace was first introduced by Janner (1983). The physical relevance of such a form might be revealed by comparing this form with the one obtained by constructing mbc's of next nearest neighbour bonds parallel to the physical space. Though very intriguing, this is not worked out in the current paper. Here, as a first approximation, we only consider mbc's consisting of first nearest neighbour bonds.

9.3.4 Crystallographic hyperplanes

The embedded incommensurately modulated crystal, described in section 9.3.1, has a lattice Λ_s. One can define crystallographic hyperplanes $(h_1h_2h_3h_4)_s$ as a straightforward extension of crystallographic planes in three dimensions by using the reciprocal lattice Λ_s^* (see Kremers et al., 1994).

Thus, a crystallographic hyperplane $(h_1h_2h_3h_4)_s$ consists of all points $\boldsymbol{x}_s$ in superspace for which

$$\boldsymbol{H}_{(h_1h_2h_3h_4),s} \cdot \boldsymbol{x}_s = \text{constant} \tag{9.11}$$

where $\boldsymbol{H}_{(h_1h_2h_3h_4),s}$ is defined as:

$$\boldsymbol{H}_{(h_1h_2h_3h_4),s} = h_1\boldsymbol{a}_{1s}^* + h_2\boldsymbol{a}_{2s}^* + h_3\boldsymbol{a}_{3s}^* + h_4\boldsymbol{a}_{4s}^*. \tag{9.12}$$

The hyperplane $(h_1h_2h_3h_4)_s$ can be regarded as a plane of dimension 3 in the $3+1$-dimensional superspace, cutting the $\boldsymbol{a}_{1s}$-axis at $1/h_1$, the $\boldsymbol{a}_{2s}$-axis at $1/h_2$, the $\boldsymbol{a}_{3s}$-axis at $1/h_3$ and the $\boldsymbol{a}_{4s}$-axis at $1/h_4$ if the constant is 1. Due to the $3+1$-dimensional lattice translational symmetry one can define a mesh volume $M_{\boldsymbol{H},s}$ in the following way:

$$M_{\boldsymbol{H},s} = \frac{V_s}{d_{\boldsymbol{H},s}} \tag{9.13}$$

where V_s is the volume of the unit cell of the lattice Λ_s and $d_{\boldsymbol{H},s}$ is the interplanar distance in a grid of identical netplanes. This interplanar distance is defined as $d_{\boldsymbol{H},s} = |\boldsymbol{d}_{\boldsymbol{H},s}|$, where

$$\boldsymbol{d}_{\boldsymbol{H},s} = \frac{\boldsymbol{H}_{(h_1h_2h_3h_4),s}}{|\boldsymbol{H}_{(h_1h_2h_3h_4),s}|^2}. \tag{9.14}$$

The intersection of a crystallographic hyperplane $(h_1h_2h_3h_4)_s$ with the physical space is given by all points $\boldsymbol{x}_s$ that satisfy both equation (9.11) and $x_{4s} = q_1x_{1s} + q_2x_{2s} + q_3x_{3s}$. In this way one derives that these are the points $\boldsymbol{x}$ in the physical space that satisfy

$$\boldsymbol{H}_{(h_1h_2h_3h_4)} \cdot \boldsymbol{x} = x_1(h_1 + h_4q_1) + x_2(h_2 + h_4q_2) + x_3(h_3 + h_4q_3) = \text{constant}.$$

The intersection of a hyperplane $(h_1h_2h_3h_4)_s$ with the physical space is, therefore, exactly a (satellite) plane $(h_1h_2h_3h_4)$. Furthermore, the grid of netplanes $(h_1h_2h_3h_4)_s$, with interplanar distance $d_{\boldsymbol{H},s}$ in superspace, intersects the physical space exactly in the grid of netplanes $(h_1h_2h_3h_4)$ with interplanar distance $d_{(h_1h_2h_3h_4)}$, given by equation (9.5).

Hence, it follows that (at least) all bonds cut by a single (satellite) plane $(h_1h_2h_3h_4)$ in the physical crystal are also cut by one hyperplane $(h_1h_2h_3h_4)_s$ in the embedded crystal in superspace. In the next section we even show that, at least for planes $(h_1h_2h_3h_4)$ that are not perpendicular to the modulation wave vector $\boldsymbol{q}$, exactly the same bonds are cut by one mesh volume $M_{\boldsymbol{H},s}$ of the hyperplane $(h_1h_2h_3h_4)_s$ in superspace as by the (satellite) plane $(h_1h_2h_3h_4)$ in the physical crystal. This opens the way to the calculation of surface free energies $\Gamma_{(h_1h_2h_3h_4)}$ in superspace.

9.4 The one-to-one correspondence between crystallographic hyperplanes and (satellite) planes in the physical crystal

In this section we show how to calculate the average energy of mbc bonds, that are cut in the physical crystal by a certain plane $(h_1h_2h_3h_4)$. In order to obtain the surface free energy $\Gamma_{(h_1h_2h_3h_4)}$, this average energy must be multiplied for each kind of mbc with the mbc density, which is the number of that kind of mbc's that intersect the plane per unit area. The surface free energy $\Gamma_{(h_1h_2h_3h_4)}$ that we calculate is therefore the average energy per unit area that is necessary to create an infinitely large plane $(h_1h_2h_3h_4)$ by cutting bonds.

In order to find the average energy of all bonds cut by a certain plane $(h_1h_2h_3h_4)$ in the physical crystal, we use the fact that the physical space is a subspace of the superspace and that there is lattice translational symmetry in the latter. Each intersection point of the plane $(h_1h_2h_3h_4)$ with the mbc's of one kind in the physical space is in some unit cell of the lattice Λ_s. Due to the lattice translational symmetry there is in all cases an equivalent point in the first unit cell (containing the origin) of Λ_s. We consider the infinite set of points thus obtained in this first unit cell. The average energy that we seek is exactly the average energy of the bonds corresponding to the points in this set.

In addition, we calculate the intersection points of the corresponding hyperplane $(h_1h_2h_3h_4)_s$ with the uniform bond density in superspace that corresponds to the chosen mbc. Again, all of these points are equivalent to points in the first unit cell of Λ_s. In this unit cell we thus again obtain an infinite set of points. This set must contain the set of points that was constructed out of the intersection points in the physical crystal, because the physical crystal is contained in the embedded crystal and the mbc's are contained in the uniform bond density. For all planes, except a plane perpendicular to a $\boldsymbol{q}$ with an incommensurate *length*, it is hereafter even shown that the two sets are identical. In these cases there is a one-to-one correspondence between (satellite) planes and crystallographic hyperplanes as the calculation of surface free energies is concerned.

It is instructive to consider the following four cases:
satellite faces non-perpendicular to the modulation wave vector,
main faces non-perpendicular to the modulation wave vector,
faces perpendicular to a modulation wave vector with an incommensurate *direction* and
faces perpendicular to a modulation wave vector with an incommensurate *length*.

9.4.1 Satellite faces non-perpendicular to the modulation wave vector

Here, the situation is outlined for $(h_1h_2h_3h_4)$ planes, $h_4 \neq 0$, that are not perpendicular to $\boldsymbol{q}$. In this case, it is not necessary to discriminate between a $\boldsymbol{q}$ with an incommensurate *direction* and a $\boldsymbol{q}$ with an incommensurate *length*. The presented analysis applies for both types. This case can be considered as the generic case.

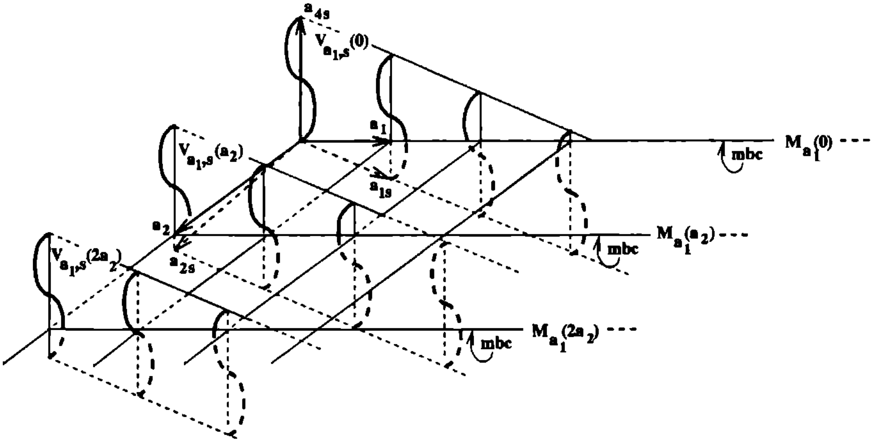

Figure 9.4 A section at constant x_{3s}-coordinate of the superspace embedding of an incommensurately modulated crystal The vectors $\boldsymbol{a}_1$ and $\boldsymbol{a}_2$ define a plane in the physical crystal The rest of the figure is outside the physical crystal There is only one kind of atom, represented by the wavy lines, the solid parts are above the plane and the dashed parts are below The modulation amplitude vector $\boldsymbol{f}$ is parallel to $\boldsymbol{a}_1$ and mbc's are considered for which $\boldsymbol{b} = \boldsymbol{a}_1$ Furthermore, $q_1 \neq 0$ and $q_2 \neq 0$, because $\boldsymbol{a}_{1s}$ differs from $\boldsymbol{a}_1$ and $\boldsymbol{a}_{2s}$ differs from $\boldsymbol{a}_2$ Three subspaces $M_{\boldsymbol{a}_1}(\boldsymbol{n})$, that all represent a mbc of the same kind, have been drawn and the corresponding planes $V_{\boldsymbol{b}}(\boldsymbol{n})$ have been indicated

As described before, a mbc is represented by means of the subspace $M_{\boldsymbol{b}}$ around which the mbc winds its way. Although not essential, we assume for the ease of analysis, that $M_{\boldsymbol{b}}$ contains the origin. To indicate this, it is denoted $M_{\boldsymbol{b}}(\mathbf{o})$. Due to the fact that the incommensurately modulated crystal can be considered as a deformed 3-dimensional basis structure that has a lattice Λ, all 1-dimensional subspaces

$$M_{\boldsymbol{b}}(\boldsymbol{n}), \quad \boldsymbol{n} = (n_1, n_2, n_3) \in \Lambda, \tag{9.15}$$

represent a mbc of the same kind. $M_{\boldsymbol{b}}(\boldsymbol{n})$ is the 1-dimensional subspace obtained by translating all points of $M_{\boldsymbol{b}}(\mathbf{o})$ over the vector $\boldsymbol{n}$ in the physical space. The points $\boldsymbol{x}$, in these subspaces $M_{\boldsymbol{b}}(\boldsymbol{n})$ can be written as follows:

$$\boldsymbol{x} = x_{b1}\boldsymbol{b} + \boldsymbol{n}, \quad \forall x_{b1} \in \mathbb{R}; \; n_1, n_2, n_3 \in \mathbb{Z}, \tag{9.16}$$

where $\boldsymbol{b}$ is given by equation (9.9). Transforming to the basis of the lattice Λ_s in superspace, these points become (see section 9.3.1):

$$\boldsymbol{x}_s = (x_{b1}\boldsymbol{b} + \boldsymbol{n}, (x_{b1}\boldsymbol{b} + \boldsymbol{n}) \cdot \boldsymbol{q}). \tag{9.17}$$

It is important to keep in mind that all the points $\boldsymbol{x}_s \in M_{\boldsymbol{b}}(\boldsymbol{n})$ are in the physical space, although their coordinates are given with respect to Λ_s.

The uniform bond density that is obtained in superspace for these mbc's can accordingly be represented by planes

$$V_{\boldsymbol{b},s}(\boldsymbol{n}), \quad \boldsymbol{n} \in \Lambda \tag{9.18}$$

and the points on these planes can thus be written:

$$\boldsymbol{x}_s = (x_{b1}\boldsymbol{b} + \boldsymbol{n}, x_{b2}), \quad \forall x_{b1}, x_{b2} \in \mathbb{R}. \tag{9.19}$$

In figure 9.4 an example is given of a crystal with only one kind of atom. Only a particular section (constant x_{3s} coordinate) of the superspace has been drawn. Mbc's are considered for which $\boldsymbol{b} = \boldsymbol{a}_1$ and $\boldsymbol{f} \parallel \boldsymbol{a}_1$. Three 1-dimensional subspaces $M_{\boldsymbol{a}_1}(\mathrm{o})$, $M_{\boldsymbol{a}_1}(\boldsymbol{a}_2)$ and $M_{\boldsymbol{a}_1}(2\boldsymbol{a}_2)$ have been drawn. The corresponding planes $V_{\boldsymbol{a}_1,s}(\mathrm{o})$, $V_{\boldsymbol{a}_1,s}(\boldsymbol{a}_2)$ and $V_{\boldsymbol{a}_1,s}(2\boldsymbol{a}_2)$ have been indicated.

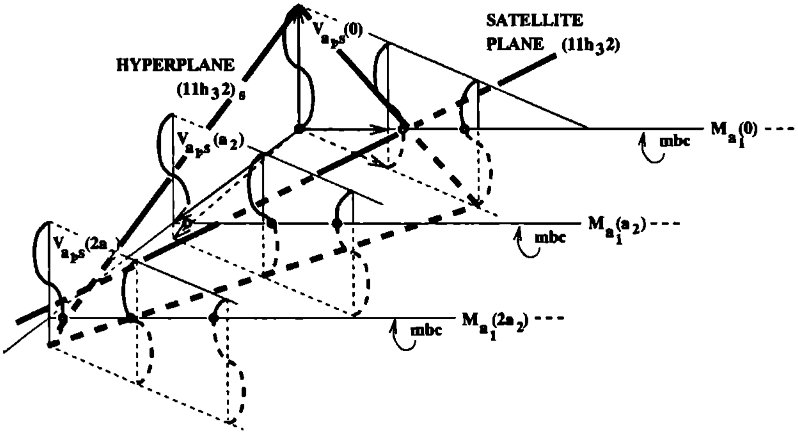

Figure 9.5 The orientation of one hyperplane from the grid $(11h_32)_s$ in the same superspace embedding as used in figure 9.4. The hyperplane cuts the $\boldsymbol{a}_{1s}$-axis at 2, the $\boldsymbol{a}_{2s}$-axis at 2, the $\boldsymbol{a}_{3s}$-axis at $\frac{2}{h_3}$ and the $\boldsymbol{a}_{4s}$-axis at 1. The intersection of this hyperplane with the physical crystal is the satellite plane $(11h_32)$, which cuts the $\boldsymbol{a}_1$-axis at $\frac{2}{1+2q_1}$, the $\boldsymbol{a}_2$-axis at $\frac{2}{1+2q_2}$ and the $\boldsymbol{a}_3$-axis at $\frac{2}{h_3+2q_3}$.

Consider now a crystallographic hyperplane $(h_1h_2h_3h_4)_s$. It has been shown in section 9.3.4 that this hyperplane contains the satellite plane $(h_1h_2h_3h_4)$. This is demonstrated in figure 9.5 by drawing the $(11h_32)_s$ plane and the satellite plane $(11h_32)$ for the same situation as represented in figure 9.4. The intersections of the hyperplane with the subspaces $M_{\boldsymbol{b}}(\boldsymbol{n})$ represent, therefore, the intersection points of the (satellite) plane with the physical crystal. On the other hand, the intersections of the hyperplane with the planes $V_{\boldsymbol{b},s}(\boldsymbol{n})$ represent the intersection points of the hyperplane with the embedded structure in superspace, concerning the mbc under study.

As described in section 9.3.4, the crystallographic hyperplane $(h_1h_2h_3h_4)_s$ consists of all points $\boldsymbol{x}_s$ in superspace for which

$$\boldsymbol{H}_{(h_1h_2h_3h_4),s} \cdot \boldsymbol{x}_s = \text{constant}. \tag{9.20}$$

In figure 9.5 this constant is 2.

If we shift all points of the plane over a vector $\boldsymbol{d}_{\boldsymbol{H},s}$, we get a plane that is described by the following equation:

$$\boldsymbol{H}_{(h_1h_2h_3h_4),s} \cdot \boldsymbol{x}_s = \text{constant} + 1. \tag{9.21}$$

In the case that h_1, h_2, h_3 and h_4 have no common divisor larger than 1, this plane is translationally equivalent to the plane given by equation (9.20).

The intersection of the considered plane with the mbc's in the physical crystal is now obtained by substituting $\boldsymbol{x}_s \in M_{\boldsymbol{b}}(\boldsymbol{n})$ (equation (9.17)) for $\boldsymbol{x}_s$ in equation (9.20) and solving it for x_{b1}. The solution is:

$$x_{b1} = \frac{\text{constant} - \boldsymbol{H}_{(h_1h_2h_3h_4),s} \cdot (\boldsymbol{n}, \boldsymbol{n}\cdot\boldsymbol{q})}{\boldsymbol{H}_{(h_1h_2h_3h_4),s} \cdot (\boldsymbol{b}, \boldsymbol{b}\cdot\boldsymbol{q})} = \frac{\text{constant} - \boldsymbol{H}_{(h_1h_2h_3h_4)} \cdot \boldsymbol{n}}{\boldsymbol{H}_{(h_1h_2h_3h_4)} \cdot \boldsymbol{b}}. \tag{9.22}$$

For each subspace $M_{\boldsymbol{b}}(\boldsymbol{n})$ the searched intersection point is determined by substituting this x_{b1} in equation (9.17). The intersection point is denoted $P_{\boldsymbol{b},\boldsymbol{H}}(\boldsymbol{n})$, but we immediately drop the $\boldsymbol{H}$ dependence in the notation and write $P_{\boldsymbol{b}}(\boldsymbol{n})$.

There is no solution in case the bond-chain vector $\boldsymbol{b}$ is parallel to the plane $(h_1h_2h_3h_4)$, which suggests that the plane does not cut any bonds. However, the atoms may be shifted out of the plane if their modulation amplitude vector has a component perpendicular to the plane. The bonds of the mbc are then not necessarily parallel to the plane and can, therefore, be cut by the plane. Nevertheless, we do not take these mbc's into account, because it is usually possible to shift the plane in the direction of its normal, so that the bonds of the mbc are no longer cut. This corresponds to a lower surface free energy and is, therefore, more favourable. We are interested, of course, in the lowest possible surface free energy.

Next, we calculate the intersection of the hyperplane $(h_1h_2h_3h_4)_s$ with the planes $V_{\boldsymbol{b},s}(\boldsymbol{n})$ by substituting $\boldsymbol{x}_s \in V_{\boldsymbol{b},s}$ (equation (9.19)) in equation (9.20). The solution is the line:

$$x_{b1} = \frac{\text{constant} - \boldsymbol{H}_{(h_1h_2h_3h_4),s} \cdot (\boldsymbol{n}, x_{b2})}{\boldsymbol{H}_{(h_1h_2h_3h_4),s} \cdot (\boldsymbol{b}, 0)}. \tag{9.23}$$

These lines should now be denoted $L_{b,H}(\boldsymbol{n})$, but again we drop the $\boldsymbol{H}$ dependence. The lines $L_b(\boldsymbol{n})$, of course, contain the points $P_b(\boldsymbol{n})$. This is demonstrated in figure 9.6, again for the same situation as presented in figure 9.4.

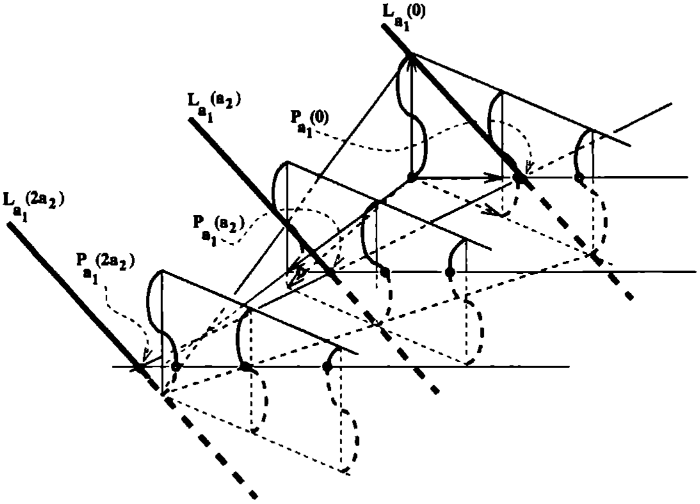

Figure 9.6 The intersection of the hyperplane $(11h_32)_s$ (see figure 9.5) with the embedded mbc's (see figure 9.4) can be represented by lines $L_{a_1}(\boldsymbol{n})$. These lines have the points $P_{a_1}(\boldsymbol{n})$ in common with the physical crystal. The satellite plane $(11h_32)$ intersects the subspaces $M_{a_1}(\boldsymbol{n})$ exactly in these points $P_{a_1}(\boldsymbol{n})$.

Making use of the lattice translational symmetry in superspace one can translate the points $P_b(\boldsymbol{n})$ and the lines $L_b(\boldsymbol{n})$ to the $V_{b,s}(\mathrm{o})$ plane, by using the translation

$$\boldsymbol{n}_s = (-n_1, -n_2, -n_3, 0). \tag{9.24}$$

The obtained translationally equivalent points are denoted $P'_b(\boldsymbol{n})$ and the lines are denoted $L'_b(\boldsymbol{n})$. In figure 9.7 these have been drawn for the example used in this section.

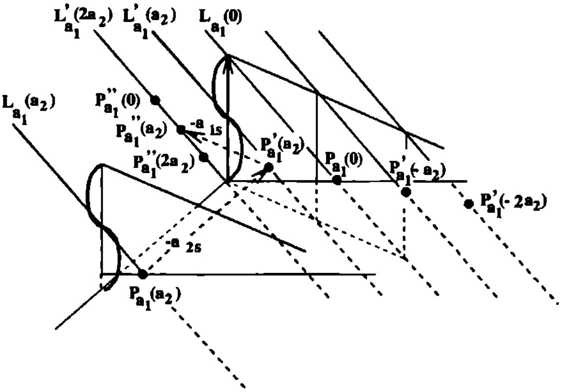

Figure 9.7 Using translation vectors of the lattice Λ_s, it is possible to find, in one $V_{b,s}$ plane, lines $L'_{a_1}(n)$ equivalent to the lines $L_{a_1}(n)$ that have been obtained in figure 9.6. As the intersection points $P_{a_1}(n)$ can be found on the lines $L_{a_1}(n)$, translationally equivalent points $P'_{a_1}(n)$ can be found on the lines $L'_{a_1}(n)$ In the plane $V_{b,s}$ there is a lattice Λ_b. Using translation vectors of this lattice, it is possible to show that all lines $L'_{a_1}(n)$ are translationally equivalent. The line $L'_{a_1}(a_2)$, for example, is translationally equivalent (using the vector a_{1s}) to the line $L'_{a_1}(2a_2)$ As the points $P'_{a_1}(n)$ are on the lines $L'_{a_1}(n)$, translationally equivalent points $P''_{a_1}(n)$ can be found on the line $L'_{a_1}(2a_2)$. This line can be considered as a lattice plane defined on Λ_b in $V_{b,s}$. It can be shown that the points $P''_{a_1}(n)$ become dense on a single mesh area of this 1 + 1-dimensional lattice plane.

If we use the set of two coordinates with respect to the basis of the lattice Λ_b on $V_{b,s}(\mathrm{o})$, we obtain:

$$P'_b(n) = (x_{b1},\ \ x_{b1}\,(q \cdot b) + q \cdot n)_{V_{b,s}(\mathrm{o})} \tag{9.25}$$

with x_{b1} given by equation (9.22) and

$$L'_b(n) = (x_{b1},\ \ x_{b2})_{V_{b,s}(\mathrm{o})},\quad x_{b2} \in \mathbb{R} \tag{9.26}$$

with x_{b1} given by equation (9.23).

The set of lines $L'_b(n)$ in the plane $V_{b,s}(\mathrm{o})$ are equivalent to a grid of netplanes $(h_1b_1+h_2b_2+h_3b_3, h_4)_s$ in the embedding of an incommensurately modulated 1-dimensional crystal, with an average periodicity $a = |b|$ and modulation wave vector $q = (q \cdot b)a^*$. We have shown in a previous paper (Kremers et al., 1994) that in such a 1 + 1-dimensional case all members of the grid of netplanes $(h_1h_2)_s$ (here corresponding to the lines $L'_b(n)$) are translationally equivalent and that all intersection points of the grid with the 1-dimensional modulated crystal (here corresponding to the subspace $M_b(\mathrm{o})$) become dense on a single mesh area $M_{(h_1h_2),s}$ of one member of the grid, if translations of the 1 + 1-dimensional lattice are used. The only difference between that case and the present one is that the points $P'_{\boldsymbol{b}}(\boldsymbol{n})$ in which we are interested are not all in the 1-dimensional physical subspace $M_{\boldsymbol{b}}(\mathrm{o})$, but instead only one point is. For the example this can be seen in figure 9.7.

However, for the same reasons as described by Kremers et al. (1994), all lines $L'_{\boldsymbol{b}}(\boldsymbol{n})$ are translationally equivalent (unless $h_1b_1 + h_2b_2 + h_3b_3$ and h_4 have a common divisor larger than 1). Consequently, we arrive at the important conclusion that the intersection of a hyperplane $(h_1h_2h_3h_4)_s$ with the uniform bond density corresponding to a mbc with bond-chain vector $\boldsymbol{b}$ can be found by considering one mesh area of one line $L'_{\boldsymbol{b}}(\boldsymbol{n})$ in a $1+1$-dimensional description of the mbc.

Subsequently we want to show, that also all points $P'_{\boldsymbol{b}}(\boldsymbol{n})$ become dense on one such mesh area of a line $L'_{\boldsymbol{b}}(\boldsymbol{n})$. This can be made clear in the following way. Since the lines $L'_{\boldsymbol{b}}(\boldsymbol{n})$ behave as a grid of netplanes on the lattice Λ_b of $V_{\boldsymbol{b},s}(\mathrm{o})$ one can find, for each single line, a translation

$$\boldsymbol{n}_v = (n_{b1}, n_{b2})_{V_{\boldsymbol{b},s}(\mathrm{o})}, \qquad n_{b1}, n_{b2} \in \mathbb{Z} \tag{9.27}$$

such, that the line is translated onto one specific line $L'_{\boldsymbol{b}}$. Thus we obtain points $P''_{\boldsymbol{b}}(\boldsymbol{n})$ (see figure 9.7) that are on the chosen line $L'_{\boldsymbol{b}}$, having a coordinate $x_{b1} - n_{b1}$ with $n_{b1} \in \mathbb{Z}$ and x_{b1} given by equation (9.22). Due to the incommensurability x_{b1} is always an irrational number and, therefore, also $x_{b1} - n_{b1}$ is irrational. On the line $L'_{\boldsymbol{b}}$ there is a periodicity of h_4 in the x_{b1}-coordinate, because the slope is equal to $-\frac{h_1b_1+h_2b_2+h_3b_3}{h_4}$. Due to this periodicity and the irrationality of $x_{b1} - n_{b1}$ the points $P''_{\boldsymbol{b}}(\boldsymbol{n})$ become dense on the line $L'_{\boldsymbol{b}}$. This can be proven by following the same arguments as used in the proof of the existence of a uniform bond density in the $1+1$-dimensional superspace of an incommensurately modulated 1-dimensional crystal, as has been given by Kremers et al. (1994).

Thus, we have shown that also the intersection of a (satellite) plane with a mbc of the physical crystal, having bond-chain vector $\boldsymbol{b}$, can be found by considering one mesh area of one single line $L'_{\boldsymbol{b}}(\boldsymbol{n})$ in a $1+1$-dimensional embedding of the mbc. This opens the way for inspecting the bonds that are cut by the satellite plane by means of a graphical method. For each mbc, one draws the corresponding $1+1$-dimensional embedding of the mbc. The intersection points can then be found by drawing the $1+1$-dimensional plane $(h_1b_1 + h_2b_2 + h_3b_3, h_4)_s$.

In case that $h_1b_1 + h_2b_2 + h_3b_3$ and h_4 have some common divisor $d \in \mathbb{Z}$, not all lines $L'_{\boldsymbol{b}}(\boldsymbol{n})$ are translationally equivalent, but there are d different, non-translationally equivalent lines. However, for each of these lines there still are infinitely many translationally equivalent lines $L'_{\boldsymbol{b}}(\boldsymbol{n})$. The points $P''_{\boldsymbol{b}}(\boldsymbol{n})$ on one such subset of all lines $L'_{\boldsymbol{b}}(\boldsymbol{n})$ become dense on a single line of the subset. This holds for all d different non-translationally equivalent lines.

It is concluded that for planes $(h_1h_2h_3h_4)$ non-perpendicular to $\boldsymbol{q}$ there exists a one-to-one correspondence between the intersection of the hyperplane $(h_1h_2h_3h_4)_s$ with the embedded structure and the intersection of the (satellite) plane with the physical crystal.

Furthermore, this conclusion can be drawn for each value of the constant in equation (9.20). This implies that there is also a one-to-one correspondence between the satellite planes corresponding to two hyperplanes $(h_1h_2h_3h_4)_s$ that are an integer number times $\boldsymbol{d}_{\boldsymbol{H},s}$ apart, because these hyperplanes are translationally equivalent. Therefore, the average energy of the bonds cut by a plane $(h_1h_2h_3h_4)$ in the physical crystal is equal to that of the bonds cut by a plane with the same orientation but shifted over a vector $\boldsymbol{d}_{(h_1h_2h_3h_4)}$ with respect to the original plane. Consequently, the physical crystal can be partitioned in slices with thickness $\mid \boldsymbol{d}_{(h_1h_2h_3h_4)} \mid$ that all have exactly the same energy content $E_{\boldsymbol{H}}$. The difference between this $E_{\boldsymbol{H}}$ and the classical notion E_{slice} is addressed in the discussion. The remaining question is, whether the surface free energy depends on the exact position of the surface of the slice. This position is determined by the value of the constant in equation (9.20).

In this section, it has been shown that, in order to find the average energy of the bonds that are cut in the physical crystal by a plane $(h_1h_2h_3h_4)$, it is sufficient to average over the energy of the embedded bonds that are cut in superspace by a hyperplane $(h_1h_2h_3h_4)_s$. However, the latter is equal to averaging over one mesh volume $M_{\boldsymbol{H},s}$ of the hyperplane, because the embedded structure has a lattice. This, in turn, is equal to averaging over all embedded bonds that are cut in one unit cell of Λ_s by the grid of netplanes $(h_1h_2h_3h_4)_s$ (Heijmen et al., 1994).

9.4.2 Main faces non-perpendicular to the modulation wave vector

Main faces, on the incommensurately modulated crystals that we consider, are $(h_1h_2h_30)$ planes. Here, we consider only those $h_4 = 0$ planes that are not perpendicular to the modulation wave vector $\boldsymbol{q}$. In case that $\boldsymbol{q}$ has an incommensurate *direction*, there even is no main face perpendicular to it. Although $(h_1h_2h_30)$ planes have the same orientation as $(h_1h_2h_3)$ planes would have if the modulation were absent, their surface free energy can definitely be changed by the modulation. Using the generic case that has been described in section 9.4.1, one can derive that there is again a one-to-one correspondence between a main face $(h_1h_2h_30)$ and the crystallographic hyperplane $(h_1h_2h_30)_s$.

Such a hyperplane has a special orientation in superspace in the sense that it is parallel to the internal space. This means that all lines $L_{\boldsymbol{b}}$, obtained by intersecting the hyperplane with an embedded mbc, are also parallel to the internal space. Following the same procedure as described in section 9.4.1, one finds lines

$$L'_{\boldsymbol{b}}(\boldsymbol{n}) \quad = \quad (x_{b1}, x_{b2})_{V_{\boldsymbol{b},s}(\mathbf{O})}, \qquad x_{b2} \in I\!R$$

where

$$x_{b1} \quad = \quad \frac{\text{constant} - \boldsymbol{H}_{(h_1h_2h_30)} \cdot \boldsymbol{n}}{\boldsymbol{H}_{(h_1h_2h_30)} \cdot \boldsymbol{b}}$$

is independent of x_{b2}. These lines $L'_{\boldsymbol{b}}(\boldsymbol{n})$ can be translated onto $|h_1b_1+h_2b_2+h_3b_3|$ lines $L'_{\boldsymbol{b}}$ through the first unit cell of the lattice Λ_b. The points $P''_{\boldsymbol{b}}(\boldsymbol{n})$ on these lines that are translationally equivalent to the intersection points of the main face $(h_1h_2h_30)$ with the physical crystal, then have x_{b2}-coordinate:

$$x_{b2} = (\boldsymbol{q}\cdot\boldsymbol{b})\frac{\text{constant}-\boldsymbol{H}_{(h_1h_2h_30)}\cdot\boldsymbol{n}}{\boldsymbol{H}_{(h_1h_2h_30)}\cdot\boldsymbol{b}}+(\boldsymbol{q}\cdot\boldsymbol{n}).$$

Since there is a translational periodicity of 1 on the x_{b2}-coordinate, the points $P''_{\boldsymbol{b}}(\boldsymbol{n})$ become dense on the $|h_1b_1+h_2b_2+h_3b_3|$ lines. Therefore, the same bonds are cut in the intersection of a main face $(h_1h_2h_30)$ with the physical crystal as in the intersection of one mesh volume $M_{\boldsymbol{H},s}$ of the hyperplane $(h_1h_2h_30)_s$ with the embedded mbc. This can be inspected graphically by drawing 1 + 1-dimensional $(h_1b_1+h_2b_2+h_3b_3,0)_s$ planes in the corresponding 1 + 1-dimensional embeddings of the mbc's present in the crystal.

Furthermore, for the same reasons as given in section 9.4.1, the crystal can be partitioned in $(h_1h_2h_30)$ slices with thickness $|\boldsymbol{d}_{(h_1h_2h_30)}|$ that all have exactly the same energy content and surface free energy. The latter, however, may depend on the exact position of the surface.

9.4.3 Faces perpendicular to a modulation wave vector with an incommensurate direction

The only faces perpendicular to a modulation wave vector $\boldsymbol{q}$ with an incommensurate *direction* are $(000h_4)$ planes. Also for these planes one can follow the lines of thought as used in the generic case that has been described in section 9.4.1. The lines $L'_{\boldsymbol{b}}(\boldsymbol{n})$ are then found to be:

$$L'_{\boldsymbol{b}}(\boldsymbol{n}) = \left(x_{b1}, \frac{\text{constant}}{\text{h}_4}\right)_{V_{\boldsymbol{b},s}(\text{O})}, \quad x_{b1}\in\mathbb{R}.$$

Therefore, they are all equal and parallel to the $\boldsymbol{b}_s$-axis. The points $P''_{\boldsymbol{b}}(\boldsymbol{n})$, corresponding to the intersection points in the physical crystal have x_{b1}-coordinates:

$$x_{b1} = \frac{\text{constant}-h_4(\boldsymbol{q}\cdot\boldsymbol{n})}{h_4(\boldsymbol{q}\cdot\boldsymbol{b})}$$

on this line.

If we choose $h_4 = 1$, the intersection points in the physical crystal can be inspected graphically by drawing $(01)_s$ planes in the 1 + 1-dimensional embeddings of the mbc's present in the crystal.

In this case, the crystal can be partitioned in (0001) slices with thickness $|\boldsymbol{d}_{(0001)}|$ that all have the same energy content and the same surface free energy. Again it is expected that this surface free energy depends on the exact position of the surface.

9.4.4 Faces perpendicular to a modulation wave vector with an incommensurate length

In case that one is dealing with a modulation wave vector $\boldsymbol{q}$, having an incommensurate *length*, there is a special plane that requires a treatment clearly different from the analysis outlined in section 9.4.1. This is the plane that is perpendicular to $\boldsymbol{q}$. It has been explained in section 9.2.3 that on such a plane there does exist a 2-dimensional unit cell, contrary to the cases that have been treated in the sections 9.4.1, 9.4.2 and 9.4.3. Therefore, there can only be a finite number of different bonds that are cut by that plane.

In view of the sections 9.4.2 and 9.4.3 it is interesting to realise that the plane can be considered to be a main plane $(h_1, h_1\frac{q_2}{q_1}, h_1\frac{q_3}{q_1}, 0)$ with $h_1\frac{q_2}{q_1}$ and $h_1\frac{q_3}{q_1} \in \mathbb{Z}$ as well as a $(000h_4)$ satellite plane. (We have conveniently taken $q_1 \neq 0$.) This implies that the plane perpendicular to $\boldsymbol{q}$ is contained in the hyperplane $(h_1, h_1\frac{q_2}{q_1}, h_1\frac{q_3}{q_1}, 0)_s$ as well as in the hyperplane $(000h_4)_s$. It is, therefore, (contained in) the intersection of these two hyperplanes. We want to point out that an analogous situation is encountered for quasi-periodic tilings (Heijmen et al., 1995). For such tilings, however, the situation is generic, whereas it is a special case for an incommensurately modulated crystal.

Although we are dealing with a special situation, it is still possible to use the superspace embedding of the structure in order to find the intersection points of the plane perpendicular to $\boldsymbol{q}$ with the physical crystal. Consider the hyperplane $(h_1, h_1\frac{q_2}{q_1}, h_1\frac{q_3}{q_1}, 0)_s$. Its intersections with the subspaces $M_{\boldsymbol{b}}(\boldsymbol{n})$ that represent the mbc's can be calculated in the same way as described in section 9.4.1. The intersection points $P_{\boldsymbol{b}}(\boldsymbol{n})$ are given by putting x_{b1} in equation (9.17) equal to

$$x_{b1} = \frac{\text{constant} - \frac{h_1}{q_1}(\boldsymbol{q} \cdot \boldsymbol{n})}{h_1 b_1 + h_1\frac{q_2}{q_1} b_2 + h_1\frac{q_3}{q_1} b_3}. \tag{9.28}$$

One then finds the following condition for the x_{b2}-coordinate:

$$x_{b2} = \frac{q_1}{h_1}\text{constant}. \tag{9.29}$$

This condition, however, exactly expresses that all intersection points $P_{\boldsymbol{b}}(\boldsymbol{n})$ are on a crystallographic hyperplane $(000h_4)_s$. The points $P_{\boldsymbol{b}}(\boldsymbol{n})$ can again be translated to the $V_{\boldsymbol{b},s}(\mathbf{o})$ plane with lattice vectors of the lattice Λ_s, so that equivalent points $P'_{\boldsymbol{b}}(\boldsymbol{n})$ are obtained. Using the set of two coordinates $(x_{b1}, x_{b2})_{V_{\boldsymbol{b},s}(\mathbf{o})}$ defined with respect to the basis of the lattice Λ_b on this plane, the points $P'_{\boldsymbol{b}}(\boldsymbol{n})$ can be written:

$$P'_{\boldsymbol{b}}(\boldsymbol{n}) = \left(x_{b1}, \ \frac{q_1}{h_1}\text{constant}\right)_{V_{\boldsymbol{b},s}(\mathbf{o})}$$

where x_{b1} is given by equation (9.28). All the points $P'_{\boldsymbol{b}}(\boldsymbol{n})$ lie on the lines $L'_{\boldsymbol{b}}(\boldsymbol{n})$ that would have been found if the intersection lines $L_{\boldsymbol{b}}(\boldsymbol{n})$ of the embedded mbc with the hyperplane $(h_1, h_1\frac{q_2}{q_1}, h_1\frac{q_3}{q_1}, 0)_s$ would have been translated to the $V_{\mathbf{b},s}(\mathbf{o})$ plane. Therefore, it is tempting to look at the situation again as a grid of $(h_1b_1 + h_2b_2 + h_3b_3, 0)_s$ planes in the $1+1$-dimensional embedding of the mbc. However, this case differs from the situation described in section 9.4.2, as the points now all have equal x_{b2}-coordinate. Therefore, if one tries to translate these point to points $P''_{\mathbf{b}}(\boldsymbol{n})$ in the first unit cell of the lattice Λ_b only $|h_1b_1 + h_2b_2 + h_3b_3|$ different points $P''_{\mathbf{b}}(\boldsymbol{n})$ are obtained, instead of infinitely many. This could be expected, because a 2-dimensional unit cell can be defined on the plane and, as we show in section 9.6, the mbc density is indeed $|h_1b_1 + h_2b_2 + h_3b_3|$ divided by the area of that 2-dimensional unit cell.

The intersection points with the physical crystal of a plane perpendicular to a $\boldsymbol{q}$ that has an incommensurate *length* can thus be found by considering the intersection points of a grid of $(h_1b_1 + h_2b_2 + h_3b_3, 0)_s$ planes with a $(0,1)_s$ hyperplane in a $1+1$-dimensional embedding of a mbc. This situation is clearly exceptional, because it is the only one in which there is no one-to-one correspondence between the plane in the physical crystal and the corresponding hyperplane.

Furthermore, one can in this case not derive that it is possible to partition the crystal in $(h_1, h_1\frac{q_2}{q_1}, h_1\frac{q_3}{q_1}, 0)$ slices with the same energy content nor with the same surface free energy. Namely, if we consider a plane $(h_1, h_1\frac{q_2}{q_1}, h_1\frac{q_3}{q_1}, 0)$ that has been shifted over a vector $\boldsymbol{d}_{(h_1, h_1\frac{q_2}{q_1}, h_1\frac{q_3}{q_1}, 0)}$ with respect to the plane just described, similar results to (9.28) and (9.29) are found, the only difference being that the value of the constant has increased with 1. This means that the points $P'_{\mathbf{b}}(\boldsymbol{n})$ are again on the grid of $(h_1b_1 + h_2b_2 + h_3b_3, 0)_s$ planes, but have a different x_{b2} coordinate

$$x_{b2} = \frac{q_1}{h_1}\text{constant} + \frac{q_1}{h_1}.$$

One thus obtains a different set of $|h_1b_1 + h_2b_2 + h_3b_3|$ points, which means that the average energy of the bonds that are cut by the plane is, in principle, also different. Shifting the plane any integer, $p \in \mathbb{Z}$, times $\boldsymbol{d}_{(h_1, h_1\frac{q_2}{q_1}, h_1\frac{q_3}{q_1}, 0)}$, never gives an equivalent set of intersection points, because in all these cases an irrational number $p\frac{q_1}{h_1}$ is added to the x_{b2} coordinate of the points $P'_{\mathbf{b}}(\boldsymbol{n})$ and there is a translational periodicity of 1 in the x_{b2}-coordinate.

In order to study the average energy of the bonds that are cut as a function of position of the plane, one must vary the position of the grid $(h_1b_1 + h_2b_2 + h_3b_3, 0)_s$ as well as the position of the $(0,1)_s$ hyperplane. Each set of intersection points, that is obtained in this way, corresponds to some position of the plane perpendicular to $\boldsymbol{q}$ in the physical crystal.

Thus, this case is indeed exceptional.

9.5 Principle of selective cuts

In this section we demonstrate the principle of selective cuts. It has been shown by Kremers et al. (1994) how, for an incommensurately modulated 1-dimensional crystal, this principle is the cause of the stabilisation of (satellite) faces, i.e. the lowering of surface free energy. Also for incommensurately modulated 3-dimensional crystals there is a lowering of the surface free energy caused by the principle of selective cuts.

In section 9.4, it has been shown that the average energy of the bonds that are cut in the physical crystal by a certain $(h_1h_2h_3h_4)$ plane, can be found, in general, in superspace by averaging over all embedded bonds that are cut by one mesh volume of the corresponding hyperplane $(h_1h_2h_3h_4)_s$. Although the approach of section 9.4 is not valid for commensurately modulated crystals (q_1, q_2, $q_3 \in Q$), it can be applied to incommensurately modulated crystals for which the modulation amplitude vector $\boldsymbol{f}$ has zero length. In that case, however, the structure does not differ from the non-modulated crystal. The wavy lines in superspace that represent the atoms become straight lines and the modulated bond chains are no longer modulated. Let us conveniently consider mbc's that consist of one type of atom and one type of bond. In the embedding of this mbc, only one bond length is found in the uniform bond density in superspace. Consequently, the average length of the embedded bonds that are cut by the mesh volume of any hyperplane is a constant, i.e. equal to the length of the non-modulated bond. This implies that, for a crystal that is not modulated, it is the number of intersected bonds per unit area, which is the so-called mbc density, that determines the surface free energy. It is well known, however, that in that case only for (hkl) planes cusps appear in a polar plot of the surface free energy, i.e. a Wulff plot (Bennema and van der Eerden, 1987). Only these planes, therefore, can appear on the equilibrium form of a non-modulated crystal.

Let us now consider an incommensurately modulated crystal with a non-zero modulation amplitude. Although the atoms are displaced due to the modulation, we have assumed that with respect to pbc's for the non-modulated case no bonds disappear and no extra bonds appear in mbc's of the modulated crystal. This means, that for an infinite plane the average number of intersected mbc's per unit area is the same as the number of intersected in the non-modulated case, unless the modulation amplitude is very large. Since we calculate surface free energies as average broken-bond energies over infinite planes it can not be this mbc density that changes the surface free energy for an incommensurately modulated crystal. Therefore, if the surface free energy of satellite faces can be lowered due to the modulation, so that they have a chance of appearing on the equilibrium form, this must be caused by the fact that the average broken-bond energy can be lower than the energy of a non-modulated bond. This implies that a mesh volume of a hyperplane must only intersect a selection of all possible bonds that can be found in superspace. The average length of all possible different bonds in superspace is namely equal to the length of a non-modulated bond. We reach the conclusion that the stabilisation of (satellite) planes must be caused by a principle of selective cuts. This principle is now demonstrated for the four cases described in section 9.4. We treat them in the order of increasing possible stabilisation of surface free energy.

9.5.1 Main faces non-perpendicular to the modulation wave vector

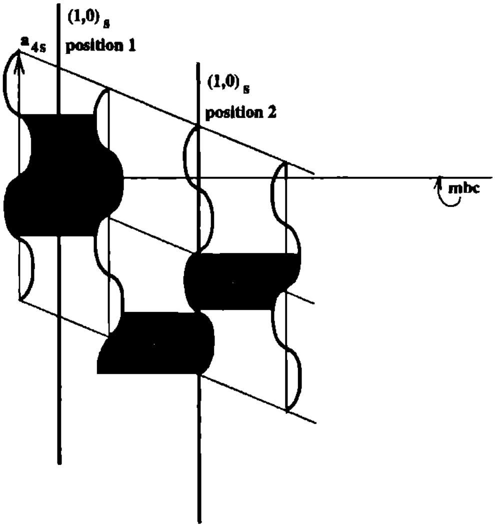

Figure 9.8 Demonstration of the principle of selective cuts for the (1110) plane cutting mbc's for which $\boldsymbol{b} = \boldsymbol{a}_1$ and $\boldsymbol{f} \parallel \boldsymbol{a}_1$. The situation can be represented with a $(1,0)_s$ plane intersecting the bonds in a 1 + 1-dimensional embedding of the mbc. The cut bonds have been shaded. The two different positions for the plane represent the variation of surface free energy within a distance $d_{(1110)}$.

It has been shown in section 9.4.2 that for main faces one must inspect the embedded bonds that are cut by a grid of $(h_1b_1 + h_2b_2 + h_3b_3, 0)_s$ planes in the 1 + 1-dimensional embedding of a mbc. As an example we take $\boldsymbol{b} = \boldsymbol{a}_1$ and $\boldsymbol{f} \parallel \boldsymbol{a}_1$ and consider the (1110) plane, so that the grid is $(1,0)_s$. From the analysis in section 9.4.2, we have also learned that the surface free energy is expected to depend on the position of the plane, with a periodicity of $|\boldsymbol{d}_{(h_1h_2h_30)}|$.

In figure 9.8 the situation is presented for two (1110) planes at different positions and the bonds that are cut by one mesh area have been indicated. For the first position all possible different bonds are cut, so that the average energy is equal to the energy of a non-modulated bond. The second position, however, demonstrates that it is possible to position the plane such that relatively more long than short bonds are cut. This is an example of the principle of selective cuts. The average energy will be lower than the energy of the non-modulated bond. Main faces, non-perpendicular to the modulation wave vector can thus have a lower surface free energy than they would have in the non-modulated case.

The amount of stabilisation for a certain plane depends, of course, on the shape of the modulation function u, the magnitude and direction of the modulation amplitude vector $\boldsymbol{f}$ and the magnitude and direction of the modulation wave vector $\boldsymbol{q}$. It is not straightforward to predict the dependence on u. The dependence on $\boldsymbol{f}$ is, however, clear. The larger the amplitude $|\boldsymbol{f}|$ and the larger the value of $|\boldsymbol{f} \cdot \boldsymbol{b}|$, the larger the amount of stabilisation. In both cases, namely, a larger value implies that larger bond lengths can be found in the crystal.

For the influence of the direction of the modulation wave vector, one must again discriminate between a modulation wave vector with an incommensurate *length* and with an incommensurate *direction*. In case of an incommensurate *length*, there can be mbc's for which $\boldsymbol{b} \perp \boldsymbol{q}$. These must then be *periodic* bond chains. They can differ from what they would be in case that the modulation were absent, if they are built out of more than one kind of bond. Nevertheless, these mbc's contain only a finite number of different bonds, so that in their embedding also only a finite number of different bond lengths appear. This implies that there can be no selective cutting. In case of a modulation wave vector with an incommensurate *direction*, all mbc's are indeed modulated, so that every mbc contains an infinite number of different bonds. Furthermore, the distinction between the two types of modulation wave vector is essential for the amount of stabilisation of planes perpendicular to $\boldsymbol{q}$. This, however, is explicitly treated below.

Also the length of the modulation wave vector influences the amount of stabilisation. As explained in section 9.4.1, one can consider the $1+1$-dimensional embedding of the mbc to have a modulation wave vector $q = (\boldsymbol{q} \cdot \boldsymbol{b})a^*$. The dependence on the length of such a vector q has already been outlined by Kremers et al. (1994) for a longitudinal modulation, $\boldsymbol{f} \| \boldsymbol{b}$. In that paper, we have studied the dependence on the value of q_1 for an incommensurately modulated 1-dimensional crystal and we refer to figure 5 of this reference. This figure can still be used for the overall behaviour in case that the modulation is not longitudinal.

9.5.2 Satellite faces non-perpendicular to the modulation wave vector

The case of satellite faces $(h_1h_2h_3h_4)$, $h_4 \neq 0$, has been treated in section 9.4.1. In figure 9.9 the $(1,2)_s$ plane has been drawn representing the (1112) plane and the $(0,1)_s$ plane representing the (0111) plane. Here, also $\boldsymbol{b} = \boldsymbol{a}_1$ and $\boldsymbol{f} \parallel \boldsymbol{a}_1$. The positions of the planes can again be varied over distances $|\boldsymbol{d}_{(1112)}|$ and $|\boldsymbol{d}_{(0111)}|$ respectively, in order to study the dependence of the surface free energy on the position. For the (1112) plane, this is equal to varying the position at which the hyperplane cuts the $\boldsymbol{a}_{4s}$-axis between $0\boldsymbol{a}_{4s}$ and $\frac{1}{2}\boldsymbol{a}_{4s}$. For the (0111) plane the intersection point at the $\boldsymbol{a}_{4s}$-axis must be varied between

$0a_{4s}$ and $1a_{4s}$.

Figure 9.9 clearly shows that the $(0,1)_s$ plane cuts only a small fraction of all possible bonds, whereas the $(1,2)_s$ plane cuts all possible different bonds at least once, and a large fraction of them even twice. It is important to realise that the $(01)_s$ plane is so selective in figure 9.9, due to the fact that the value of q_1 in this 1 + 1-dimensional embedding is about 0.26. The largest stabilisation of the $(01)_s$ plane can be reached for $q_1 = 0.35$ (see Kremers et al., 1994). In case that q_1 would be close to 0.65 one would expect $(1\bar{1})$ to be highly selective.

The amount of stabilisation with respect to the non-modulated crystal again depends on the modulation function u, the modulation amplitude vector $\boldsymbol{f}$ and the modulation wave vector $\boldsymbol{q}$ in the same way as described in section 9.5.1. Furthermore, figure 9.9 shows that, in general, there can be more stabilisation in case the mesh area of the $(h_1b_1 + h_2b_2 + h_3b_3, h_4)_s$ plane is smaller. In order to have such a small mesh area, both $h_1b_1 + h_2b_2 + h_3b_3$ and h_4 must be small. Therefore, as a rule of thumb one can state that the smaller the indices h_1, h_2, h_3 and h_4 the larger the stabilisation. The same rule of thumb is often used for $(h_1h_2h_3)$ planes on non-modulated crystals.

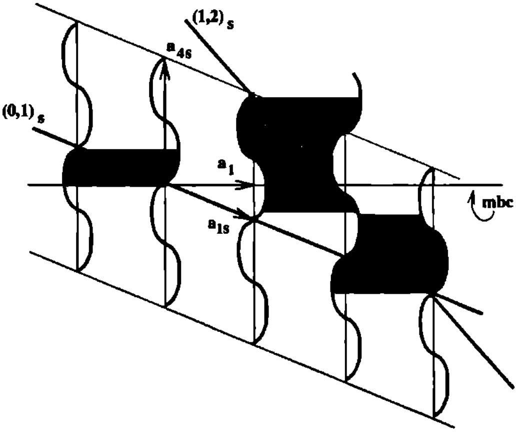

Figure 9.9 Demonstration of the principle of selective cuts for the satellite faces (1112) and (0111). The situations can be represented with a $(1,2)_s$ and $(0,1)_s$ plane respectively. The embedded mbc is the same as in figure 9.8. The cut bonds have been shaded. It is clear that bonds of the mbc are much more selectively cut by the (0111) plane than by the (1112) plane.

In general, one can expect that there exists a selected number of satellite faces that have a relatively larger stabilisation than the main faces. This causes satellite faces to have a chance of appearing on the equilibrium form.

9.5.3 Faces perpendicular to a modulation wave vector with an incommensurate direction

From section 9.4.3 we have learned that one must study the $(0,1)_s$ plane in the 1 + 1-dimensional embedding of each and every mbc in the crystal in the case of a face perpendicular to a $\boldsymbol{q}$ with an incommensurate *direction*. In section 9.5.2 it has been shown for the (0111) plane that such a $(0,1)_s$ plane is highly selective in cutting bonds in case that the corresponding value of q_1 is close to 0.35. The same applies, of course, here. However, the stabilisation of the (0001) plane, that is considered here, can even be larger than the stabilisation of a plane like the (0111) plane. This is caused by the fact that in case of the (0001) plane we must consider for each and every mbc a $(0,1)_s$ plane. On the other hand, in case of, for example, the (0111) plane this is the case for a mbc with $\boldsymbol{b} = \boldsymbol{a}_1$, but for a mbc with $\boldsymbol{b} = \boldsymbol{a}_2$, not the $(0,1)_s$ but the $(1,1)_s$ plane would have to be considered. Of course the value of $\boldsymbol{q} \cdot \boldsymbol{b}$ determines the degree of selectivity, but, for any value of $\boldsymbol{q} \cdot \boldsymbol{b}$, the average energy of the embedded bonds cut by the $(01)_s$ plane is lower than the average energy of the bonds cut by the $(11)_s$ plane (see figure 5 Kremers et al., 1994).

The amount of stabilisation for the (0001) plane in case of a $\boldsymbol{q}$ with an incommensurate direction again depends on the modulation function, the modulation amplitude vector and the modulation wave vector as described in section 9.5.1.

9.5.4 Faces perpendicular to a modulation wave vector with an incommensurate length

The largest stabilisation possible is reached in case of a plane perpendicular to a $\boldsymbol{q}$ with an incommensurate *length*. This is due to the fact that there is a 2-dimensional lattice periodicity on this plane. Therefore, this is the only case in which a finite number of different bonds is cut.

In figure 9.10 this is demonstrated for $\boldsymbol{q} \parallel \boldsymbol{a}_1$, $\boldsymbol{f} \parallel \boldsymbol{a}_1$ and the mbc for which $\boldsymbol{b} = \boldsymbol{a}_1$. It has been explained in section 9.4.4 that one must average, in this case, over all intersection points of a $(0,1)_s$ plane with a $(1,0)_s$ grid in one unit cell of the lattice Λ_b on the plane $V_{\boldsymbol{b},s}$. The figure shows that for the chosen example only one bond is cut. Thus the $(1,0)_s$ grid and the $(0,1)_s$ plane can be positioned such that precisely the longest bond is cut, which has the lowest energy possible for that bond. Of course, this gives the largest stabilisation. This stabilisation may be so large, that (other) satellite faces loose their chance of appearing on the equilibrium morphology. In that case, only main faces determine the morphology together with this one exceptional face.

Although it is equally well possible to consider the plane perpendicular to a $\boldsymbol{q}$ with an incommensurate *length* as a satellite face, we choose to consider it as a main face, because a face with the same orientation can be present on the crystal if the modulation is absent.

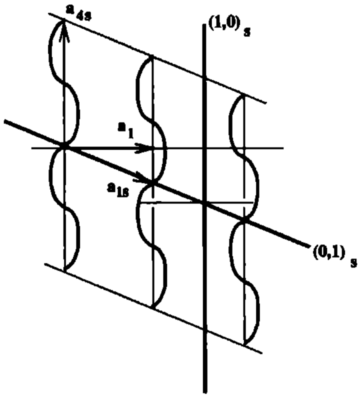

Figure 9.10 Demonstration of the principle of selective cuts for the (1000) plane perpendicular to the vector $\boldsymbol{q} = q_1\boldsymbol{a}^*$. The bonds intersected by this plane in the physical crystal are found by the construction described in section 9.4.4. In this case only one bond is cut, which has been drawn. The (1000) plane is thus stabilised considerably.

9.6 Model calculations

In order to obtain in our broken-bond model the surface free energy $\Gamma_{(h_1h_2h_3h_4)}$ for the plane $(h_1h_2h_3h_4)$ one must calculate, for each type of mbc specified by the bond-chain vector $\boldsymbol{b}_i$, both the mbc density $S_{\boldsymbol{b}_i}^{-1}$ on the plane and the average energy $\overline{\gamma}_{\boldsymbol{b}_i,(h_1h_2h_3h_4)}$ of all bonds, belonging to the mbc, that are cut by the (infinitely large) plane. The surface free energy is then given by

$$\Gamma_{(h_1h_2h_3h_4)} = \sum_{\boldsymbol{b}_i} S_{\boldsymbol{b}_i}^{-1}\overline{\gamma}_{\boldsymbol{b}_i,(h_1h_2h_3h_4)} \tag{9.30}$$

where the summation is performed over all mbc's that are present in the crystal. In case that the crystal is not modulated, one should substitute $\gamma_{\boldsymbol{b}_i}$ for $\overline{\gamma}_{\boldsymbol{b}_i,(h_1h_2h_3h_4)}$ in equation (9.30), because the energies of the cut bonds are then not modulated. Moreover, there is, of course, no average then, that can depend on the indices h_1, h_2, h_3 and h_4.

The mbc density $S_{\boldsymbol{b}_i}^{-1}$ is determined from the average surface area $S_{\boldsymbol{b}_i}$ on the plane for each mbc of type $\boldsymbol{b}_i$. It is the same for both the modulated and the non-modulated crystal.

$$S_{\boldsymbol{b}_i}^{-1} = n_i\frac{|\boldsymbol{b}_i \cdot \boldsymbol{H}_{(h_1h_2h_3h_4)}|}{|\boldsymbol{H}_{(h_1h_2h_3h_4)}|} = n_i\,|\boldsymbol{b}_i \cdot \boldsymbol{H}_{(h_1h_2h_3h_4)}|\,d_{(h_1h_2h_3h_4)} \tag{9.31}$$

where n_i is the average number of mbc's of type i passing through a unit volume in the crystal.

The average energy $\overline{\gamma}_{\boldsymbol{b}_i}$ is calculated in superspace by using the one-to-one correspondence between (satellite) planes and crystallographic hyperplanes as has been outlined in section 9.4. A numerical integration is performed over the energy of the bonds that are cut by the grid of netplanes $(h_1h_2h_3h_4)_s$ within one unit cell of the lattice Λ_s in superspace. The energy γ of a bond is e.g. taken to be inversely proportional to the length l of the bond:

$$\gamma = \frac{\chi}{l}.$$

We take $\chi = 1$ in our calculations.

The dependence of $\Gamma_{(h_1h_2h_3h_4)}$ on the position of the plane within one $d_{(h_1h_2h_3h_4)}$ in the physical crystal is studied by calculating $\Gamma_{(h_1h_2h_3h_4)}$ for 750 equidistant planes $(h_1h_2h_3h_4)_s$ within one $d_{\boldsymbol{H},s}$ in superspace. It is important to realise that, for all mbc's $\boldsymbol{b}_i$, the average energies $\overline{\gamma}_{\boldsymbol{b}_i}$ that are put in equation (9.30) must be calculated for the same position of the hyperplane in superspace. One of these positions will, thus, approximate the smallest surface free energy that is possible for this plane. We assume that the plane $(h_1h_2h_3h_4)$ always takes the corresponding position (mod. $d_{(h_1h_2h_3h_4)}$) in the physical crystal. Therefore, this minimal surface free energy for each face $(h_1h_2h_3h_4)$ is used for a standard Wulff plot in order to construct the equilibrium morphology.

In case that we are dealing with a modulation wave vector with an incommensurate *length*, a plane $(h_1h_2h_30)$, perpendicular to it, is treated separately in the way that has been explained in section 9.4.4. The positions of both the $(0001)_s$ plane and the grid of $(h_1h_2h_30)_s$ planes are varied over their corresponding $d_{\boldsymbol{H},s}$ in superspace in order to find the minimal surface free energy of this plane.

The surface free energies of planes $(h_1\ h_2\ h_3\ h_4)$ that one thus obtains only depend on the orientation of the plane. This means that a plane $(\overline{h_1}\ \overline{h_2}\ \overline{h_3}\ \overline{h_4})$ has the same surface free energy as the plane $(h_1\ h_2\ h_3\ h_4)$. Furthermore, only planes have to be considered for which the indices have 1 as largest common divisor. In the model calculations that are presented in this paper the maximum used value for h_1 and h_2 is 2, whereas for h_3 and h_4 it is 3.

The model crystal that we consider is an incommensurately modulated simple cubic crystal with only one kind of atom and three mbc's: $\boldsymbol{b}_1 = \boldsymbol{a}_1$, $\boldsymbol{b}_2 = \boldsymbol{a}_2$ and $\boldsymbol{b}_3 = \boldsymbol{a}_3$. The edges of the cubic unit cell of Λ have length 5 (units of length). The modulation wave function is $u(\tau) = \cos(\tau)$. We have chosen this model crystal, because it is one of the simplest possible. Therefore, it allows to study in detail the behaviour of the equilibrium morphology as a function of the length as well as the direction of both the modulation amplitude vector $\boldsymbol{f}$ and the modulation wave vector $\boldsymbol{q}$. The results are presented in the following subsections.

9.6.1 The equilibrium morphology as a function of the direction of the modulation amplitude vector

In figures 9.11, 9.12 and 9.13 the equilibrium morphology as obtained from a Wulff plot is shown for $\boldsymbol{f} \parallel \boldsymbol{a}_1$, $\boldsymbol{f} \parallel \boldsymbol{a}_2$ and $\boldsymbol{f} \parallel \boldsymbol{a}_3$ respectively. The length of the modulation amplitude vector is $|\boldsymbol{f}| = 1.75$ (units of length) for all three figures. The modulation wave vector $\boldsymbol{q}$ has an incommensurate *direction*, but is infinitely close to $0.6\boldsymbol{a}_1^* + 0.3\boldsymbol{a}_3^*$.

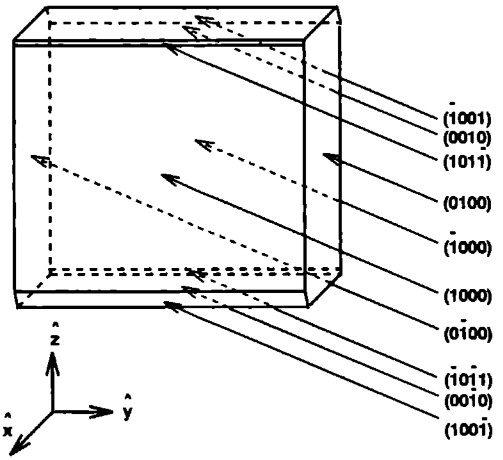

Figure 9.11 Equilibrium morphology of an incommensurately modulated simple cubic crystal with only mbc's along the crystallographic axes. The modulation wave vector has an incommensurate direction, but is infinitely close to $0.6\boldsymbol{a}_1^* + 0.3\boldsymbol{a}_3^*$. The modulation amplitude vector is $\boldsymbol{f} = (0.35, 0, 0)$

In table 9.1 all faces are listed that occur on at least one of these three crystal morphologies. The surface free energies of the faces are given for the case that the modulation amplitude is zero (non-modulated crystal) and for the three cases represented in figures 9.11, 9.12 and 9.13. Furthermore, the (0111) face has been added. Also the mbc densities $S_{\boldsymbol{a}_1}^{-1}$, $S_{\boldsymbol{a}_2}^{-1}$ and $S_{\boldsymbol{a}_3}^{-1}$ are given for all faces. The mbc density does not depend on the modulation amplitude vector. It is therefore the same for all considered cases. The faces that appear on the equilibrium morphology are enclosed by boxes in table 9.1. In case that there is no modulation ($\boldsymbol{f} = 0$), only the faces (1000), (0100) and (0010) appear and have all the same surface free energy. The equilibrium form is, therefore, a cube. In case that there is a modulation, the equilibrium morphology is different. Here, we describe the dependence of this morphology on the direction of the modulation amplitude vector.

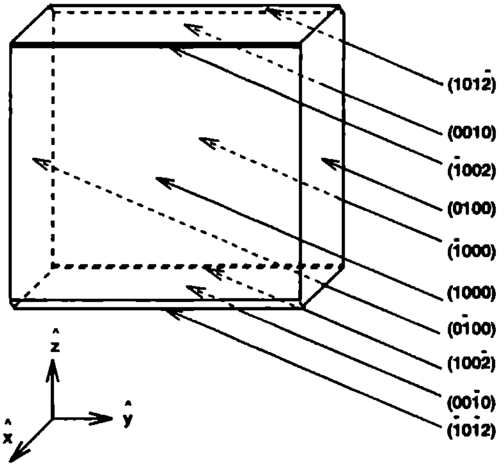

Figure 9.12 Equilibrium morphology of an incommensurately modulated simple cubic crystal with only mbc's along the crystallographic axes. The modulation wave vector has an incommensurate direction, but is infinitely close to $0.6\boldsymbol{a}_1^* + 0.3\boldsymbol{a}_3^*$. The modulation amplitude vector is $\boldsymbol{f} = (0, 0.35, 0)$.

In section 9.5.1 it has been explained that the amount of stabilisation for the energy $\bar{\gamma}_{\boldsymbol{b}}$ of a certain mbc with bond vector $\boldsymbol{b}$ is expected to be larger if the value of $|\boldsymbol{f} \cdot \boldsymbol{b}|$ is larger. Furthermore, one knows from equation (9.30) that a larger mbc density $S_{\boldsymbol{b}}^{-1}$ means that this stabilisation is more effective in decreasing the surface free energy $\Gamma_{(h_1 h_2 h_3 h_4)}$ of the plane. Therefore, the lowest surface free energy is expected if the modulation amplitude vector is parallel to the bond-chain vector of the mbc that has the largest mbc density. Table 9.1 shows that this is indeed the case for the planes (1000), (0010), (0001), $(100\bar{1})$, $(100\bar{2})$ and (0111). This, of course, also holds for many other planes that are not given in the table. Note, that both main faces and satellite faces can be stabilised due to the modulation. For the face (0100) the mbc density is largest for $\boldsymbol{b} = \boldsymbol{a}_2$, but the corresponding mbc is not modulated, since $\boldsymbol{q} \cdot \boldsymbol{a}_2 = 0$, so that there can be no stabilisation for $\bar{\gamma}_{\boldsymbol{a}_2}$.

In case of the faces $(101\bar{1})$ and $(101\bar{2})$ the mbc density is largest for $\boldsymbol{b} = \boldsymbol{a}_3$. Nevertheless, the stabilisation of the surface free energy is not largest for $\boldsymbol{f} \parallel \boldsymbol{a}_3$. In order to understand this, one must consider the $1+1$-dimensional embedding of the mbc's. For example, in case of the $(101\bar{1})$ plane, the grid $(11)_s$ has to be considered for both the mbc with $\boldsymbol{b} = \boldsymbol{a}_1$ and the mbc with $\boldsymbol{b} = \boldsymbol{a}_3$. However, the corresponding values of q_1 in the $1+1$-dimensional embeddings equal $\boldsymbol{q} \cdot \boldsymbol{b}$, which is $q_1 = 0.6$ for $\boldsymbol{b} = \boldsymbol{a}_1$ and $q_1 = 0.3$ for

$\boldsymbol{b} = \boldsymbol{a}_3$. In figure 5 of Kremers et al. (1994) it is shown that for $q_1 = 0.6$ the stabilisation of the $(1\bar{1})_s$ plane is much larger than for $q_1 = 0.3$. This is the reason that, although the mbc density is largest for $\boldsymbol{b} = \boldsymbol{a}_3$, $\Gamma_{(101\bar{1})}$ is lowest for $\boldsymbol{f} \parallel \boldsymbol{a}_1$.

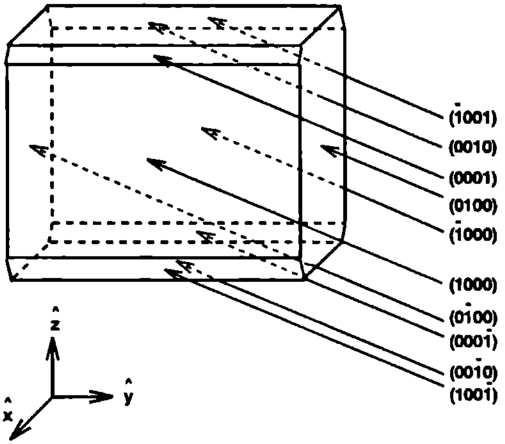

Figure 9.13 Equilibrium morphology of an incommensurately modulated simple cubic crystal with only mbc's along the crystallographic axes. The modulation wave vector has an incommensurate direction, but is infinitely close to $0.6\boldsymbol{a}_1^* + 0.3\boldsymbol{a}_3^*$. The modulation amplitude vector is $\boldsymbol{f} = (0, 0, 0.35)$.

The importance of the 1 + 1-dimensional embedding is further demonstrated by the fact that for $\boldsymbol{f} \parallel \boldsymbol{a}_1$ the satellite faces $(100\bar{1})$ and $(101\bar{1})$ appear on the equilibrium form. For both of them one must consider the grid $(1\bar{1})_s$ for the mbc with $\boldsymbol{b} = \boldsymbol{a}_1$. The value of $\boldsymbol{q} \cdot \boldsymbol{b}$ is $q_1 = 0.6$ which is very favourable for $(1\bar{1})_s$. On the other hand, the satellite faces (0001) and $(100\bar{1})$ appear on the equilibrium form in case that $\boldsymbol{f} \parallel \boldsymbol{a}_3$. For these faces one must consider the grid $(01)_s$ for the mbc with $\boldsymbol{b} = \boldsymbol{a}_3$. The value of $\boldsymbol{q} \cdot \boldsymbol{b}$ is $q_1 = 0.3$, which is very favourable for $(01)_s$ (see again figure 5 Kremers et al., 1994).

In section 9.5.3 it has been predicted that, in case of a modulation wave vector with an *incommensurate* direction, the (0001) plane is stabilised more than the (0111) plane. The results in table 9.1 confirm this prediction. The surface free energy of the (0111) plane is, in case of $\boldsymbol{f} \parallel \boldsymbol{a}_3$ for example, 9.64% lower than its value for the non-modulated crystal. The surface free energy of the (0001) plane is, however, for the same $\boldsymbol{f}$ even 15.89% lower than its value for the non-modulated crystal. Indeed, (0001) is stabilised more than (0111) due to the fact that in case of (0001) only $(01)_s$ planes must be considered, whereas for (0111) also $(11)_s$ planes are relevant.

The influence of the direction of $\boldsymbol{f}$ can now be summarised as follows. The largest

face	$\Gamma(\boldsymbol{f}=0)$	$\Gamma(\boldsymbol{f} \parallel \boldsymbol{a}_1)$	$\Gamma(\boldsymbol{f} \parallel \boldsymbol{a}_2)$	$\Gamma(\boldsymbol{f} \parallel \boldsymbol{a}_3)$	$S^{-1}_{\boldsymbol{a}_1}$	$S^{-1}_{\boldsymbol{a}_2}$	$S^{-1}_{\boldsymbol{a}_3}$
(1000)	$\boxed{0.0080}$	$\boxed{0.0059}$	$\boxed{0.0073}$	$\boxed{0.0073}$	1	0	0
(0100)	$\boxed{0.0080}$	$\boxed{0.0080}$	$\boxed{0.0080}$	$\boxed{0.0080}$	0	1	0
(0010)	$\boxed{0.0080}$	$\boxed{0.0075}$	$\boxed{0.0075}$	$\boxed{0.0066}$	0	0	1
(0001)	0.0107	0.0088	0.0098	$\boxed{0.0090}$	0.89	0	0.45
$(100\bar{1})$	0.0112	$\boxed{0.0086}$	0.0100	$\boxed{0.0089}$	0.80	0	0.30
$(101\bar{1})$	0.0109	$\boxed{0.0092}$	0.0101	0.0097	0.50	0	0.87
$(101\bar{2})$	0.0107	0.0098	$\boxed{0.0093}$	0.0099	0.45	0	0.89
$(100\bar{2})$	0.0101	0.0094	$\boxed{0.0093}$	0.0084	0.32	0	0.95
(0111)	0.0133	0.0122	0.0126	0.0120	0.34	0.57	0.74

Table 9.1 Surface free energies and mbc densities for important faces on the equilibrium morphologies of an incommensurately modulated simple cubic crystal with only mbc's along the crystallographic axes. The four columns with surface free energies give the results for four different modulation amplitude vectors: $\boldsymbol{f} = 0$, $\boldsymbol{f} = (0.35, 0, 0)$, $\boldsymbol{f} = (0, 0.35, 0)$ and $\boldsymbol{f} = (0, 0, 0.35)$ respectively. The equilibrium morphologies of the latter three cases are given in figures 9.11, 9.12 and 9.13. The enclosing of a value of the surface free energy by a box indicates that the corresponding face appears on the equilibrium form of the crystal. The modulation wave vector has an incommensurate direction, but is infinitely close to $0.6\boldsymbol{a}_1^* + 0.3\boldsymbol{a}_3^*$.

stabilisation for $\Gamma_{(h_1h_2h_3h_4)}$ can be expected if $|\, \boldsymbol{f} \cdot \boldsymbol{b} \,|$ is largest for the mbc that is most effective. This effectiveness can be increased by both a large mbc density and a favourable value of $q_1 = \boldsymbol{q} \cdot \boldsymbol{b}$ for the grid $(h_1b_1 + h_2b_2 + h_3b_3, h_4)_s$ that must be considered for this plane.

9.6.2 The equilibrium morphology as a function of the length of the modulation amplitude vector

In this section we present calculations on the equilibrium morphology of the same simple cubic crystal as in section 9.6.1. The modulation wave vector again is $\boldsymbol{q} = 0.6\boldsymbol{a}_1^* + 0.3\boldsymbol{a}_3^*$ and the modulation amplitude vector $\boldsymbol{f}$ is parallel to $\boldsymbol{a}_2$. The surface free energies have been calculated for three different lengths of the modulation amplitude vector: $|\boldsymbol{f}| = 0.5$, $|\boldsymbol{f}| = 1.0$ and $|\boldsymbol{f}| = 2.25$. The results are given in table 9.2 and the faces that appear on the equilibrium morphology are enclosed by a box. In addition, the surface free energies for the non-modulated crystal are given and also the mbc densities for the three mbc's that are present in the crystal.

It is clear that for all faces the stabilisation increases with the modulation amplitude, as expected. Moreover, the larger the modulation amplitude the more faces can appear on the equilibrium morphology. This is caused by the fact that the dependence on the modulation amplitude can be different for different faces. For example, the satellite face

face	$\Gamma(\boldsymbol{f}=0)$	$\Gamma(\mid\boldsymbol{f}\mid=0.5)$	$\Gamma(\mid\boldsymbol{f}\mid=1.0)$	$\Gamma(\mid\boldsymbol{f}\mid=2.25)$	$S^{-1}_{\boldsymbol{a}_1}$	$S^{-1}_{\boldsymbol{a}_2}$	$S^{-1}_{\boldsymbol{a}_3}$
(1000)	$\boxed{0.0080}$	$\boxed{0.0079}$	$\boxed{0.0077}$	$\boxed{0.0069}$	1	0	0
(0100)	$\boxed{0.0080}$	$\boxed{0.0080}$	$\boxed{0.0080}$	$\boxed{0.0080}$	0	1	0
(0010)	$\boxed{0.0080}$	$\boxed{0.0079}$	$\boxed{0.0078}$	$\boxed{0.0072}$	0	0	1
$(101\bar{2})$	0.0107	$\boxed{0.0106}$	$\boxed{0.0102}$	$\boxed{0.0087}$	0.45	0	0.89
$(201\bar{2})$	0.0107	0.0106	0.0104	$\boxed{0.0093}$	0.89	0	0.45
$(100\bar{2})$	0.0101	0.0100	0.0098	$\boxed{0.0089}$	0.32	0	0.95
(1200)	0.0107	0.0107	0.0106	$\boxed{0.0102}$	0.45	0.89	0
$(1\bar{2}00)$	0.0107	0.0107	0.0106	$\boxed{0.0102}$	0.45	0.89	0
(0210)	0.0107	0.0107	0.0106	$\boxed{0.0103}$	0	0.89	0.45
$(02\bar{1}0)$	0.0107	0.0107	0.0106	$\boxed{0.0103}$	0	0.89	0.45

Table 9.2 Surface free energies Γ and mbc densities S^{-1} for important faces on the equilibrium morphologies of an incommensurately modulated simple cubic crystal with only mbc's along the crystallographic axes. The four columns with surface free energies give the results for four different lengths of the modulation amplitude vector parallel to $\boldsymbol{a}_2$: $\mid\boldsymbol{f}\mid=0$, $\mid\boldsymbol{f}\mid=0.5$, $\mid\boldsymbol{f}\mid=1.0$ and $\mid\boldsymbol{f}\mid=2.25$ respectively. The enclosing of a value of the surface free energy by a box indicates that the corresponding face appears on the equilibrium form of the crystal. The modulation wave vector has an incommensurate direction, but is infinitely close to $0.6\boldsymbol{a}_1^* + 0.3\boldsymbol{a}_3^*$.

$(101\bar{2})$ and the main face (0210) have equal surface free energy for $\mid\boldsymbol{f}\mid=0$. For $\mid\boldsymbol{f}\mid\neq 0$, however, the surface free energy is smaller for the $(101\bar{2})$ face than for the (0210) face.

In order to explain this, we consider the $1+1$-dimensional embedding of a mbc consisting of one type of atom and one type of bond, $u(\tau)=\cos(\tau)$ and $\boldsymbol{f} \parallel \boldsymbol{b}$. One can easily derive that the (largest) average length of the embedded bonds cut by a $(10)_s$ plane is

$$\bar{l}_{(10)_s} = |\boldsymbol{b}| + 4\,|\boldsymbol{f}|\,(1-\cos q_1)\,.$$

On the other hand, the (largest) average length of the bonds cut by a $(01)_s$ plane is

$$\bar{l}_{(01)_s} = |\boldsymbol{b}| + \frac{2}{q_1}\,|\boldsymbol{f}|\,(1-\cos q_1)$$

and the (largest) average length of the bonds cut by a $(1\bar{1})_s$ plane is

$$\bar{l}_{(1\bar{1})_s} = |\boldsymbol{b}| + \frac{2}{1-q_1}\,|\boldsymbol{f}|\,(1-\cos q_1)\,.$$

Note that in all cases the average length increases linearly with $\mid\boldsymbol{f}\mid$, but the value of q_1 determines which proportionality constant is larger. For $q_1 < 0.5$ the average length is largest for the $(01)_s$ plane, smallest for the $(1\bar{1})_s$ plane and the value for the $(10)_s$ plane is in between. For $q_1 > 0.5$ this order is reversed.

In table 9.2 it can be seen that the dependence of the surface free energy on the modulation amplitude is stronger for (1000) than for (0010). The reason for this difference lies exactly in the fact that for the (1000) plane a $(10)_s$ plane must be considered with $q_1 = 0.6$, whereas for the (0010) plane a $(10)_s$ plane must be considered with $q_1 = 0.3$. For $q_1 = 0.6$, the average length of the cut bonds is larger than for $q_1 = 0.3$. Therefore, the (1000) plane is stabilised more than the (0010) plane.

The sensitivity of the amount of stabilisation for the length of the modulation amplitude vector is thus determined by (among others) the values of $q_1 = \boldsymbol{q} \cdot \boldsymbol{b}$ for the 1 + 1-dimensional embeddings of the mbc's present in the crystal. The influence of the modulation amplitude is, therefore, not independent of the modulation wave vector. Which faces appear on the equilibrium shape with increasing $|\,\boldsymbol{f}\,|$ is thus mainly determined by the modulation wave vector $\boldsymbol{q}$. However, in general, one can say that more faces can appear if $|\boldsymbol{f}|$ is larger.

9.6.3 The equilibrium morphology as a function of the length of the modulation wave vector

From the preceding subsections 9.6.1 and 9.6.2 we have learned that the values of $q_1 = \boldsymbol{q}\cdot\boldsymbol{b}$ for the 1 + 1-dimensional embeddings of the mbc's that are present in the crystal are essential parameters for the equilibrium morphology. These values depend, of course, on the length of the modulation wave vector. Therefore, three additional model calculations have been performed for the simple cubic crystal with $\boldsymbol{f} = (0, 0.2, 0)$ and a modulation

face	$\Gamma(\boldsymbol{q} = (0.4, 0, 0.2))$	$\Gamma(\boldsymbol{q} = (0.6, 0, 0.3))$	$\Gamma(\boldsymbol{q} = (0.8, 0, 0.4))$	$\Gamma(\boldsymbol{q} = (0.9, 0, 0.45))$
(1000)	$\boxed{0.0077}$	$\boxed{0.0077}$	$\boxed{0.0079}$	$\boxed{0.0080}$
(0100)	$\boxed{0.0080}$	$\boxed{0.0080}$	$\boxed{0.0080}$	$\boxed{0.0080}$
(0010)	$\boxed{0.0079}$	$\boxed{0.0078}$	$\boxed{0.0077}$	$\boxed{0.0077}$
(0001)	$\boxed{0.0104}$	0.0104	0.0105	0.0106
$(101\bar{2})$	$\boxed{0.0098}$	$\boxed{0.0102}$	$\boxed{0.0098}$	$\boxed{0.0088}$
$(100\bar{1})$	0.0098	0.0108	$\boxed{0.0104}$	$\boxed{0.0092}$
$(100\bar{2})$	$\boxed{0.0105}$	0.0098	0.0109	0.0110
$(201\bar{2})$	0.0104	0.0104	$\boxed{0.0105}$	$\boxed{0.0105}$

Table 9.3 Surface free energies for important faces on the equilibrium morphologies of an incommensurately modulated simple cubic crystal with only mbc's along the crystallographic axes. The four columns with surface free energies give the results for four different lengths of the modulation wave vector. In all cases the modulation amplitude vector is $\boldsymbol{f} = (0, 0.2, 0)$. The enclosing of a value of the surface free energy by a box indicates that the corresponding face appears on the equilibrium form of the crystal. The modulation wave vector has in all cases an incommensurate *direction* infinitely close to $\boldsymbol{q} = (2\gamma, 0, \gamma)$.

wave vector $\boldsymbol{q}$ with the same incommensurate *direction* as used in section 9.6.2, but having different lengths. The results are summarised in table 9.3.

It can be observed clearly that those faces appear on the equilibrium morphology for which there exist favourable $q_1 = \boldsymbol{q} \cdot \boldsymbol{b}$ values for the $(h_1b_1 + h_2b_2 + h_3b_3, h_4)_s$ planes in the 1 + 1-dimensional embeddings of the mbc's.

9.6.4 The equilibrium morphology as a function of the direction of the modulation wave vector

So far, we have only considered modulation wave vectors with an incommensurate *direction*. However, as explained in section 9.5.4 one expects that faces perpendicular to a modulation wave vector with an incommensurate *length* can be stabilised more by the modulation than all other possible faces. Therefore, model calculations have been per-

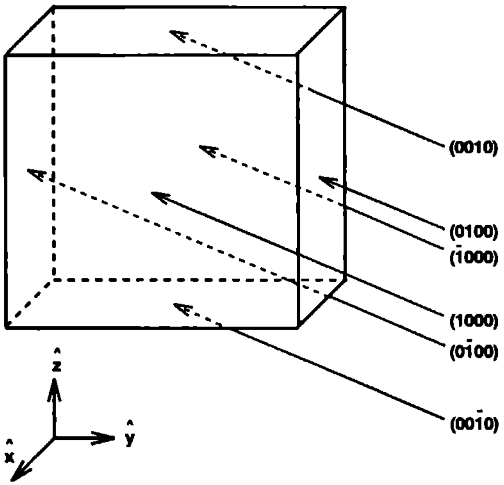

Figure 9.14 Equilibrium morphology of an incommensurately modulated simple cubic crystal with only mbc's along the crystallographic axes The modulation wave vector has an incommensurate *length* $\boldsymbol{q} = 0\ 3\boldsymbol{a}_3^*$ The plane perpendicular to $\boldsymbol{q}$ is (0010) The modulation amplitude vector is $\boldsymbol{f} = (0, 0\ 2, 0)$

formed for the simple cubic crystal with $\boldsymbol{f} = (0, 0.2, 0)$ and three different directions for the modulation wave vector, infinitely close to: $\boldsymbol{q} = (0, 0, 0.3)$, $\boldsymbol{q} = (0\ 6, 0, 0.3)$ and $\boldsymbol{q} = (0.1, 0.2, 0.3)$. All these $\boldsymbol{q}$ vectors are taken to have an incommensurate *length*. The faces perpendicular to these $\boldsymbol{q}$ vectors are (0010), (2010) and (1230) respectively. The morphologies are presented in figures 9.14, 9.15 and 9.16.

The surface free energies of the faces appearing in figure 9.15 for the case where $\boldsymbol{q} = 0.6\boldsymbol{a}_1^* + 0.3\boldsymbol{a}_3^*$, are given in table 9.4

These results should be compared with the ones given in table 9.2 for $\mid \boldsymbol{f} \mid = 1.0$, because, besides the character of the modulation wave vector, this is the same crystal. It is very clear that only when $\boldsymbol{q}$ has an incommensurate *length*, the face (2010) perpendicular to it is stabilised so much, that it appears on the equilibrium morphology.

Furthermore, the direction of $\boldsymbol{q}$, of course, determines the values of $q_1 = \boldsymbol{q} \cdot \boldsymbol{b}$ in the $1+1$-dimensional embeddings of the mbc's. As we know already, a change of these values can change the equilibrium morphology considerably. Again, this is demonstrated by the differences between figures 9.14, 9.15 and 9.16.

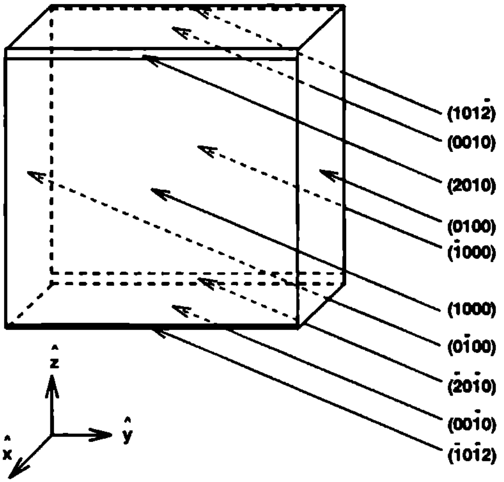

Figure 9.15 Equilibrium morphology of an incommensurately modulated simple cubic crystal with only mbc's along the crystallographic axes. The modulation wave vector has an incommensurate *length* $\boldsymbol{q} = 0.6\boldsymbol{a}_1^* + 0.3\boldsymbol{a}_3^*$. The plane perpendicular to $\boldsymbol{q}$ is (2010). The modulation amplitude vector is $\boldsymbol{f} = (0, 0.2, 0)$.

face	$\Gamma(q = (0\ 6, 0, 0\ 3))$
(1000)	$\boxed{0\ 0077}$
(0100)	$\boxed{0\ 0080}$
(0010)	$\boxed{0\ 0078}$
$(101\bar{2})$	$\boxed{0\ 0102}$
(2010)	$\boxed{0\ 0102}$

Table 9.4 Surface free energies for the faces on the equilibrium morphology of an incommensurately modulated simple cubic crystal with only mbc's along the crystallographic axes The modulation wave vector is $q = 0\ 6a_1^* + 0\ 3a_3^*$ It has an incommensurate *length* The modulation amplitude vector is $f = (0, 0\ 2, 0)$ The enclosing of a value of the surface free energy by a box indicates that the corresponding face appears on the equilibrium form of the crystal

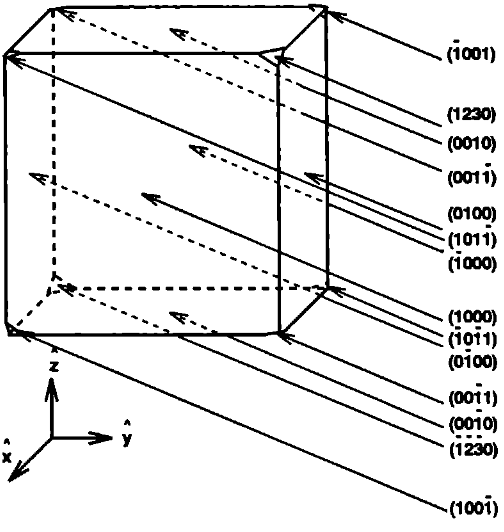

Figure 9.16 Equilibrium morphology of an incommensurately modulated simple cubic crystal with only mbc's along the crystallographic axes The modulation wave vector has an incommensurate *length* $q = 0\ 1a_1^* + 0\ 2a_2^* + 0\ 3a_3^*$ The plane perpendicular to q is (1230) The modulation amplitude vector is $f = (0, 0\ 2, 0)$

9.6.5 The equilibrium morphology as a function of the modulation function

In order to study the influence of the modulation function u on the equilibrium morphology, it is perhaps best to consider figure 5 of Kremers et al. (1994). The modulation function used for the calculation of that figure is $u(\tau) = \cos(\tau)$. In this paper we have often refered to this figure, because it gives the information of the average energy of the bonds cut by a $(h_1b_1 + h_2b_2 + h_3b_3, h_4)_s$ plane in the 1 + 1-dimensional embedding of a mbc. However, if the modulation function is different, the shape of the curves in this figure changes.

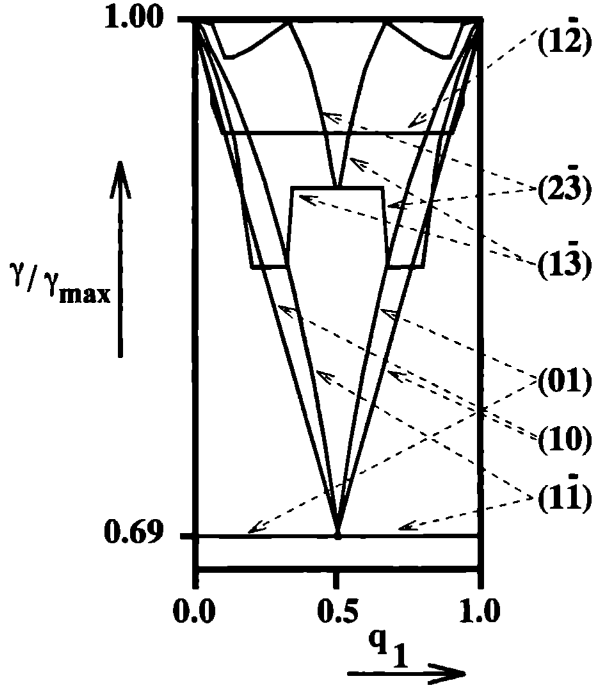

Figure 9.17 Normalised minimal average energies $\frac{\gamma}{\gamma_{max}}$ of the bonds cut by $(h_1b_1 + h_2b_2 + h_3b_3, h_4)_s$ planes in a 1 + 1-dimensional embedding of a mbc consisting out of one type of atom. The modulation function u has a square wave behaviour. The modulation amplitude is $f = 0\ 2b$.

In figure 9.17 the result is presented of a similar calculation, but in this case the modulation function is a square wave: $u(\tau) = f, \quad \text{for} \quad \tau \in [0, \frac{1}{2})$ and $u(\tau) = -f, \quad \text{for} \quad \tau \in [\frac{1}{2}, 1)$. It is very instructive to see that, for example, for the plane $(1\bar{1})_s$ a constant average energy is found for the cut bonds if $q_1 > 0.5$. This is in sharp contrast with the case of the modulation function $u(\tau) = \cos(\tau)$, for which a relatively sharp dip can be observed for $q_1 = 0.65$. $(1\bar{1})_s$ planes will, of course, often be relevant for satellite planes $(h_1h_2h_3\bar{1})$ with at least one of the h_1, h_2 or h_3 equal to one. Therefore, in case of a block wave modulation, there will be much more mbc's with favourable $q_1 = \boldsymbol{q} \cdot \boldsymbol{b}$ values for the $(1\bar{1})_s$ planes than in case of a sinusoidal modulation. The same kind of reasoning applies to the $(01)_s$ plane, which is of course also often relevant for satellite planes. Furthermore, it is very interesting that for the plane $(10)_s$ the dip in average energy at $q_1 = 0.5$ is much sharper for the square wave modulation than for the sinusoidal modulation. $(10)_s$ planes will, of course, often be relevant for main planes $(h_1h_2h_30)$ with at least one of the h_1, h_2 or h_3 equal to one. Therefore, in case of a square wave modulation, there will be less mbc's with favourable $q_1 = \boldsymbol{q} \cdot \boldsymbol{b}$ values for the $(10)_s$ planes than in case of a sinusoidal modulation.

The influence of the modulation function u can now be summarised as follows. If the modulation function resembles a square wave function, one expects satellite planes to be stabilised more and main planes to be stabilised less as compared to the case that the modulation wave resembles a sinusoidal behaviour.

9.7 Discussion

In this paper we have presented a broken-bond model for the calculation of surface free energies $\Gamma_{(h_1h_2h_3h_4)}$ for (satellite) planes $(h_1h_2h_3h_4)$ on incommensurately modulated crystals. Due to the incommensurateness it is, in general, not possible to define a mesh area $M_{(h_1h_2h_3h_4)}$ on such planes. In consequence, surface free energies have been calculated by averaging over infinite planes. One of the key assumptions is, then, that the thus obtained surface free energies $\Gamma_{(h_1h_2h_3h_4)}$ have the same meaning for the morphology as surface free energies $\Gamma_{(h_1h_2h_3)}$ for non-modulated crystals. With such an assumption it is possible to calculate equilibrium morphologies by using these surface free energies $\Gamma_{(h_1h_2h_3h_4)}$ for a Wulff plot. This plot is intended to give a crystal shape that has minimal total surface free energy. The assumption can, therefore, be expected to be valid if the planes on the equilibrium shape are not too small. In our opinion, even micron sized crystals already have faces so large that the difference between the actual average surface free energy and the $\Gamma_{(h_1h_2h_3h_4)}$ for the infinite plane is negligible.

By means of a superspace approach it has been shown that both main faces and satellite faces can be stabilised due to the principle of selective cuts. In order to make an estimate of the possible amount of stabilisation for an actual incommensurately modulated crystal, we consider the example of the mineral calaverite $AuTe_2$. The modulation amplitude is about 0.4 Å for the Te atoms and the average length of the crystallographic axes $\boldsymbol{a}_1$, $\boldsymbol{a}_2$ and $\boldsymbol{a}_3$ is 5.4 Å (Schutte and de Boer, 1988). It seems reasonable to compare this with the case $|\boldsymbol{f}| = 0.5$ and $|\boldsymbol{a}| = 5$ for the simple cubic crystal in table 9.2. In this way we estimate that the surface free energy for faces appearing on $AuTe_2$ is in the order of one percent less than what it would be without the influence of the modulation, assuming the potential used to be relevant.

It is striking that, as a consequence, in a Wulff plot highly singular cusps appear in the polar plot of the surface free energies. For (low index) main faces there still exists a cusp in the Wulff plot, having the same shape as for the non-modulated crystal. However, at the center of the cusp the Wulff plot is discontinuous, contrary to the non-modulated case. This center, being exactly one point, is displaced (in the order of one percent) towards the origin of the Wulff plot. There are, of course, many high index planes that have face normals pointing to a position somewhere in the cusp. However, their indices are in general so high that there is virtually no stabilisation for these planes as a result of the modulation. The shape of the cusp is, therefore, not altered at that position.

However, for a satellite face the shape of the cusp is different. If the crystal were non-modulated, the polar plot of the surface free energy would have a convex shape in the direction of the face normal. The only change due to the modulation is that again exactly one point is displaced towards the origin, so that also for a satellite face the Wulff plot is discontinuous.

These singular cusps for both main faces and satellite faces seem to indicate that a finite amount of energy is necessary for any tilt of the surface of a face, however small. At present it is unclear to us whether this has any physical relevance.

The presented analysis has shown, that the surface free energy $\Gamma_{(h_1 h_2 h_3 h_4)}$ depends, for a given crystal, on both the orientation of the plane (defined by $\boldsymbol{H}_{(h_1 h_2 h_3 h_4)}$) and the position of the plane with respect to the origin. It is interesting that, with one exception, for all planes there exists a periodicity in the surface free energy. The period length is exactly $d_{(h_1 h_2 h_3 h_4)}$. This can be considered as a generalisation of the situation for non-modulated crystals, where this period length is $d_{(h_1 h_2 h_3)}$. Consequently, there is, for non-modulated crystals, within each distance $d_{(h_1 h_2 h_3)}$ a position of minimal surface free energy. It is common to assume that the plane takes exactly this position when it bounds the crystal. Therefore, the minimal surface free energy is used for a Wulff plot. For (satellite) planes on incommensurately modulated crystals, the situation can be considered to be no different. Within each distance $d_{(h_1 h_2 h_3 h_4)}$ there exists a position of minimal surface free energy. It can thus be assumed that a $(h_1 h_2 h_3 h_4)$ plane takes this position and that the corresponding minimal surface free energy is to be used in a Wulff plot. The exception is, of course, the plane perpendicular to a modulation wave vector that has an incommensurate *length*. For this plane there is no positional periodicity in the surface free energy. Nevertheless, in the Wulff plot we have again taken the minimal surface free energy that could be found for the plane. This can be justified by assuming that the phase of the modulation wave can be pinned to a surface that bounds the crystal. It is well known that, for example, defects can pin the phase of the modulation wave. The surface of a crystal can be considered to be an intrinsic defect.

There is a further interesting aspect of the positional periodicity in the surface free energy, because for non-modulated crystals it is believed that this periodicity is one of the main reasons that crystals grow with layers of thickness $d_{(h_1h_2h_3)}$. Although the analysis presented in this paper is not meant to explain the growth mechanism of (satellite) faces on incommensurately modulated crystals, we feel that the positional periodicity in $\Gamma_{(h_1h_2h_3h4)}$, together with the fact that all slices $(h_1h_2h_3h_4)$ have the same energy content, should be considered as a serious indication for the possibility of a layer growth mechanism. We would like to stress that the growth of satellite faces on incommensurately modulated crystals can not be viewed as more extraordinary than the growth of main planes. The first experimental indications of a layer growth mechanism have been reported by (Dam, 1985b), who could observe growth spirals on the satellite face $(101\bar{2})$ of a crystal of $((CH_3)_4N)_2ZnCl_4$. It would be very interesting to measure the height of steps on (satellite) faces in order to see whether these steps are built of layers with thickness $d_{(h_1h_2h_3h_4)}$. Furthermore, one could expect that the face perpendicular to a modulation wave vector with an incommensurate *length* shows exceptional growth behaviour, because for such a face there does not exist a positional periodicity in the surface free energy.

The energy content $E_{\boldsymbol{H}}$ of a slice can be found in the following way. One divides every bond in the crystal in equal infinitesimal pieces that all have the same infinitesimal energy content dE. This is done in such a way, of course, that integrating the energies dE over the bond gives exactly the bond energy. $E_{\boldsymbol{H}}$ can then be calculated by integrating all those energies dE that correspond to the intersection of a $(h_1h_2h_3h_4)$ plane with a bond, for all positions of the plane within the slice. For such a calculation, a similar superspace approach can be used as for the calculation of surface free energies. This energy $E_{\boldsymbol{H}}$ includes the energy of the bond pieces within the slice that are part of the bonds that are intersected by the surfaces of the slice. If one omits the contributions of these bond pieces to $E_{\boldsymbol{H}}$, the so-called quantity E_{slice} is found. This quantity is of importance for the crystal growth theory of non-modulated crystals (Bennema and van der Eerden, 1987). It thus differs from $E_{\boldsymbol{H}}$. Nevertheless, one can calculate E_{slice} also for modulated crystals by subtracting the surface free energy $\Gamma_{(h_1h_2h_3h_4)}$ from $E_{\boldsymbol{H}}$ (and taking the appropriate units and dimensions into account, of course). The dependence of $E_{\boldsymbol{H}}$ and E_{slice} on the modulation properties has not been considered in this paper. However, it may be of importance for the growth of modulated crystals.

It has to be remarked, that all calculations presented in this paper are essentially for zero temperature. For finite temperatures one is faced with additional problems. It is well known that faces on non-modulated crystals have a roughening temperature T_R. Below T_R the face is flat and there is a finite step free energy. However, at T_R there is a phase transition (of infinite order) at which the step free energy becomes zero. The face roughens, because steps can be created without cost. The face can then no longer be uniquely identified. Consequently, one only takes those faces into account that have a roughening temperature higher than the actual temperature. In case of incommensurately modulated crystals it is even not yet known, whether a roughening transition exists, though we want to mention the work of Dam (1985b) who observed the roughening of a 'satellite' face upon a change of the modulation wave vector from one commensurate value to another. Nevertheless, from an experimental point of view, it is clear that both flat main faces and flat satellite faces do show up. This means that, if there is a roughening transition, there will be (satellite) faces that have a non-zero T_R. Moreover, if such a roughening transition is related to the step free energy, one could use the same lines of thought as presented in this paper for the calculation of these step free energies by making use of the embedding of the crystal in superspace. On the other hand, one can expect that $(h_1h_2h_3h_4)$ planes for which there exists a zero step free energy are in any case roughened, for the same reasons as $(h_1h_2h_3)$ planes are in non-modulated crystals.

It would, therefore, be sensible to check whether there are faces for which the step free energy is zero. This can be done analogously to the procedure that is commonly used for non-modulated crystals (Hartman and Perdok, 1955). First, the crystal is represented by a graph. The vertices of the graph represent the growth units and the connections between the vertices represent the bonds. However, in the graph there is no information about the energies of the bonds. For non-modulated crystals it is then checked whether within a $(h_1h_2h_3)$ slice of thickness $d_{(h_1h_2h_3)}$ a connected net can be defined. A connected net is a 2-dimensional net in which all vertices are connected with each other. The edge free energy for the face $(h_1h_2h_3)$ is expected to be zero in case that it is not possible to find such a connected net. The graph of an incommensurately modulated crystal is equal to the graph of the same crystal without modulation if one assumes that due to the modulation no bonds disappear and no extra bonds appear. It follows, that one can neglect the modulation for checking the connectedness of nets. It has been shown that an incommensurately modulated crystal can be partitioned in slices $(h_1h_2h_3h_4)$ with thickness $d_{(h_1h_2h_3h_4)}$, that all have an equal energy content. Therefore, it seems justified to search for connected nets in precisely such slices. If there is no connected net, the face $(h_1h_2h_3h_4)$ can be expected to have a zero edge free energy. It will then be rough. Such an approach has been used by Vogels et al. (1992a).

In this paper we have studied the influence of the length and the direction of both the modulation wave vector and the modulation amplitude vector on the (equilibrium) morphology. Also the influence of the modulation function has been outlined. The obtained results now allow us to get a first understanding of the differences in morphology of two well-known occurring incommensurate crystals, $((CH_3)_4N)_2ZnCl_4$ and $AuTe_2$.

Crystals of $((CH_3)_4N)_2ZnCl_4$ that have been grown at a temperature for which the structure is incommensurate, almost always show only main faces. Several satellite faces can be observed, however, if a sphere growth experiment is performed (Dam (1986), Vogels et al. (1992b)). In such an experiment, a single crystal is polished into a spherical shape, which is subsequently exposed to a slightly supersaturated solution so that it grows for a short time. All stable faces then show up as small flat regions on the sphere. On the other hand, the sphere roughens up in the regions where no stable faces are present. The incommensurate phase of $((CH_3)_4N)_2ZnCl_4$ can be characterised with an orthorhombic lattice Λ, $|\boldsymbol{a}_1| = 12.258$ Å, $|\boldsymbol{a}_2| = 8.987$ Å and $|\boldsymbol{a}_3| = 15.503$ Å (Madariaga et al., 1987). Furthermore, the modulation wave vector $\boldsymbol{q} \approx 0.4\boldsymbol{a}_3^*$ can be assumed to have an incommensurate *length* and the modulation amplitude vector with maximum length is $\boldsymbol{f} \approx 0.047\boldsymbol{a}_2$ for one of the chlorine atoms. For a large temperature region in the incommensurate phase it is a reasonable assumption to take the modulation function sinusoidal.

Contrary to the case of $((CH_3)_4N)_2ZnCl_4$, numerous as well as large satellite faces can be found on as-grown crystals of $AuTe_2$, both for mineral crystals found in nature (Dam et al., 1985) and for synthetically prepared crystals (Balzuweit et al., 1991). The incommensurate structure of $AuTe_2$ can be characterised with a monoclinic lattice Λ, $\beta = 90.038^0$, $|\boldsymbol{a}_1| = 7.1947$ Å, $|\boldsymbol{a}_2| = 4.4146$ Å and $|\boldsymbol{a}_3| = 5,0703$ Å (Schutte and de Boer, 1988). The modulation wave vector $\boldsymbol{q} \approx -0.4076\boldsymbol{a}_1^* + 0.4479\boldsymbol{a}_3^*$ can be assumed to have an incommensurate *direction* and the largest modulation amplitude vector $|\boldsymbol{f}| \approx 0.4$ Å is found for the Te atoms. The modulation functions for the different atoms contain first, second and third order harmonics.

Already from these structural data, we can get a fairly good understanding why satellite faces appear much more easily on crystals of $AuTe_2$ than on crystals of $((CH_3)_4N)_2ZnCl_4$. The analysis presented in this paper has shown that the appearance of satellite faces is favoured by a large modulation amplitude, a modulation wave vector with an incommensurate *direction* and a modulation function that resembles a square wave behaviour. With respect to all these three aspects, $AuTe_2$ indeed has a more favourable structure than $((CH_3)_4N)_2ZnCl_4$. The modulation amplitude of $AuTe_2$ is larger with respect to the lengths of the crystallographic axes than the modulation amplitude of $((CH_3)_4N)_2ZnCl_4$. In addition, the modulation wave vector of $((CH_3)_4N)_2ZnCl_4$ has an incommensurate *length*. Therefore, the $\{0010\}$ faces perpendicular to it may be stabilised so much that they dominate the morphology and that, consequently, satellite faces do not appear. In case of $AuTe_2$ the modulation wave vector has an incommensurate *direction*, so that there is no face perpendicular to the modulation wave vector that can dominate the morphology. Furthermore, the modulation functions for the atoms in $AuTe_2$ can be considered to be in closer resemblance with a square wave behaviour than the modulation functions for the atoms in $((CH_3)_4N)_2ZnCl_4$. Therefore, the relative stabilisation of satellite faces with respect to the stabilisation of main faces is expected to be larger for $AuTe_2$ than for $((CH_3)_4N)_2ZnCl_4$.

In order to get a more complete insight in the differences in morphology for $AuTe_2$ and $((CH_3)_4N)_2ZnCl_4$, one should perform calculations as described in section 9.6 using reasonable choices of bonds that build mbc's. Such calculations will be presented in a forthcoming paper.

Finally, we would like to point out that the superspace approach, that has been used here, is not restricted to incommensurate displacively modulated 3-dimensional crystals.

Instead of taking modulated positions that define modulated bonds, one can also take only modulated bond energies and leave the positions unaffected by the modulation. The same kind of theory applies as outlined in section 9.4 and the same kind of computer program is needed to calculate surface free energies numerically. Of course, also incommensurately modulated 2-dimensional crystals can be dealt with using a similar superspace approach.

Another, very interesting, class of crystals is formed by the incommensurate composite crystals. Also these crystals can be embedded in a superspace (Janner and Janssen (1980), van Smaalen (1992)). Here, we will not go in detail, but they may be considered as a collection of incommensurately modulated crystals. So far, little attention has been paid to the morphology of these crystals. It will be clear that the analysis presented in this paper immediately applies to each incommensurately modulated crystal from the collection that builds the incommensurate composite crystal. Special attention must be paid to bonds between atoms belonging to different incommensurately modulated structures from the collection. However, since incommensurate composite crystals can be embedded, we are confident that the superspace approach for the morphology can be extended to the case of these crystals.

There is still another class of incommensurate crystals that can be described using an embedding in a superspace. This class is formed by the so-called quasi-crystals. The Fibonacci chain of atoms is a famous example of a 1-dimensional quasi-crystal. It has been shown by Heijmen et al. (1994) that the morphology of this chain can be dealt with in a superspace approach. In a forthcoming paper (Heijmen et al., 1995) it will be shown that the same holds for quasi-periodic tilings.

In summary, one can say that the superspace approach for the morphology is promising for all classes of incommensurate crystals.

9.8 Conclusions

It has been shown, that in an incommensurately modulated crystal one can define modulated bond chains that are characterised by a bond-chain vector $\boldsymbol{b}$. By means of the $3+1$-dimensional embedding of the modulated crystal in superspace it is found that $1+1$-dimensional embeddings can be defined for these mbc's. The corresponding value for q_1 depends on the actual modulation wave vector $\boldsymbol{q}$ and on the bond-chain vector $\boldsymbol{b}$, $q_1 = \boldsymbol{q} \cdot \boldsymbol{b}$. The bonds of the mbc's that are intersected by a (satellite) plane $(h_1h_2h_3h_4)$ in the physical crystal can be found by intersecting the uniform bond density in superspace with a $(h_1b_1 + h_2b_2 + h_3b_3, h_4)_s$ grid in the $1+1$-dimensional embedding of the mbc. Moreover, it has been shown that these are also exactly the bonds that are intersected by a crystallographic hyperplane in superspace. Therefore, one can state that there is a one-to-one correspondence between crystallographic hyperplanes $(h_1h_2h_3h_4)_s$ and (satellite) planes $(h_1h_2h_3h_4)$ in the physical crystal as the morphology is concerned. This correspondence gives the possibility to calculate numerically average surface free energies $\Gamma_{(h_1h_2h_3h_4)}$

by means of a superspace approach for arbitrarily complex incommensurately modulated structures.

In the 1 + 1-dimensional embeddings of mbc's one can see immediately that there is a principle of selective cutting. A (satellite) plane $(h_1h_2h_3h_4)$ in the physical crystal intersects only a selection of the infinite number of different bonds that exist due to the modulation. The (satellite) plane can be positioned such that the plane is stabilised with respect to the non-modulated crystal. This explains the occurrence of satellite planes on incommensurately modulated crystals. In principle, planes perpendicular to a modulation wave vector with an incommensurate *length* can be stabilised more than satellite planes perpendicular to a modulation wave vector with an incommensurate *direction*. The latter can have, however, more stabilisation than other satellite planes. These, in turn, can be stabilised more than main planes non-perpendicular to the modulation wave vector. Generally, it can be said, that the amount of stabilisation depends on the length of the mesh area of the 1-dimensional $(h_1b_1+h_2b_2+h_3b_3,h_4)_s$ plane. Therefore, low index planes can be stabilised more than high index planes in correspondence with the classical case.

Furthermore, it has been found that an incommensurately modulated crystal can be partitioned, for any orientation $(h_1h_2h_3h_4)$, in slices of thickness $d_{(h_1h_2h_3h_4)}$ that have the same energy content and the same surface free energy. This can be seen as a generalisation of the situation in non-modulated crystals. There is one exception, which is the case of a plane perpendicular to a modulation wave vector that has an incommensurate *length*.

The surface free energies $\Gamma_{(h_1h_2h_3h_4)}$ give very singular, discontinuous cusps in a Wulff plot. The equilibrium morphologies, that have been constructed by means of such a Wulff plot for several incommensurately modulated model crystals, can be understood in detail. The reason for this is that we have elucidated the influence of several structural aspects on the morphology.

A (satellite) plane is stabilised more when the value of $|\boldsymbol{f}\cdot\boldsymbol{b}|$ is larger for important mbc's intersecting that plane. This is the influence of the direction of the modulation amplitude vector. On the other hand, the amount of stabilisation increases with the length of the modulation amplitude vector. Also the number of (satellite) faces that appear on the morphology increases with the modulation amplitude. Both the length and the direction of the modulation wave vector $\boldsymbol{q}$ determine the value of $q_1=\boldsymbol{q}\cdot\boldsymbol{b}$ in the 1+1-dimensional embedding of the mbc with bond-chain vector $\boldsymbol{b}$. The amount of stabilisation then depends on this value of q_1, but differs for different $(h_1b_1+h_2b_2+h_3b_3,h_4)_s$ planes. This dependence has already been outlined in a previous paper for a sinusoidal modulation (Kremers et al., 1994). In this paper, we have discussed the dependence for a square wave modulation. One can state, that if the modulation function resembles a square wave, satellite faces are stabilised more with respect to main faces as compared to the case of a sinusoidal wave.

In view of these structural influences on the morphology, we have made it plausible why satellite faces do appear on $AuTe_2$ crystals and not on $((CH_3)_4N)_2ZnCl_4$ crystals.

9.9 Acknowledgments

The authors would like to thank both Prof. A. Janner and Prof. T. Janssen for their continuous interest, enthousiasm and help. We would like to acknowledge Dr. S. van Smaalen for the very critical and exciting discussions on the subject. This work is part of the research program of the Stichting voor Fundamenteel Onderzoek der Materie (Foundation for Fundamental Research on Matter).

References

Balzuweit, K., Meekes, H., and Bennema, P., *J. Phys. D: Appl. Phys.* **24**, 203 (1991).
Bennema, P., and van der Eerden, J. P., *Morphology of crystals* Part A, edited by Sunagawa, I., 1 (Tokyo: Terra Scientific; Dordrecht: Reidel, 1987).
Bennema, P., Balzuweit, K., Dam, B., Meekes, H., Verheijen, M.A., and Vogels, L.J.P., *J. Phys. D* **24**, 186 (1991).
Bennema, P., *Handbook of crystal growth* Ch. 7, edited by Hurle, D. T. J. (Elsevier, 1993).
Bennema, P., Kremers, M., Meekes, H., Balzuweit, K., and Verheijen, M. A., *Discuss. Faraday. Soc.* **95**, 2 (1993).
Bennema, P., Kremers, M., Meekes, H., and Verheijen, M. A., *Phys. Stat. Sol. (a)* **146**, 13 (1994).
Dam, B., Janner, A., Bennema, P., van der Linden, W.H., and Rasing, Th., *Phys. Rev. Lett.* **50**, 849 (1983).
Dam, B., Janner, A., and Donnay, J.D.H., *Phys. Rev. Lett.* **55**, 2301 (1985).
Dam, B., *Phys. Rev. Let.* **55**, 2806 (1985).
Dam, B., *Acta Cryst.* B**42**, 69 (1986).
Frenkel, Y.I., and Kontorova, T., *Zh. éksp. teor. Fiz.* **8**, 1340 (1938).
Goldschmidt, V., Palache, Ch. and Peacock, M., *Neues Jahrb. Mineral.* **63**, 1 (1931).
Hartman, P., and Perdok, W. G.,
Acta Crystallogr. **8**, 49 (1955)
Acta Crystallogr. **8**, 521 (1955)
Acta Crystallogr. **8**, 525 (1955).
Heijmen, T. G. A., Kremers, M., and Meekes, H., *Philosophical Magazine, in press* (1994).
Heijmen, T. G. A., Kremers, M., Meekes, H., and Janssen, T., *to be published* (1995).
Herring, C., *Phys. Rev.* **82**, 87 (1951).
Herring, C., *Structure and Properties of Solid Surfaces* edited by Gomer, R., and Smith, C. S., 5 (University of Chicago Press, 1953).
Janner, A., and Janssen, T., *Phys. Rev.* B**15**, 643 (1977).
Janner, A., and Janssen, T., *Acta Crystallogr.* A**36**, 408 (1980).
Janner, A., Rasing, Th., Bennema, P., and van der Linden, W.H., *Phys. Rev. Lett.* **45**, 1700 (1980).

Janner, A., *Studies in Physical and Theoretical Chemistry* **23**, 461 (Amsterdam: Elsevier, 1983).

Janner, A., Janssen, T., and de Wolff, P. M., *Acta Cryst.* A**39**, 671 (1983).

Janner, A., and Dam, B., *Acta Crystallogr.* A**45**, 115 (1989).

Janssen, T., *Incommensurate phases in dielectrics I* edited by Blinc, R., and Levanyuk, A.P., 67 (Amsterdam: North-Holland, 1986).

Janssen, T., and Janner, A., *Adv. Phys.* **36**, 519 (1987).

Kremers, M., Meekes, H., Bennema, P., Balzuweit, K., and Verheijen, M. A., *Philosophical Magazine* B**69**, 69 (1994).

Madariaga, G., Zuñiga, F.J., Pérez-Mato, J.M., and Tello, M.J., *Acta Cryst* B**43**, 356 (1987).

Schutte, W. J., and de Boer, J. L., *Acta Cryst.* B**44**, 486 (1988).

Selke, W., *Modulated structure materials* edited by Tsakalakos, T., 23 (Dordrecht: Nijhoff, 1984).

van Smaalen, S., *Materials Science Forum* **100, 101**, 173 (1992).

van Smaalen, S., *Phys. Rev. Lett.* **70**, 2419 (1993).

van Smaalen, S., *Private communications*, (1994).

Sueno, S., Kimata, M., and Ohmasa, M., *Modulated Structures*, edited by Cowley, J. M., Cohen, J. B., Salamon, M. B., and Wuensch, B. J., *AIP Conf. Proc* **53**, 333 (1979).

van Tendeloo, G., Gregoriades, P., and Amelinckx, S., *J. Solid State Chem.* **50**, 321, 335 (1983).

Vogels, L.J.P., Balzuweit, K., Meekes, H., and Bennema, P., *J. Crystal Growth* **116**, 397 (1992a).

Vogels, L.J.P., Verheijen, M.A., Meekes, H., and Bennema, P., *J. Crystal Growth* **121**, 697 (1992b).

de Wolff, P. M., *Acta Cryst.* A**30**, 777 (1974).

de Wolff, P. M., Janssen, T., and Janner, A., *Acta Cryst.* A**37**, 625 (1981).

Chapter 10

A superspace description for the morphology of quasi-crystals

A superspace description for the morphology of quasi-crystals

T. G. A. Heijmen, M. Kremers and H. Meekes

Abstract

An approach is investigated to determine the equilibrium morphology of quasi-crystals by using a superspace embedding. We discuss the case of the Fibonacci chain of atoms, a one-dimensional structure that can be regarded both as a quasi-crystal and as an incommensurately modulated crystal. Consequently, two different ways can be followed to find the equilibrium form. The results indicate that the description as a quasi-crystal deals with the symmetry of the model in a more natural way. An analogous method is applied to the case of the two-dimensional octagonal quasi-crystal. It is shown that the number of bonds cut by a crystallographic face depends on its position in both the one- and the two-dimensional case.

10.1 Introduction

A common feature of classical crystals is their lattice translational symmetry in three independent directions. It can be described by a lattice spanned by three vectors $\boldsymbol{a}_1$, $\boldsymbol{a}_2$ and $\boldsymbol{a}_3$. For several decades, however, incommensurate crystal phases have been known as well (Janssen and Janner, 1987 and references therein). These phases show long-range order, but unlike the classical crystals, there is no three-dimensional lattice periodicity.

The class of incommensurate crystals includes the quasi-crystals. In a first approximation, quasi-crystals can be characterised as quasi-periodic space-filling patterns built from two or more structural units (Janssen and Janner, 1987 and references therein). Their X-ray diffraction patterns have symmetries that are not compatible with lattice periodicity in three dimensions. Five-, eight-, ten- and twelvefold rotational symmetries have been observed. A detailed survey has been given elsewhere (Steurer, 1990). These typical symmetries are also reflected in the morphology of the quasi-crystals (Balzuweit et al. (1993), Beeli et al. (1993) and references therein).

Another type of incommensurate crystal phases is formed by the incommensurately modulated crystals. These crystal phases can be obtained from a basic (non-modulated) crystal structure by means of a small periodic deformation, called modulation. If the period length of this modulation is not commensurate with any integral combination of $\boldsymbol{a}_1$, $\boldsymbol{a}_2$ and $\boldsymbol{a}_3$, lattice translational symmetry is lost in at least one direction. The crystal is then called incommensurate, otherwise, it is called commensurately modulated. Since the modulation is periodic, the average crystal structure can be described by the original basic structure. The spots in the X-ray diffraction patterns of incommensurately modulated crystals can be classified into main reflections, originating from the average structure, and satellite reflections, whose coordinates are not simple fractions with respect to the lattice of main reflections. On the other hand, the spots in the diffraction patterns of quasi-crystals cannot be divided into main and satellite reflections, since there is no average crystal structure which is lattice periodic.

Crystals can be characterised at a macroscopic level by their morphology. Many crystals are bounded by flat faces that can be labeled with a set of integral indices (hkl). These indices represent a reciprocal lattice vector $\boldsymbol{H}_{hkl}$ perpendicular to the face:

$$\boldsymbol{H}_{hkl} = h\boldsymbol{a}_1^* + k\boldsymbol{a}_2^* + l\boldsymbol{a}_3^* \,, \tag{10.1}$$

where $\boldsymbol{a}_1^*$, $\boldsymbol{a}_2^*$ and $\boldsymbol{a}_3^*$ span the reciprocal lattice. A crystallographic face (hkl) can be constructed by cutting $1/h$ of $\boldsymbol{a}_1$, $1/k$ of $\boldsymbol{a}_2$ and $1/l$ of $\boldsymbol{a}_3$ and taking the plane through these points. In each face (hkl) a two-dimensional lattice can be defined. There exists a corresponding two-dimensional unit cell, the mesh area $M_{(hkl)}$, which is very useful in the calculation of the stability of crystal faces.

Like the classical crystals, incommensurate crystal phases are often also bounded by flat faces. It has been observed (Janner et al. (1980), Dam et al. (1985), Bennema et al. (1991)) that the faces of incommensurately modulated crystals with a one-dimensional modulation are perpendicular to vectors that are integral linear combinations of four vectors from the reciprocal space. Consequently, these faces can be labeled with four integral indices $(hklm)$. Three of the four vectors, $\boldsymbol{a}_1^*$, $\boldsymbol{a}_2^*$ and $\boldsymbol{a}_3^*$, span the reciprocal lattice of the average structure, while the fourth is the modulation wave vector $\boldsymbol{q}$. A face $(hklm)$ is thus perpendicular to the vector

$$\boldsymbol{H}_{hklm} = h\boldsymbol{a}_1^* + k\boldsymbol{a}_2^* + l\boldsymbol{a}_3^* + m\boldsymbol{q} \,. \tag{10.2}$$

Suppose that $\boldsymbol{q} = \alpha\boldsymbol{a}_1^*$, the face then cuts the $\boldsymbol{a}_1$ axis at $(h + m\alpha)$. If the modulation is incommensurate, α is irrational.

Spots in the X-ray diffraction patterns of quasi-crystals can be characterised by a set of more than three integers. This corresponds to the basic property that the wave vectors of the Fourier transform of the charge density have the following form:

$$\boldsymbol{H}_{h_1 \ldots h_d} = h_1\boldsymbol{a}_1^* + h_2\boldsymbol{a}_2^* + \ldots + h_d\boldsymbol{a}_d^*, \quad d > 3 \,. \tag{10.3}$$

Faces of quasi-crystals are perpendicular to these vectors. Thus, as in the case of incommensurately modulated crystals, more than three integral indices are needed to label such a face.

Neither in quasi-crystals nor in incommensurately modulated crystals there is lattice translational symmetry in three independent directions. Therefore, it is generally not possible to define a planar elementary cell as a mesh area on a crystallographic face.

Periodicity is used in explaining the equilibrium form of classical crystals. Therefore, a different explanation is needed for the equilibrium form of incommensurate crystals. In two previous papers (Bennema et al. (1993), Kremers et al. (1994)), a concept has been elaborated that deals with this problem for the case of incommensurately modulated crystals. This concept makes use of the embedding of modulated crystals in a so-called superspace (Janssen and Janner, 1987 and references therein), which has a dimension higher than three. The advantage of this superspace embedding is that the embedded structure has full lattice translational symmetry. The physical crystal is a three-dimensional section of the embedded structure. It is possible to generalise crystallographic faces to hyperfaces in superspace. This generalisation can be used to calculate the surface free energy of crystallographic faces in order to explain their stability.

In the present paper, we apply the method discussed above to the case of quasi-crystals. First, we consider the simple case of the Fibonacci chain of atoms, which can be described both as a one-dimensional modulated crystal and as a one-dimensional quasi-crystal. This duality allows us to compare the two types of incommensurate crystal phases. Sections 10.2 and 10.3 discuss the superspace description of the chain, regarded as a modulated crystal and as a quasi-crystal, respectively. In section 10.4 it is shown that these two descriptions are equivalent. Section 10.5 deals with the extension of the Wulff–Herring construction determining morphologies to include superspace descriptions. Model calculations are presented in section 10.6. It is shown that both descriptions of the Fibonacci chain of atoms yield the same results. However, the description as a quasi-crystal proves to be more natural.

Section 10.8 discusses how the superspace approach can be extended to the case of the two-dimensional octagonal quasi-crystal in order to determine the average surface free energy of a grid of netplanes $(hklm)$. It was shown by Ho (1991) that the stability of a single crystal face in a two- or three-dimensional quasi-crystal is independent of the position of the face if atoms and bonds are defined in a specific way. However, the results of section 10.8 of the current paper demonstrate that if other definitions are used, the surface free energy does depend on the position of the face. Part II of the paper (Heijmen et al., 1995) will present a method to determine the stabilities of single faces $(hklm)$ in a two-dimensional octagonal quasi-crystal.

10.2 The Fibonacci chain as a modulated structure

The Fibonacci chain of atoms is a one-dimensional crystal with two different interatomic distances. It contains a quasi-periodic ordering of long and short intervals between the atoms (Janssen and Janner, 1987 and references therein). The ratio of the long and the short interval lengths equals the golden ratio $\tau = \frac{1}{2}(\sqrt{5}-1)$.

In general, the atomic positions of a one-dimensional monoatomic modulated crystal are described in the following way. If in the basic structure the position of the atom in the nth unit cell is given by $x_0 + na$, the corresponding position in the modulated structure is given by

$$x_n = x_0 + na + f(qna + \phi_0), \tag{10.4}$$

with $q = \alpha a^*$, $0 \le \alpha < 1$; $f(y)$ is the periodic modulation function. The one-dimensional crystal with $f(y) = \cos(y)$ has been discussed previously (Kremers et al. (1994), Bennema et al. (1993)).

It is possible to define a lattice in a 1+1-dimensional superspace, spanned by the vectors

$$\boldsymbol{a}_s = (a, -\alpha d) \quad \text{and} \quad \boldsymbol{d}_s = (0, d). \tag{10.5}$$

The first coordinate of each of these vectors represents the component in the physical space, which is called external space in the superspace description, the second the component in a perpendicular internal space; d is an arbitrary real number. The corresponding reciprocal lattice is spanned by

$$\boldsymbol{a}_s^* = (a^*, 0) \quad \text{and} \quad \boldsymbol{d}_s^* = (q, d^*), \tag{10.6}$$

where $aa^* = dd^* = 1$. Note that if $d = 1/q$, the angle between $\boldsymbol{a}_s$ and the physical space equals 45° and the unit of length in the internal space has the same periodicity length as the modulation wave in real space (Janner, 1983).

The Fibonacci chain of atoms, drawn in figure 10.1, can be regarded as a one-dimensional crystal with a saw-tooth shaped modulation. The positions of the atoms of such a structure are given by

$$x_n = x_0 + na + b\Big(1 - 2\,\mathrm{frac}(qna + \phi_0)\Big). \tag{10.7}$$

The function frac(y) assigns to y the value y minus the largest integer smaller than or equal to y; ϕ_0 is an arbitrary phase. Eqn. (10.7) describes the positions of the atoms in the Fibonacci chain if the following values are assigned to the parameters a, b and α:

$$a = 3\tau - 1 \quad , \quad b = \frac{1}{2}(1-\tau) \quad , \quad \alpha = \tau. \tag{10.8}$$

The atoms of the chain described by eqn. (10.7) can be embedded in the 1+1-dimensional superspace. The atomic positions are then given by

$$\boldsymbol{r}_s(n,\phi) = \Big[na + b\Big(1 - 2\,\mathrm{frac}(qna + \phi + \phi_0)\Big), \phi\Big], \tag{10.9}$$

where ϕ is a phase which runs along the internal axis. This equation describes an infinite set of (discontinuous) lines, called world lines, which represent the atoms in the superspace description. If the parameters a, b and α are given the values of eqn. (10.8), then eqn. (10.9) describes the superspace embedding of the Fibonacci chain of atoms, as is shown in figure 10.2. The section of the two-dimensional structure with the physical space yields the Fibonacci chain of figure 10.1.

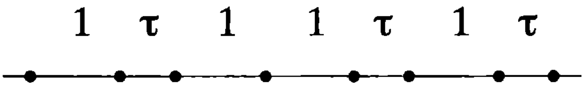

Figure 10.1 A section of the Fibonacci chain of atoms. The interatomic distances equal to 1 and τ are indicated.

If the superspace description is to be used in explaining the equilibrium form of an incommensurate crystal, a number of crystallographic concepts have to be extended to superspace. These extensions have been discussed in detail by Kremers et al. (1994), a summary is given below.

The concept of chemical bonds can be generalised to superspace by defining a density of bonds connecting the atoms in superspace with each other for each phase ϕ along the internal axis. These bonds are defined parallel to the physical space. A (one-dimensional) crystallographic hyperplane $(hm)_s$ can be defined by taking a plane perpendicular to the vector

$$\boldsymbol{H}_{(hm),s} = h\boldsymbol{a}_s^* + m\boldsymbol{d}_s^* \tag{10.10}$$

from reciprocal space. A grid of netplanes $(hm)_s$ can be constructed in superspace with interplanar distance

$$d_{(hm),s} = \frac{1}{|\boldsymbol{H}_{(hm),s}|} \, . \tag{10.11}$$

Related to the idea of interplanar distance is the concept of mesh area M. It is defined as the surface area of a planar elementary cell of a hyperplane $(hm)_s$,

$$M_{(hm),s} = \frac{V_s}{d_{(hm),s}} \, , \tag{10.12}$$

where V_s is the area of the 1+1-dimensional unit cell of the lattice given by eqn. (10.5).

The surface free energy Γ can be used as a criterion for the stability of a crystal face: the lower Γ, the more stable the face. We make use of a broken bond model in which the surface free energy corresponds to the energy per unit area needed for cutting bonds in order to create the face from an infinitely large crystal. In equilibrium, the form of a crystal is such that the total surface free energy is minimal.

It has been discussed above that the bonds of the physical quasi-crystal are represented in superspace by a uniform bond density. The lattice periodicity of the 1+1-dimensional embedded structure implies that each bond in the physical crystal that is intersected by a grid of netplanes $(hm)_s$ is translationally equivalent to a bond in superspace intersected by one specific hyperplane $(hm)_s$. This is illustrated by figure 10.2 for the grid of netplanes $(1\bar{1})_s$. The bonds of the physical quasi-crystal that are intersected by the grid are therefore represented in superspace by the part of the uniform density of bonds that is intersected by a single hyperplane $(hm)_s$. Consequently, calculating the broken bond energy per mesh area of a single hyperplane $(hm)_s$ in superspace is equivalent to calculating the average energy of the bonds in the physical crystal that are cut by a grid of netplanes $(hm)_s$.

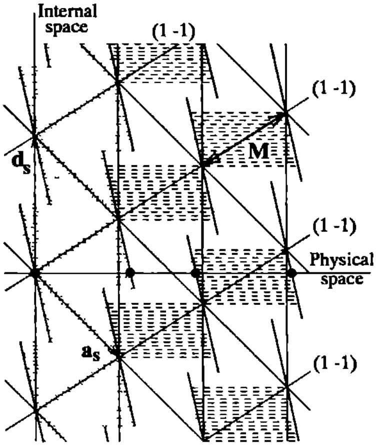

Figure 10.2 The superspace embedding of the Fibonacci chain of atoms, regarded as a modulated crystal. The positions of the atoms are indicated by the full circles. In superspace atoms are represented by discontinuous world lines. In the left part of the figure, the extension of the concept of chemical bonds to superspace is shown with the help of the dotted lines. In the right part, the principle of selective cuts is demonstrated for the face $(1\bar{1})$. The bonds that are selectively cut are indicated by the hatched areas. The mesh area $M_{(1\bar{1}),s}$ is indicated by the symbol **M**.

Figure 10.2 shows that the grid of netplanes $(1\bar{1})_s$ intersects only part of the dense set of bonds in superspace. In general, the ratio between the fractions of long and short bonds that are intersected is different for each grid of netplanes $(hm)_s$. Since the bond energy is assumed to be only a function of the bond length, this implies that the broken bond energy per mesh area in superspace generally differs for each face $(hm)_s$. In the current paper, this so-called principle of selective cuts is used to discriminate between the stabilities of different faces on one- and two-dimensional quasi-crystals.

Each phase ϕ along the internal $\boldsymbol{d}_s$ axis corresponds to a crystal with a different phase factor $\phi + \phi_0$ but with the same two periodicities which occur in the same ordering. The minimum surface free energy for each face $(hm)_s$ can therefore be found by varying the phase at which the corresponding hyperplane intersects the $\boldsymbol{d}_s$ axis. This is equivalent to varying the phase ϕ_0 in eqn. (10.9), as has been discussed by Kremers et al. (1994).

10.3 The Fibonacci chain as a quasi-crystal

Since there are a finite number (two) of intervals, which are ordered in a quasi-periodic way, the Fibonacci chain of atoms can be regarded as a one-dimensional quasi-crystal. The procedure for embedding a quasi-crystal in a higher-dimensional superspace is different from that for embedding an incommensurately modulated crystal (Janssen and Janner, 1987 and references therein). A lattice is defined which is spanned by two vectors

$$\boldsymbol{e}_{1s} = (\,\delta, 1\,) \quad \text{and} \quad \boldsymbol{e}_{2s} = (\,1, -\delta\,)\,, \tag{10.13}$$

which are defined on an orthonormal basis $\{\,\hat{e}_E, \hat{e}_I\,\}$, where $\hat{e}_E$ and $\hat{e}_I$ denote unit vectors along the external and internal axis, respectively. The corresponding reciprocal lattice is spanned by

$$\boldsymbol{e}^*_{1s} = \frac{1}{1+\delta^2}(\,\delta, 1\,) \quad \text{and} \quad \boldsymbol{e}^*_{2s} = \frac{1}{1+\delta^2}(\,1, -\delta\,)\,. \tag{10.14}$$

Atoms are represented in superspace by line elements, defined as the projection of the unit cell on the internal space. These line elements, generally called atomic surfaces, are attached with their centers at the vertices of the superlattice. The points of the 1+1-dimensional embedded structure are given by

$$m\boldsymbol{e}_{1s} + n\boldsymbol{e}_{2s} + (\,0, t\,), \quad m, n \text{ integers}, \quad t \in \Big\langle -\frac{1+\delta}{2}, \frac{1+\delta}{2}\Big]\,. \tag{10.15}$$

The superspace embedding of the Fibonacci chain of atoms, regarded as a one-dimensional quasi-crystal, is shown by figure 10.3.

The physical quasi-crystal is the intersection of the embedded structure with the physical space; its atomic positions are

$$x_{m,n} \;=\; m\delta + n, \quad -\frac{1+\delta}{2} < n\delta - m \le \frac{1+\delta}{2}\,. \tag{10.16}$$

The definition of the atomic surfaces ensures that the number of intersection points does not change if the embedded structure is shifted with respect to the physical space.

Eqn. (10.16) describes the atomic positions of the Fibonacci chain of atoms if δ equals the golden ratio τ.

The crystallographic concepts discussed in the previous section can also be generalised to the superspace embedding of a quasi-crystal. To extend the concept of chemical bonds to superspace, a density of bonds parallel to the physical space is defined between neighbouring atomic surfaces (see figure 10.3). A bond from this dense set has the same length as either the long or the short bond in the physical crystal.

A crystallographic hyperplane $(hm)_s$ is defined perpendicular to the vector

$$\boldsymbol{H}_{(hm),s} = h\boldsymbol{e}^*_{1s} + m\boldsymbol{e}^*_{2s} \,. \tag{10.17}$$

The generalisations of the concepts of interplanar distance and mesh area are again given by eqns. (10.11) and (10.12), respectively.

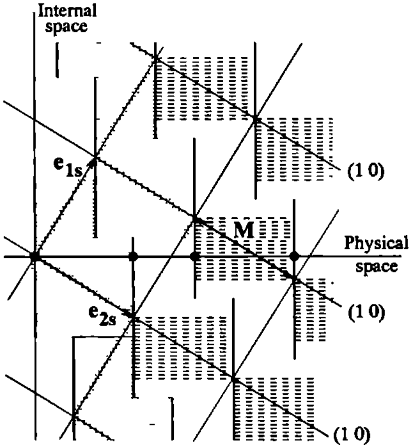

Figure 10.3 The superspace embedding of the Fibonacci chain of atoms, regarded as a quasi-crystal. The positions of the atoms are indicated by the full circles. In superspace atoms are represented by line elements parallel to the internal space. In the left part of the figure, the extension of the concept of chemical bonds to superspace is shown with the help of the dotted lines. In the right part, the principle of selective cuts is demonstrated for the face (10). The bonds that are selectively cut are indicated by the hatched areas. The mesh area $M_{(10),s}$ is indicated by the symbol **M**.

Using the same argumentation as in the previous section, it can be shown that the average energy of the bonds in the physical crystal that are cut by a grid of netplanes $(hm)_s$ is equal to the broken bond energy per mesh area of a single hyperplane $(hm)_s$ in superspace. The principle of selective cuts can again be used to discriminate between the stabilities of different faces $(hm)_s$. The principle is illustrated by figure 10.3 for a grid of netplanes $(10)_s$, which only intersect part of the dense set of bonds in superspace.

If the embedded structure in figure 10.3 is shifted along the internal axis, its intersection with the physical space forms a quasi-periodic structure with the same ordering of long and short intervals as the original intersection. Therefore, we can again assume that it is legitimate to minimise the broken bond energy by varying the phase at which the hyperplane $(hm)_s$ intersects the internal axis.

10.4 Equivalence of the two descriptions of the Fibonacci chain

A grid of netplanes $(hm)_s$ in the superspace embedding as a modulated crystal divides the physical structure into intervals of length

$$d_{hm}^{\text{mod}} = \frac{1}{|ha^* + mq|} , \tag{10.18}$$

where a^* and q are the projections on the physical space of the vectors $\boldsymbol{a}_s^*$ and $\boldsymbol{d}_s^*$, respectively, given by eqn. (10.6). On the other hand, a grid of netplanes $(hm)_s$ in the superspace embedding as a quasi-crystal divides the physical structure into intervals of length

$$d_{hm}^{\text{qc}} = \frac{1}{|he_1^* + me_2^*|} , \tag{10.19}$$

where e_1^* and e_2^* denote, respectively, the projections on the physical space of $\boldsymbol{e}_{1s}^*$ and $\boldsymbol{e}_{2s}^*$, given by eqn. (10.14).

It can be proved that eqn. (10.7) in section 10.2 is equivalent to eqn. (10.16) in section 10.3, i.e., describes the atomic positions of the same structure, if the parameters of the former are given the following values:

$$a = \frac{1+\delta^2}{1+\delta} \quad , \quad b = \frac{1}{2}(1-\delta) \quad , \quad \alpha = \frac{1}{1+\delta} . \tag{10.20}$$

The corresponding expressions for a^* and q are

$$\begin{aligned} a^* &= \frac{1}{a} = \frac{1+\delta}{1+\delta^2} = e_1^* + e_2^* , \\ q &= \alpha a^* = \frac{1}{1+\delta^2} = e_2^* . \end{aligned} \tag{10.21}$$

This implies that the physical crystal is cut in intervals of the same length by both a grid of netplanes $(hm)_s$ in the embedding as a modulated crystal and a grid of netplanes $(h(h+m))_s$ in the embedding as a quasi-crystal.

It has been discussed above that it is allowed to shift a grid of netplanes $(hm)_s$ with respect to the 1+1-dimensional superlattice in order to find the minimum broken bond energy. Consequently, this minimum value only depends on the length of the intervals in which the grid cuts the physical crystal. Hence, the minimum broken bond energy is identical for both a grid of netplanes $(hm)_s$ in the embedding as a modulated crystal and a grid of netplanes $(h(h+m))_s$ in the embedding as a quasi-crystal. Therefore, a face $(hm)_s$ in the former description is morphologically equivalent to a face $(h(h+m))_s$ in the latter. Figures 10.2 and 10.3 illustrate this for the faces $(1\bar{1})_s$ and $(10)_s$, respectively. This equivalence corresponds to the fact that since it is the same crystal that is embedded in superspace in two different ways, the equilibrium form of the crystal – as all physical properties – must be the same in either of both descriptions.

10.5 The generalised Wulff–Herring plot

A method for determining the equilibrium morphology from calculated surface free energies has been developed by Herring (1951) (see also Herring, 1953). A radius vector is drawn for each crystallographic face. This vector has the same direction as the corresponding face normal while its length is linearly proportional to the surface free energy. A plane is constructed perpendicular to this vector, through its tip. The resulting construction is called a Wulff–Herring plot. The equilibrium form of the crystal is determined by the points that can be reached from the origin without crossing any of the constructed planes. It is obvious that faces on the equilibrium form correspond to sharp cusps in the polar plot of the surface free energies. Bennema et al. (1993) have discussed how to extend this method in order to include superspace descriptions. They used an extended Wulff–Herring plot to determine the equilibrium form of modulated one-dimensional crystals.

Since only bonds parallel to the physical space have been defined, a face parallel to this space cannot cut bonds. Consequently, the surface free energy for such a face is equal to zero. The polar plot of surface free energies of a one-dimensional incommensurate crystal embedded in a 1+1-dimensional superspace therefore shows an infinitely deep cusp at $\theta = \pm\pi/2$, where θ is the angle between the face normal and the physical space. Accordingly, the dimension of the equilibrium form is reduced from two to one, the dimension of the physical crystal. Each plane constructed in the extended Wulff–Herring plot intersects the physical crystal in a point. The equilibrium form is bounded by the faces that correspond to the planes for which the distance γ between their intersection with the physical crystal and the origin is minimal. The distance γ is related to the surface free energy Γ in the following way:

$$\gamma = \frac{\Gamma}{|\cos\theta|}\,. \tag{10.22}$$

The equilibrium form is thus bounded by two faces, opposite with respect to the origin, for which γ is minimal. In general, the value of γ is assumed to be inversely proportional to the morphological importance (MI) of a face.

10.6 Calculations of surface free energies

Calculations have been done on the surface free energies $\Gamma_{(hm)}$ of a general one-dimensional quasi-crystal with two different interatomic distances. Both superspace descriptions discussed above have been used. $\Gamma_{(hm)}$ is defined as

$$\Gamma_{(hm)} = \frac{\sigma \; |\cos(\theta_{(hm)})|}{M_{(hm),s}} \int_{M_{(hm),s}} dM \, \Phi(\, l(M)\,) \, , \tag{10.23}$$

where σ denotes the bond density taken equal to 1 m^{-1}, $\theta_{(hm)}$ the angle between the face normal and the physical space, $M_{(hm),s}$ the mesh area of the hyperplane $(hm)_s$ and $\Phi(l)$ the energy of a bond, expressed as a function of its length:

$$\Phi(\, l\,) = \frac{\chi}{l} \, . \tag{10.24}$$

To calculate $\Gamma_{(hm)}$, an integration is performed over one mesh area $M_{(hm),s}$. Because of lattice periodicity, the mesh area of a (hyper)plane is translationally equivalent to those parts of the corresponding grid of netplanes that are found inside one unit cell. This is illustrated by figure 10.4 for the hyperplane $(2\bar{1})_s$ in the superspace embedding of the Fibonacci chain of atoms, regarded as a modulated crystal. The superspace embedding on a square lattice, depicted in figure 10.3, shows a third way to determine $\Gamma_{(hm)}$. Integrating over one unit cell of this lattice is equivalent to integrating over one atomic surface if the bonds on only one side of the surface are accounted.

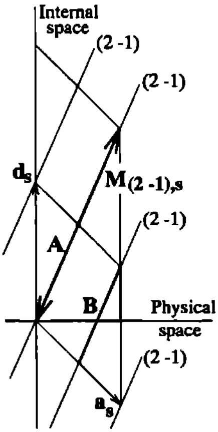

Figure 10.4 The line elements **A** and **B** represent the intersections of the grid of netplanes $(2\bar{1})$ with one unit cell in superspace. Together, these line elements are translationally equivalent with one mesh area $M_{(2\bar{1}),s}$.

Surface free energies $\Gamma_{(hm)}$ have been calculated for crystallographic faces $(hm)_s$, with $-3 \leq h, m \leq 3$, as a function of the parameter δ of eqns. (10.16) and (10.20). Calculations have been performed for 50 values of δ between 0 and 1. If the structure was regarded as a modulated crystal, $\Gamma_{(hm)}$ was calculated according to eqn. (10.23); in the case where the structure was described as a quasi-crystal, $\Gamma_{(hm)}$ was determined by performing an integration over one atomic surface. In both cases integrals were calculated by means of numerical integration over 750 points. The hyperplanes were shifted along the internal space with a phase ϕ, which was also varied over 750 values. The bond strength parameter χ in eqn. (10.24) was taken equal to 1.

If δ is varied from 0 to 1, all nonequivalent quasi-crystals are considered. It is possible to show that a quasi-crystal with $\delta = \delta_0$ is identical to a quasi-crystal with $\delta = -\delta_0$; therefore, only values of $\delta \geq 0$ have to be considered. A quasi-crystal with $\delta = \delta_0$ is also equivalent to a quasi-crystal with $\delta = 1/\delta_0$ if in the former the interval lengths are scaled by a factor δ_0. Since energies are divided by the average energy $1/a$, they are independent of the absolute length of the intervals and structures with $\delta = \delta_0$ and $\delta = 1/\delta_0$ are equivalent in our calculations. Consequently, δ only has to be varied from 0 to 1, which corresponds to varying α from $\frac{1}{2}$ to 1, because of the relation $\alpha = 1/(1+\delta)$.

10.7 Results

Figure 10.5 shows the generalised Wulff–Herring plot for the Fibonacci chain of atoms. The indexing of the faces corresponds to the superspace embedding of the chain as a modulated crystal; the indices according to the embedding as a quasi-crystal are found by replacing $(hm)_s$ with $(h(h+m))_s$. Results obtained from the two descriptions agree to a high extent. The two circles in the plot correspond to the case of a crystal with zero-amplitude modulation. The surface free energy Γ can then be written as

$$\Gamma(\theta) = \Gamma_0 \, |\cos\theta| \; . \tag{10.25}$$

In this case, all faces $(hm)_s$ have the same value of γ and, consequently, the same morphological importance. The line elements intersecting the circles represent the values of $\Gamma_{(hm)}$ that have been obtained from our calculations on the Fibonacci chain varying the phase ϕ; their end points correspond to the minimum and maximum values of $\Gamma_{(hm)}$. Dashed lines have been drawn, perpendicular to the face normal, from the end points corresponding to the minimum values. The distances between the origin and the intersection points of these lines with the physical space represent γ, defined by eqn. (10.22).

In the broken bond model the faces $(hm)_s$ and $(\bar{h}\bar{m})_s$, which are parallel, are morphologically equivalent. Hence, the right and the left side of figure 10.5 contain the same information. The figure reveals that the faces $(10)_s$, $(01)_s$, $(1\bar{1})_s$ and $(1\bar{2})_s$ have the same (minimum) value of γ. These four faces (which are not parallel in superspace) can be positioned in the embedded structure in such a way that only long bonds are cut. Since the bond energy is inversely proportional to the bond length, this situation corresponds to a minimum surface free energy. Obviously, it is possible to construct grids of netplanes $(hm)_s$ in superspace which intersect merely long bonds in the physical space, although the Fibonacci chain of atoms is only quasi-periodic. The faces $(10)_s$, $(01)_s$, $(1\bar{1})_s$ and $(1\bar{2})_s$ are labeled $(11)_s$, $(01)_s$, $(10)_s$ and $(1\bar{1})_s$, respectively, in the description as a quasi-crystal.

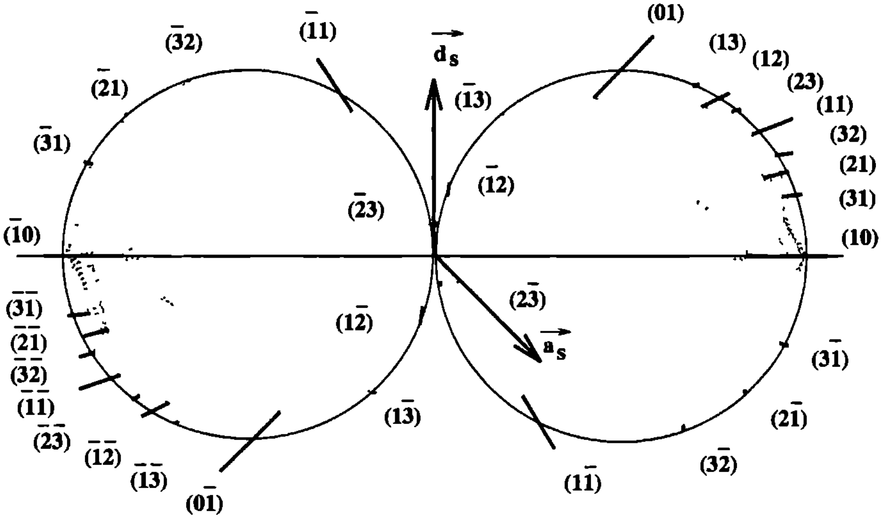

Figure 10.5 Extended Wulff–Herring plot for the Fibonacci chain of atoms The faces have been labeled according to the description as a modulated crystal The indices in the quasi-crystal description are found by replacing (hm) by $(h(h+m))$ Faces with indices up to 3 have been plotted

Figure 10.6 plots $\gamma = \Gamma^{\min}_{(hm)} / |\cos\theta|$ as a function of $\alpha = 1/(1+\delta)$, where $\Gamma^{\min}_{(hm)}$ denotes the minimum surface free energy. The energies have been normalised, i.e., they have been divided by the average bond energy, which is proportional to $1/a = (1+\delta^2)/(1+\delta)$. Faces have been labeled according to the superspace embedding as a quasi-crystal. The indices in the description as a modulated crystal are found by replacing $(hm)_s$ with $(h(h-m))_s$. There is a good agreement between the results obtained from the two descriptions.

The minimised surface free energies of the faces $(hm)_s$ and $(m\bar{h})_s$, labeled according to the quasi-crystal description, are found to be equal. This is caused by a symmetry that is not directly obvious from the embedding as a modulated crystal but which is understandable if the embedding as a quasi-crystal is considered.

Figure 10.7 shows this embedded structure emphasising the areas in which either long or short bonds are present. The hatched areas only contain short bonds while those that

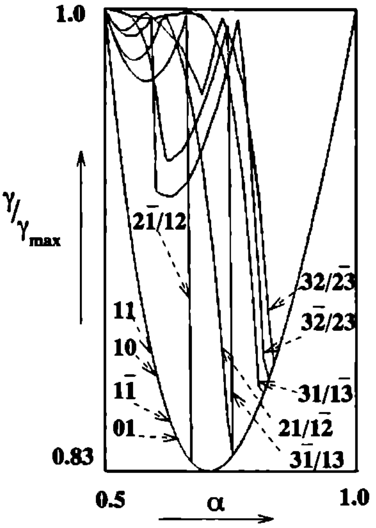

Figure 10.6 Normalised $\gamma = \Gamma / |\cos\theta|$ values for 50 α points, calculated by minimising over 750 phases The smallest value of γ corresponds to the highest morphological importance The faces have been labeled according to the quasi-crystal description The indices in this description are found by replacing (hm) by $(h(m-h))$ Faces with indices up to 3 have been plotted The value of α for the Fibonacci chain is indicated

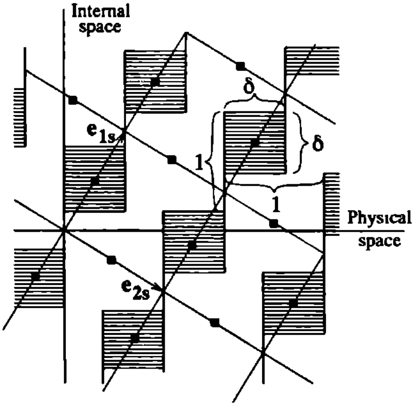

Figure 10.7 Fourfold symmetry in the pattern of areas in which short (hatched) and long (not hatched) bonds occur in the Fibonacci chain of atoms, embedded as a quasi-crystal Fourfold symmetry axes have been indicated

are not hatched only comprise long bonds. Both types of areas are square; their sizes are $\delta \times \delta$ and 1×1, respectively. Figure 10.7 reveals that there are fourfold axes of symmetry at the centers of the edges of the unit cell, i.e., at $(0, \frac{1}{2})^{qc}$, $(\frac{1}{2}, 0)^{qc}$ and at translationally equivalent positions. (The superscript qc denotes that the positions are defined with respect to the square superlattice, spanned by the vectors of eqn. (10.13).) Note that only the pattern of areas in which short and long bonds occur show this symmetry, the embedded structure itself does not, because of the filling of the 1+1-dimensional unit cell. The fourfold symmetry causes two faces $(hm)_s$ and $(m\bar{h})_s$, which are perpendicular, to cut long and short bonds in the same ratio. Since this ratio determines the surface free energy, the faces $(hm)_s$ and $(m\bar{h})_s$ have the same morphological importance. The grid of netplanes $(m\bar{h})_s$ generally divides the physical quasi-crystal into intervals with a different length compared to the grid of netplanes $(hm)_s$. Nevertheless, the two grids intersect short and long bonds in the same ratio. This is another example of a symmetry aspect understood directly if the superspace description is used.

In the quasi-crystal description all faces, except $(11)_s$, $(10)_s$, $(1\bar{1})_s$ and $(01)_s$, start to cut only long bonds at a critical minimal value of α. (The four exceptional faces can be positioned, for any value of α, in such a way that they do not cut short bonds.) The critical value is relatively low for faces with low indices and relatively high for faces with high indices, as can be seen from figure 10.6. Consequently, faces with low indices in the embedding as a quasi-crystal generally have either a smaller or the same surface free energy compared to faces with high indices and thus have a larger or equal morphological importance. This correlation is less obvious from the embedding as a modulated crystal. Since a description is preferred in which the faces with the lowest indices have the largest morphological importance, we state that a one-dimensional quasi-crystal is embedded in superspace less naturally if it is regarded as a one-dimensional modulated crystal.

10.8 The two-dimensional octagonal quasi-crystal

The surface free energy in superspace of a face $(hm)_s$ in the Fibonacci chain of atoms proves to be dependent on its position. The current section examines whether this is also the case for a face in a two-dimensional octagonal quasi-crystal. For this purpose, the superspace approach is used to calculate the average surface free energy of a grid of netplanes $(hklm)_s$.

A model is used in which the atoms of the quasi-crystal are located at the vertices of a quasi-periodic two-dimensional tiling. A tiling is a structure that is obtained if the space is quasi-periodically filled with tiles from a set of two or more. Tilings were described mathematically before quasi-crystalline phases were discovered (Penrose, 1979).

The vertices of an octagonal tiling form a rank four module M that is spanned by four vectors which point, together with their opposites, to the vertices of a regular octagon. The positions of the vertices of the tiling are given by vectors $\boldsymbol{n}$, defined on an orthonormal basis:

$$n = \sum_{i=1}^{4} n_i \, a_i, \quad n_i \text{ integers },$$

$$a_1 = (1,0), \quad a_2 = \frac{1}{2}\sqrt{2}(1,1), \qquad (10.26)$$

$$a_3 = (0,1), \quad a_4 = \frac{1}{2}\sqrt{2}(-1,1).$$

The tiling can be built from two prototiles, a square one and a rhombic one with angles of 45° and 135°. The edges of both prototiles are equal; their length is that of the basis vectors $\{a_i\}$. Figure 10.8 shows a part of an octagonal tiling.

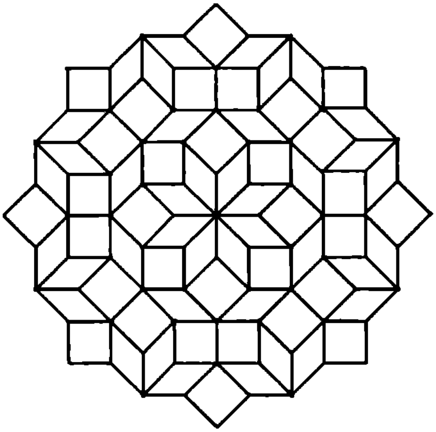

Figure 10.8 A part of a two-dimensional octagonal tiling If we assume that the vertices of the tiling correspond to atomic positions and the edges of the tiling to chemical bonds, this figure also represents the two-dimensional octagonal quasi-crystal

The superspace embedding of the four generators $\{a_i\}$ of the vector module M with respect to an orthonormal basis is given by (Janner, 1991):

$$a_{1s} = (1,0;1,0), \quad a_{2s} = \frac{1}{2}\sqrt{2}(1,1;-1,1), \qquad (10.27)$$

$$a_{3s} = (0,1;0,-1), \quad a_{4s} = \frac{1}{2}\sqrt{2}(-1,1;1,1).$$

The first two coordinates of these vectors represent the component in the physical space, the last two the component in the internal space. Note that the lattice is hypercubic since the basis $\{a_{is}\}$ is orthogonal and its vectors all have the same length.

The following procedure is adopted to embed a two-dimensional octagonal quasi-crystal in superspace (Janner, 1991). Two-dimensional atomic surfaces are attached to the vertices of the 2+2-dimensional hypercubic lattice. These atomic surfaces, representing the atoms in the embedded structure, are defined as the projection of the unit cell on the internal space. Consequently, they have no component in the physical space. The surfaces are attached to the vertices of the lattice in their 'centers of gravity'. Accordingly, the embedded structure is given by:

$$\sum_{i=1}^{4} k_i \, \boldsymbol{a}_{is} + V_p, \quad k_i \text{ integers }, \tag{10.28}$$

$$V_p \ = \ \left\{ \boldsymbol{x} \in V_I \,\middle|\, \boldsymbol{x} = \sum_{i=1}^{4} \lambda_i \boldsymbol{a}_{is,I} \ , \ \ \lambda_i \in [\, -\frac{1}{2}, \frac{1}{2} \rangle \right\} ,$$

where V_p represents the atomic surfaces; $\boldsymbol{a}_{is,I}$ denotes the internal component of the vector $\boldsymbol{a}_{is}$. The octagonal quasi-crystal is formed by the intersection of the embedded structure with the physical space. Note that an atomic surface intersects the physical space in, at most, a single point.

The atoms of the two-dimensional quasi-crystal can be connected by bonds in several ways. In the current paper, we only define bonds between atoms separated by one of the vectors $\{ a_i \}$ of eqn. (10.26). In other words, each edge of the tiling is equivalent to a bond. An edge of the tiling in the physical space corresponds to an edge of a hypercubic unit cell in superspace. Accordingly, only bonds are defined between atoms corresponding to atomic surfaces connected by an edge of a hypercubic unit cell. Our definition of bonds is therefore a natural choice in the superspace description. It is discussed above that all edges of the tiling have the same length. Since the bond energy is only a function of the bond length, all bonds have the same energy.

The concept of chemical bonds can be extended to the 2+2-dimensional superspace by defining a density of bonds of equal length connecting the atomic surfaces in superspace with each other for each pair of phases (ϕ_1, ϕ_2) along the two internal axes. As in the one-dimensional case, these bonds are defined parallel to the physical space. A bond between two atoms along an edge of the two-dimensional tiling in the physical space corresponds to a dense set of bonds between two first-nearest neighbours in superspace, where first-nearest neighbours are atomic surfaces whose centers of gravity are connected by an edge of a unit cell. Since the unit cell of the superlattice is 2+2-dimensional, each atomic surface has first-nearest neighbours in four directions. Hence, there are four different types of bonds between an atomic surface and its first-nearest neighbours. In contrast with the one-dimensional case, bonds are only found in specific sections of the superspace. Inside these sections, the bond density is uniform.

Analogously to the one-dimensional case, a number of crystallographic concepts can be extended to the 2+2-dimensional superspace. A three-dimensional crystallographic hyperplane $(hklm)_s$ is defined perpendicular to the vector

$$\boldsymbol{H}_{(hklm),s} = h\boldsymbol{a}_{1s} + k\boldsymbol{a}_{2s} + l\boldsymbol{a}_{3s} + m\boldsymbol{a}_{4s} \ . \tag{10.29}$$

The extensions of the concepts of interplanar distance and mesh area are analogous to eqns. (10.11) and (10.12), respectively. A grid of netplanes $(hklm)_s$ with interplanar distance $d_{(hklm),s}$ can be constructed in superspace. The intersection of such a grid with the physical space forms an infinite set of equidistant lines.

Owing to the lattice periodicity of the 2+2-dimensional embedded structure, each bond in the physical space that is intersected by a grid of netplanes $(hklm)_s$ is translationally equivalent to a bond in superspace intersected by one specific hyperplane $(hklm)_s$. Therefore, the part of the uniform density of bonds this hyperplane intersects represents the bonds in the physical space that are intersected by the grid of netplanes $(hklm)_s$. Analogously to the one-dimensional case, this implies that calculating the broken bond energy per mesh area of a single hyperplane $(hklm)_s$ is equivalent to calculating the average surface energy of the intersection of the grid of netplanes $(hklm)_s$ with the physical space.

In general, a grid of netplanes $(hklm)_s$ intersects only part of the dense set of bonds in superspace. Therefore, the surface free energy Γ in superspace is generally different for each hyperplane $(hklm)_s$. This selectivity principle can be used to distinguish between the stabilities of different grids. The principle implies that Γ generally depends on the position of the origin. Consequently, the minimum value of Γ can be found by shifting the hyperplane with respect to the origin.

Analogously to the one-dimensional case, a quantity γ_{grid} can be defined as

$$\gamma_{\text{grid}} = \frac{\Gamma}{|\cos\theta|}, \tag{10.30}$$

where θ denotes the angle between the normal vector $\boldsymbol{H}_s$ in superspace and its projection on the physical space. The value of γ_{grid} has been taken as a measure for the morphological importance of a face $(hklm)_s$.

Calculations have been done for faces $(hklm)_s$ for which $-2 \leq h, k, l, m \leq 2$. Integrations have been performed numerically. In order to minimise Γ, hyperplanes have been shifted along their normal vectors over 750 different phases.

The plane symmetry of a two-dimensional octagonal tiling is 8mm (Steurer, 1990). Because of the eightfold symmetry axis the face $(hklm)_s$ is equivalent to the face $(\bar{m}hkl)_s$; because of the two mirror operations the face $(hklm)_s$ is equivalent to both the face $(mlkh)$ and the face $(lkh\bar{m})_s$. The number of morphologically nonequivalent faces is largely reduced by this symmetry.

Calculations have shown that the values of γ_{grid} depend on the position of the grid. In other words, γ_{grid} generally alters if the grid of netplanes is shifted in the direction of the normal vector. The calculated minimum values of γ_{grid} are listed in table 10.1. It is seen that faces with the same orientation in the physical space have different minimum values of γ_{grid}. Compare, e.g., the faces $(0110)_s$, $(1001)_s$ and $(1111)_s$; in table 10.1, the face $(0110)_s$ is represented by the face $(1100)_s$, which is equivalent because of the eightfold symmetry.

face	γ	*face*	γ
$\{1000\}$	2.822	$\{21\bar{1}1\}$	3.029
$\{1100\}$	2.611	$\{2\bar{1}11\}$	3.109
$\{1010\}$	2.698	$\{2120\}$	2.805
$\{1001\}$	3.112	$\{2201\}$	3.034
$\{1110\}$	2.706	$\{2210\}$	2.885
$\{1\bar{1}10\}$	2.704	$\{2102\}$	3.069
$\{1101\}$	2.992	$\{2021\}$	3.133
$\{1111\}$	2.834	$\{2\bar{1}02\}$	3.056
$\{11\bar{1}1\}$	3.151	$\{2\bar{1}20\}$	2.805
$\{2100\}$	3.085	$\{2211\}$	2.972
$\{2010\}$	3.130	$\{2121\}$	3.122
$\{2001\}$	3.108	$\{2112\}$	3.139
$\{2110\}$	3.058	$\{221\bar{1}\}$	2.742
$\{2101\}$	2.969	$\{22\bar{1}1\}$	3.128
$\{2011\}$	3.008	$\{2\bar{1}21\}$	3.131
$\{210\bar{1}\}$	2.826	$\{21\bar{1}2\}$	2.976
$\{201\bar{1}\}$	2.948	$\{2\bar{1}\bar{1}2\}$	3.145
$\{20\bar{1}1\}$	3.080	$\{2221\}$	3.013
$\{2\bar{1}01\}$	2.817	$\{2212\}$	3.139
$\{2111\}$	3.012	$\{2\bar{2}21\}$	3.007
$\{211\bar{1}\}$	3.114	$\{22\bar{1}2\}$	2.962

Table 10.1: Calculated values of γ_{grid} for the two–dimensional octagonal quasi-crystal. Only faces that are not symmetry equivalent are shown.

10.9 Discussion

The morphology of the two-dimensional pentagonal quasi-crystal has been discussed by Ho (1991). The quasi-crystal was represented there by a Penrose tiling. Each tile was regarded as an atom and bonds were defined between neighbouring tiles with bond directions perpendicular to the edges of the tiling. It was shown that the surface free energy of an arbitrary face is independent of its position for this structure. The argumentation leading to this conclusion is also valid for the two-dimensional octagonal tiling. Therefore, the surface free energy in a two-dimensional octagonal quasi-crystal would not depend on the position of the face if atoms were represented by tiles and if bonds are defined between neighbouring tiles, with bond directions perpendicular to the edges of the tiling.

In the current paper, atoms are represented by the vertices of the tiling and each edge is considered to be a bond. It has been found that in this case the surface free energy of a grid of netplanes $(hklm)_s$ is dependent on the position of the grid. If the surface free energy of a single face $(hklm)_s$ were independent of its position, γ_{grid} would *not* depend on the position of the grid. Thus, it is proved that in our model the surface free energy of a single face is dependent on its position. Therefore, the result found by Ho is a consequence of the definitions of atoms and bonds used. In general, it will not hold if other definitions are used. Since the surface free energy of a single face $(hklm)_s$ depends on its position, grids of netplanes $(hklm)_s$ which have the same orientation in the physical space generally have different surface free energies, as is shown by Table 1. This result will be used in part II of the paper (Heijmen et al., 1995) to determine the surface free energy of a single face $(hklm)_s$.

10.10 Conclusions

The present paper shows that the superspace description for the morphology of one-dimensional incommensurately modulated crystals can be generalised to the case of one-dimensional quasi-crystals.

The Fibonacci chain of atoms can be embedded in a 1+1-dimensional superspace in two different ways. The two descriptions prove to be equivalent in determining the stabilities of crystal faces. Crystallographic faces are labeled with different indices in the quasi-crystal embedding compared to the embedding as a modulated crystal. Calculated surface free energies indicate that low-index faces are more stable than high-index faces in the quasi-crystal description. This correlation is less strong in the description as a modulated crystal.

Several symmetry aspects concerning the equilibrium forms of quasi-crystals can be explained more easily if the superspace description is used. It is found that a one-dimensional quasi-periodic chain of atoms can be cut in intervals of equal length in such a way that only long bonds are broken. In addition, the superspace description as a quasi-crystal shows that the grids of netplanes $(hm)_s$ and $(m\bar{h})_s$ intersect long and short bonds in the same ratio, although the two grids generally have different interplanar distances in the physical space.

The superspace approach can be extended to the case of the two-dimensional octagonal quasi-crystal. In the present paper, it is used to calculate the average surface free energies of grids of netplanes. The results provide evidence that the stability of a single crystal face depends on its position. On the other hand, Ho (1991) has found that the stability is independent of the position of the face if specific definitions of atoms and bonds are chosen. Obviously, the problem of determining the stability of crystallographic faces in quasi-crystals is more complex than Ho's approach suggests.

The superspace description of quasi-crystals proves to be of great help in solving this problem. In part II of the present paper (Heijmen et al., 1995), we will use this description to give an explanation for the equilibrium form of the two-dimensional octagonal quasi-crystal. Our final aim is a theory, based on the superspace description, which enables us to deal with three-dimensional quasi-crystals for arbitrary definitions of atoms and chemical bonds.

Acknowledgments

The authors are greatly indebted to M.A. Verheijen and Professor P. Bennema for their collaboration, especially in an early stage of the project, and stimulating interest. We want to thank Prof. T. Janssen for helpful discussions.

References

Balzuweit, K., Meekes, H., and Bennema, P., *J. Phys. D: Appl. Phys.* **24**, 203 (1991).

Balzuweit, K., Meekes, H., van Tendeloo, G., and de Boer, J.L., *Phil. Mag.* B**67**, 513 (1993).

Beeli, C., and Nissen, H.U., *Phil. Mag.* B**68**, 487 (1993).

Bennema, P., Balzuweit, K., Dam, B., Meekes, H., Verheijen, M.A., and Vogels, L.P.J., *J. Phys. D: Appl. Phys.* **24**, 1986 (1991).

Bennema, P., Kremers, M., Meekes, H., Balzuweit, K., and Verheijen, M.A., *Faraday Discuss.* **95/2** (1993).

Dam, B., Janner, A., and Donnay, J.D.H., *Phys. Rev. Lett.* **21**, 2301 (1985).

Heijmen, T.G.A., Kremers, M., Meekes, H., and Janssen, T., to be published, (1995).

Herring, C., *Phys. Rev.* **82**, 87 (1951).

Herring, C., *Structure and Properties of Solid Surfaces*, edited by R. Gomer and C.S. Smith, (Chicago: Press, 1953).

Ho, T.L., *Quasicrystals: The State of the Art*, edited by D.P. DiVincenzo and P. Steinhardt, (Singapore: World Scientific, 1991).

Janner, A., *Studies in Physical and Theoretical Chemistry*, Vol. 23 (Amsterdam: Elsevier, 1983).

Janner, A., *Acta Cryst.* A**47**, 577 (1991).

Janner, A., Rasing, Th., Bennema, P., and van der Linden, W.H., *Phys. Rev. Lett.* **45**, 1700 (1980).

Janssen, T., and Janner, A., *Adv. in Phys.* **36**, 519 (1987).

Kremers, M., Meekes, H., Bennema, P., Balzuweit, K., and Verheijen, M.A., *Phil. Mag.* B**69**, 69 (1994).

Penrose, R., *Math. Intell.* **2**, 32 (1979).

Steurer, W., *Z. Krist.* **190**, 179 (1990).

Summary

This thesis has been devoted to the study of both optical and morphological properties of incommensurate crystals. In this class of crystals one can distinguish incommensurately modulated crystals, incommensurate composite crystals and quasi-crystals. All of them have in common that they have a structure involving more than three fundamental Fourier wave vectors (all the others being expressible as integral linear combinations of these fundamental ones). Therefore, these crystals do not possess 3-dimensional lattice translational symmetry. The presence of such a symmetry, however, is one of the classical definitions of a crystal. Incommensurately modulated crystals are non-classical in this sense.

The description of physical properties of classical crystals is essentially based on the lattice translational symmetry. This thesis treats some of the consequences of the absence of such a symmetry in the case of incommensurate crystals. Two points of view can be taken in this respect. In part I the experimental search is described for physical properties that can only result from the incommensurateness. This is done by trying to detect optical properties of incommensurately modulated crystals that were previously predicted in a theoretical approach and that would not be allowed if there were no modulation. In part II the other point of view is taken. There, a theoretical model is discussed allowing to interpret morphological observations. In this approach the possibility of embedding an incommensurate crystal in a so-called superspace is used. The advantage is that the embedded crystal again has a translation lattice, although the dimension of this lattice is that of the superspace.

In part I, first a macroscopic phenomenological description is given of classical crystal optics. The optical properties of incommensurately modulated crystals can be treated along similar lines if long wavelength Fourier components of optical material tensors are taken into consideration. In this way one derives that gyration effects may occur in incommensurately modulated crystals, even if they are centrosymmetric if one averages the effect of the modulation. In the same way it is found that a rotation of the optical indicatrix can occur in incommensurately modulated crystals that are orthorhombic after such an averaging. Experimentally, the optical properties of incommensurately modulated crystals are studied by means of a High Accuracy Universal Polarimeter (HAUP). This apparatus is suited for the measurement of several very small optical effects which are simultaneously present together with a large linear birefringence. First, this method is critically reviewed. The necessary expressions are rigorously derived and the relevant fitting procedures are accurately reconsidered. The behaviour of the systematic errors of the method is studied by means of test experiments. Several flaws in both the experimental set-up and the interpretation of the measurements are detected and the necessary improvements are described. In this way, both the sensitivity and reliability of HAUP have been increased to a definitely acceptable level for the study of the optical properties of incommensurately modulated crystals.

There are several examples of coloured incommensurate crystals. These absorb light and can, therefore, be dichroic. There is, therefore, a need for a method of measuring the optical properties of dichroic crystals. It is shown that HAUP is suited for this purpose. The corresponding, so-called unified HAUP intensity formula is derived. This gives the possibility of determining the (complex) eigenpolarisations of an arbitrary sample, provided that the reciprocal linear birefringence (or the reciprocal linear dichroism) is relatively large. In the case of $NiSO_4 \cdot 6H_2O$ measurements of the linear birefringence, linear dichroism, circular birefringence and circular dichroism are presented. It is even possible to measure, with this method, non-reciprocal optical effects that can occur in magnetically ordered crystals.

The HAUP method is subsequently put to use for the simultaneous measurement of linear birefringence and optical activity in the incommensurately modulated phase of $((CH_3)_4N)_2ZnCl_4$. This phase is centrosymmetric if one averages the effect of the modulation. For the three components g_{11}, g_{13} and g_{33} of the gyration tensor that are studied with the thoroughly tested set-up the values are always zero or too small to be detected. Clearly non-zero values have been found, however, by other authors for the same material. The reasons for this controversy may be found in the sample quality, thermal treatment of the samples or an incorrect interpretation of the measurements.

After this, the optical properties of dichroic $((CH_3)_4N)_2CuCl_4$ crystals are studied with HAUP. Two samples are used that have been prepared in such a way that both the components g_{33} and g_{13} of the gyration tensor can be measured. The measurements reveal that the crystals have a low defect concentration. The linear birefringence clearly shows the presence of the incommensurate modulation, contrary to the linear dichroism. Two effects are observed that are symmetry-forbidden by the centrosymmetric, orthorhombic structure that is believed to result from averaging the effect of the modulation. The first of them is the rotation of the optical indicatrix, that is forbidden in an orthorhombic crystal. The second is non-zero optical activity g_{13}, forbidden in centrosymmetric media. However, the observed behaviour is again different from that found by other authors. One has to add that the precise symmetry of the incommensurate phase has not yet been determined.

The last set of measurements are performed on non-dichroic crystals of $((CH_3)_4N)_2ZnCl_{2.8}Br_{1.2}$. Although this is a solid solution, it is still possible to obtain sharp diffraction spots in an X-ray diffraction experiment. The presence of an incommensurately modulated phase can be observed in this way. The difference of Cl and Br can not be neglected, however, for the optical properties. The inversion symmetry is broken already in the high temperature phase that precedes the incommensurate phase. A non-zero optical activity is indeed observed in this high temperature phase. This, however, allows one to study the influence of the modulation on a non-zero optical activity. This influence is clearly shown for a sample in which the modulation is believed to lock at several commensurate values.

In part II of this thesis the equilibrium forms of incommensurate crystals are studied from a theoretical point of view. The more or less academic case of an incommensurately modulated 1-dimensional crystal is treated first. It is shown that crystallographic concepts can be generalised to superspace. Using these generalisations one recognises that a principle of selective cuts holds in superspace. Subsequently, it is made plausible that this principle explains the occurrence of so-called satellite faces on the crystals. These are non-classical crystal faces whose orientations can be characterised by two integral indices. Such a face is then perpendicular to a vector of the $\mathbb{Z}$-module that characterises the Fourier transform of the density of the crystal. The necessity of two indices distinguishes incommensurately modulated from classical crystals for which only a single index is needed.

Subsequently the approach is extended to the case of 3-dimensional incommensurately modulated crystals. As a result, at least four indices are needed four modulated crystal faces, whereas in the case of classical crystal faces three indices are necessary and sufficient. This aspect was found already in experiments. Concerning the morphology a one-to-one correspondence exists between faces on the actual physical crystal and crystallographic hyperplanes that can be identified in the embedded crystal in superspace. It is shown that the stability of satellite faces can indeed be attributed to the principle of selective cuts. Within a broken-bond model a calculation method is developed for determining surface free energies of faces on incommensurately modulated crystals of arbitrary complexity. By studying the dependence of the calculated equilibrium morphology of a modulated cubic crystal on several structural parameters, a first understanding is possible of the differences in morphology of $AuTe_2$ and $((CH_3)_4N)_2ZnCl_4$ crystals. In addition, it is explained that it is very likely that the superspace approach can successfully be applied to incommensurate composite crystals and quasi-crystals as well.

For the latter case already some results are given for a 1-dimensional quasi-crystal model: the Fibonacci chain of atoms. This chain can also be considered as an incommensurately modulated 1-dimensional crystal. The equilibrium morphology can, consequently, be calculated in two different ways. It turns out that the quasi-crystal description deals with the occurring symmetry in a more natural way. A first investigation of 2-dimensional quasi-crystals is also made for the case of the octagonal tiling. It is found that the surface free energy of a crystallographic face with fixed orientation is not independent of the position of that face.

Samenvatting

Dit proefschrift is gewijd aan de bestudering van zowel optische als morfologische eigenschappen van incommensurabele kristallen. In deze klasse van kristallen kan men incommensurabel gemoduleerde kristallen, incommensurabel samengestelde kristallen en quasikristallen onderscheiden. Alle incommensurabele kristallen hebben gemeenschappelijk dat er in hun structuur meer dan drie fundamentele Fourier golfvectoren zijn (alle andere kunnen worden uitgedrukt als geheeltallige lineaire combinaties van deze fundamentele golfvectoren). Ten gevolge daarvan hebben deze kristallen geen 3-dimensionale roostertranslatiesymmetrie. De aanwezigheid van zo'n symmetrie is echter een van de klassieke definities van het begrip kristal. Incommensurabele kristallen zijn, in deze zin, niet klassiek.

De beschrijving van fysische eigenschappen van klassieke kristallen gaat vaak uit van roostertranslatiesymmetrie. Dit proefschrift behandelt enkele gevolgen van het ontbreken van zo'n symmetrie in het geval van incommensurabele kristallen. Twee uitgangspunten kunnen in dit verband gekozen worden. Deel I beschrijft het experimentele zoeken naar fysische eigenschappen die alleen veroorzaakt kunnen worden door de aanwezigheid van incommensurabiliteit. Dit wordt gedaan door te proberen optische eigenschappen van incommensurabel gemoduleerde kristallen te vinden die reeds eerder voorspeld waren in een theoretische benadering en die niet toegestaan zouden zijn als er geen modulatie was. In deel II wordt het andere uitgangspunt gekozen. Er wordt daar een theoretisch model gepresenteerd waarmee morphologische waarnemingen geïnterpreteerd kunnen worden. In deze aanpak wordt gebruik gemaakt van de mogelijkheid een incommensurabel kristal in te bedden in een zogenaamde superruimte. Het voordeel daarvan is dat het ingebedde kristal weer een translatierooster heeft, hoewel de dimensie van dit rooster gelijk is aan die van de superruimte.

In deel I wordt eerst een macroscopische fenomenologische beschrijving gegeven van klassieke kristal optica. De optische eigenschappen van incommensurabel gemoduleerde kristallen kunnen behandeld worden op een gelijksoortige manier wanneer lange golflengte Fourier componenten van optische materiaaltensoren worden meegenomen. Men leidt op deze manier af dat gyratie effecten kunnen optreden in incommensurabel gemoduleerde kristallen zelfs wanneer deze centrosymmetrisch zijn als het effect van de modulatie wordt uitgemiddeld. Op dezelfde manier wordt gevonden dat een rotatie van de optische indicatrix kan voorkomen in incommensurabel gemoduleerde kristallen die na zo'n middeling orthorhombisch zijn.

De optische eigenschappen van incommensurabel gemoduleerde kristallen worden experimenteel onderzocht met behulp van een High Accuracy Universal Polarimeter (HAUP). Dit apparaat is geschikt voor het meten van verschillende zeer kleine optische effecten die tegelijkertijd met een grote lineaire dubbelbreking aanwezig zijn. Deze methode wordt eerst kritisch bekeken. De benodigde uitdrukkingen worden rigoureus afgeleid en de relevante fitprocedures worden nauwkeurig beschouwd. Het gedrag van de systematische fouten van de methode wordt bestudeerd middels testexperimenten. Verschillende zwakke punten in zowel de experimentele opzet als de interpretatie van de metingen worden opgespoord en de noodzakelijke verbeteringen worden beschreven. Zowel de gevoeligheid als de betrouwbaarheid van HAUP zijn hierdoor vergroot tot een voldoende acceptabel niveau voor de bestudering van de optische eigenschappen van incommensurabel gemoduleerde kristallen.

Er zijn verschillende voorbeelden van gekleurde incommensurabele kristallen. Deze absorberen licht en kunnen, daarom, dichroïsch zijn. Om deze reden bestaat er een behoefte aan een methode voor het meten van de optische eigenschappen van dichroïsche kristallen. Er wordt aangetoond dat HAUP voor dit doel geschikt is. De corresponderende, zogenaamde unificerende HAUP intensiteitformule wordt afgeleid. Dit geeft de mogelijkheid om de (complexe) optische eigenpolarisaties van een willekeurig kristal te bepalen, onder de voorwaarde dat de reciproke lineaire dubbelbreking (of het reciproke lineaire dichroïsme) relatief groot is. Voor het geval van $NiSO_4 \cdot 6H_2O$ worden metingen getoond van de lineaire dubbelbreking, het lineaire dichroïsme, de circulaire dubbelbreking en het circulaire dichroïsme. Met deze methode is het zelfs mogelijk niet reciproke optische effecten te meten die kunnen optreden in magnetisch geordende kristallen.

De HAUP methode wordt vervolgens ingezet voor het gelijktijdig meten van lineaire dubbelbreking en optische activiteit in de incommensurabel gemoduleerde fase van $((CH_3)_4N)_2ZnCl_4$. Deze fase is centrosymmetrisch wanneer het effect van de modulatie uitgemiddeld wordt. In het geval van de drie gyratie tensor componenten g_{11}, g_{13} en g_{33} die onderzocht worden met de uitvoerig geteste methode, zijn de waarden steeds nul of te klein om opgemerkt te worden. Andere auteurs hebben echter duidelijk waarden verschillend van nul gevonden voor hetzelfde materiaal. De oorzaken voor deze controverse kunnen liggen in de kristal kwaliteit, de thermische behandeling van de preparaten of in een onjuiste interpretatie van de metingen.

Vervolgens worden de optische eigenschappen van dichroïsche $((CH_3)_4N)_2CuCl_4$ kristallen bestudeerd met HAUP. Twee samples worden gebruikt die zodanig geprepareerd zijn dat beide gyratietensorcomponenten g_{33} en g_{13} gemeten kunnen worden. De metingen laten zien dat de kristallen een lage defectconcentratie hebben. De lineaire dubbelbreking toont duidelijk de aanwezigheid van de incommensurabele modulatie, in tegenstelling tot het lineair dichroïsme. Er worden twee effecten waargenomen die om symmetrieredenen verboden zijn in de centrosymmetrische orthorhombische structuur die vermoed wordt het resultaat te zijn indien het effect van de modulatie uitgemiddeld zou worden. Het eerste effect is de rotatie van de optische indicatrix, wat verboden is in een orthorhombisch kristal. Het tweede is een eindige optische activiteit g_{13}, verboden in centrosymmetrische media. Het waargenomen gedrag is echter, helaas, opnieuw anders dan dat gevonden door andere auteurs. Er moet worden opgemerkt dat de symmetrie van de incommensurabele fase nog niet precies bepaald is.

De laatste set metingen wordt verricht aan niet dichroïsche kristallen van

$((CH_3)_4N)_2ZnCl_{2.8}Br_{1.2}$. Hoewel dit een zogenaamd mengkristal is, is het toch mogelijk om scherp gedefinieerde diffractieintensiteiten te krijgen in een röntgendiffractieexperiment. De aanwezigheid van een incommensurabel gemoduleerde fase kan zo worden aangetoond. Het verschil tussen Cl en Br is echter niet verwaarloosbaar voor de optische eigenschappen. De inversiesymmetrie is al verbroken in de hoge temperatuurfase die aan de incommensurabele fase voorafgaat. Een van nul verschillende optische activiteit wordt dan ook al waargenomen in deze hoge temperatuurfase. Dit geeft echter de mogelijkheid om de invloed van de modulatie op een van nul verschillende optische activiteit te bestuderen. Deze invloed wordt duidelijk getoond in het geval van een kristal waarvan kan worden aangenomen dat de modulatie meerdere commensurabele waarden aanneemt.

In deel II van dit proefschrift worden de evenwichtsvormen van incommensurabele kristallen bestudeerd middels een theoretische aanpak. Het min of meer academische geval van een incommensurabel gemoduleerd 1-dimensionaal kristal wordt eerst behandeld. Er wordt aangetoond dat kristallografische concepten naar de superruimte gegeneraliseerd kunnen worden. Met behulp van deze generalisaties herkent men een principe van selectieve sneden in de superruimte. Het wordt vervolgens aannemelijk gemaakt dat dit principe het verschijnen van zogenaamde satellietvlakken op de kristallen verklaart. Satellietvlakken zijn niet klassieke vlakken wier oriëntaties gekarakteriseerd kunnen worden met twee heeltallige indices. Zo'n vlak staat dan loodrecht op een vector van de $\mathbb{Z}$-module die de Fouriergetransformeerde van de dichtheid van het kristal karakteriseert. De noodzaak van twee indices onderscheid incommensurabele van klassieke kristallen voor welke slechts één index nodig is.

Vervolgens wordt de aanpak uitgebreid naar het geval van incommensurabel gemoduleerde 3-dimensionale kristallen. Het gevolg is dat voor de incommensurabele kristalvlakken tenminste vier indices nodig zijn, terwijl voor klassieke kristalvlakken drie indices nodig en voldoende zijn. Dit aspect werd al experimenteel waargenomen. Wat betreft de morfologie bestaat er een één op één correspondentie tussen vlakken op het fysische kristal en kristallografische hypervlakken in de superruimte. Er wordt aangetoond dat de stabiliteit van satellietvlakken inderdaad kan worden toegeschreven aan het principe van selectieve sneden. Binnen een gebroken binding model wordt een berekeningsmethode ontwikkeld om de oppervlakte vrije energieën van vlakken op incommensurabel gemoduleerde kristallen met een willekeurig complexe structuur te bepalen. Door de afhankelijkheid van verscheidene structurele parameters te bestuderen voor berekende evenwichtsvormen van een gemoduleerd kubisch kristal is een eerste inzicht mogelijk betreffende de verschillende morfologieën van $AuTe_2$ en $((CH_3)_4N)_2ZnCl_4$ kristallen. Verder wordt uitgelegd dat het erg waarschijnlijk is dat de superruimteaanpak ook met succes kan worden toegepast op incommensurabel samengestelde structuren en quasikristallen

Betreffende het laatste geval worden enige resultaten getoond voor een 1-dimensionaal quasikristal model: de Fibonacciketen van atomen. Deze keten kan ook worden beschouwd als een incommensurabel gemoduleerd 1-dimensionaal kristal. De evenwichtsmorfologie kan, daarom, op twee verschillende manieren worden berekend. De beschrijving als quasikristal behandelt de optredende symmetrie op een meer natuurlijke manier. Een eerste studie van 2-dimensionale quasikristallen wordt ook gemaakt voor het geval van de zogenaamde octagonale vlakvulling. Er wordt gevonden dat de oppervlakte vrije energie van een kristallografisch vlak met vaste oriëntatie niet onafhankelijk is van de positie van dat vlak.

List of Publications

1. Kremers, M.,
   "Calaverite, a study of its optical properties"
   Master Thesis, University of Nijmegen (1989a).
2. Kremers, M.,
   "Theory and applications of reflection in crystal optics"
   Master Thesis, University of Nijmegen (1989b).
3. Dijkstra, E., Kremers, M. and Devillers, M.A.C.,
   "Optical properties of calaverite, $AuTe_2$ "
   Z. Phys. B - Condensed Matter **76**, 487 (1989).
4. Kremers, M.,
   "Point-contact spectroscopy of incommensurately modulated calaverite"
   Master Thesis, University of Nijmegen (1990a).
5. Kremers, M., Krutzen, B. C. H. and Dijkstra, E.,
   "Reflection experiments on incommensurately modulated calaverite"
   Ferroelectrics **105**, 119 (1990b).
6. Krutzen, B. C. H. and Kremers, M.,
   "Calculated optical properties of approximate structures
   for incommensurately modulated calaverite"
   Ferroelectrics **105**, 125 (1990).
7. Dijkstra, E., Meekes, H. and Kremers, M.,
   "The high-accuracy universal polarimeter"
   J. Phys. D: Appl. Phys **24**, 1861 (1991).
8. Dijkstra, E., Kremers, M. and Meekes, H.,
   "Birefringence and optical activity of $((CH_3)_4N)_2ZnCl_4$ "
   J. Phys.: Condens. Matter **4**, 715 (1992).
9. Bennema, P., Kremers, M., Meekes, H., Balzuweit, K. and Verheijen, M.,
   "Explanation for the Occurrence of $\{hklm\}$ Faces on Modulated Crystals"
   Discuss. Faraday Soc. **95**, 2 (1993).
10. Kremers, M., Meekes, H., Bennema, P., Balzuweit, K. and Verheijen, M.,
    "A superspace description for the morphology of modulated crystals:
    an explanation for the occurrence of faces $(hklm)$"
    Philosophical Magazine B **69**, 69 (1994).
11. Bennema, P., Kremers, M., Meekes, H., and Verheijen, M.,
    "Morphology of Modulated Crystals"
    Phys. Stat. Sol. (a) **146**, 13 (1994).

12. Heijmen, T., Kremers, M. and Meekes, H.,
"A superspace description for the morphology of quasicrystals.
I. The Fibonacci chain of atoms"
Philosophical Magazine B, in press (1994).

13. Kremers, M. and Meekes, H.,
"The interpretation of HAUP measurements:
a study of the systematic errors"
submitted to J. Phys. D.: Appl. Phys. (1994).

14. Kremers, M., Dijkstra, E. and Meekes, H.,
"Optical Activity in the Incommensurate Phase of $((CH_3)_4N)_2ZnCl_4$
a Controversy"
submitted to Phys. Rev. B (1994).

15. Kremers, M., Meekes, H., Bennema, P., Verheijen, M. A., and van der Eerden J.P.
"Equilibrium morphology of incommensurately modulated crystals,
a superspace description"
submitted to Acta Cryst. A (1994)

16. Kremers, M. and Meekes, H.,
"Influence of the incommensurate modulation
on the optical properties of $((CH_3)_4N)_2CuCl_4$ "
submitted to Phys. Rev. B (1994).

17. Kremers, M. and Meekes, H.,
"Influence of the incommensurate modulation
on the optical properties of the solid solution $((CH_3)_4N)_2ZnCl_{2.8}Br_{1.2}$ "
submitted to Phys. Rev. B (1994).

18. Kremers, M. and Meekes, H.,
"Application of the High Accuracy Universal Polarimeter
to magnetic and absorbing crystals"
submitted to J. Phys. D.: Appl. Phys. (1994).

Curriculum Vitae

Marcel Kremers

Geboren:	24 mei 1967 te Gassel, gemeente Beers
1979-1985	Voorbereidend Wetenschappelijk Onderwijs Merletcollege te Cuijk
augustus 1985	aanvang Scheikunde studie Katholieke Universiteit Nijmegen
augustus 1986	propaedeutisch examen
februari 1990	doctoraal examen Scheikunde behaald met het predikaat *cum laude*
	hoofdvak: op de afdeling Vaste Stof Chemie van Prof. Dr. P. Bennema
	bijvak: op de afdeling Vaste Stof Fysica II van Prof. Dr. H. van Kempen
mei 1990	Prijs van de faculteit der Natuurwetenschappen voor het verrichte wetenschappelijke werk gedurende de gehele afstudeerfase
februari-augustus 1990	onderzoeker bij de afdeling Theoretische Fysica van Prof. Dr. A.G.M. Janner Katholieke Universiteit Nijmegen
augustus 1990 - november 1994	Promotieonderzoek als Onderzoeker In Opleiding voor de Stichting voor Fundamenteel Onderzoek der Materie (FOM) bij de afdelingen: Theoretische Fysica van Prof. Dr. A.G.M. Janner en Vaste Stof Chemie van Prof. Dr. P. Bennema Katholieke Universiteit Nijmegen